

ELECTRONIC STRUCTURES AND
REACTIVITY PATTERNS OF
DIPALLADIUM(II,II) AND
DIPLATINUM(II,II) COMPLEXES

Thesis by

Alec Charles Durrell

In Partial Fulfillment of the Requirements for the

degree of

Doctor of Philosophy

CALIFORNIA INSTITUTE OF TECHNOLOGY

Pasadena, California

2012

(Defended 11 April 2012)

© 2012

Alec Charles Durrell

All Rights Reserved

ACKNOWLEDGEMENTS

During my time at Caltech, I have been fortunate enough to work and interact with a number of brilliant people who have had a huge impact on my scientific path and to whom I owe a great deal of thanks. First and foremost, I must thank my advisor, Harry Gray. I am constantly amazed at Harry's indefatigable enthusiasm and support for me and all his students. He is the model for the chemist I aspire to be. I am a proud member of the Gray Nation. I would also like to thank Jay Winkler. Jay is the prototypical scientist. He is methodical and thorough and goes only where the data takes him. While my enthusiasm sometimes gets the best of me, I have tried to emulate these traits as they can never lead you astray. I am grateful to the other members of my committee, Mitchio Okumura, Nate Lewis, and John Bercaw. While committee meetings were never too common they were always willing to respond to me if I needed them. John, in particular, was always willing to discuss any chemistry concerns I was having.

I owe special thanks to Nilay Hazari. I was incredibly fortunate to begin a collaboration with him that ultimately sparked the bulk of my thesis project. More than that, he has been a great friend to me and I look forward to further developing that friendship upon my move to New Haven.

Brian Leigh mentored me when I first arrived at Caltech. Beyond showing me the ropes around lab, he welcomed me into his social circle, showed me all the best lunch spots in town, and let me join his flag football team. His generosity made my transition to grad school and the West Coast much easier. Paul Oblad, Charlotte Whited, Josh Palmer, and Heather Williamson were a great class to come through the group with. Paul and Charlotte

continue to be great friends and I have enjoyed keeping up with them as their lives have taken them to other parts of the country. I am grateful to Josh both for his friendship and for our collaborations, which allow me to make the dubious claim that I am an expert in corrole photophysics. Ian Tonks is another member of the class with whom I was able to work closely on occasion. I enjoyed our collaborations a great deal. Kyle Lancaster was a wonderful office mate, except for those two months when he would not stop quoting from *Silence of the Lambs*. Despite that, he continues to be a great friend and colleague and I wish him continued success in his scientific pursuits. I thank Bryan Stubbert for many helpful discussions, some of which were even related to science. Jillian Dempsey and I spent a good deal of time together as both TAs for 153 and GLAs in the laser lab. She set a high standard in both and I did my best to maintain that level in my TA and GLA duties after she graduated. As I leave those duties behind, I have complete confidence in Maraia Ener to carry on the standard of excellence. Gretchen Keller has been a great friend and coworker. I am especially grateful to have her as a collaborator on certain difficult projects, where her expertise and demeanor have made things much easier. I have enjoyed working with Yan Choi Lam on his platinum project, and I am happy knowing that he continues to keep d^8-d^8 chemistry alive. Paul Bracher was an amazing person to have down the hall. I deeply enjoyed our conversations on a wide range of topics. Peter Agbo, if you're reading this, get back to work.

During my tenure in the group I was fortunate enough to overlap with many talented postdocs. Matt Hartings was always available for helpful discussions on a broad range of topics. Hema Karunadasa (along with James McKone and Bryan Stubbert) taught me a

great deal about electrochemistry. Astrid Mueller's knowledge and experience with the laser systems was truly beneficial. Jeff Warren was always helpful and in good spirits, despite my constant pestering of him.

Megan Jackson began working with me as a SURF student her freshman year. From the very beginning, she brought enthusiasm and skill to her work. Had she not joined the lab, the last chapter of my thesis may have been much sparser. I am happy that she will be carrying on d^8-d^8 chemistry in her final year at Caltech and wish her continued success in whatever she decides to do next.

I am deeply grateful for all the love and support my family has shown me while in graduate school. I owe a lot to my mom, who has always been supportive in the pursuit of my goals. I would not be who I am today without her hard work. I would also like to thank my dad, who pushed me to always do my best, and who I deeply miss. Living in Pasadena has given me the opportunity to spend more time with my brother-in-law Eric Notarnicola. Despite him being much cooler than me, he is always eager to come hang out or grab dinner. Finally, I must thank my wife. Cristina, you've been there for me since the beginning. You have been supportive, patient, and understanding throughout the entire process. Without your constant encouragement, I probably would not be writing this dissertation. Marrying you was easily the best decision I made while at Caltech. Thank you for putting up with me through almost all these years of grad school.

ABSTRACT

This work explores the electronic structures and reactivity patterns of diplatinum(II, II) and dipalladium(II, II) complexes. Complexes containing metal-metal bonds play important roles in both inorganic and organometallic chemistry. Among the many examples of these complexes, dimers of square planar Rh^{I} , Ir^{I} , and Pt^{II} centers comprise a special class that feature attractive d^8-d^8 interactions. The unique electronic structure characteristic of these complexes gives rise to chemical, photochemical, and photophysical properties that have engaged researchers for the past 35 years.

One of the best-known examples of these compounds is *tetrakis*(μ -pyrophosphito)platinum(II), $\text{Pt}(\text{pop})$. Herein, the photophysical properties of $\text{Pt}(\text{pop})$ are compared with its fluoroborated analogue, $\text{Pt}(\text{pop-BF}_2)$. This complex possesses eight BF_2 groups that replace the hydrogen atoms located between each “pop” ligand. When compared with $\text{Pt}(\text{pop})$, $\text{Pt}(\text{pop-BF}_2)$ has a much greater singlet lifetime (1.56 ns) and singlet quantum yield (0.27). The enhancement is the result of a drastically slower $^1\text{A}_{2u} \rightarrow ^3\text{A}_{2u}$ intersystem crossing rate. In particular, the thermal barrier to intersystem crossing is significantly higher in $\text{Pt}(\text{pop-BF}_2)$ (2230 cm^{-1} vs. 1190 cm^{-1}). We believe this is primarily the result of the increased rigidity of the complex afforded by the BF_2 groups. The rigidity increases the energy of symmetry-lowering vibrational modes, which are necessary to promote spin-orbit mixing of the $^1d\sigma^*p\sigma$ and $^3d\sigma^*p\sigma$ states.

Despite the many examples of M-M bonded d^8-d^8 complexes of Rh^{I} , Ir^{I} , and Pt^{II} in the literature, until recently there were no Pd^{II} complexes fitting this description. Our investigations of clamshell-shaped Pd^{II} dimers $[(2\text{-phenylpyridine})\text{Pd}(\mu\text{-X})]_2$ and $[(2\text{-}p\text{-tolylpyridine})\text{Pd}(\mu\text{-X})]_2$ ($\text{X} = \text{OAc}$ or TFA) revealed short Pd–Pd distances ($\sim 2.85 \text{ \AA}$). The

molecules adopt this unusual geometry in part because of a d^8-d^8 bonding interaction between the two Pd centers. Density functional theory (DFT) and *ab initio* (AI) analyses confirm the presence of a Pd–Pd bonding interaction in [(2-phenylpyridine)Pd(μ -X)]₂ and show that the HOMO is a $d_{z^2} \sigma^*$ Pd–Pd antibonding orbital, while the LUMO and proximal unoccupied orbitals are mainly located on the 2-phenylpyridine rings. Computational analyses of other Pd^{II}–Pd^{II} dimers that have short Pd–Pd distances yield an orbital ordering similar to that of [(2-phenylpyridine)Pd(μ -X)]₂, but quite different from that found for d^8-d^8 dimers of Rh, Ir, and Pt. This difference in orbital ordering arises because of the unusually large energy gap between the 4d and 5p orbitals in Pd, and may explain why Pd d^8-d^8 dimers do not exhibit the distinctive photophysical properties of related Rh, Ir, and Pt species.

Our work on Pd^{II}–Pd^{II} electronic structures led us to employ these complexes as electrocatalysts in the regioselective chlorination of C–H bonds. Previous work on d^8-d^8 complexes has established that when treated with halogens (Cl₂, Br₂, or I₂), the complex undergoes two-center oxidative addition to form an axially coordinated X– d^7-d^7 –X species. Similar products are observed following electrochemical oxidation in the presence of a halide (Cl[–], Br[–], or I[–]). Recently, related Pd^{II}–Pd^{II} complexes were found to selectively chlorinate benzo[*h*]quinoline through reductive elimination from a Cl–Pd^{III}–Pd^{III}–Cl species. This led us to probe the viability of the analogous electrochemical route. Cyclic voltammetry, spectroelectrochemistry, and bulk electrolysis measurements confirm that electrochemical oxidation of Pd^{II}–Pd^{II} yields the identical Cl–Pd^{III}–Pd^{III}–Cl intermediate, which is capable of reductive chlorination of C–H bonds. Additional evidence for formation of axially coordinated bromide and acetate species is also presented. Over 10

turnovers of 10-chlorobenzo[*h*]quinoline were achieved at 80% isolated yield. Further research into the area may lead to a potentially versatile, useful, and green route for C–H bond functionalization reactions.

TABLE OF CONTENTS

Acknowledgements	iii
Abstract	vi
Table of Contents	ix
List of Figures	xi
List of Schemes	xiv
List of Tables	xv
Chapter 1: Electronic structures, photophysical and photochemical properties, and reactivity of d^8-d^8 binuclear complexes	1
1.1 Introduction	2
1.2 Electronic structures	3
1.3 Photophysical properties	8
1.4 Chemical properties	11
1.5 Photochemical properties	12
1.6 Binuclear palladium(II) complexes	15
1.7 References	17
Chapter 2: Twist it to mix it! $^1A_{2u}$ -to- $^3A_{2u}$ intersystem crossing in diplatinum(II,II) complexes	20
2.1 Abstract	21
2.2 Introduction	22
2.3 Photophysical properties	27
2.4 Concluding remarks	49
2.5 References	50
Chapter 3: Electronic structures of palladium(II) dimers	53
3.1 Abstract	54
3.2 Introduction	55
3.3 Results and discussion	58
3.4 Concluding remarks	93
3.5 Materials and methods	93
3.6 References	98
Chapter 4: Carbon-chlorine bond formation from a binuclear palladium(II) electrocatalyst	101
4.1 Abstract	102
4.2 Introduction	102
4.3 Results and discussion	110
4.4 Concluding remarks	124
4.5 Materials and methods	124

4.6 References	127
Appendix A: Electron transfer triggered by optical excitation of PTZ- <i>tris</i> (<i>meta</i> -phenylene ethynylene)-(CO) ₃ (bpy)(py)rhenium(I).....	129
A.1 Abstract	130
A.2 Introduction.....	130
A.3 Results and discussion.....	131
A.4 Concluding remarks	150
A.5 Materials and methods.....	151
A.6 References.....	166
Appendix B: Photophysics of Ir(III) corroles	170
B.1 Abstract	171
B.2 Introduction.....	172
B.3 Results and discussion	173
B.4 Concluding remarks.....	183
B.5 Materials and methods.....	183
B.6 References	189
Appendix C: Supplemental information: Electronic structures of Pd ^{II} dimers	191

LIST OF FIGURES

<i>Number</i>	<i>Page</i>
1.1. Orbital energy level diagram for d^8-d^8	5
1.2. Examples of d^8-d^8 binuclear complexes.....	6
2.1 Electronic structures of d^8-d^8 complexes	23
2.2 Structure of Pt(pop) and its conversion to Pt(pop-BF ₂)	24
2.3 Absorption spectrum of Pt(pop-BF ₂).....	30
2.4 Emission and excitation spectra of Pt(pop-BF ₂).....	31
2.5 Temperature dependence of the emission spectrum of Pt(pop-BF ₂)	33
2.6. Temperature-dependence of the quantum yield of Pt(pop-BF ₂)	34
2.7. Phosphorescence rise and fluorescence decay of Pt(pop-BF ₂)	36
2.8. Fluorescence decay of Pt(pop-BF ₂) measured with a streak camera	37
2.9. Phosphorescence rise of Pt(pop-BF ₂) measured with a streak camera	38
2.10. Temperature-dependent fluorescence decay of Pt(pop-BF ₂)	41
2.11. Fitted temp-dependence of Pt(pop-BF ₂) lifetime and quantum yield	42
3.3. Orbital energy level diagram for d^8-d^8	56
3.2. The structures of compounds 1-4	61
3.3. Selected bond distances in 1-4	63
3.4. The structure of [(2-phenylpyridine)Pd(μ -Cl)] ₂ (5).....	64
3.5. Cyclic voltammograms of 1-4 in CH ₂ Cl ₂ solution	66

3.6. Differential pulse voltammograms of compounds 1–4	67
3.7. Electronic absorption spectra of 1–6 in 2-MeTHF solutions	72
3.8. Emission spectrum of 1 in a 2-MeTHF glass at 77 K	74
3.9. Absorption and excitation spectra of 2 in 2-MeTHF at 77 K.....	77
3.10. Selected molecular orbitals of 1	82
3.11. Molecular orbital diagram for 1	83
3.12. Complexes with short Pd–Pd interactions for DFT calculations	85
3.13. Complexes with d^8 – d^8 interactions selected for DFT calculations	86
3.14. Plot of charge density and Laplacian against M-M distance	88
4.1. Orbital energy level diagram for d^8 – d^8	109
4.2. Cyclic voltammogram of Pd ^{II} –Pd ^{II} in dichloromethane.....	112
4.3. CV of [(2-phenylpyridine)Pd ^{II} (μ -OAc)] ₂ as with increasing chloride....	115
4.4. Absorbance spectrum from electrochemical oxidation of Pd ^{II} –Pd ^{II}	116
4.5. UV–vis spectrum following oxidation of Pd ^{II} –Pd ^{II} with chloride	118
4.6. Spectra following oxidation of Pd ^{II} –Pd ^{II} with bromide and acetate	118
4.7. Cyclic voltammogram of tris(acetylacetonato)iron(III)	123
A.1. Absorption (a) and corrected emission (b) spectra of PTZ-bridge-Re...	135
A.2. Quantum yield measurements of PTZ-bridge-Re.....	136
A.3. Time-resolved emission decay profiles of PTZ-bridge-Re	139
A.4. Concentration-dependent luminescence of PTZ-bridge-Re	140
A.5. Stretched-exponential fit of the rapid decay component	141
A.6. NNLS fitting of the rapid decay component.....	142
A.7. Structural models of PTZ-bridge-Re.....	143

A.8. Absorption spectra of PTZ-bridge-Re at various concentrations	145
A.9. Emission spectra of PTZ-bridge-Re at various concentrations	146
A.10. ¹ H-NMR spectra of PTZ-bridge-Re at various concentrations.	147
A.11. Calculated <i>m</i> -phenylene-ethynylene fragment from DFT	149
B.1. Iridium(III) corroles	173
B.2. UV-vis spectra of Ir(III) corroles.....	174
B.3 Emission spectra of Ir(III) corroles a. 298 K; b. 77 K.....	175
B.4. Normalized excitation profiles of Ir(III) corroles	176
B.5. Shifts of the second Soret peak as a function of solvent polarizability..	179
B.6. Shifts of other absorption bands as a function of solvent polarizability.	180
B.7. Raman spectra of 1-Ir(tma)₂ , 1b-Ir(tma)₂ , and 1-Ir(py)₂	181
C.1. Cyclic voltammograms of 1–4 in CH ₂ Cl ₂	191
C.2. Cyclic voltammograms of 1–5 in MeCN	192
C.3. Steady-state emission spectra of 1–4 , 77 K, λ _{ex} = 355 nm	193
C.4. Steady-state emission spectra of 1–5 , 77 K, λ _{ex} = 355 nm	194
C.5. Excitation spectrum of 1–4 , 77 K, λ _{em} = 460 nm.....	195
C.6. Excitation spectrum of 1–4 , 77 K, λ _{em} = 790 nm.....	196
C.7. Luminescence decay of 1 at 77 K at 460 nm (a) and 720 nm (b).....	198
C.8. Luminescence decay of 2 at 77 K at 460 nm (a) and 720 nm (b).....	199
C.9. Luminescence decay of 3 at 77 K at 460 nm (a) and 720 nm (b).....	200
C.10. Luminescence decay of 4 at 77 K at 460 nm (a) and 720 nm (b).....	201
C.11. Luminescence decay of 5 at 77 K at 460 nm	202

LIST OF SCHEMES

<i>Number</i>	<i>Page</i>
4.4. Selective chlorination of benzo[<i>h</i>]quinoline by Pd ^{II} -Pd ^{II}	106
4.5. Electrocatalytic chlorination catalyzed by Pd ^{II} -Pd ^{II}	120
A.1. Synthesis of PTZ-bridge-Re	133

LIST OF TABLES

<i>Number</i>	<i>Page</i>
1.6. Metal–metal bond distances for selected selected d^8 – d^8 complexes.....	7
1.7. Absorption properties for selected d^8 – d^8 binuclear complexes.....	9
1.3 Photophysical parameters for selected d^8 – d^8 binuclear complexes	10
1.4 Ground and excited state $\nu(M-M)$ frequencies for selected complexes	13
2.1 Absorption and emission properties of Pt(pop-BF ₂) and Pt(pop)	32
2.2 Temperature dependence of Pt(pop-BF ₂) quantum yields	35
2.3 Temperature dependence of Pt(pop-BF ₂) fluorescence lifetime.....	43
2.4 Kinetics parameters for $^1A_{2u}$ excited states of Pt(pop-BF ₂) and Pt(pop) ...	44
3.1 Selected bond distances in 1–4	56
3.2 Reduction potentials for compounds 1–4 in CH ₂ Cl ₂	68
3.3 Reduction potentials for compounds 1–5 in CH ₃ CN	70
3.4 Absorption and emission data for 1–5	76
3.5 Energy of the $nd \rightarrow (n+1)p$ transition.....	90
3.6 Relative contribution of the d, s, and p orbitals to the M–M orbitals	92
B.1 Photophysical data for Ir(III) corroles in toluene solution.....	177
B.2 Values for solvatochromic effects iridium(III) corroles	181

Chapter 1

Electronic structures, photophysical and photochemical properties, and reactivity of
 d^8-d^8 binuclear complexes

1.1 Introduction

Binuclear metal complexes are attractive systems of study for the activation of organic substrates due to the potential cooperativity between the two metal sites.¹ Many biological processes are driven by metalloenzymes with multiple metal centers and catalyze a diverse array of difficult multi-electron reactions including, nitrogen fixation,² oxygen reduction,³ methane hydroxylation,⁴ water oxidation,⁵ and carbon dioxide reduction. Despite their prominence in Nature, the majority of synthetic work has focused on mononuclear catalysts for performing many reactions, particularly those involved in the functionalization of C–H bonds.

Binuclear complexes with square planar Rh^{I} , Ir^{I} , and Pt^{II} centers are members of a special class that feature attractive d^8 – d^8 interactions, as documented by optical and vibrational spectroscopy,^{6–8} x-ray crystallography,^{9,10} extended x-ray absorption fine structure,¹¹ and *ab initio* electronic structure theory.^{12,13} The first report of these complexes occurred in 1975, when Mann et al. reported the electronic spectroscopic characterization of $[\text{Rh}(\text{CNPh})_4]_n^{\text{nt}}$ ($n = 1, 2, \text{ or } 3$) in acetonitrile solution and proposed that aggregation occurred through a direct Rh–Rh interaction. This aggregation was attributable to the unsupported metal–metal interaction between the monomers along the z-axis. Since this initial discovery, many d^8 – d^8 dimers of Rh^{I} , Ir^{I} , and Pt^{II} have been discovered. These complexes possess similar electronic structures and interesting chemical, photophysical, and photochemical properties.

Much of the work in this field has focused on complexes of Rh^{I} , Ir^{I} , and Pt^{II} , while binuclear Pd^{II} complexes have been largely ignored owing to their lack of

photophysical and photochemical properties when compared to traditional d^8-d^8 species. However, the recent discovery of productive thermal reactivity of Pd^{II} dimers has rejuvenated interest in these complexes.¹⁴⁻¹⁷ Electronic structure studies have provided insight into the characteristics that make binuclear Pd^{II} complexes chemically unique.¹⁸

1.2 Electronic structures

The electronic structures of d^8-d^8 complexes can be interpreted in terms of a simple molecular orbital (MO) model where two d^8 square planar fragments combine along the z-axis in a face-to-face orientation (Figure 1.1).⁷ This leads to substantial interaction between the orbitals on each metal center, particularly those with substantial electron density along the z-axis. This electronic configuration results in a metal-metal antibonding $d\sigma^*$ HOMO and a metal-metal bonding $p\sigma$ LUMO. Formally, d^8-d^8 complexes have no metal-metal bond, as the contributions of four filled bonding orbitals are cancelled by four filled antibonding orbitals. However, perturbational mixing between the d_{z^2} and p_z orbitals stabilizes the metal-metal $d\sigma$ and $d\sigma^*$ orbitals (and raises the corresponding $p\sigma$ and $p\sigma^*$ orbitals), resulting in a net bonding interaction. Such d^8-d^8 interactions most commonly lead to discrete dimers or trimers, although in some cases higher-order oligomers are formed.^{7,19} In the excited state, an electron is promoted to the $p\sigma$ molecular orbital, resulting in formation of a metal-metal single bond.

Complexes with d^8-d^8 interactions exist in two principal geometries. The most common is the face-to-face orientation, where two ML_4 square-planar fragments come together along an axis perpendicular to the ML_4 plane (limiting D_{4h}

symmetry). This is the preferred geometry of many d^8-d^8 species, including the original dirhodium(I) isocyanide species as well as many ligand-supported d^8-d^8 architectures. Alternatively, certain ligands can force d^8-d^8 complexes to adopt a “clamshell” or “A-frame” orientation (limiting C_{2v} symmetry).²⁰ Examples of these two geometries are shown in Figure 1.2. In this case, the two ML_4 fragments combine at an angle to one another. This has the effect of decreasing the extent of electronic interaction between the two fragments due to decreased orbital overlap. The relative ordering of the molecular orbitals remains largely unaffected.

Despite the lack of a formal bond, the observed metal–metal bond strength for these complexes can be quite significant.²¹ Resonance Raman and low-temperature emission studies of several complexes show $\nu(M-M)$ frequencies to be in the range of 50–100 cm^{-1} .²² Spectroscopic analysis of $Rh_2(bridge)_4^{4-}$ (bridge = 1,3-diisocyanopropane) calculated a Rh–Rh ground-state bond energy of 12 ± 6 kcal/mol, consistent with a fractional Rh–Rh bond.²³ By contrast, spectroscopic calculations of the excited state show the bond energy to increase to 36 ± 6 kcal/mol, consistent with a metal–metal single bond.

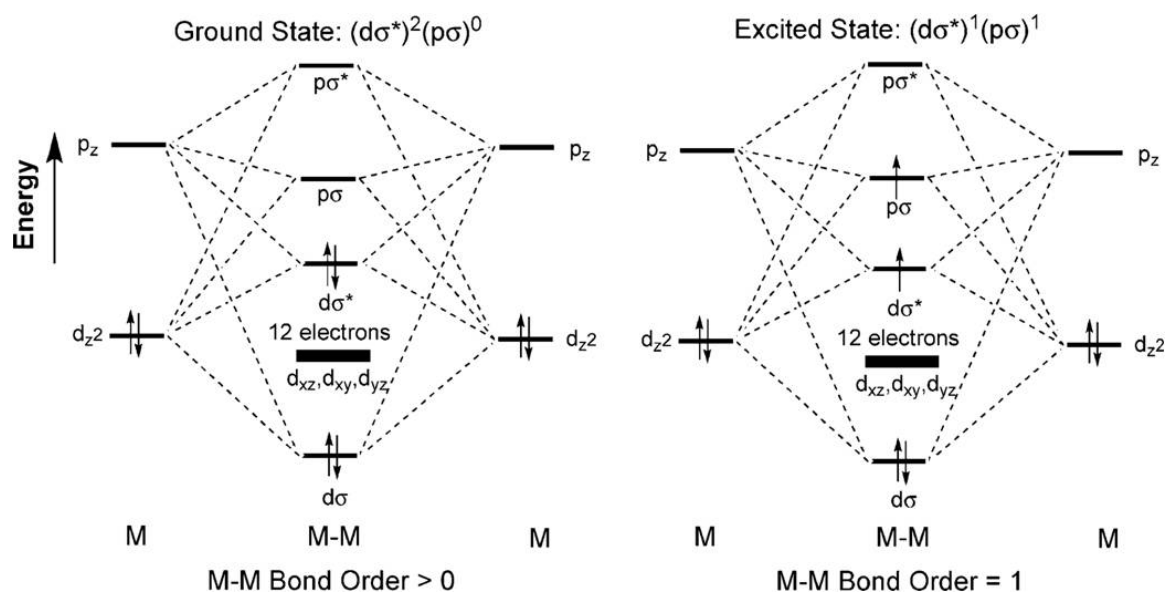


Figure 1.1. Orbital energy level diagram for interaction along the metal–metal axis of two d^8 square-planar units, in both ground (left) and excited (right) states

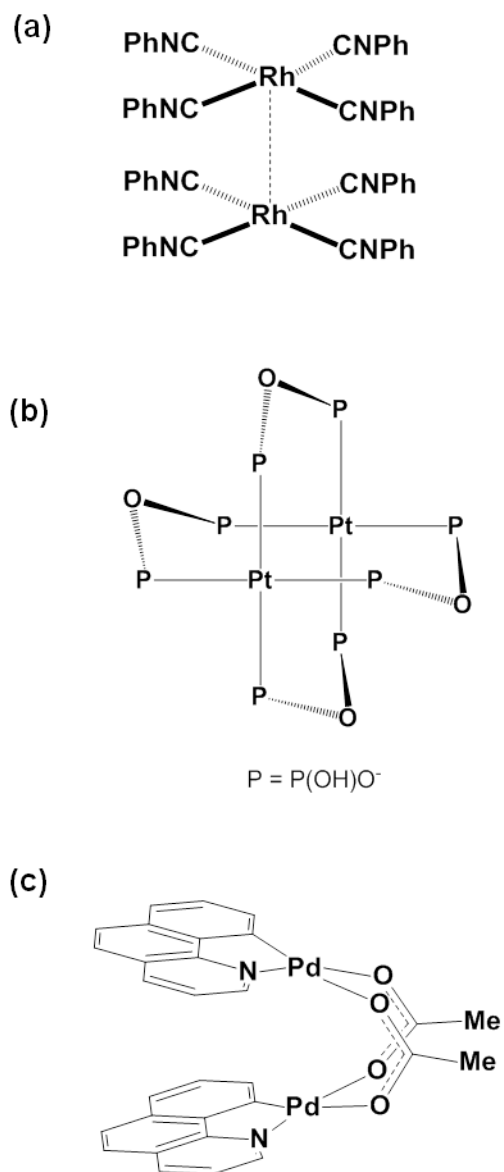


Figure 1.2. Examples of d^8 - d^8 binuclear complexes: (a) Unsupported dimer of *tetrakis*(phenyl isocyanide) rhodium(I), (b) supported face-to-face d^8 - d^8 binuclear complex, *tetrakis*(μ -pyrophosphito)diplatinum(II), and (c) supported “clamshell” complex benzo[*h*]quinolinyl palladium acetate dimer

Table 1.1. Metal–metal bond distances for selected selected d^8 – d^8 complexes as determined by x-ray crystallography

Complex	$d(M-M)$, Å	Reference
$[Rh_2(CNPh)_8]^{2+}$	3.193	6
$[Rh_2(\text{bridge})_4]^{2+}$ ^a	3.243	24
$[Rh_2(\text{TMB})_4]^{2+}$ ^b	3.262	23
$[Ir_2(\text{TMB})_4]^{2+}$	3.119	25, 26
$[Rh_2(\text{dimen})_4]^{2+}$ ^c	3.861	24
$[Ir(\mu\text{-pz})\text{COD}]_2$ ^d	3.216	20
$[Pt_2(\mu\text{-P}_2\text{O}_5\text{H}_2)_4]^{4-}$	2.925	27, 28
$[(\text{bzq})_2\text{Pd}_2(\mu\text{-OAc})_2]$ ^e	2.842	16

^abridge = 1,3-diisocyanopropane, ^bTMB = 2,5-dimethyl-2,5-diisocyanohexane, ^cdimen = 1,8-diisocyanop-menthane, ^dpz = pyrazolyl, COD = 1,5-cyclooctadiene, ^e bzq = benzo[*h*]quinoline

1.3 Photophysical properties

The photophysical properties of these complexes are strongly influenced by electronic structure. Monomeric d^8 species often display little color in the visible region as their strong ligand-to-metal-charge-transfer (LMCT) bands are often in the ultraviolet region, particularly amongst 4d and 5d metals.²⁹ By contrast, the optical spectrum of bimetallic d^8 complexes are often brightly colored.^{23,30-33} Their spectrum is dominated by the $d\sigma^* \rightarrow p\sigma$ electronic transition, which removes an electron from a metal-metal antibonding orbital and places it in a metal-metal bonding orbital. Direct triplet $d\sigma^* \rightarrow p\sigma$ absorption bands are weak and often obscured beneath the allowed singlet transition. The absorption properties for several complexes are presented in Table 1.2.

Photophysical studies of numerous d^8 - d^8 complexes have found them to luminesce from both the lowest energy singlet and triplet excited states derived from the $(d\sigma)^2(d\sigma^*)^1(p\sigma)^1$ electronic configuration.^{24,26,31-36} Typically, the singlet excited state is short, owing to rapid intersystem crossing rates. The lifetimes for most complexes are well below 1 ns. The triplet state, as expected, is much longer lived, with lifetimes ranging from 30 ns to 10 μ s. The emission properties for several complexes are presented in Table 1.3.

Table 1.2. Absorption properties for selected d⁸-d⁸ binuclear complexes

Compound	¹ (dσ*→pσ)		³ (dσ*→pσ)		Ref.
	λ _{max} , nm	ε, M ⁻¹ cm ⁻¹	λ _{max} , nm	ε, M ⁻¹ cm ⁻¹	
[Rh ₂ (CNPh) ₄] ²⁺	568	n/a			7
[Rh ₂ (bridge) ₄] ²⁺	565	670			32
[Rh ₂ (TMB) ₄] ²⁺	517	13600			32
[Ir ₂ (TMB) ₄] ²⁺	625	11200			21
[Ir(μ-pz)COD] ₂	498	9100	585	260	31
[Pt ₂ (μ-P ₂ O ₅ H ₂) ₄] ⁴⁺	372	452	110	33400	33

Table 1.3. Photophysical parameters for selected d^8-d^8 binuclear complexes. All measurements were conducted at room temperature in fluid solution unless otherwise specified.

Compound	$^1(d\sigma^* \rightarrow p\sigma)$			$^3(d\sigma^* \rightarrow p\sigma)$			Ref.
	λ_{max} , nm	τ , ns	Φ	λ_{max} , nm	τ , ns	Φ	
$[\text{Rh}_2(\text{bridge})_4]^{2+}$	656	1.3	0.07	865	8300	0.32	34
$[\text{Rh}_2(\text{TMB})_4]^{2+}$	614	0.820	0.055	780	30	0.001	32
$[\text{Rh}_2(\text{Dimen})_4]^{2+}$	600	0.23	0.0016	690sh ^a	<1	< 10^{-4}	24
$[\text{Ir}_2(\text{TMB})_4]^{2+}$	735	<2	0.0025	1080	210		26, 35
$[\text{Ir}(\mu\text{-pz})\text{COD}]_2$	564	<0.1	1×10^{-4}	687	250	7.8×10^{-3}	31
$[\text{Pt}_2(\mu\text{-P}_2\text{O}_5)_4]^{4-}$	407	<0.04	1.5×10^{-4}	514	9400	0.61	33, 36

^aObserved in PMMA film at 25°C. No phosphorescence was detected at room temperatures in fluid solution.

The excited state can be interpreted as a metal-centered diradical, with one electron localized on the exterior of the metal–metal core (in the $d\sigma^*$ orbital) and the other between the two metal centers (in the $p\sigma$ orbital). The excited state possesses a formal bond order of one, which results in significantly higher metal–metal bond strengths relative to the ground state. This observation is confirmed by both resonance Raman^{22,26,32,34,35,37} and absorption/emission studies on several d^8 – d^8 species.^{24,38} The ground- and excited-state M–M stretching frequencies for several d^8 – d^8 complexes are shown in Table 1.4. A M–M bond length contraction of approximately 0.2–0.3 Å in the excited state has been observed in $\text{Pt}_2(\mu\text{-P}_2\text{O}_5\text{H}_2)_4^{4-}$ (Pt_2) by time-resolved x-ray and electronic spectroscopies.^{39,40} This value is consistent with the Franck-Condon analysis of Pt_2 which predicted a similar contraction in the excited state ($\Delta r = 0.279$ Å).⁴¹

1.4 Chemical properties

Binuclear d^8 – d^8 complexes frequently react with electrophilic reagents (X–Y), undergoing two-center oxidative addition to the axially-ligated d^7 – d^7 (X–M–M–Y) species.^{16,42–45} Most commonly, reactivity is observed with halogens as well as alkyl halides. For Pt_2 , chlorine addition was shown to occur through a mixed-valence Pt_2X intermediate,^{46,47} which has been isolated in the solid state.⁴⁸ In addition, it was shown that chemical or electrochemical oxidation of Pt_2 in the presence of certain ligands results in the reversible formation of Pt_2X_2 species (X = Cl, Br, I, H_2O , SCN, MeCN, imidazole).^{49,50}

As expected from the simple MO picture for d^8-d^8 complexes, oxidation will remove two electrons from the M–M antibonding $d\sigma^*$ orbital and result in the formation of a metal–metal single bond. This is accompanied by a contraction of the metal–metal bond. The degree of contraction is dependent on the extent of electron donation into the $d\sigma^*$ orbital by the axial ligands. For Pt_2 , Pt–Pt distances range from 2.695 Å (Pt_2Cl_2) to 2.782 Å (Pt_2CH_3I). For reference, unmodified Pt_2 has a Pt–Pt distance of 2.925 Å.^{27,28} Similar chemical behavior is displayed by d^8-d^8 complexes of Rh and Ir.⁵¹

1.5 Photochemical properties

The relatively long lifetimes of the $^3[(d\sigma^*)^1(p\sigma)^1]$ excited state allow for bimolecular reactions to take place. The excited states of metal complexes are simultaneously more powerful reductants and oxidants than the ground-state species. The excited states of d^8-d^8 complexes are often strong reductants. Electrochemical and spectroscopic measurements allow a modified Latimer diagram to be constructed that shows $E^0(M_2^+/M_2^*)$ to range from -0.8 to -2.0 V vs. SSCE.^{31,33} Bimolecular quenching studies of the A-frame dimer $[Ir(\mu-pz)COD]_2$ (pz = pyrazole, COD = 1,4-cyclooctadiene) using a series of pyridinium electron acceptors with varying reduction potentials support these calculations.³¹ The strongly reducing excited state of $[Ir(\mu-pz)COD]_2$, estimated to be ~ -1.8 V vs. SSCE,³¹ has been exploited in fundamental electron transfer experiments. Photoexcited $[Ir(\mu-pz)COD]_2$ has been used to probe the electron transfer “inverted region” in covalent systems as well as to facilitate long-range electron transfer in frozen glasses.^{52,53}

Table 1.4. Ground and excited state metal–metal stretching frequencies for selected d^8 – d^8 complexes

Compound	Ground state $\nu(\text{M-M}), \text{cm}^{-1}$	Excited state $\nu(\text{M-M}), \text{cm}^{-1}$	Reference
$[\text{Rh}_2(\text{CNPh})_4]^{2+}$	60	162	22
$[\text{Rh}_2(\text{bridge})_4]^{2+}$	79	144	34
$[\text{Rh}_2(\text{TMB})_4]^{2+}$	55	151	32
$[\text{Ir}_2(\text{TMB})_4]^{2+}$	53	132	26, 35
$[\text{Pt}_2(\mu\text{-P}_2\text{O}_5)_4]^{2-}$	118	156	37

Atom-transfer reactions

Photoexcited d^8-d^8 complexes are particularly active in atom-transfer reactions.^{21,25,33} These reactions are promoted by the diradical nature of the excited state, which places a hole in the $d\sigma^*$ that extends away from the open coordination sites of the metals. Multiple d^8-d^8 systems are capable of H-atom abstraction from a variety of organic and organometallic substrates. Following excitation into the $d\sigma^* \rightarrow p\sigma$ transition, ($\lambda_{\text{max}} = 372 \text{ nm}$) Pt_2^* will react with hydrogen-atom donors such as $(\text{CH}_3)_2\text{CHOH}$, $\text{PhCH}(\text{OH})\text{CH}_3$, Bu_3SnH , Et_3SiH , and H_3PO_3 .^{46,54,55} Rates of reaction of Pt_2^* with Ph_3EH ($\text{E} = \text{Sn}, \text{Ge}, \text{Si}$) decrease as E-H bond strengths increase.^{33,56}

A great deal of mechanistic work on hydrogen-atom in d^8-d^8 complexes has focused on the light-induced conversion of isopropanol to acetone by Pt_2 .⁵⁷ The reaction occurs through initial abstraction of the α -hydrogen to form a monohydride Pt_2H species and the alcohol radical. The monohydride complex has been observed through transient absorption spectroscopy before decaying to form the dihydride Pt_2H_2 complex and acetone. This reaction can be observed with UV-vis through the disappearance of the $d\sigma \rightarrow d\sigma^*$ transition at 372 nm and the appearance of the Pt_2H_2 $d\sigma \rightarrow d\sigma^*$ transition at 325 nm. Pt_2H_2 thermally decomposes into H_2 and Pt_2 ; however, this reaction can be accelerated by photoexcitation into the $d\sigma \rightarrow d\sigma^*$ transition of the d^7-d^7 complex, which rapidly liberates H_2 .⁵⁸

In addition, Pt_2^* is readily quenched by halogen atom transfer from alkyl and aryl halides.⁵⁹ For reactions with aryl halides, reaction rate is again inversely

proportional to Ar–X bond strength. Similarly to the ground-state reaction to X_2 , halogen atom abstraction proceeds by initial formation of mixed-valence Pt_2X , followed by disproportionation to Pt_2X_2 and Pt_2 .

In a similar fashion, illumination of $Ir_2(TMB)_4^{2+}$ into the $d\sigma^* \rightarrow p\sigma$ transition ($\lambda_{max} = 625$ nm) in the presence of 9,10-dihydroanthracene (C–H bond strength 77 kcal/mol) results in formation of $Ir_2(TMB)_4H_2^{2+}$ and anthracene. NMR spectroscopy following illumination confirms formation of anthracene as well as $Ir_2(TMB)_4H_2^{2+}$. The dihydride species has also been chemically isolated and structurally characterized.²⁵ $Ir_2(TMB)_4^{4+}$ has also showed photoreactivity with cyclohexadiene, forming benzene.

1.6 Binuclear Pd^{II} complexes

The great majority of research into d^8 – d^8 complexes has focused on complexes of Pt^{II} , Rh^I , and Ir^I . However, many examples of Pd^{II} dimers with short M–M distances exist in the literature. The lack of reports on the photophysical and photochemical properties of these species are due to the fact that these properties are largely nonexistent. In fact, there are no reports of photochemical reactivity for bimetallic Pd^{II} species. Some complexes have been shown to luminesce at cryogenic temperatures,¹⁸ and at least one recent report has identified room-temperature emission from a Pd^{II} dimer.⁶⁰

Experimental and computational work suggests the unique behavior of binuclear Pd^{II} species is a result of their altered electronic structure with respect to traditional d^8 – d^8 species. Both systems possess a $d\sigma^*$ M–M-antibonding HOMO. However, rather than a $p\sigma$ M–M-bonding LUMO, as is the case for most dimeric

Pt^{II}, Rh^I, and Ir^I species, the LUMO of most Pd₂ species appear to be ligand-based π^* orbitals. The resulting excited state places a large amount of electron density on the ligands. As a result, the Pd₂* excited state is often short-lived. In this excited state, the bond order is roughly one-half.

The altered electronic structure that leads to a ligand- π^* orbital rather than a $p\sigma$ orbital is a result of the unusually large 4d–5p splitting found in Pd^{II}. Gas-phase atomic absorption measurements show this splitting to be nearly 10,000 cm⁻¹ higher than what is observed for Pt^{II}, Rh^I, and Ir^I.⁶¹ As such, the $p\sigma$ orbital is raised in energy above the ligand- π^* . Importantly, this large 4d–5p separation also serves to decrease the extent of d–p mixing. This mixing stabilizes the occupied $d\sigma$ and $d\sigma^*$ orbitals, resulting in a net bonding interaction in the ground state, resulting in substantially weaker ground-state metal–metal interactions in palladium.

Despite their limited photochemical properties, binuclear complexes featuring Pd^{II} have demonstrated chemical reactivity that has made them particularly relevant for study. The complex [(benzo[*h*]quinoline)Pd^{II}(μ -OAc)]₂ (Pd₂) has been shown to facilitate regioselective C–X bond-forming reactions.¹⁵¹⁶ Moreover, this reaction operates through a cooperative interaction between the two Pd centers. Oxidative addition of X₂ (X = Cl, Br) by Pd₂^{II} occurs with concomitant formation of a metal–metal bond to yield a [(benzo[*h*]quinoline)Pd^{III}(μ -OAc)X]₂ intermediate which thermally undergoes reductive elimination, releasing a chlorinated benzo[*h*]quinoline product. This reactivity is analogous to the chemical reactivity of traditional d⁸–d⁸ systems, which yield a d⁷–d⁷ (X–M–M–X) complex upon treatment with X₂ (X = Cl, Br, I). Further, it suggests that Pd₂^{II,II/III,III} redox cycles

are catalytically relevant, in addition to the more established monometallic Pd^{0/II} and Pd^{II/IV} cycles. Since this initial report, additional reactivity of Pd^{II} dimers has been discussed.¹⁴

1.7 References

- (1) Cotton, F. A. *Inorg. Chem.* **1998**, *37*, 5710–5720.
- (2) Lancaster, K. M.; Roemelt, M.; Ettenhuber, P.; Hu, Y.; Ribbe, M. W.; Neese, F.; Bergmann, U.; DeBeer, S. *Science* **2011**, *334*, 974–977.
- (3) Solomon, E. I.; Sundaram, U. M.; Machonkin, T. E. *Chem. Rev.* **1996**, *96*, 2563–2606.
- (4) Merckx, M.; Kopp, D. A.; Sazinsky, M. H.; Blazyk, J. L.; Müller, J.; Lippard, S. J. *Angew. Chem. Int. Ed. Engl.* **2001**, *40*, 2782–2807.
- (5) Ferreira, K. N.; Iverson, T. M.; Maghlaoui, K.; Barber, J.; Iwata, S. *Science* **2004**, *303*, 1831–1838.
- (6) Mann, K. R.; Gray, H. B. In *Inorganic Compounds with Unusual Properties - II*; Advances in Chemistry; ACS, **1979** vol. 173, pp. 225–235.
- (7) Mann, K. R.; Gordon, J. G.; Gray, H. B. *J. Am. Chem. Soc.* **1975**, *97*, 3553–3555.
- (8) Rice, S. F.; Milder, S. J.; Gray, H. B.; Goldbeck, R. A.; Kliger, D. S. *Coord. Chem. Rev.* **1982**, *43*, 349–354.
- (9) Osborn, R. S.; Rogers, D. *J. Chem. Soc., Dalton Trans.* 1002–1004.
- (10) Connick, W. B.; Marsh, R. E.; Schaefer, W. P.; Gray, H. B. *Inorg. Chem.* **1997**, *36*, 913–922.
- (11) Carr, N.; Crossley, J. G.; Dent, A. J.; Gouge, J. R.; Greaves, G. N.; Jarrett, P. S.; Orpen, A. G. *J. Chem. Soc., Chem. Commun.* **1990**, 1369–1371.
- (12) Novoa, J. J.; Aullon, G.; Alemany, P.; Alvarez, S. *J. Am. Chem. Soc.* **1995**, *117*, 7169–7171.
- (13) Aullón, G.; Alvarez, S. *Chem. Eur-J* **1997**, *3*, 655–664.
- (14) Powers, D. C.; Ritter, T. *Acc. Chem. Res.* **2011**.
- (15) Powers, D. C.; Geibel, M. A. L.; Klein, J. E. M. N.; Ritter, T. *J. Am. Chem. Soc.* **2009**, *131*, 17050–17051.
- (16) Powers, D. C.; Ritter, T. *Nat Chem* **2009**, *1*, 302–309.
- (17) Lyons, T. W.; Sanford, M. S. *Chemical Reviews* **2010**, *110*, 1147–1169.
- (18) Bercaw, J. E.; Durrell, A. C.; Gray, H. B.; Green, J. C.; Hazari, N.; Labinger, J. A.; Winkler, J. R. *Inorg. Chem.* **2010**, *49*, 1801–1810.
- (19) Wong, K. M.-C.; Yam, V. W.-W. *Acc. Chem. Res.* **2011**, *44*, 424–434.
- (20) Beveridge, K. A.; Bushnell, G. W.; Dixon, K. R.; Eadie, D. T.; Stobart, S. R.; Atwood, J. L.; Zaworotko, M. J. *J. Am. Chem. Soc.* **1982**, *104*, 920–922.
- (21) Smith, D. C.; Gray, H. B. *Coord. Chem. Rev.* **1990**, *100*, 169–181.
- (22) Dallinger, R. F.; Miskowski, V. M.; Gray, H. B.; Woodruff, W. H. *J. Am. Chem. Soc.* **1981**, *103*, 1595–1596.

- (23) Rice, S. F.; Miskowski, V. M.; Gray, H. B. *Inorg. Chem.* **1988**, *27*, 4704–4708.
- (24) Miskowski, V. M.; Rice, S. F.; Gray, H. B.; Dallinger, R. F.; Milder, S. J.; Hill, M. G.; Exstrom, C. L.; Mann, K. R. *Inorg. Chem.* **1994**, *33*, 2799–2807.
- (25) Smith, D. C.; Marsh, R. E.; Schaefer, W. P.; Loehr, T. M.; Gray, H. B. *Inorg. Chem.* **1990**, *29*, 534–538.
- (26) Smith, D. C. Ph. D. Thesis. California Institute of Technology, Pasadena, CA, **1989**.
- (27) Dos Remedios Pinto, M. A. F.; Sadler, P. J.; Neidle, S.; Sanderson, M. R.; Subbiah, A.; Kuroda, R. *J. Chem. Soc., Chem. Commun.* **1980**, 13–15.
- (28) Marsh, R. E.; Herbstein, F. H. *Acta Crystallogr. Sect. B-Struct. Sci.* **1983**, *39*, 280–287.
- (29) Mason, W. R.; Gray, H. B. *J. Am. Chem. Soc.* **1968**, *90*, 5721–5729.
- (30) Marshall, J. L.; Hopkins, M. D.; Miskowski, V. M.; Gray, H. B. *Inorg. Chem.* **1992**, *31*, 5034–5040.
- (31) Marshall, J. L.; Stobart, S. R.; Gray, H. B. *J. Am. Chem. Soc.* **1984**, *106*, 3027–3029.
- (32) Smith, D. C.; Miskowski, V. M.; Mason, W. R.; Gray, H. B. *J. Am. Chem. Soc.* **1990**, *112*, 3759–3767.
- (33) Roundhill, D. M.; Gray, H. B.; Che, C. M. *Acc. Chem. Res.* **1989**, *22*, 55–61.
- (34) Rice, S. F.; Gray, H. B. *J. Am. Chem. Soc.* **1981**, *103*, 1593–1595.
- (35) Harvey, P. D. *Coord. Chem. Rev.* **2001**, *219–221*, 17–52.
- (36) Che, C. M.; Butler, L. G.; Gray, H. B. *J. Am. Chem. Soc.* **1981**, *103*, 7796–7797.
- (37) Bradley, P. G.; Kress, N.; Hornberger, B. A.; Dallinger, R. F.; Woodruff, W. H. *J. Am. Chem. Soc.* **1981**, *103*, 7441–7446.
- (38) Miskowski, V. M.; Rice, S. F.; Gray, H. B.; Milder, S. J. *J. Phys. Chem.* **1993**, *97*, 4277–4283.
- (39) Christensen, M.; Haldrup, K.; Bechgaard, K.; Feidenhans'l, R.; Kong, Q.; Cammarata, M.; Russo, M. L.; Wulff, M.; Harrit, N.; Nielsen, M. M. *J. Am. Chem. Soc.* **2008**, *131*, 502–508.
- (40) van der Veen, R. M.; Cannizzo, A.; van Mourik, F.; Vlček, A.; Chergui, M. *J. Am. Chem. Soc.* **2010**, *133*, 305–315.
- (41) Fordyce, W. A.; Brummer, J. G.; Crosby, G. A. *J. Am. Chem. Soc.* **1981**, *103*, 7061–7064.
- (42) Che, C. M.; Schaefer, W. P.; Gray, H. B.; Dickson, M. K.; Stein, P. B.; Roundhill, D. M. *J. Am. Chem. Soc.* **1982**, *104*, 4253–4255.
- (43) Che, C. M.; Mak, T. C. W.; Gray, H. B. *Inorg. Chem.* **1984**, *23*, 4386–4388.
- (44) Coleman, A. W.; Eadie, D. T.; Stobart, S. R.; Zaworotko, M. J.; Atwood, J. L. *J. Am. Chem. Soc.* **1982**, *104*, 922–923.
- (45) Maverick, A. W.; Smith, T. P.; Maverick, E. F.; Gray, H. B. *Inorg. Chem.* **1987**, *26*, 4336–4341.

- (46) Bryan, S. A.; Dickson, M. K.; Roundhill, D. M. *Inorg. Chem.* **1987**, *26*, 3878–3886.
- (47) Che, C. M.; Lee, W. M.; Cho, K. C. *J. Am. Chem. Soc.* **1988**, *110*, 5407–5411.
- (48) Che, C. M.; Herbstein, F. H.; Schaefer, W. P.; Marsh, R. E.; Gray, H. B. *J. Am. Chem. Soc.* **1983**, *105*, 4604–4607.
- (49) Bryan, S. A.; Dickson, M. K.; Roundhill, D. M. *J. Am. Chem. Soc.* **1984**, *106*, 1882–1883.
- (50) Bryan, S. A.; Schmehl, R. H.; Roundhill, D. M. *J. Am. Chem. Soc.* **1986**, *108*, 5408–5412.
- (51) Cotton, F. A. *Multiple bonds between metal atoms*. Springer, **2005**.
- (52) Fox, L. S.; Kozik, M.; Winkler, J. R.; Gray, H. B. *Science* **1990**, *247*, 1069–1071.
- (53) Wenger, O. S.; Leigh, B. S.; Villahermosa, R. M.; Gray, H. B.; Winkler, J. R. *Science* **2005**, *307*, 99–102.
- (54) Harvey, E. L. Ph. D. Thesis. California Institute of Technology, Pasadena, CA, **1990**.
- (55) Roundhill, D. M.; Atherton, S. J.; Shen, Z. P. *J. Am. Chem. Soc.* **1987**, *109*, 6076–6079.
- (56) Vlcek, A.; Gray, H. B. *Inorg. Chem.* **1987**, *26*, 1997–2001.
- (57) Roundhill, D. M. *J. Am. Chem. Soc.* **1985**, *107*, 4354–4356.
- (58) Sweeney, R. J.; Harvey, E. L.; Gray, H. B. *Coord. Chem. Rev.* **1990**, *105*, 23–34.
- (59) Che, C. M.; Lee, W. M.; Cho, K. C.; Harvey, P. D.; Gray, H. B. *J. Phys. Chem.* **1989**, *93*, 3095–3099.
- (60) Santana, M. D.; García-Bueno, R.; García, G.; Sánchez, G.; García, J.; Kapdi, A. R.; Naik, M.; Pednekar, S.; Pérez, J.; García, L.; Pérez, E.; Serrano, J. L. *Dalton Trans.* **2012**, *41*, 3832–3842.
- (61) Moore, C. E. *Atomic Energy Levels, Vol. III (Molybdenum through Lanthanum and Hafnium through Actinium)*. Circular of the National Bureau of Standards 467, U.S. Government Printing Office, Washington DC, **1958**.

Chapter 2

Twist it to mix it! $^1A_{2u}$ -to- $^3A_{2u}$ intersystem crossing in diplatinum (II,II) complexes

This work is a collaborative effort between Alec C. Durrell, Gretchen E. Keller, Yan Choi Lam, Jan Sykora, Harry B. Gray, and Tony Vlcek.

2.1 Abstract

The photophysical properties of *tetrakis*(μ -pyrophosphito)diplatinate(II), abbreviated Pt(pop), are compared with its fluoroborated analogue, Pt(pop-BF₂). This complex possesses eight BF₂ groups that replace the hydrogen atoms that are located between each “pop” ligand. When compared with Pt(pop), Pt(pop-BF₂) has a much greater singlet lifetime (1.5 ns) and singlet quantum yield (0.27). The enhancement is the result of a drastically slower $^1A_{2u} \rightarrow ^3A_{2u}$ intersystem crossing rate. In particular, the thermal barrier to intersystem crossing is significantly higher in Pt(pop-BF₂) (2230 cm⁻¹ vs. 1190 cm⁻¹). We believe this is primarily the result of the increased rigidity of the complex afforded by the BF₂ groups. The rigidity increases the energy of symmetry-lowering vibrational modes, which are necessary to promote spin-orbit mixing of the $^1d\sigma^*p\sigma$ and $^3d\sigma^*p\sigma$ states.

2.2 Introduction

Face-to-face d^8-d^8 complexes of Pt^{II} , Rh^I , and Ir^I possess truly remarkable spectroscopic, photophysical, and photochemical properties.¹⁻⁵ Electronic excitation from a metal-metal antibonding $(n-1)d\sigma^*$ orbital to an $np\sigma$ bonding orbital creates a net metal-metal bond (Figure 2.1); as a result, the metal-metal distance shrinks in both singlet and triplet ($^1,^3d\sigma^*p\sigma$) excited states. In addition to strong phosphorescence, some of these complexes also show weak fluorescence; and, of the complexes studied to date, fluorescence is most prominent for certain Ir^I-Ir^I complexes whose $^1d\sigma^*p\sigma$ states are able to reduce very low potential substrates.⁶⁻⁹

Tetrakis(μ -pyrophosphito)diplatinate(II), $[Pt_2(\mu-P_2O_5H_2)_4]^{4-}$, abbreviated Pt(pop), is the prototypal photoactive d^8-d^8 complex.¹ Its molecular structure (Figure 2.2, left) consists of two parallel PtP_4 square planar units held in a rigid configuration by four P-O-P bridges. The eight terminal P(O)(OH) groups, which are exposed to solvent, likely play a role in excited-state deactivation.^{10,11} Pt(pop) shows very weak fluorescence from a $^1d\sigma^*p\sigma$ state that decays on a tens-of-ps timescale with temperature- and solvent-dependent lifetimes,^{10,11} and the corresponding triplet state exhibits intense green phosphorescence. Owing to its long lifetime ($\sim 10 \mu s$)¹² and biradical character,^{13,14} the $^3d\sigma^*p\sigma$ state reacts with a variety of substrates, including alcohols, hydrocarbons, alkylhalides,²⁻⁵ DNA,¹⁵ and metal complexes.^{13,14,16} These reactions, which involve transfer of hydrogen or halogen atoms, can be viewed as photochemical oxidative-addition or inner-sphere electron-transfer processes.

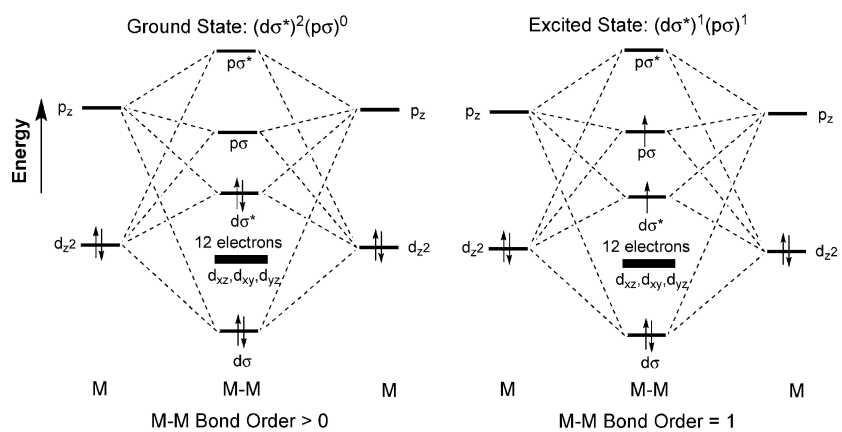


Figure 2.1. Electronic structures of d^8-d^8 complexes in ground (left) and lowest triplet excited states (right)

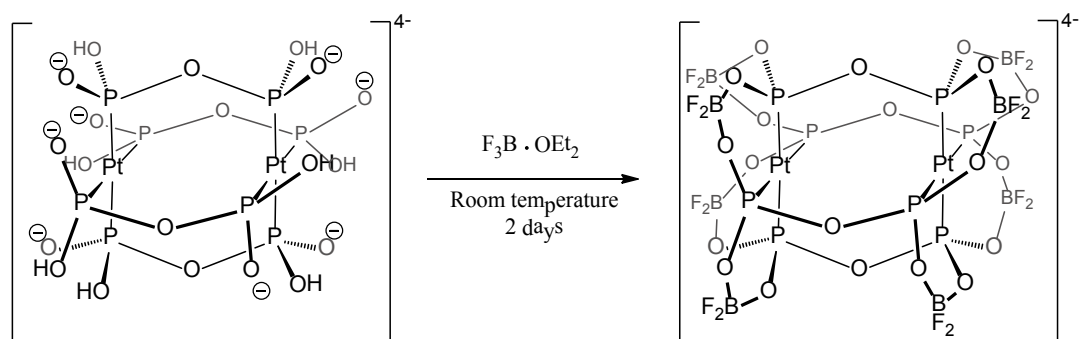


Figure 2.2. Structure of Pt(pop), left, and its conversion to Pt(pop-BF₂), right

The structures and dynamics of Pt(pop) $^1,3d\sigma^*p\sigma$ excited states have been extensively investigated. Evidence that a Pt–Pt bond is formed upon $d\sigma^*\rightarrow p\sigma$ excitation has been extracted from Frank-Condon analysis of the vibronic structure associated with $d\sigma^*\rightarrow p\sigma$ absorption bands measured on single crystals at low temperatures (the Pt–Pt stretching frequency increases from 118 cm^{-1} in the ground state¹⁷ to about 150 cm^{-1} in both excited states,^{12,18} and 155 cm^{-1} was found for the triplet by transient Raman spectroscopy).¹⁷ A femtosecond time-resolved spectroscopic study¹¹ reported long-lasting (several ps) coherent oscillations of stimulated fluorescence with a 224 fs period corresponding to a 149 cm^{-1} stretching vibration, a finding that documented the harmonic nature of the $^1d\sigma^*p\sigma$ potential energy surface with respect to the Pt–Pt coordinate. The structure of the $^3d\sigma^*p\sigma$ state studied by time-resolved x-ray diffraction from a Pt(pop) single crystal showed a Pt–Pt bond contraction of 0.28 \AA .¹⁹ The most detailed information on the $^3d\sigma^*p\sigma$ structure so far has been obtained by time-resolved x-ray absorption spectroscopy:²⁰ the appearance of a new pre-edge absorption feature upon excitation demonstrated creation of an electron vacancy (“hole”) in the $d\sigma^*$ orbital; EXAFS analysis showed that the Pt–Pt distance contracts by 0.31 \AA relative to that in the ground state; and the Pt–P bonds elongate by 0.01 \AA , with Pt atoms shifting inward from the planes formed by the four phosphorus donor atoms, a structural picture that accords with excited-state DFT calculations.^{21,22} Understanding and controlling relaxation pathways of electronically excited d^8 – d^8 complexes remains a major challenge. In particular, several different mechanisms could account for

singlet→triplet conversion (i.e., intersystem crossing).^{10,11,23} It is of special interest that $^1d\sigma^*p\sigma$ excited-state lifetimes vary from a few ps to almost 1 ns in a d^8-d^8 Rh_2 complex,²⁴ and that substantially different chemical reactivities have been found for singlet and triplet $d\sigma^*p\sigma$ states of Ir_2 derivatives.^{6,24-26} A major goal of our work is to understand the factors that control the lifetimes of these energy-rich singlet states, as potentially they could be key players in photocatalysis and light-energy-harvesting schemes.

Although Pt(pop) offers few opportunities for tuning its photobehavior by structural variations, replacing each bridging $-O-$ atom by a $-CH_2-$ group, which shortens the $^3d\sigma^*p\sigma$ lifetime to 55 ns, and accelerates its atom- and electron-transfer reactions.^{27,28} Since the terminal P(O)(OH) groups are the only other sites that can be derivatized, we set out to study the effects of substituting all eight pop hydrogen atoms by BF_2 groups, each linking oxygen atoms of two different pop ligands (Figure 2.2). Such “perfluoroboration” creates a rigid covalent cage around the Pt–Pt central motif, shields it from solvent, and removes potentially energy-accepting $-O-H\cdots O-$ vibrations. Moreover, the $^3d\sigma^*p\sigma$ state is expected to become a stronger oxidant, owing to the presence of electron-withdrawing BF_2 groups. We report here that perfluoroboration profoundly changes the properties the $^1d\sigma^*p\sigma$ state of Pt(pop). Perfluoroboration was found to dramatically lower the rate of intersystem crossing, resulting in a profoundly larger singlet lifetime ($\sim 100\times$) and quantum yield ($\sim 1000\times$) when compared to the parent Pt(pop) complex. We believe this is primarily the result of the increased rigidity of the complex afforded

by the BF_2 groups. The rigidity increases the energy of symmetry-lowering vibrational modes, which are necessary to promote spin-orbit mixing of the $^1\text{d}\sigma^*\text{p}\sigma$ and $^3\text{d}\sigma^*\text{p}\sigma$ states.

2.3 Photophysical Properties

The absorption spectrum of $\text{Pt}(\text{pop-BF}_2)$ exhibits an intense band at 365 nm attributable to the $\text{d}\sigma^*\rightarrow\text{p}\sigma$ ($^1\text{A}_{1\text{g}}\rightarrow^1\text{A}_{2\text{u}}$) transition, an assignment based on work on $\text{Pt}(\text{pop})$, which has a similar absorption feature at 372 nm (Figure 2.3 and Table 2.1).^{12,18,29} The corresponding spin-forbidden $\text{d}\sigma^*\rightarrow\text{p}\sigma$ transition ($^1\text{A}_{1\text{g}}\rightarrow^3\text{A}_{2\text{u}}$) gives rise to a $\sim 200\times$ weaker band at 454 nm, virtually identical with that of $\text{Pt}(\text{pop})$.¹² Both complexes show qualitatively similar spectral patterns at shorter wavelengths [three relatively weak bands at 293 (1/26 main peak intensity), 261 (1/13), and 234 nm (1/4.4) in the spectrum of $\text{Pt}(\text{pop-BF}_2)$, and at 315 (1640), 285 (2550) and 246 (3770) nm for $\text{Pt}(\text{pop})$]. The 2100–3200 cm^{-1} high-energy shifts of these bands upon perfluoroboration are in line with their LMCT character, as revealed by TD-DFT calculations on $\text{Pt}(\text{pop})$.^{21,22,30}

The emission spectra of $\text{Pt}(\text{pop-BF}_2)$ and $\text{Pt}(\text{pop})$ are very different in terms of the relative intensities of $\text{p}\sigma\rightarrow\text{d}\sigma^*$ fluorescence and phosphorescence. The spectrum of $\text{Pt}(\text{pop-BF}_2)$ shows intense $^3\text{A}_{2\text{u}}\rightarrow^1\text{A}_{2\text{u}}$ phosphorescence at 512 nm and equally strong fluorescence at 393 nm (Figure 2.4 and Table 2.2). Owing to phosphorescence quenching by traces of O_2 , the intensity ratio of the two bands depends on sample preparation; a limiting phosphorescence:fluorescence peak-intensity ratio of 1.15 was obtained from a high-vacuum degassed solution. While

Pt(pop) in MeCN also shows strong phosphorescence at 511 nm, the fluorescence at 398 nm is extremely weak,^{12,31} as documented quantitatively by emission quantum yields: whereas room-temperature phosphorescence yields of the two complexes are comparable, the fluorescence yield is three orders of magnitude larger for Pt(pop-BF₂) than for Pt(pop) (2.7×10^{-1} and 1.5×10^{-4} , respectively)¹². The excitation spectra of Pt(pop-BF₂) measured at 405 and 512 nm are virtually identical and match perfectly the strong $^1A_{1g} \rightarrow ^1A_{2u}$ absorption band at 363 nm (Figure 2.4); and the phosphorescence:fluorescence peak-intensity ratio is independent of excitation wavelength from 350 to 380 nm. Both the fluorescence band intensity and quantum yield decrease with increasing temperature, accompanied by a concomitant increase in phosphorescence intensity and yield (Figures 2.5 and 2.6, and Table 2.2). The total emission quantum yield of ~ 0.75 is temperature independent, behavior that indicates direct conversion of the fluorescent state ($^1A_{2u}$) to the phosphorescent state ($^3A_{2u}$). This conclusion was confirmed by observing identical single-exponential kinetics of fluorescence decay and phosphorescence rise, both occurring with a 1.6 ns lifetime (Figures 2.7, 2.8, and 2.9); the fluorescence and phosphorescence time profiles were measured under exactly the same conditions, except for detection wavelengths, 405 and 512 nm, respectively; and the same results also were obtained using two different techniques, TCSPC (373 nm, ~ 80 ps excitation) and streak camera detection (355 nm, 1 ps excitation). Our findings clearly demonstrate the presence of slow

$^1A_{2u} \rightarrow ^3A_{2u}$ intersystem crossing (ISC) that occurs without any apparent intermediates in Pt(pop-BF₂).

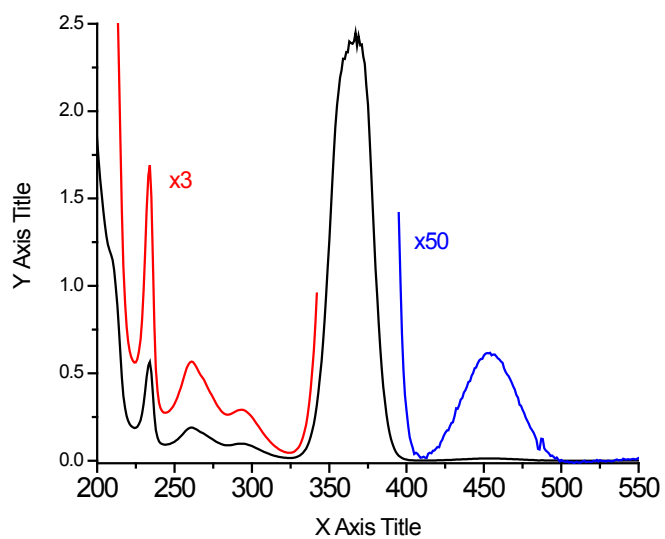


Figure 2.3. Absorption spectrum of Pt(pop-BF₂) in MeCN solution

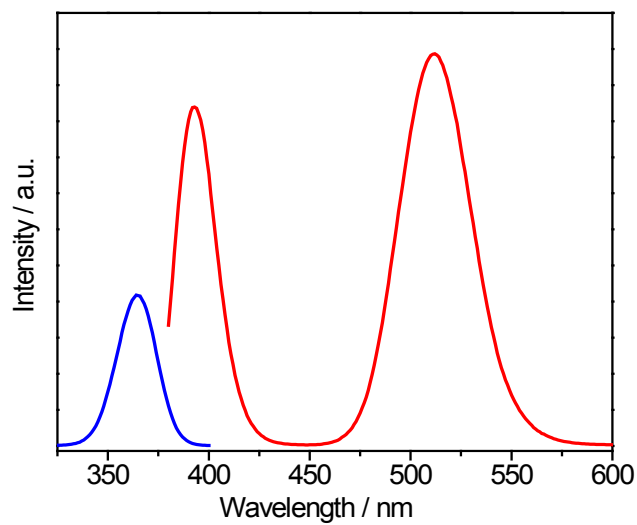


Figure 2.4. Red: emission spectrum of Pt(pop-BF₂) measured using 373 nm excitation. Blue: normalized excitation spectra of in MeCN obtained at $\lambda_{em} = 405$ and 512 nm (the two spectra are indistinguishable. Measured in a MeCN solution at 21 °C, freeze-pump-thaw degassed at 4×10^{-5} mbar

Table 2.1. Absorption and emission properties of Pt(pop-BF₂) and Pt(pop) in MeCN

Pt(pop-BF ₂)	Pt(pop) ^a	Assignment ^b
Absorption, nm (ϵ , M ⁻¹ cm ⁻¹)		
234 (1/4.4)	246 (3770)	LMCT ^c
261 (1/13)	285 (2550)	LMCT ^c
293 (1/26)	315 (1640)	LMCT ^c
365 (1/1)	372 (33400)	¹ (d σ^* →p σ) ¹ A _{1g} → ¹ A _{2u}
454 (1/200)	454 (155)	³ (d σ^* →p σ) ¹ A _{1g} → ³ A _{2u}
Emission, nm (lifetime at 21 °C)		
393 (1.6 ns)	398 (~ 8 ps)	¹ (p σ →d σ^*) ¹ A _{2u} → ¹ A _{1g}
512 (8.4 μ s)	511 (9.4 μ s)	³ (p σ →d σ^*) ³ A _{2u} → ¹ A _{1g}
Emission Stokes shift, cm ⁻¹		
1760	2230	Fluorescence
2460	2500	Phosphorescence

^a Absorption data and emission lifetimes from reference 12, emission wavelengths from reference 31. ^bBased on references 12, 21, and 22. ^cThe principal excitations are directed to the p σ LUMO accompanied by smaller contributions from Pt-localized excitations.

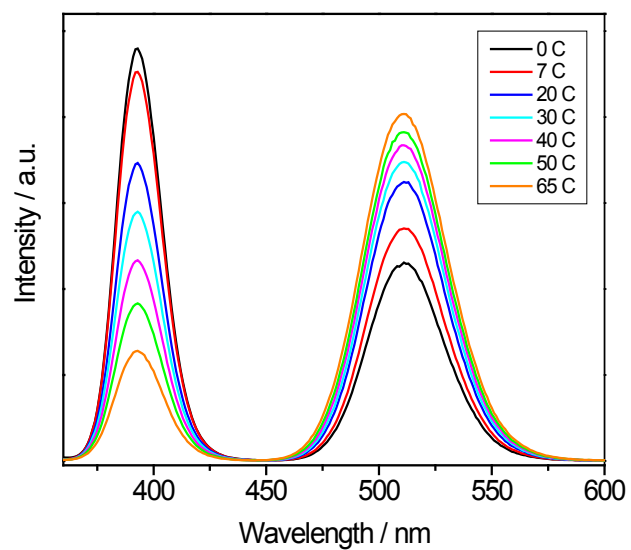


Figure 2.5. Temperature dependence of the emission spectrum of Pt(pop-BF₂) in MeCN solution. Excitation at 355 nm

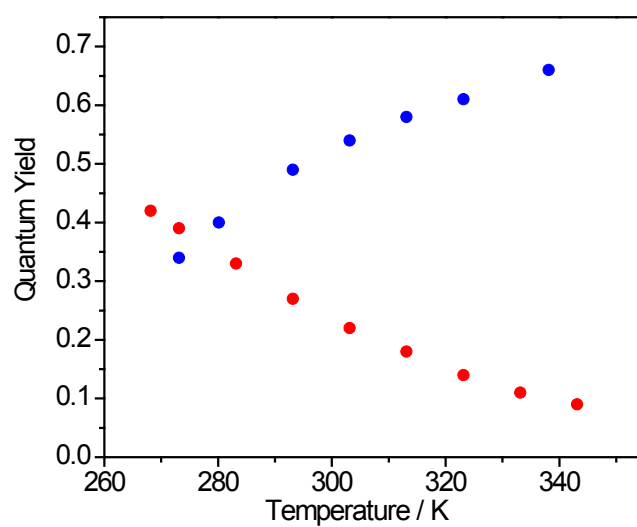


Figure 2.6. Temperature-dependence of the fluorescence (red) and phosphorescence (blue) quantum yield of Pt(pop-BF₂) in MeCN

Table 2.2. The temperature dependence of Pt(pop-BF₂) fluorescence (ϕ_f) and phosphorescence (ϕ_{ph}) quantum yields measured in degassed MeCN solution

T [°C]	T [K]	ϕ_f	ϕ_{ph}	$\phi_f + \phi_{ph}$
-5	268.15	0.42	-	-
0	273.15	0.39	0.34	0.73
7	280.15	-	0.40	-
10	283.15	0.33	-	-
20	293.15	0.27	0.49	0.76
30	303.15	0.22	0.54	0.76
40	313.15	0.18	0.58	0.76
50	323.15	0.14	0.61	0.75
60	333.15	0.11	-	-
65	338.15	-	0.66	-
70	343.15	0.09	-	-

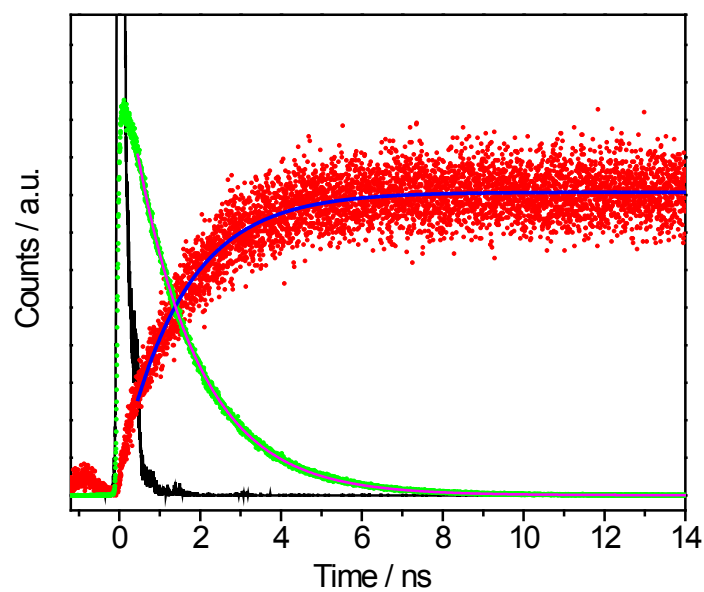


Figure 2.7. Phosphorescence rise (red), fluorescence decay (green) of Pt(pop-BF₂) in MeCN, shown together with a 373 nm excitation-pulse profile (black). Fluorescence and phosphorescence intensities were measured at 405 and 512 nm, respectively. The blue and magenta curves are single-exponential fits in the 0.3–17.2 ns interval with lifetimes of 1.56 ± 0.02 and 1.58 ± 0.001 ns, respectively.

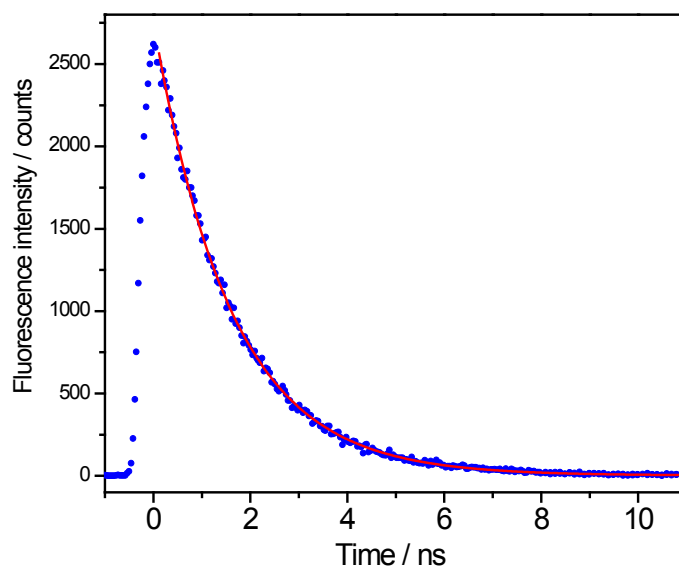


Figure 2.8. Fluorescence decay of Pt(pop-BF₂) in MeCN measured with a streak camera, excited at 355 nm, 10 ps. Emission in the 400–415 nm range was selected by a bandpass filter. Red curve: single-exponential fit with $\tau = 1.58 \pm 0.01$ ns

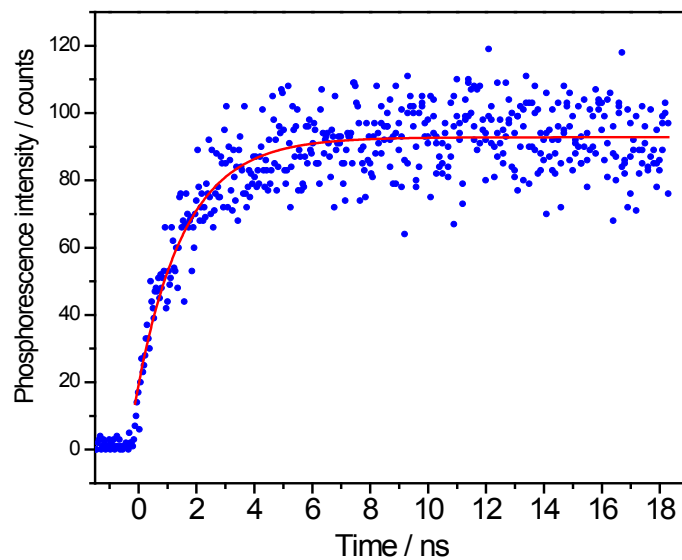


Figure 2.9. Phosphorescence rise of Pt(pop-BF₂) in MeCN measured with a streak camera, excited at 355 nm, 1 ps pulse. Emission wavelengths > 500 nm were selected by a cut-off filter. Red curve: single-exponential fit with $\tau = 1.62 \pm 0.09$ ns

The Pt(pop-BF₂) room-temperature fluorescence lifetime of 1.6 ns is about 100 times longer than the 8–18 ps values reported for Pt(pop) in MeCN¹² and similar solvents.^{10,11} Figure 2.10 shows that the Pt(pop-BF₂) fluorescence decay is strongly dependent on temperature, and the kinetics are predominantly³² single-exponential (lifetimes are collected in Table 2.3). To analyze the temperature dependence of the fluorescence lifetime and quantum yield (Figure 2.11), we express the nonradiative decay rate constant k_{nr} as a sum of ISC rate constants, k_{ISC} , and the nonradiative decay to the ground state, k_d (eq. 1). Owing to the long fluorescence lifetime, the latter cannot be *a priori* neglected, as in the case of Pt(pop). k_{ISC} is assumed to follow Arrhenius-like behavior (eq. 1), as proposed¹⁰ for Pt(pop).

$$k_{nr} = k_d + k_{ISC} = k_d + \left(k_0 + \frac{A}{\sqrt{k_B T}} e^{-E_a/k_B T} \right) \quad (1)$$

The lifetime and quantum yield are then given by equations 2 and 3, respectively.

$$\frac{1}{\tau} = k_r + k_{nr} = k_r + k_d + k_0 + \frac{A}{\sqrt{k_B T}} e^{-E_a/k_B T} \quad (2)$$

$$\frac{1}{\phi_{fl}} = 1 + \frac{k_{nr}}{k_r} = 1 + \frac{k_d + k_0}{k_r} + \frac{A}{k_r \sqrt{k_B T}} e^{-E_a/k_B T} \quad (3)$$

Fitting the experimental data to these equations gives: $k_r + k_d + k_0 = (2.55 \pm 0.07) \times 10^8 \text{ s}^{-1}$; $A = (3.0 \pm 0.2) \times 10^{14} \text{ cm}^{1/2} \text{ s}^{-1}$; $E_a = 2229 \pm 20 \text{ cm}^{-1}$ for the lifetime, and $(k_d + k_0)/k_r = 0.6 \pm 0.1$; $A/k_r = (1.7 \pm 0.5) \times 10^6 \text{ cm}^{1/2}$; $E_a = 2233 \pm 75 \text{ cm}^{-1}$ for the quantum yield (Figure 2.10). The activation energies from these two fits are

virtually identical, in accordance with eqs. 2–3 and the assumption of T-independent k_r and k_d (T-dependent k_d would require two exponential terms, for which we have no evidence). The radiative rate constant (k_r) can be estimated to be $1.7 \times 10^8 \text{ s}^{-1}$, which is $\sim 8 \times$ larger than that of Pt(pop) ($2 \times 10^7 \text{ s}^{-1}$);¹² and $8.5 \times 10^7 \text{ s}^{-1}$ is the rate for T-independent nonradiative decay ($k_d + k_0$).

Pt(pop-BF₂) phosphorescence decay was observed on a longer timescale, occurring with a slightly temperature-dependent lifetime: 8.6, 8.4, and 7.6 μs at 0, 20, and 80 °C, respectively. In absolute terms, the phosphorescence lifetime is comparable to that of Pt(pop), 9.4 μs , which, however, was reported to be independent of temperature.¹²

The presence of a long-lived strongly emissive singlet excited state together with a strongly phosphorescent triplet are the distinctive photophysical properties of Pt(pop-BF₂). The $^1A_{2u} \rightarrow ^3A_{2u}$ ISC in Pt(pop) has been studied in detail both experimentally^{10,11} and theoretically,²³ but the mechanism is still open to debate. Herein, we will concentrate on the dramatic ISC slowdown caused by perfluoroboration of the complex. In both Pt(pop) and Pt(pop-BF₂), ISC proceeds by a two-channel mechanism, eq. (2): the corresponding kinetics parameters for the two complexes are compared in Table 2.3.

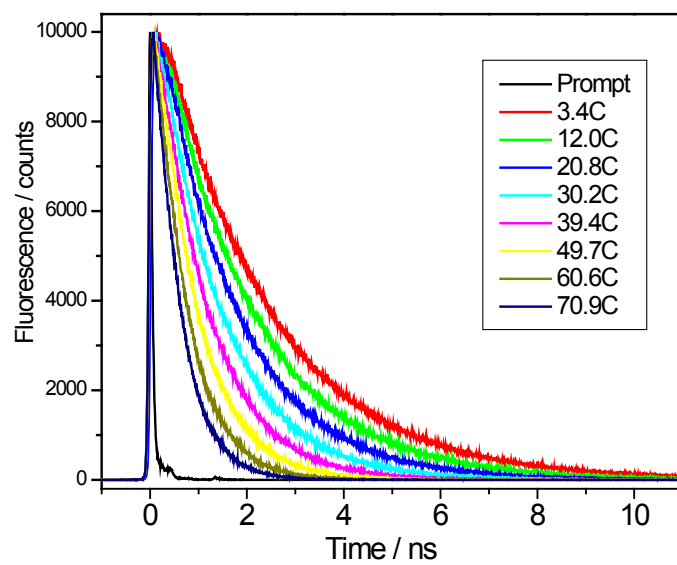


Figure 2.10. Temperature-dependent fluorescence decay of Pt(pop-BF₂) in MeCN solution. Excitation at 373 nm; emission detected at 405 nm

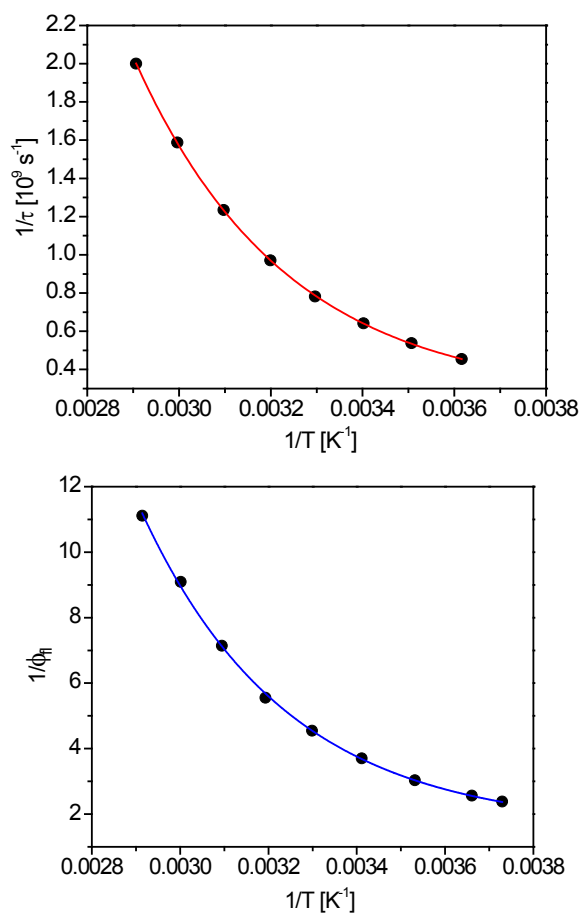


Figure 2.11. Temperature dependence of Pt(pop-BF₂) fluorescence lifetime and quantum yield fitted to equations 2 (red) and 3 (blue), respectively. Data from Tables 2.3 and 2.4.

Table 2.3. Temperature dependence of Pt(pop-BF₂) fluorescence lifetime. The values were obtained by deconvolution of the TCSPC signal and the actual excitation pulse profile. The nonradiative ¹A_{2u} decay rate constants k_{nr} were calculated as $1/\tau - k_r$; assuming $k_r = 1.7 \times 10^8 \text{ s}^{-1}$.

t [°C]	T [K]	τ_1 [ns]	τ [ns]	A ₁ [%]	A ₂ [%]	k_{nr} [10^8 s^{-1}]
3.4	276.55	0.29	2.20	5	95	2.8
12.0	285.15	0.12	1.86	8	95	3.7
20.8	293.95	0.20	1.56	9	91	4.7
30.2	303.35	0.20	1.28	9	91	6.1
39.4	312.55	0.14	1.03	10	90	8.0
49.7	322.85	0.12	0.81	11	89	10.6
60.6	333.75	0.08	0.63	12	88	14.2
70.9	344.05	0.06	0.50	13	87	18.3

Table 2.4. Decay kinetics parameters for the $^1A_{2u}$ excited states of Pt(pop-BF₂) and Pt(pop)

Parameter	Pt(pop-BF ₂)	Pt(pop) ^a
k_r	$1.7 \times 10^8 \text{ s}^{-1}$	$2 \times 10^7 \text{ s}^{-1}$
k_0	$< 8.5 \times 10^7 \text{ s}^{-1}$ ^c	$1.5 \times 10^9 \text{ s}^{-1}$
A	$3.0 \times 10^{14} \text{ cm}^{1/2} \text{ s}^{-1}$	$2.6 \times 10^{14} \text{ cm}^{1/2} \text{ s}^{-1}$
E_a	2230 cm^{-1}	1190 cm^{-1}
$A/\sqrt{k_B} \times 293$	$2.1 \times 10^{13} \text{ s}^{-1}$	$1.8 \times 10^{13} \text{ s}^{-1}$
$\exp(-E_a/k_B \times 293)$	1.749×10^{-5}	2.893×10^{-3}
k_{nr} ^b	$4.7 \times 10^8 \text{ s}^{-1}$	$5.4 \times 10^{10} \text{ s}^{-1}$

^a k_r from reference 12 measured in MeCN. Other parameters from reference 10, measured in a 2-MeTHF/propionitrile mixture. ^b For Pt(pop-BF₂), see Table 2.3. For Pt(pop): calculated from the parameters reported in the Table. ^c Value corresponds to $k_0 + k_a$ and thus represents an upper limit of k_0 .

We assume that ISC rates are given by eq. (4), where H_{SO} is the spin-orbit (SO) operator and FC is the Franck-Condon factor that accounts for the thermally weighted overlap between vibrational wavefunctions of the initial and final states.

$$k_{ISC} \propto \left\langle {}^1A_{2u} \left| H_{SO} \right| {}^3A_{2u} \right\rangle^2 FC \quad (4)$$

Temperature-independent ${}^1A_{2u} \rightarrow {}^3A_{2u}$ direct tunneling (k_0) is more than 18 times slower than that for Pt(pop). Note that direct ISC between states of identical symmetries is allowed only in point groups where one of the rotation components belongs to the totally symmetric representation [it is forbidden in the D_{4h} group of the $Pt_2(P-O-P)_4$ core (i.e., $\langle {}^1A_{2u} | H_{SO} | {}^3A_{2u} \rangle = 0$), but it is allowed in C_{4h} , C_{2h} , or C_2]. However, even in D_{4h} , ISC could become partially allowed by SO mixing with higher triplet states^{33–35} and/or through a spin-vibronic mechanism.^{23,36–38} In particular, SO coupling between ${}^1A_{2u}$ and 3E_u LMCT is symmetry allowed, admixing triplet character into ${}^1A_{2u}$ that then can undergo internal conversion to E_u and/or A_{1u} spin components of the ${}^3A_{2u}$ state. In both Pt(pop-BF₂) and Pt(pop), the higher-lying 3E_u LMCT is the likely coupling state.²³ As documented by UV spectra, perfluoroboration raises the energy of LMCT states relative to ${}^1A_{2u}$, thereby diminishing the ${}^3A_{2u}$ - 3E_u coupling, which in turn slows ISC (eq. 5).

$$k_{ISC} \propto \frac{\left\langle {}^1A_{2u} \left| H_{SO} \right| {}^3E_u \right\rangle^2}{E({}^3E_u) - E({}^1A_{2u})} FC \quad (5)$$

Irrespective of the details of the indirect spin-orbit interaction, the ISC tunneling pathway is expected to be disfavored in Pt(pop-BF₂) because of the smaller FC factor. Since the ${}^1A_{2u}$ and ${}^3A_{2u}$ states largely behave as two imbedded

Pt–Pt harmonic oscillators,¹¹ the overlap between their vibrational wavefunctions is small and solvent vibrations gain in importance as energy-accepting modes, as clearly manifested by the strong solvent dependence of the Pt(pop) k_0 .¹⁰ As BF₂ groups are much bulkier than –O–H···O– units, they will exclude direct interactions between the solvent and terminal P(=O)O groups, as well as with the Pt atoms. Perfluoroboration thus diminishes the ability of the solvent to provide vibrational coupling between the singlet and triplet states, which is required to accept the $\sim 5650\text{ cm}^{-1}$ released during ISC.

The thermally activated ISC channel slows 160 times at 293 K on going from Pt(pop) to Pt(pop-BF₂) (the activation-energy increases from 1190 to 2230 cm^{-1} , Table 2.3) and is primarily responsible for the lengthened singlet lifetime observed in Pt(pop-BF₂). For Pt(pop), the activated pathway may involve thermal population of a higher-lying $d\sigma^* \rightarrow d_{x^2-y^2}$ $^3B_{2u}$ state from $^1A_{2u}$, followed by fast $^3B_{2u}$ decay to $^3A_{2u}$.¹⁰ However, 3E_u LMCT is a much more likely candidate for the intermediate state, as $^3B_{2u}$ is not coupled to $^1A_{2u}$ by first-order SO (it is at much higher energy than thought previously).^{21,22,30} Perfluoroboration, which shifts LMCT states to higher energies (Table 2.1), should raise the $^1A_{2u} \rightarrow ^3E_u$ barrier, in line with experiment. Although thermal population of an intermediate electronic state is the conventional explanation of T-dependent excited-state nonradiative decay in transition metal complexes, for Pt(pop) and Pt(pop-BF₂) it is not likely,³³ as we have no evidence for suitable intermediate states. Indeed, a recent ultrafast study of vibrational coherence in the Pt(pop) $^1A_{2u}$ state demonstrated that its potential

energy surface has harmonic character, which would suggest the absence of an avoided crossing with any low-lying intermediate state. For the same reason, it would be hard to justify an assumption of strong coupling (i.e., surface crossing) between $^1A_{2u}$ and $^3A_{2u}$, whose potential energy surfaces appear to be imbedded, owing to the very similar structures of these states. (Note, however, that the Stokes shift is larger for phosphorescence than fluorescence, indicating that $^3A_{2u}$ is more distorted with respect to the ground state than $^1A_{2u}$.)

An alternative way to explain the activated channel is to assume that thermal population of higher levels of certain vibrational modes provide stronger $^1A_{2u} - ^3A_{2u}$ SO coupling than in the ground state. In other words, activated ISC would not occur from the $\nu = 0$ level of $^1A_{2u}$, but from higher levels that are in resonance with target-state ($^3A_{2u}$) vibrational levels. In this scheme, the most efficient ISC activation would be associated with thermal excitation of deformation modes that lower the symmetry to C_{4h} , C_{2h} , or C_2 , allowing first-order $^1A_{2u} - ^3A_{2u}$ SO coupling. Since the states involved in ISC are strongly localized along the Pt–Pt bond, it is not expected that symmetry lowering due to changes in the mutual orientation of peripheral BF_2 (or, in Pt(pop), $-O-H\cdots O-$ groups) would strongly affect the ISC rate. Instead, the distortion would come from excitation of asymmetric vibrations of the $Pt_2(P-O-P)_4$ core. Such distortions also could induce mixing between $^1,3d\sigma^*p\sigma$ and LMCT states, thereby facilitating indirect SO coupling as well. The increase of the apparent activation energy upon perfluoroboration is attributable to the rigidity of covalent $-BF_2-$ linkages that

increases the energy of activating vibrational modes, so that higher temperatures are required for distortion amplitudes sufficient to induce SO coupling.

Long-lived singlet excited states are rare for transition-metal complexes. For example, the $^1\text{MLCT}$ states of $[\text{M}^{\text{II}}(\text{bpy})_3]^{2+}$ ($\text{M} = \text{Fe}, \text{Ru}$) decay to the corresponding triplets in less than 30 fs,^{39,40} while 80–150 fs lifetimes have been reported for the singlet excited states of Re^{I} carbonyl-diimine sensitizers.^{41–43} Besides $\text{Pt}(\text{pop})$, ps-lived singlet states were observed at ambient temperatures for d^8 – d^8 complexes of Rh and Ir.^{6,24,44–46} In particular, $[\text{Rh}_2(1,3\text{-disocyanopropane})_4]^{2+}$ exhibits room-temperature-solution fluorescence and phosphorescence lifetimes of 1.3 ns and 8.3 μs , respectively, but the fluorescence quantum yield is only 0.07, owing to rapid nonradiative decay to the ground state.⁴⁵ Other examples of long-lived excited singlets include quadruply-bonded metal-metal dimers such as $\text{Mo}_2\text{X}_4(\text{PR}_3)_4$ ($\text{X} = \text{Cl}, \text{Br}, \text{I}; \text{R} = \text{Me}, n\text{-Bu}$) and $[\text{Re}_2\text{X}_8]^{2-}$ ($\text{X} = \text{Cl}, \text{Br}$); these complexes possess $^1\delta\delta^*$ states that have 16–140 ns lifetimes, with $^3\delta\delta^*$ states that are largely bypassed during $^1\delta\delta^*$ decay.^{47,48} The $^1\delta\delta^*$ lifetimes reported for these complexes thus correspond to internal conversion directly to the ground state, the ISC to $^3\delta\delta^*$ being much slower, owing to the very large singlet-triplet splitting and vanishing $^1\delta\delta^* \rightarrow ^3\delta\delta^*$ SO coupling. $^3\delta\delta^*$ states have been detected only very recently by time-resolved IR spectroscopy of $\text{M}_2(\text{O}_2\text{CR})_4$ complexes ($\text{M} = \text{Mo}, \text{W}; \text{R} = \text{Bu}$), for which lifetimes of 40 and 50 ps were determined for $^1\text{MLCT} \rightarrow ^3\delta\delta^*$ and $^1\delta\delta^* \rightarrow ^3\delta\delta^*$ ISC processes.⁴⁹ And $\text{M}_2(\text{O}_2\text{CR})_4$ complexes with electron-accepting substituents R show weakly emissive $\delta \rightarrow \pi^*(\text{O}_2\text{CR})$ $^1\text{MLCT}$ states that decay to the

corresponding nonemissive triplets in 4 to 20 ps.^{50,51} Among mononuclear complexes, picosecond ISC times have been reported for ¹MLCT states of flattened-tetrahedral complexes of Cu^I (13–16 ps)³⁸ and Pt⁰ (3.2 ps).⁵² Symmetry-forbidden first-order SO coupling between optically excited singlet and lowest triplet states is a common feature for all systems with ps-ns singlet lifetimes. Still, forbidden ISC in metal complexes is many orders of magnitude faster than ISC in organic molecules. Theories of spin-vibronic coupling and ISC rates have been elaborated in detail for organic systems that are characterized by very weak SO and small structural perturbations.^{23,36–38} Understanding the dynamics of SO-coupled states of metal-containing molecules and developing systems capable of harvesting singlet excitation energy is a major goal of contemporary transition-metal photophysics.³³

2.4 Concluding remarks

We have shown that modifying all eight P–O–H...O–P peripheral sites of Pt(pop) strongly affects its photophysical properties. Pt(pop-BF₂), which possesses an unusually long-lived singlet excited state, displays very intense fluorescence *and* phosphorescence. Excited-state decay of Pt(pop-BF₂) is mainly determined by these two radiative pathways along with relatively slow singlet-to-triplet ISC. Nonradiative decay to the ground state is far less important. We can conclude that the dramatic ISC slowing relative to Pt(pop) is attributable to a combination of three effects: (i) the electron-withdrawing power of BF₂, which raises pop→pσ LMCT relative to dσ*→pσ state energies and diminishes indirect SO coupling; (ii)

a much more rigid structure, owing to covalent $-\text{BF}_2-$ bridges linking the pop ligands; and (iii) steric protection by BF_2 groups, which shield the $\text{Pt}_2(\text{P}-\text{O}-\text{P})_4$ core from solvent. The distinctive photophysical features of $\text{Pt}(\text{pop}-\text{BF}_2)$ provide a unique opportunity to investigate independently the structures, dynamics, and reactivities of both singlet and triplet $d\sigma^* \rightarrow p\sigma$ excited states in the same molecule. We expect that long-lived vibrational coherence will be observed for the singlet state, and that excited-state reactivity will reflect the asymptotic zwitterionic character of the singlet^{53,54} and the radical-like behavior of the triplet.^{2,3,5,13,14}

2.5 References

- (1) Roundhill, D. M.; Gray, H. B.; Che, C.-M. *Acc. Chem. Res.* **1989**, *22*, 55.
- (2) Smith, D. C.; Gray, H. B. *Coord. Chem. Rev.* **1990**, *100*, 169.
- (3) Smith, D. C.; Gray, H. B. In *ACS Symposium Series 394. The Challenge of d and f Electrons.*; Salahub, D. R., Zerner, M. C., Eds. American Chemical Society, Washington, DC, **1989**, p. 356.
- (4) Marshall, J. L.; Stiegman, A. E.; Gray, H. B. In *Excited States and Reactive Intermediates. ACS Symposium Series.*; Lever, A. B. P., Ed. American Chemical Society, Washington, DC, **1986**; vol. 307, p. 166.
- (5) Sweeney, R. J.; Harvey, E. L.; Gray, H. B. *Coord. Chem. Rev.* **1990**, *105*, 23.
- (6) Fox, L. S.; Kozik, M.; Winkler, J. R.; Gray, H. B. *Science* **1990**, *247*, 1069.
- (7) Fox, L. S.; Marshall, J. L.; Gray, H. B. *J. Am. Chem. Soc.* **1987**, *109*, 6901.
- (8) Farid, R. S.; Chang, I.-J.; Winkler, J. R.; Gray, H. B. *J. Phys. Chem.* **1994**, *98*, 5176.
- (9) Gray, H. B.; Winkler, J. R.; Wiedenfeld, D. *Coord. Chem. Rev.* **2000**, *200-202*, 875.
- (10) Milder, S. J.; Brunschwig, B. S. *J. Phys. Chem.* **1992**, *96*, 2189.
- (11) van der Veen, R. M.; Cannizzo, A.; van Mourik, F.; Vlček, A., Jr.; Chergui, M. *J. Am. Chem. Soc.* **2011**, *133*, 305.
- (12) Stiegman, A. E.; Rice, S. F.; Gray, H. B.; Miskowski, V. M. *Inorg. Chem.* **1987**, *26*, 1112.
- (13) Vlček, A., Jr.; Gray, H. B. *J. Am. Chem. Soc.* **1987**, *109*, 286.
- (14) Vlček, A., Jr.; Gray, H. B. *Inorg. Chem.* **1987**, *26*, 1997.
- (15) Kalsbeck, W. A.; Gingell, D. M.; Malinsky, J. E.; Thorp, H. H. *Inorg. Chem.* **1994**, *33*, 3313.
- (16) Kirk, A. D.; Cai, L.-Z. *Inorg. Chem.* **1998**, *37*, 1051.

- (17) mChe, C.-M.; Butler, L. G.; Gray, H. B.; Crooks, R. M.; Woodruff, W. H. *J. Am. Chem. Soc.* **1983**, *105*, 5492.
- (18) Rice, S. F.; Gray, H. B. *J. Am. Chem. Soc.* **1983**, *105*, 4571.
- (19) Kim, C. D.; Pillet, S.; Wu, G.; Fullagar, W. K.; Coppens, P. *Acta Crystallogr. A* **2002**, *58*, 133.
- (20) van der Veen, R. M.; Milne, C. J.; El Nahhas, A.; Lima, F. A.; Pham, V.-T.; Best, J.; Weinstein, J. A.; Borca, C. N.; Abela, R.; Bressler, C.; Chergui, M. *Angew. Chem. Int. Ed.* **2009**, *48*, 2711
- (21) Stoyanov, S. R.; Villegas, J. M.; Rillema, D. P. *J. Phys. Chem. B* **2004**, *108*, 12175.
- (22) Novozhilova; Volkov, A. V.; Coppens, P. *J. Am. Chem. Soc.* **2003**, *125*, 1079.
- (23) Shimizu, Y.; Tanaka, Y.; Azumi, T. *J. Phys. Chem.* **1984**, *88*, 2423.
- (24) Winkler, J. R.; Marshall, J. L.; Netzel, T. L.; Gray, H. B. *J. Am. Chem. Soc.* **1986**, *108*, 2263.
- (25) McCleskey, T. M.; Winkler, J. R.; Gray, H. B. *J. Am. Chem. Soc.* **1992**, *114*, 6935.
- (26) Caspar, J. V.; Gray, H. B. *J. Am. Chem. Soc.* **1984**, *106*, 3029.
- (27) King, C.; Auerbach, R. A.; Fronczek, F. R.; Roundhill, D. M. *J. Am. Chem. Soc.* **1986**, *108*, 5626.
- (28) Roundhill, D. M.; Shen, Z.-P.; King, C.; Atherton, S. J. *J. Phys. Chem.* **1988**, *92*, 4088.
- (29) Fordyce, W. A.; Brummer, J. G.; Crosby, G. A. *J. Am. Chem. Soc.* **1981**, *103*, 7061.
- (30) Pan, Q.-J.; Fu, H.-G.; Yu, H.-T.; Zhang, H.-X. *Inorg. Chem.* **2006**, *45*, 8729.
- (31) Peterson, J. R.; Kalyanasundaram, K. *J. Phys. Chem.* **1985**, *89*, 2486.
- (32) Footnote.
- (33) Baková, R.; Chergui, M.; Daniel, C.; Vlček, A., Jr.; Zálíš, S. *Coord. Chem. Rev.* **2011**, *255*, 975.
- (34) Yersin, H.; Rausch, A. F.; Czerwieniec, R.; Hofbeck, T.; Fischer, T. *Coord. Chem. Rev.* **2011**, *255*, 2622.
- (35) Yersin, H.; Finkenzeller, W. J. In *Highly Efficient OLEDs with Phosphorescent Materials*; Yersin, H., Ed. Wiley-VCH, Weinheim, **2008**, p. 1.
- (36) Siebrand, W. *Chem. Phys. Lett.* **1970**, *6*, 192.
- (37) Lawetz, V.; Orlandi, G.; Siebrand, W. *J. Chem. Phys.* **1972**, *56*, 4058.
- (38) Siddique, Z. A.; Yamamoto, Y.; Ohno, T.; Nozaki, K. *Inorg. Chem.* **2003**, *42*, 6366.
- (39) Cannizzo, A.; van Mourik, F.; Gawelda, W.; Zgrablic, G.; Bressler, C.; Chergui, M. *Angew. Chem. Int. Ed.* **2006**, *45*, 3174.
- (40) Gawelda, W.; Cannizzo, A.; Pham, V.-T.; van Mourik, F.; Bressler, C.; Chergui, M. *J. Am. Chem. Soc.* **2007**, *129*, 8199.
- (41) Cannizzo, A.; Blanco-Rodríguez, A. M.; Nahhas, A.; Šebera, J.; Zálíš, S.; Vlček, A., Jr.; Chergui, M. *J. Am. Chem. Soc.* **2008**, *130*, 8967.

- (42) El Nahhas, A.; Cannizzo, A.; van Mourik, F.; Blanco-Rodríguez, A. M.; Záliš, S.; Vlček, A., Jr.; Chergui, M. *J. Phys. Chem. A* **2010**, *114*, 6361.
- (43) El Nahhas, A.; Consani, C.; Blanco-Rodríguez, A. M.; Lancaster, K. M.; Braem, O.; Cannizzo, A.; Towrie, M.; Clark, I. P.; Záliš, S.; Chergui, M.; Vlček, A., Jr. *Inorg. Chem.* **2011**, *50*, 2932.
- (44) Miskowski, V. M.; Rice, S. F.; Gray, H. B.; Dallinger, R. F.; Milder, S. J.; Hill, M. G.; Exstrom, C. L.; Mann, K. R. *Inorg. Chem.* **1994**, *33*, 2799.
- (45) Miskowski, V. M.; Rice, S. F.; Gray, H. B. *J. Phys. Chem.* **1993**, *97*, 4277.
- (46) Marshall, J. L.; Stobart, S. R.; Gray, H. B. *J. Am. Chem. Soc.* **1984**, *106*, 3027.
- (47) Miskowski, V. M.; Goldbeck, R. A.; Kliger, D. S.; Gray, H. B. *Inorg. Chem.* **1979**, *18*, 86.
- (48) Hopkins, M. D.; Gray, H. B. *J. Am. Chem. Soc.* **1984**, *106*, 2468.
- (49) Alberding, B. G.; Chisholm, M. H.; Gustafson, T. L. *Inorg. Chem.* **2012**, *51*, 491–498.
- (50) Byrnes, M. J.; Chisholm, M. H.; Gallucci, J. A.; Liu, Y.; Ramnauth, R.; Turro, C. J. *Am. Chem. Soc.* **2005**, *127*, 17343.
- (51) Alberding, B. G.; Chisholm, M. H.; Gallucci, J. C.; Ghosh, Y.; Gustafson, T. L. *Proc. Natl. Acad. Sci. U.S.A.* **2011**, *108*, 8152.
- (52) Siddique, Z. A.; Ohno, T.; Nozaki, K. *Inorg. Chem.* **2004**, *43*, 663.
- (53) Hopkins, M. D.; Gray, H. B.; Miskowski, V. M. *Polyhedron* **1987**, *6*, 705.
- (54) Benard, M.; Veillard, A. **1982**, *90*, 160.

Chapter 3:

Electronic structures of palladium(II) dimers

The text in this chapter was taken in part from:

Bercaw, J. E.; Durrell, A. C.; Gray, H. B.; Green, J. C.; Hazari, N.; Labinger, J. A.; Winkler, J. R. *Inorg. Chem.* **2010**, *49*, 1801–1810.

3.1 Abstract

The Pd^{II} dimers [(2-phenylpyridine)Pd(μ -X)]₂ and [(2-*p*-tolylpyridine)Pd(μ -X)]₂ (X = OAc or TFA) do not exhibit the expected planar geometry (of approximate *D*_{2h} symmetry), but instead resemble an open “clamshell” in which the acetate ligands are perpendicular to the plane containing the Pd atoms and 2-arylpyridine ligands, with the Pd atoms brought quite close to one another (approximate distance 2.85 Å). The molecules adopt this unusual geometry in part because of a d⁸-d⁸ bonding interaction between the two Pd centers. The Pd–Pd dimers exhibit two successive one-electron oxidations: Pd^{II}–Pd^{II} to Pd^{II}–Pd^{III} to Pd^{III}–Pd^{III}. Photophysical measurements reveal clear differences in the UV-visible and low-temperature fluorescence spectra between the clamshell dimers and related planar dimeric [(2-phenylpyridine)Pd(μ -Cl)]₂ and monomeric [(2-phenylpyridine)Pd(en)][Cl] (en = ethylenediamine) complexes that do not have any close Pd–Pd contacts. DFT and AIM analyses confirm the presence of a Pd–Pd bonding interaction in [(2-phenylpyridine)Pd(μ -X)]₂ and show that the HOMO is a d_{2z} σ^* Pd–Pd antibonding orbital, while the LUMO and close-lying empty orbitals are mainly located on the 2-phenylpyridine rings. Computational analyses of other Pd^{II}–Pd^{II} dimers that have short Pd–Pd distances yield an orbital ordering similar to that of [(2-phenylpyridine)Pd(μ -X)]₂, but quite different from that found for d⁸-d⁸ dimers of Rh, Ir, and Pt. This difference in orbital ordering arises because of the unusually large energy gap between the 4d and 5p orbitals in Pd, and may explain why Pd d⁸-d⁸ dimers do not exhibit the distinctive photophysical properties of related Rh, Ir, and Pt species.

3.2 Introduction

Complexes containing metal-metal bonds play an important role in both inorganic and organometallic chemistry.¹ Among the many such complexes, dimers of square planar Rh^I, Ir^I and Pt^{II} centers are members of a special class that feature attractive d⁸-d⁸ interactions, as documented by optical and vibrational spectroscopy,² x-ray crystallography,³ EXAFS⁴ and *ab initio* electronic structure theory.⁵ Overlap in the axial direction between the valence d_{z²} orbitals of the square planar metal centers results in both filled bonding (dσ) and antibonding (dσ*) orbitals; however, there is a net overall bonding interaction due to symmetry-allowed mixing with the (n+1) metal s and p_z orbitals. This creates four key orbitals (labeled according to their principal atomic character) in the following order of increasing energy: one strongly bonding (dσ), one weakly antibonding (dσ*), one weakly bonding (pσ), and one strongly antibonding (pσ*); only the first two are filled (Figure 3.1). Such d⁸-d⁸ interactions most commonly lead to discrete dimers or trimers, although in some cases higher-order oligomers are formed.

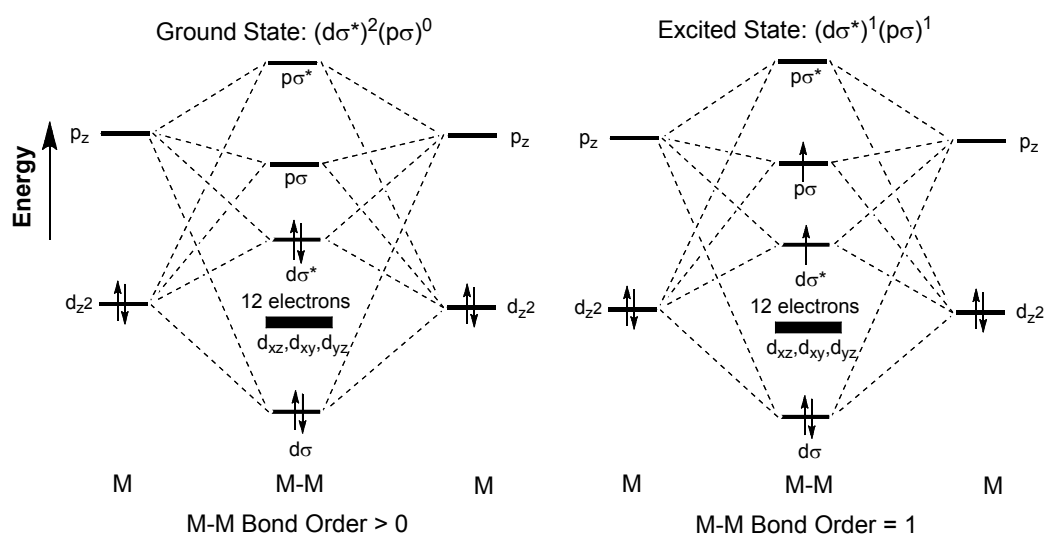


Figure 3.1: Orbital energy level diagram for interaction along the metal–metal axis of two d^8 square-planar units, in both ground and excited states

In 1975, Mann et al. reported the electronic spectroscopic characterization of $[\text{Rh}(\text{CNPh})_4]_n^{n+}$ ($n = 1, 2, \text{ or } 3$) in acetonitrile solution and proposed that aggregation occurred through a direct Rh–Rh interaction.^{2a} Since this initial discovery, many d^8 – d^8 dimers of Rh^{I} , Ir^{I} , and Pt^{II} have been found to exhibit a rich diversity of reactions resulting from photoexcitation and the accompanying increase in metal–metal bond order. A particularly widely studied d^8 – d^8 dimer is $\text{Pt}_2(\mu\text{-P}_2\text{O}_5\text{H}_2)_4^{4-}$ (Pt-pop),⁶ which exhibits electronic absorption bands at 367 and 435 nm, assigned to singlet and triplet $d\sigma^* \rightarrow p\sigma$ transitions, respectively, as well as 514 nm phosphorescence ($\tau \sim 9 \mu\text{s}$ at ambient temperature) from the lowest excited triplet and 407 nm fluorescence from a much shorter-lived (8–40 ps) excited singlet.⁷ When irradiated at 367 nm, Pt-pop exhibits very rich chemistry, including: electron transfer reactions with various substrates; hydrogen atom abstraction from hydrocarbons, alcohols, stannanes, and silanes; halogen atom abstraction from alkyl and aryl chlorides; duplex DNA cleavage; and catalytic conversion of isopropanol to acetone and hydrogen.^{6,8}

In contrast to well-studied Rh, Ir, and Pt systems, there has been little research into Pd dimers that may experience d^8 – d^8 interactions, and even fewer investigations of their photophysical properties.⁹ Several complexes have been reported with Pd–Pd distances ranging from 2.55–3.05 Å,⁹ shorter than the sum of the van der Waals radii (3.26 Å);¹⁰ but there has been no agreement on whether a metal–metal bond is present. The limited photophysical investigations have been inconclusive; a weak Pd–Pd bonding interaction in the model compounds $[\text{Pd}(\text{CN})_2(\text{PH}_3)_2]_2$ (Pd–Pd = 3.107 Å) and $[\text{Pd}(\text{CN})_2(\mu\text{-PH}_2\text{CH}_2\text{PH}_2)]_2$ (Pd–Pd =

3.020 Å) was suggested based on MP2 and TDDFT calculations.^{9b,9c} Although SCF- $X\alpha$ -SW calculations on the model compound $[\text{Pd}(\text{HNCHNH})_2]_2$ predicted an even *shorter* Pd–Pd distance (2.622 Å), it was concluded that there was *no* bonding interaction.¹¹

As part of an investigation into selective oxidation catalysts,¹² we have studied several members of a family of $[(2\text{-arylpyridine})\text{Pd}^{\text{II}}(\text{O}_2\text{CCX}_3)]_2$ dimers; notably, there has been considerable recent interest in these and related species as precursors to $\text{Pd}^{\text{III}}\text{-Pd}^{\text{III}}$ or $\text{Pd}^{\text{II}}\text{-Pd}^{\text{IV}}$ dimers that are catalytically active for C–C bond forming reactions.¹³ Here we present spectroscopic data combined with theoretical analyses, using both DFT and Atoms in Molecules (AIM) methods, that strongly support the presence of weakly bonding $d^8\text{-}d^8$ interactions in these dimers. We extend our results to a number of other Pd^{II} species with short Pd–Pd distances, and demonstrate that the ordering of unoccupied molecular orbitals differs from that found for Rh, Ir, and Pt dimers containing $d^8\text{-}d^8$ interactions, thereby accounting for striking differences in photophysical properties and reactivities.

3.3 Results and discussion

Synthesis and solid-state structures

The structure of $[(2\text{-phenylpyridine})\text{Pd}(\mu\text{-OAc})_2]$ (**1**), which also has been reported elsewhere,¹⁴ does not exhibit the expected planar geometry (of approximate D_{2h} symmetry), but instead resembles an open “clamshell” in which the acetate ligands are perpendicular to the plane containing the Pd atoms and 2-phenylpyridine ligands, with the Pd atoms brought quite close to one another, 2.86216(11) Å.¹⁵ We also synthesized the known compound $[(2\text{-}p\text{-tolylpyridine})\text{Pd}(\mu\text{-OAc})_2]$ (**2**), and

two closely related species, [(2-phenylpyridine)Pd(μ -TFA)]₂ (**3**) and [(2-*p*-tolylpyridine)Pd(μ -TFA)]₂ (**4**) using a modification of a literature procedure.¹⁶ The structures of **1–4** are closely related: all four molecules adopt the clamshell geometry (Figure 3.2 and Table 3.1), a consequence, we suggest, of both an attractive d⁸–d⁸ interaction between the two Pd centers and a parallel displaced (slipped) π -stacking interaction between the phenylpyridine rings.¹⁷ In all structures the distances between the ring centroids vary from 3.70 Å to over 4 Å, and the angles between the ring normal of the plane and the centroid vector are between 20° and 40°, consistent with the approximate upper limits for significant interaction,¹⁷ π -stacking between the phenylpyridine rings presumably contributes to the short Pd–Pd distance, but we believe that the d⁸–d⁸ interaction plays the main role in determining the overall geometry, because in principle the molecule could π -stack just as effectively if it were planar. The structures of the TFA bridged species **3** and **4** both contain 3 independent molecules, with similar bond distances and angles in the asymmetric unit, while there is disorder associated with the methyl groups of the 2-*p*-tolylpyridine ligands in **2** and **4**. The Pd–Pd distance decreases by approximately 0.01 Å when moving from phenylpyridine to the more electron donating 2-*p*-tolylpyridine, while moving from OAc to the less-electron-donating TFA increases the distance by 0.01 Å.

An interesting feature of the molecules is the relative orientation of the 2-arylpyridine rings, which may either be “*cis*”, with both pyridine rings opposite one other (approximate C_s symmetry), or “*trans*”, with each pyridine ring opposite a benzene ring (approximate C₂ symmetry). In **1** and **3** it is impossible to distinguish

between all-*cis* or a 50%-50% mixture of *cis* and *trans* (for which crystallographic averaging would give the observed structure). However, the structure of **2**, though disordered, shows a preference for the *trans* orientation, with only approximately 15% *cis*. The structure of **4** is even more highly disordered, but both orientations can be observed, again with a preference for *trans*.

In order to assess the presence of Pd–Pd bonding interactions by photophysics, we also examined control samples. The structures of the previously reported¹⁸ complexes [(2-phenylpyridine)Pd(μ -Cl)]₂ (**5**) and [(2-phenylpyridine)Pd(en)][Cl] (**6**, en = ethylenediamine) indicate the absence of any Pd–Pd interaction. **5** has a nearly flat structure, in contrast to **1–4**, with the bridging chlorides almost coplanar with the 2-phenylpyridine ligands (Figure 3.3). The dimeric units are stacked, but the closest Pd–Pd contact is 3.691 Å, which is significantly larger than the sum of the van der Waals radii of two Pd atoms. **6** exhibits normal square planar coordination geometry (Figure 3.4); the closest intermolecular Pd–Pd distance is greater than 5 Å.

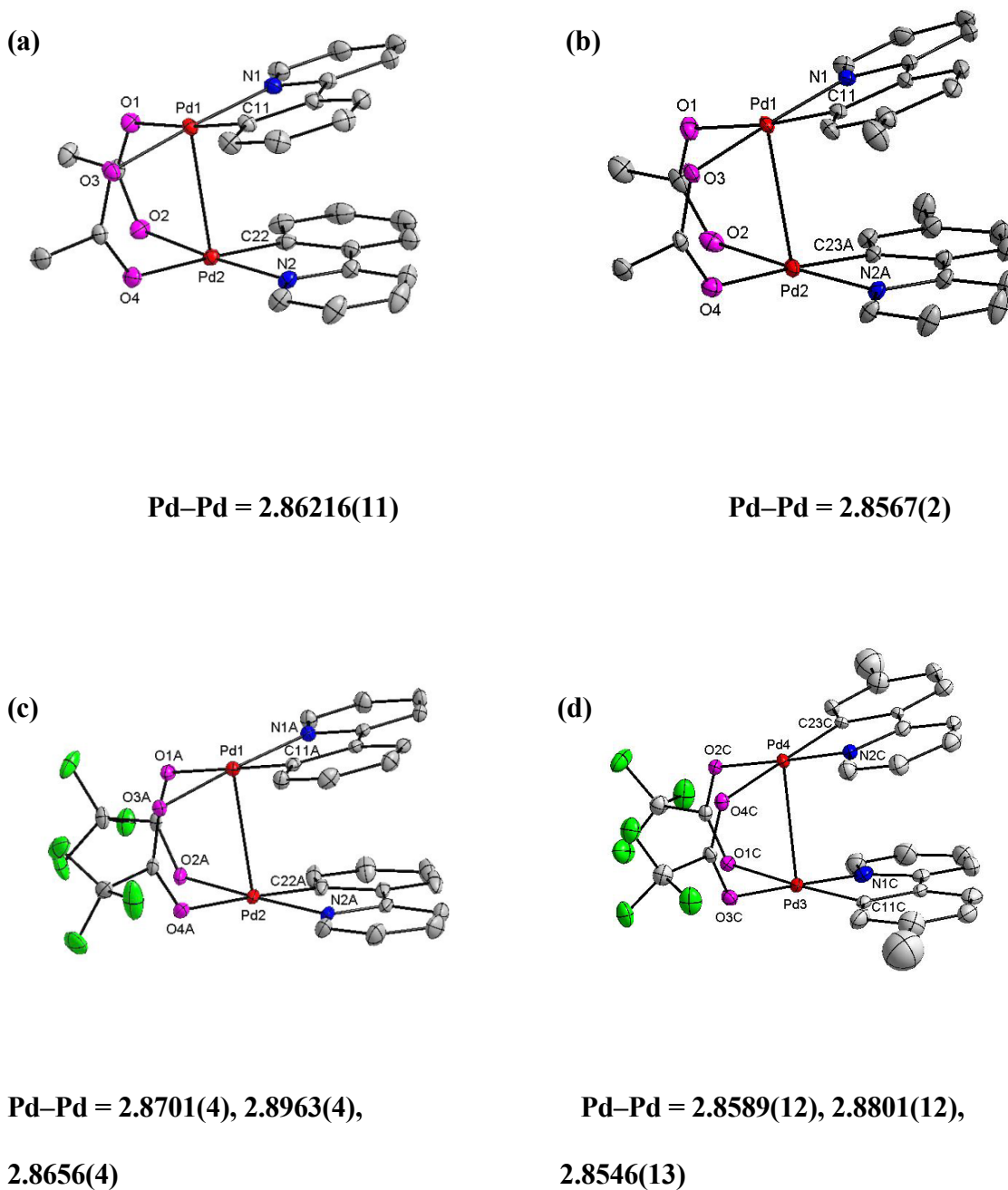


Figure 3.2. The structures of [(2-phenylpyridine)Pd(μ-OAc)₂] (**1**) (a); [(2-*p*-tolylpyridine)Pd(μ-OAc)₂] (**2**) (only major conformation drawn) (b); [(2-phenylpyridine)Pd(μ-TFA)₂] (**3**) (c); and [(2-*p*-tolylpyridine)Pd(μ-TFA)₂] (**4**) (only major conformation drawn) (d). All H atoms were omitted for clarity.

Table 3.1. Selected bond distances in **1–4**

	1	2	3^a	4^a
Pd(1)–C(11)	1.9566(8)	1.956(2)	1.969(3), 1.958(3), 1.960(4)	1.946(5), 1.925(7), 1.897(15)
Pd(1)–N(1)	2.0116(6)	2.0161(17)	2.008(3), 2.009(3), 2.005(3)	1.982(6), 1.974(6), 2.037(13)
Pd(1)–O(3)	2.0473(5)	2.0474(14)	2.093(2), 2.111(3), 2.096(2)	2.062(9), 2.081(7), 2.088(8)
Pd(1)–O(1)	2.1428(6)	2.1378(16)	2.171(2), 2.152(2), 2.184(3)	2.172(8), 2.120(7), 2.132(8)
Pd(1)–Pd(2)	2.86216(11)	2.8567(2)	2.8701(4), 2.8963(4), 2.8656(4)	2.8589(12), 2.8801(12), 2.8546(13)
Pd(2)–C(22)	1.9616(7)	1.937(2)	1.960(4), 1.964(4), 1.976(4)	1.792(9), 1.974(6), 1.894(6)
Pd(2)–N(2)	2.0052(6)	2.0590(16)	2.000(3), 1.964(4), 1.998(4)	2.195(10), 1.999(6), 2.027(6)
Pd(2)–O(2)	2.0520(6)	2.0636(17)	2.077(3), 2.097(3), 2.074(3)	2.088(11), 2.106(8), 2.096(8)
Pd(2)–O(4)	2.1562(5)	2.1407(15)	2.163(2), 2.133(3), 2.156(2)	2.117(10), 2.157(7), 2.145(9)

^aThree independent conformations

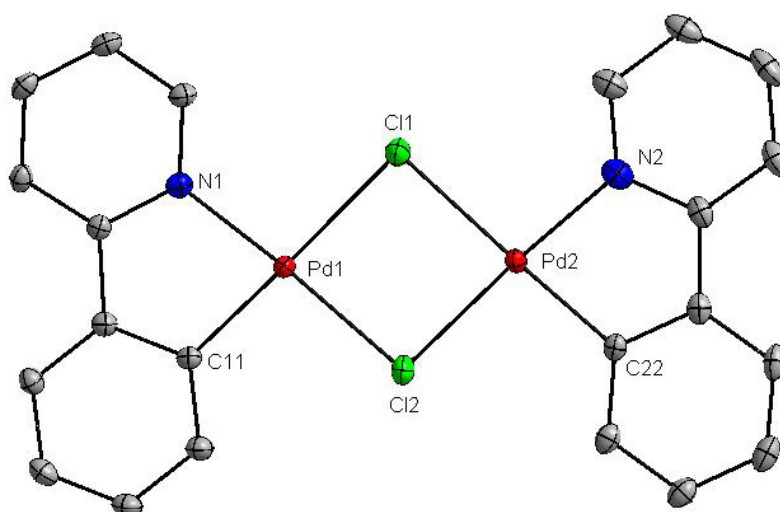


Figure 3.3. The structure of $[(2\text{-phenylpyridine})\text{Pd}(\mu\text{-Cl})]_2$ (**5**). All H atoms were omitted for clarity. Selected bond distances (\AA) of **5**: Pd(1)–C(11) 1.9865(10), Pd(1)–N(1) 2.0134(9), Pd(1)–Cl(2) 2.3633(3), Pd(1)–Cl(1) 2.4233(3), Pd(2)–C(22) 1.9869(10), Pd(2)–N(2) 2.0146(10), Pd(2)–Cl(2) 2.3725(3), Pd(2)–Cl(1) 2.4271(3).

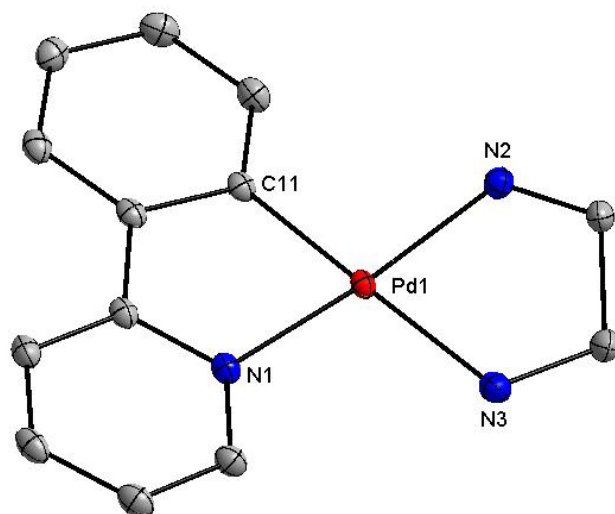
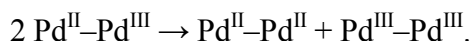


Figure 3.4. The structure of [(2-phenylpyridine)Pd(en)][Cl] (**6**). All H atoms and the Cl⁻ anion were omitted for clarity. Selected bond distances (Å) of **6**: Pd(1)–C(11) 1.9849(12), Pd(1)–N(1) 2.0195(9), Pd(1)–N(2) 2.0652(10), Pd(1)–N(3) 2.1443(11).

Electrochemistry

Cyclic voltammograms of **1–4** in CH₂Cl₂ are shown in Figure 3.5; differential pulse voltammetry (Figure 3.6) was used to further resolve the electrochemical features (Table 3.2). Compounds **1** and **2** show one reversible peak (390 and 350 mV, respectively) assigned to Pd^{III}–Pd^{II} / Pd^{II}–Pd^{II} and one irreversible peak (710 and 740 mV) assigned as the Pd^{III}–Pd^{III} / Pd^{II}–Pd^{III} couple. The decreased area under the second peak is attributable to disproportionation of the Pd^{II}–Pd^{III} mixed-valence state:



Such processes also occur in electrochemically generated Rh^I–Rh^{II} systems.¹⁹ Irreversible oxidation of the ligand occurs at anodic potentials greater than 1 V (Figure C.1). The Pd^{III}–Pd^{II} / Pd^{II}–Pd^{II} couple is shifted anodically by 300 mV in **3** and **4** and a second Pd–Pd redox event is not observed before the onset of ligand oxidation. We believe that the shift to higher potentials, seen as the bridging ligand is changed from acetate to trifluoroacetate, reflects increased withdrawal of electron density from Pd₂, stabilizing the HOMO and rendering oxidation more difficult. The potentials of Pd^{II}–Pd^{III} / Pd^{II}–Pd^{II} as well as Pd^{III}–Pd^{III} / Pd^{II}–Pd^{III} couples in **1** and **2** are comparable with those reported recently for a binuclear palladium benzoquinoline acetate complex.^{13a}

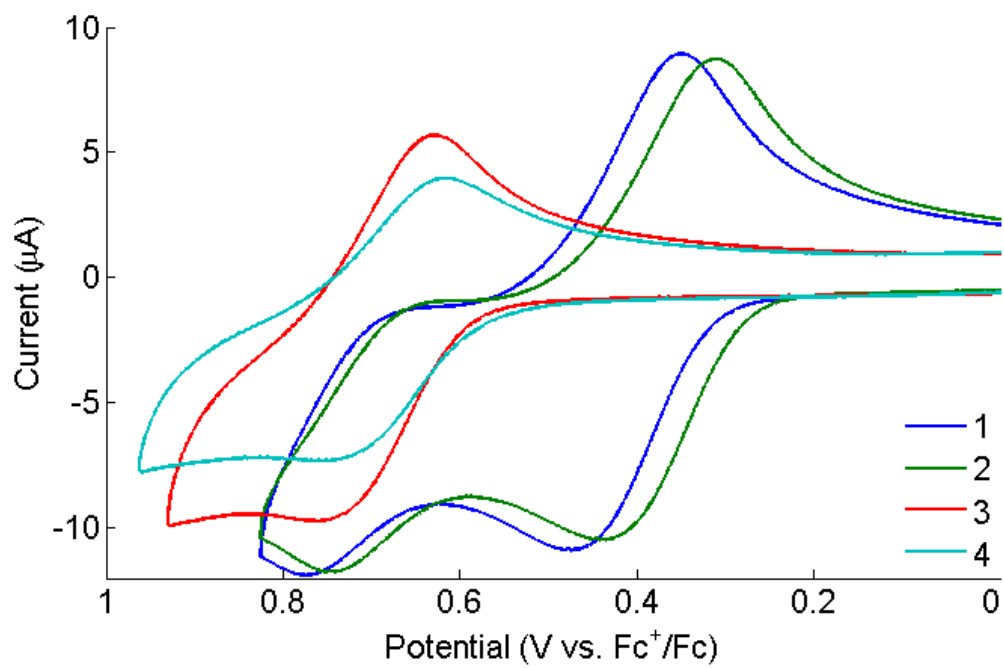


Figure 3.5. Cyclic voltammograms of 1–4 in CH₂Cl₂ solution

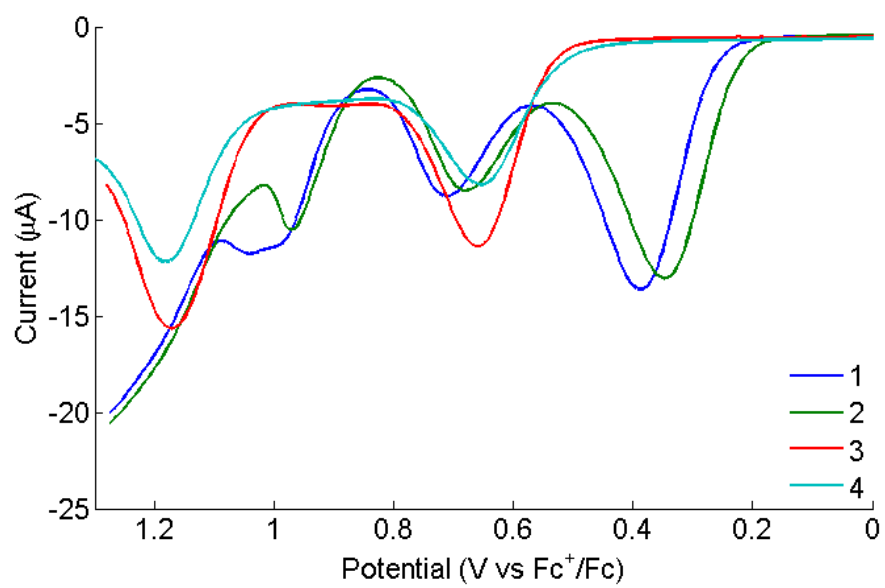


Figure 3.6. Differential pulse voltammograms of compounds **1–4** in CH₂Cl₂ solution

Table 3.2. Reduction potentials for compounds **1–4** (mV vs. Fc^+ / Fc) from DPV experiments in CH_2Cl_2

Compound	$\text{Pd}^{\text{II}}\text{-Pd}^{\text{III}} / \text{Pd}^{\text{II}}\text{-Pd}^{\text{II}}$	$\text{Pd}^{\text{III}}\text{Pd}^{\text{III}} / \text{Pd}^{\text{II}}\text{-Pd}^{\text{III}}$
1	390	710
2	350	680
3	660	Not observed
4	660	Not observed

A CV for **5** could not be obtained in CH₂Cl₂ owing to solubility problems; however, measurements made in acetonitrile reveal a single irreversible oxidation near 820 mV, assigned to Pd^{II}-Pd^{III} / Pd^{II}-Pd^{II} (Figure C.2). The CVs for **1-4** in acetonitrile are surprisingly different from those reported in CH₂Cl₂ (Table 3). The potential associated with the first oxidation depends strongly on the identity of the bridging ligand, ranging from 380 mV (vs. Fc⁺ / Fc) for acetate-bridged **2** to 1180 mV for TFA-bridged **4**, a difference that is much larger than we would have expected. Of greater interest is that the experiments in acetonitrile show clearly that **1** and **2** are more easily oxidized than **5**, which is consistent with our electronic structural model: the HOMO is Pd-Pd antibonding in **1** and **2**; it is nonbonding in **5**. DFT calculations (see below and Supporting Information for details) are consistent with the experimentally determined reduction potentials. Unfortunately, reliable electrochemical data were not obtained for **6**, owing to its low solubility in both acetonitrile and CH₂Cl₂.

Table 3.3: Reduction potentials for compounds **1–5** (mV vs Fc^+/Fc) from DPV experiments in CH_3CN

Compound	$\text{Pd}^{\text{II}}-\text{Pd}^{\text{III}}/\text{Pd}^{\text{II}}-\text{Pd}^{\text{II}}$	$\text{Pd}^{\text{III}}-\text{Pd}^{\text{III}}/\text{Pd}^{\text{II}}-\text{Pd}^{\text{III}}$
1	430	1400
2	380	1350
3	1160	1400
4	1180	1370
5	820	1340

Photophysics

UV-vis absorption spectra of **1–6** (Figure 3.7) follow Beer's Law, indicating that aggregation does not occur at concentrations below 200 μM . Intense absorption bands are observed at wavelengths shorter than 350 nm, with molar absorptivities greater than $5000 \text{ M}^{-1}\text{cm}^{-1}$ (Table 3.4). Compounds **1** and **2** exhibit weaker absorptions with maxima at 420 nm ($\epsilon = 2000 \text{ M}^{-1}\text{cm}^{-1}$), whereas absorptions of **3** and **4** in the visible region are broad and featureless. The absorption profiles of **5** and **6** are very similar to those of **1–4** in the UV region, but not at wavelengths greater than 380 nm. The higher energy bands are attributable to $[\pi-\pi^*]$ intraligand (IL) transitions, and the visible absorption peaks in the spectra of **1** and **2** are assigned to $[\text{d}\sigma^*(\text{Pd}_2)-\pi^*(\text{ppy})]$ metal–metal-to-ligand charge transfer (MMLCT). MMLCT transitions of **3** and **4** are observed as absorptions at higher energy that tail into the visible region. The blue shift is attributable to electron withdrawal from Pd_2 to the bridging TFA ligands, which stabilizes the $\text{d}\sigma^*(\text{Pd}_2)$ HOMO. The electronic spectrum of **5**, where the Pd–Pd distance is greater than 3.6 Å, is very similar to that of monometallic **6**.

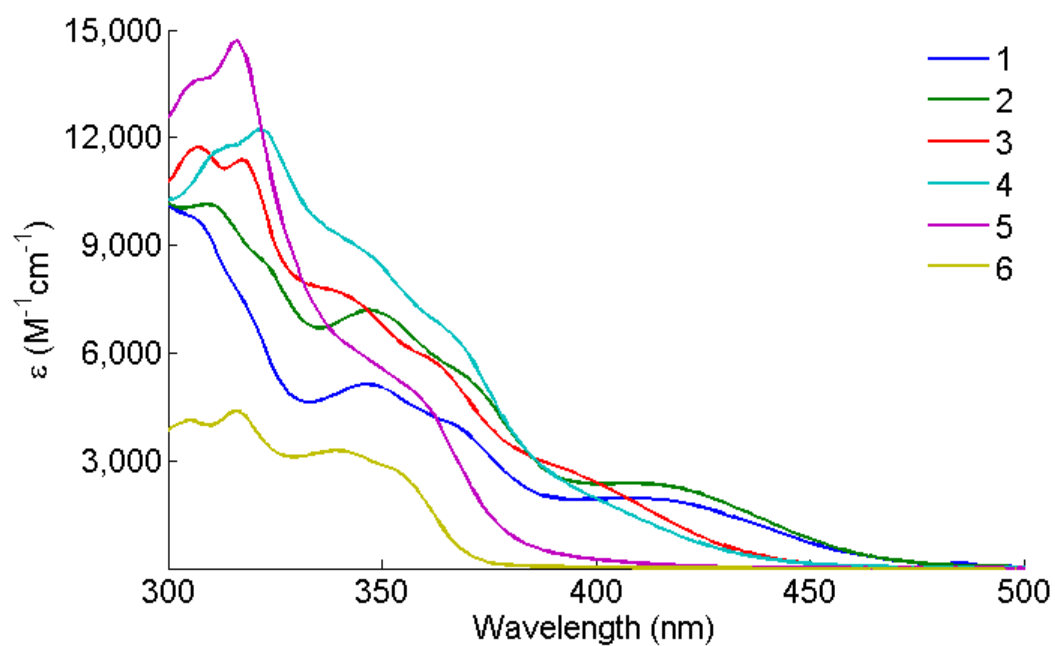


Figure 3.7. Electronic absorption spectra of **1–6** in 2-MeTHF solutions

Luminescence was not detected from any of the compounds **1–6** at room temperature; however, all were found to luminesce upon cooling to cryogenic temperatures. Excitation (355 nm) of samples in 2-methyltetrahydrofuran (2-MTHF) glasses at 77 K reveals richly structured emission features in the 450–600 nm region. Notably, there is a sharp peak at 461 nm in the emission spectrum of **1** (Figure 3.8), and the spectra of **3**, **5**, and **6** are similar; the sharp feature is red shifted by 5 nm in **2** and **4** (Table 3.4). The 450–600 nm emission system in each case is likely attributable to an electronic transition that involves a mixture of ligand-centered [π - π^*] and metal-to-ligand charge transfer (MLCT) components. Vibronic peaks spaced by 1200 cm^{-1} indicate that this transition is coupled to aromatic ring-breathing modes. Additional structure on these features with approximately 400 cm^{-1} spacings suggests that there also is excitation of ground state Pd–L stretching vibrations. Importantly, the **1–4** 450–600 nm emission profiles are similar to those of monomeric metal–phenylpyridine complexes.

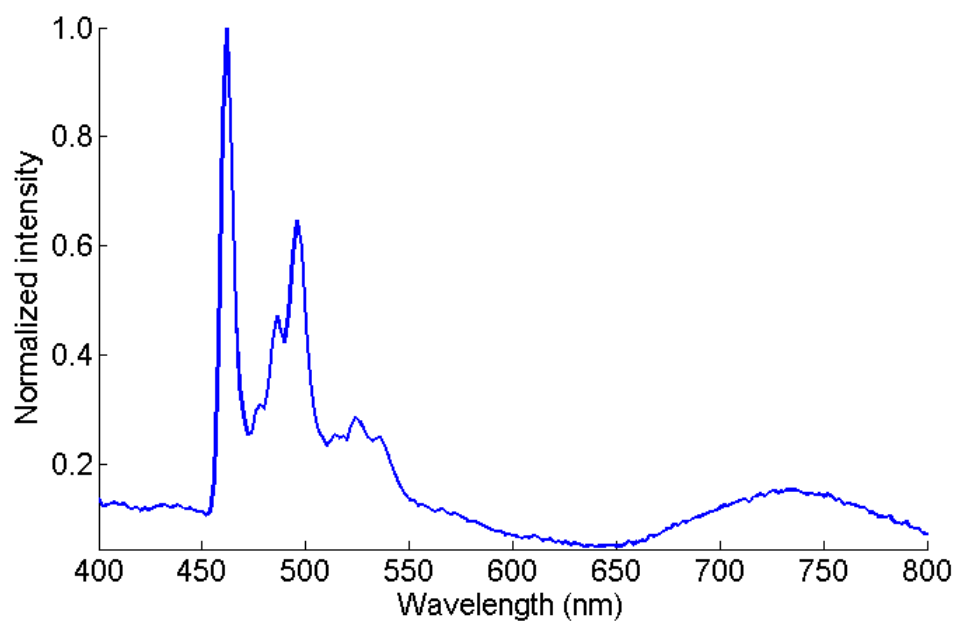


Figure 3.8. Emission spectrum of **1** in a 2-MeTHF glass at 77 K ($\lambda_{\text{ex}} = 355$ nm)

Table 3.4. Absorption and emission data

Compound	Absorption	Emission ^a
	$\lambda_{\text{max}}/\text{nm}$ ($\epsilon_{\text{max}}/\text{M}^{-1}\text{cm}^{-1}$)	$\lambda_{\text{em}}/\text{nm}$ ($\tau_0/\mu\text{s}$)
1	305 (10300), 315 (8100), 350 (5900), 410 (1800)	461 (180 (70%), 70 (30%)), 740 (150 (50%), 60 (50%))
2	309 (10000), 322 (8500), 347 (7200), 373 (5000), 410 (2300)	466 (240 (70%), 110 (30%)), 740 (65 (40%), 12 (60%))
3	307 (11800), 317 (11400), 343 (7300), 362 (5400), 400 (2300)	461 (290 (70%), 80 (30%)), 740 (50 (20%), 10 (80%))
4	313 (11700), 322 (12200), 347 (8800), 370 (4000), 400 (1900)	466 (250 (80%), 50 (20%)), 740 (60 (30%), 10 (70%))
5	307 (13800), 317 (14700), 360 (4500)	461 (320)
6	305(4100), 317 (4400), 338 (3300)	461 (350)

^aMeasurements were made on samples in 2-MTHF glasses at 77 K ($\lambda_{\text{ex}} = 355$ nm).

Emission spectra of complexes **1–4** (which have short Pd–Pd distances) also exhibit a broad system that peaks at 740 nm. This low-energy band (without any hint of vibronic structure at 77 K) is not observed in the spectra of monomeric phenylpyridine complexes (e.g., **6**) or the phenylpyridine chloride dimer **5**. We assign this feature to an MMLCT transition, in accord with our calculations of the relative energies of $d\sigma^*(Pd_2)$ HOMO and ligand π^* LUMO levels (see below). Upon changing the excitation wavelength to 420 nm, the 460 nm emission quantum yields of **1–4** decrease markedly, but the 740 nm emission intensity is largely unaffected. On varying the excitation wavelength from 300 to 420 nm and monitoring luminescence of **1** and **2** at 460 nm, we found that the absorption and excitation spectra are similar between 300 and 380 nm, but not from 380 to 420 nm, a region in which the emission intensity is extremely weak. When a similar experiment was conducted while monitoring emission at 790 nm, the excitation spectrum followed absorbance through the visible region (Figure 3.9). We therefore suggest that there are two competitive pathways for deactivation of the higher-energy IL ($\pi-\pi^*$) excited state: one is direct radiative decay to the ground state, and the other is relatively slow internal conversion to the MMLCT excited state.

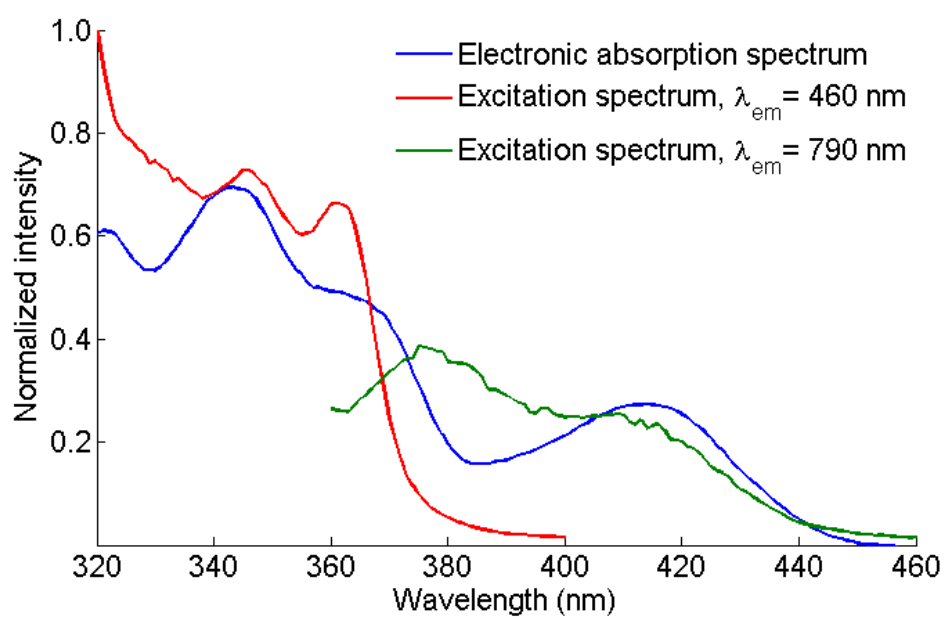


Figure 3.9. Absorption and excitation spectra of **2** in 2-MeTHF at 77 K

Measurements of radiative decay kinetics have shed light on the nature of the excited state dynamics. With excitation at 355 nm, decays from **1–4** monitored at both 460 and 720 nm are biexponential, with lifetimes in microsecond ranges. In contrast, emission decay from electronic excitation of the chloro-bridged species **5** is monoexponential, with a lifetime consistent with those determined at 77 K for other M(ppy) complexes.²⁰ All emission spectra recorded at 460 nm also exhibited a short-lived fluorescence component.²¹ We tentatively suggest that the biexponential kinetics associated with **1–4** emissions are attributable to electronically excited stereoisomers (*cis*- or *trans*-N-Pd-Pd-N geometry) in the 77 K glasses.²²

Density functional theory analysis of bonding in compounds 1–5

DFT studies were performed on **1** (with no symmetry constraints, which also serves as a model for **2**), **3** (with no symmetry constraints, which also serves as a model for **4**), and **5** (modeled using C_{2h} symmetry). In general there was good agreement between experimental and calculated structures, which suggests that our model is able to reproduce key structural parameters.²³ The calculations on **1** and **3** show that the HOMO is a $d_{z^2} \sigma^*$ Pd–Pd antibonding orbital, while the LUMO and close-lying empty orbitals are located on the 2-phenylpyridine rings and possess mainly ligand character. The Pd–Pd σ -bonding character (a mixture of both d_{z^2} and d_{xy}) is spread over two MOs (91 and 93) and mixes with both the bridging acetate and 2-phenylpyridine ligands. As expected, there are a number of occupied nonbonding metal orbitals and ligand-based orbitals between the HOMO and the

Pd–Pd bonding orbitals. Selected molecular orbitals of **1**, with the percentage contributions from different Pd atomic orbitals, are shown in Figure 3.10.

A fragment analysis was performed in which **1** was broken into Pd₂, (phenylpyridine)₂ and (OAc)₂ units; the resulting molecular orbital diagram is shown in Figure 3.11. The analysis confirms that the LUMO and slightly higher energy orbitals are based on the 2-phenylpyridine ligands. Importantly, it shows that although the HOMO is predominantly formed from the Pd d_{z²} orbitals, there also are small contributions from the 5s and 5p_z orbitals due to symmetry-allowed mixing (the HOMO in Figure 3.10 is a linear combination of the 5s and 5p_z orbitals; they also make small contributions to the 3σ_g, which predominantly has d_{z²} character). Similar mixing occurs in the orbitals with Pd–Pd bonding character (91 and 93), although the contribution from the 5s and 5p_z orbitals is smaller due to the greater disparity in orbital energies. The overall effect of this mixing is to increase overlap in the bonding interaction, while decreasing overlap in the antibonding interaction; a Pd–Pd bond order of 0.11 was calculated for **1**.²⁴ This is consistent with a weak bonding interaction and suggests the presence of d_{z²}, p_z, and s orbital mixing in **1–4**, similar to that described earlier for Pt-pop. The AIM approach,²⁵ which uses topological analysis of the electron distribution to characterize bonding interactions, confirms the presence of metal–metal bonding interactions in **1** and **3**. In both cases (3, -1), bond-critical points (indicative of the presence of a bonding interaction)²⁶ centered between the two Pd atoms were found. The ellipticity values were 0.004 and 0.003, respectively, indicating a bonding interaction.

Frequency calculations on **1** and **3** gave Pd–Pd symmetric and asymmetric stretches around 120–130 cm^{-1} , both heavily coupled to other vibrations such as ring breathing modes. We were unable to obtain direct experimental evidence for a Pd–Pd bonding interaction from polarized single-crystal Raman spectroscopy or low temperature UV-vis spectroscopy, presumably because of this coupling to other bonding modes and the absence of a well-defined uncoupled d_{z^2} σ^* -to- $p\sigma$ transition. In contrast, a highly polarized Pt–Pt stretch has been observed at 118 cm^{-1} in the Raman spectrum of Pt-pop.²⁷

Calculations on planar [(2-phenylpyridine)Pd(μ -Cl)]₂ (**5**) showed no overlap between the valence d_{z^2} orbitals on the two Pd atoms and hence no Pd–Pd bonding interaction. Instead, there are two essentially degenerate nonbonding linear combinations of the d_{z^2} orbitals, which are of a similar energy to the nonbonding linear combinations of other Pd d orbitals. As in **1** and **3**, the LUMO and close-lying empty orbitals of **5** are centered on the 2-phenylpyridine ligands. The HOMO–LUMO gap in **5** (2.40 eV) is much larger than in **1** (1.53 eV) or **3** (1.60 eV) because the HOMO in **5** is nonbonding, whereas in **1** and **3** it is an antibonding d_{z^2} Pd–Pd interaction raised in energy relative to the π^* system of the 2-phenylpyridine ligands. The larger HOMO–LUMO gap in **5** compared with **1** and **3** is consistent with the UV-visible spectroscopy, which showed bands at lower energy in **1–4** than in **5**, providing further evidence supporting our assignment of the bands at approximately 420 nm in **1** and **2** as MMLCT transitions (excitation from the Pd–Pd antibonding orbital into the 2-phenylpyridine π^* system); these bands are shifted to around 375 nm in **3** and **4** and absent in **5**. Furthermore,

imposition of a C_2 symmetry constraint allowed optimization of the structure **1** in the excited configuration, with one electron promoted from the HOMO to the LUMO; the resulting Pd–Pd distance is 2.6 Å, consistent with an increase in the Pd–Pd bond order and a large geometry change between the ground (calculated Pd–Pd distance = 2.8 Å) and excited states, which may explain the large Stokes shift observed in the emission from **1** on excitation at 420 nm.

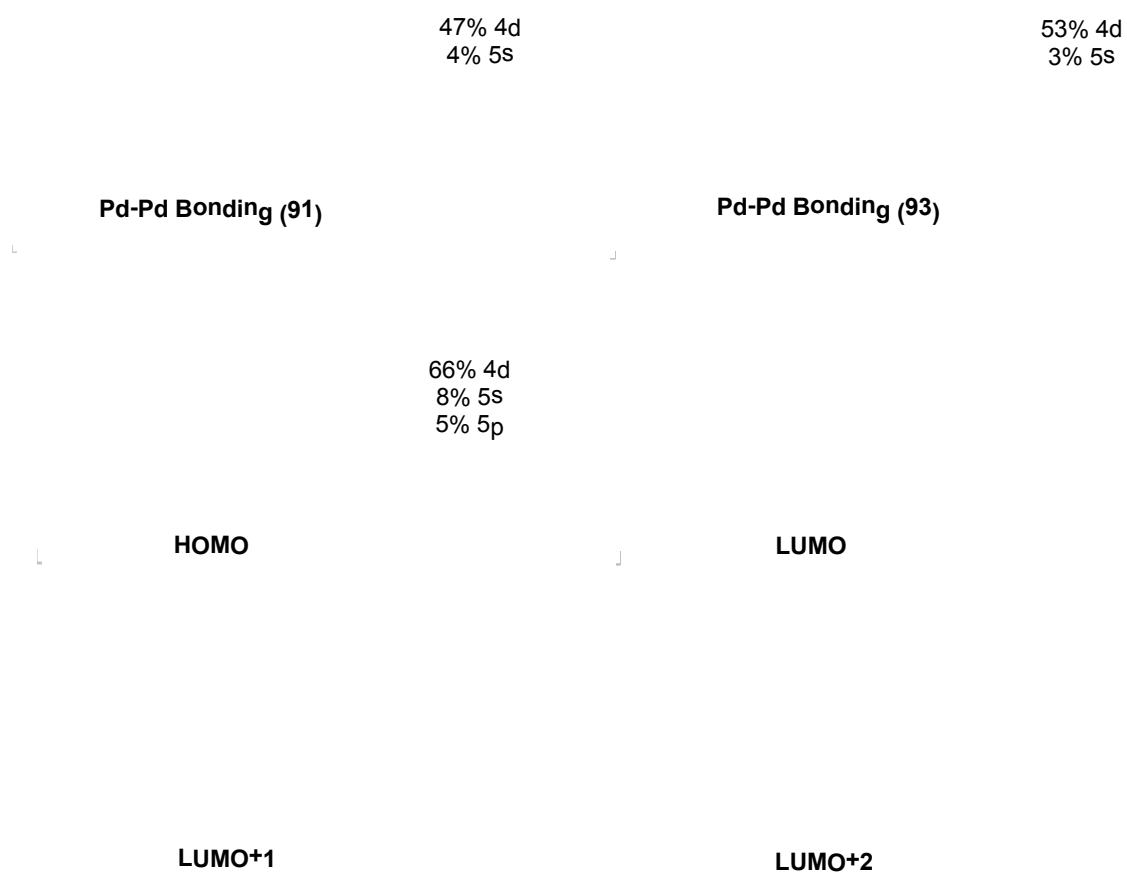


Figure 3.10. Selected molecular orbitals of **1**, with percentage contribution from different Pd atomic orbitals (balance from ligand-based orbitals)

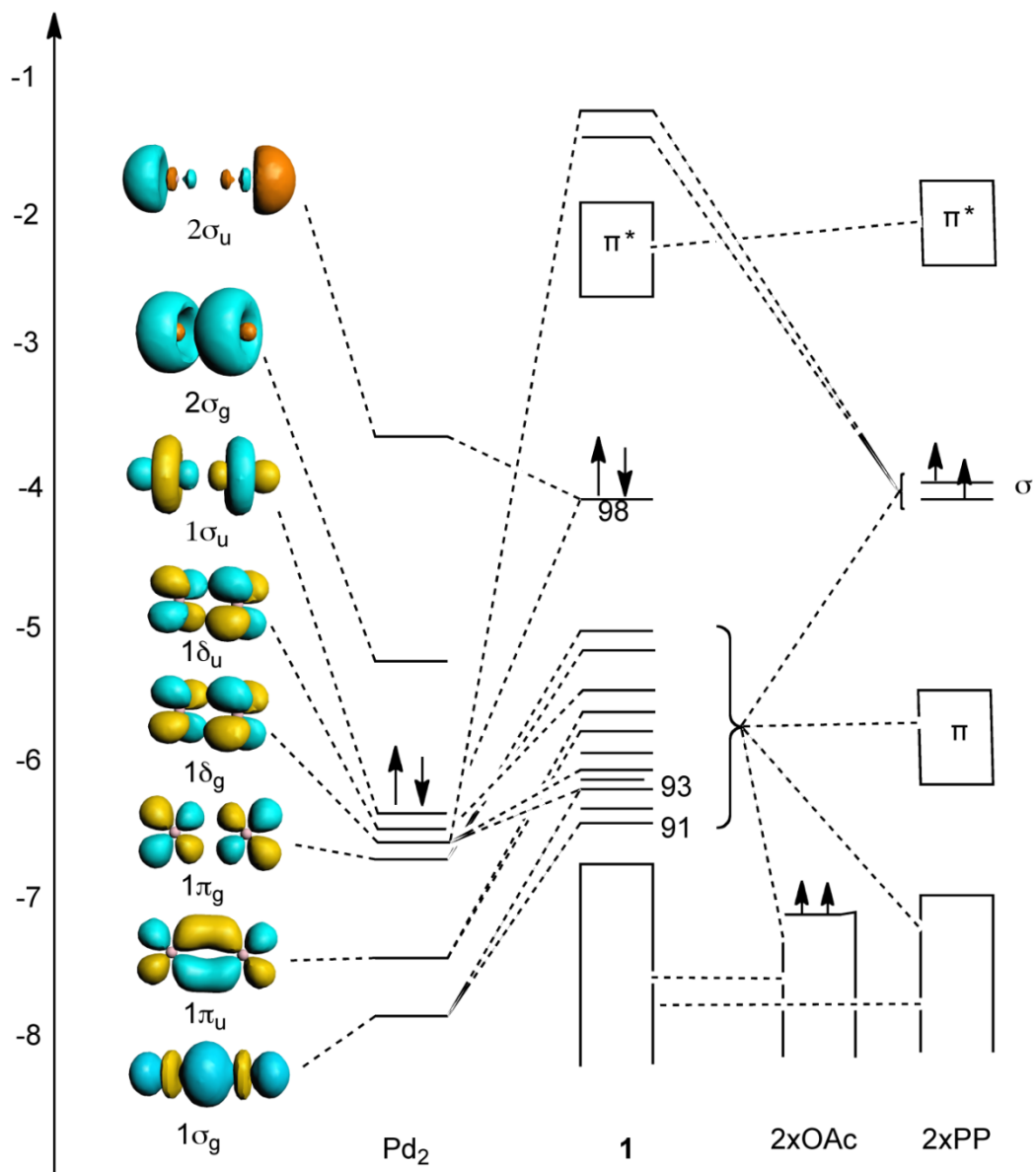


Figure 3.11. Molecular orbital diagram for **1**

DFT-based comparison of bonding interactions in Pd–Pd d^8 dimers with those in Rh–Rh, Pt–Pt, and Ir–Ir d^8 dimers

The results of the spectroscopic and computational studies on compounds **1–4** suggest that the Pd–Pd bonding interaction is different from the d^8 – d^8 interactions in Rh, Pt, and Ir dimers. In the latter systems the LUMO is a metal–metal bonding orbital with s and p_z character, whereas in **1–4** the LUMO and other close-lying unoccupied orbitals are ligand based. Indeed, it appears that the energy of the metal–metal bonding p_z orbital in **1–4** is much higher than the LUMO, which may explain why the unique photophysical properties arising from a d_{z^2} σ^* -to- $p\sigma$ transition in Pt-pop and other d^8 – d^8 dimers are not observed in the Pd dimers. To explore whether the absence of a low-energy d_{z^2} σ^* -to- $p\sigma$ transition is general to Pd complexes with short Pd–Pd interactions or is unique to **1–4**, we performed calculations on the complexes cited earlier,⁹ shown as (a–h) in Figure 3.12, as well as on Pt-pop (Pt–Pt = 2.925(1)),^{21,28} [(cod)Ir(μ -pyr)]₂ (**j**, cod = 1,5-cyclooctadiene, pyr = pyrazole, Ir–Ir = 3.216(5) Å),²⁹ and [Rh(CNMe)₄]₂²⁺ (**k**) as a model for [Rh(CNPh)₄]₂²⁺ (Rh–Rh = 3.193(0)Å)³⁰ (Figure 3.13).

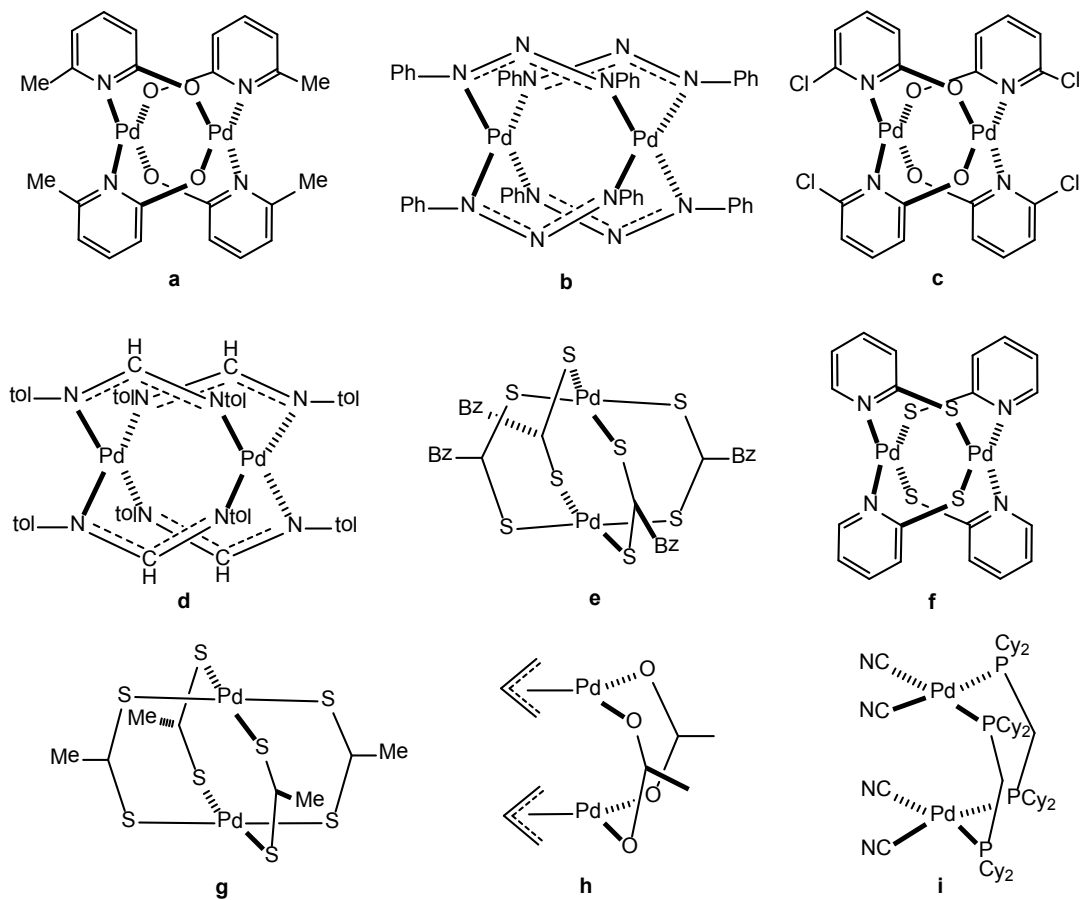


Figure 3.12. Complexes with short Pd-Pd interactions selected for DFT calculations⁹

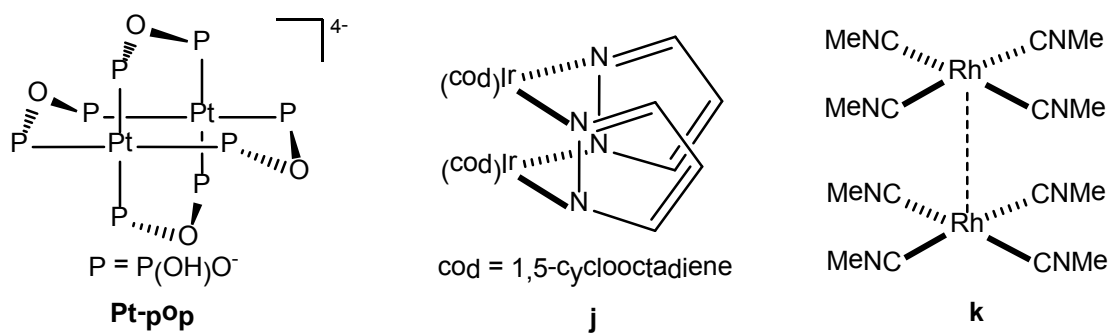


Figure 3.13: Complexes with d^8-d^8 bonding interactions selected for DFT calculations

For all the Pd complexes the calculated HOMO is an antibonding combination of the d_{z^2} orbitals, with a small contribution from the 5s and $5p_z$ orbitals, similar to that described earlier for **1**.²³ The complementary Pd–Pd σ -bonding orbital is at lower energy and also has some contribution from the 5s and $5p_z$ orbitals. For all the compounds fragment analysis reveals a favorable bonding interaction, with the bond order varying from 0.1–0.56 (this is a measure of positive orbital overlap rather than bond strength). Additional support for the presence of a Pd–Pd bonding interaction was obtained from AIM analysis: there is an excellent correlation between the Pd distance and both the charge density and the Laplacian at the bond critical points (Figure 3.14), suggesting that the Pd–Pd bonding interaction is related to the separation between the Pd atoms.

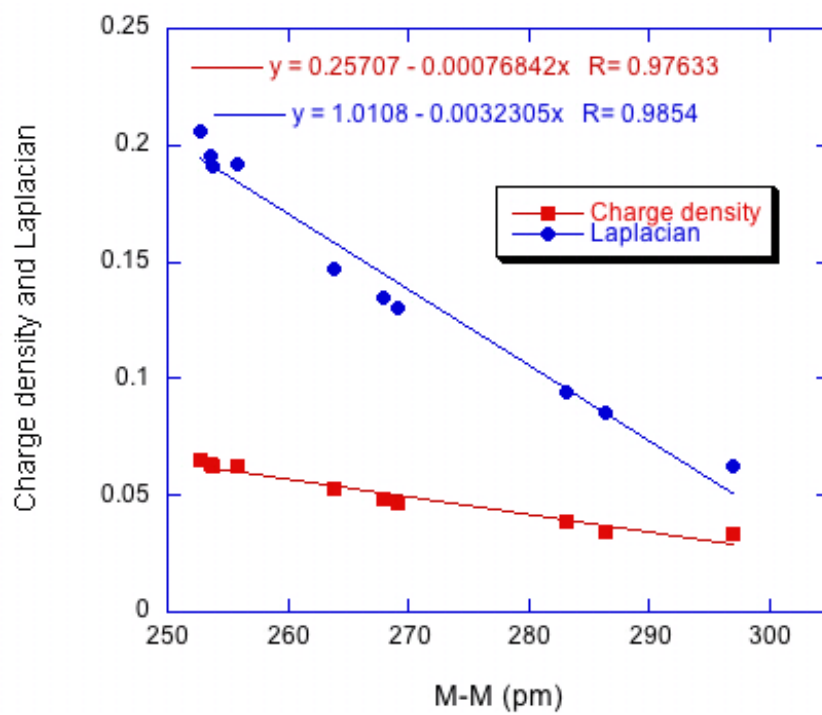


Figure 3.14. Plot of charge density and Laplacian against M-M distance in compounds **1** and (a-h)

The calculations also showed that the LUMO and close-lying empty orbitals in the Pd complexes are not based on a bonding linear combination of the s and p_z orbitals. Instead, the LUMO consists either of ligand-based orbitals or, when there are no low-lying unoccupied ligand orbitals, an antibonding combination of Pd $d_{x^2-y^2}$ and ligand orbitals.²³ In contrast, calculations on Pt-pop and [(cod)Ir(μ -pyr)]₂ (**j**) showed that the LUMO is a metal-based bonding orbital, which contains both s and p_z character.³¹ These results suggest that the larger gap between the (n+1) valence s and p orbitals and the valence d orbitals for Pd compared with Ir or Pt is crucial in determining the relative energy of the unoccupied orbitals in d^8 - d^8 dimers. Even in [Rh(CNMe)₄]₂²⁺ (**k**), the LUMO contains some s and p character mixed with a large ligand contribution, suggesting that the gap between Pd 5s and 5p orbitals and the 4d orbitals is large even compared to other elements in the same row. These trends are reflected in the atomic spectra of Rh, Pd, Ir, and Pt (Table 3.5); the lowest Pd d-to-p transition is nearly 10,000 cm^{-1} higher than a corresponding transition in the other metals.³² The ground-state atomic configuration of Pd ($4d^{10}$) is also consistent with a larger gap between d and s and p orbitals relative to Rh ($4d^8$, $5s^1$), Ir ($5d^7$, $6s^2$), and Pt ($5d^9$, $6s^1$).

Table 3.5. Energy of the $nd \rightarrow (n+1)p$ transition as calculated from atomic spectra³²

Metal	$nd \rightarrow (n+1)p / \text{cm}^{-1}$	Transition
Rh	23766	$4d^9 (^2D) \rightarrow 4d^8 (^3F) 5p (^4D^0)$
Pd	34068	$4d^{10} (^1S) \rightarrow 4d^9 (^2D_{2/2}) 5p (^3P)$
Ir	23473	$5d^8 6s (^4F) \rightarrow 5d^7 6s (^5F) 6p (^6D^0)$
Pt	26480	$5d^{10} (^1S) \rightarrow 5d^9 (^2D_{2/2}) 6p_{0/2}$

Since many of the interesting photophysical and reactivity properties of Pt-pop, Rh-Rh, and Ir-Ir d^8-d^8 dimers appear to result from the special nature of the LUMO, we suggest that Pd complexes that display similar behavior may not be attainable, and that the M-M bonding interaction is weaker for Pd because the larger energy difference between the (n+1) valence s and p orbitals and the valence d orbitals disfavors orbital mixing. This view is supported by the relative contributions of the (n+1) valence s and p orbitals to the σ^* HOMO and corresponding metal-metal σ -bonding orbital for **1** compared to Pt-pop, [(cod)Ir(μ -pyr)]₂ (**j**) and [Rh(CNMe)₄]₂²⁺ (**k**) (Table 3.6). At present there is no direct experimental data on metal-metal bond strengths that would validate this proposal.

Table 3.6. Relative contribution of the d orbitals and (n+1) valence s and p orbitals to the metal-metal bonding and antibonding orbitals in **1**, Pt-pop, $[\text{Rh}(\text{CNMe})_4]_2^{2+}$ (**k**), and $[(\text{cod})\text{Ir}(\mu\text{-pyr})]_2$ (**j**)^a

	M–M antibonding	M–M bonding	M–M bonding
1	66% 4d	47% 4d	53% 4d
	8% 5s	4% 5s	3% 5s
	5% 5p		
$[\text{Rh}(\text{CNMe})_4]_2^{2+}$ (k)	48% 4d	79% 4d	70% 4d
	29% 5s	6% 5s	2% 5s
	2% 5p		
Pt-pop	33% 5d	56% 5d	52% 5d
	50% 6s	23% 6s	7% 6s
	3% 6p	1% 6p	
$[(\text{cod})\text{Ir}(\mu\text{-pyr})]_2$ (j)	69% 5d ^b	26% 5d	67% 5d ^b
	10% 6s	20% 6s	7% 6s
	1% 6p	1% 6p	

^aWhere numbers do not add up to 100%, the remainder of the orbital is centered on the ligand. ^bThe relative d contribution to these orbitals is raised by mixing with a number of d orbitals other than the d_{z^2} .

3.4 Concluding remarks

Crystal structure analyses combined with photophysical, electrochemical and computational investigations have firmly established that there are attractive d^8-d^8 interactions in Pd^{II} dimers of the type [(2-phenylpyridine)Pd(μ -X)]₂ and [(2-*p*-tolylpyridine)Pd(μ -X)]₂ (X = OAc or TFA). The Pd–Pd HOMO is a weakly metal–metal antibonding d_{z^2} σ^* orbital and the LUMO is either a low-lying ligand orbital or a $d_{x^2-y^2}$ antibonding orbital. The M–M interaction in Pd d^8-d^8 dimers is weaker than in Rh, Ir, and Pt systems. The Pd-Pd LUMO also differs from those of d^8-d^8 complexes of Rh, Ir, and Pt, owing to the unusually large energy gap between Pd 4 d_{z^2} and 5s/5p orbitals. Since the increase in Pd–Pd bond order upon HOMO–LUMO excitation is only one-half that of other metal d^8-d^8 complexes, it is not likely that electronically excited Pd^{II} dimers will be able to abstract hydrogen or halogen atoms from substrates as efficiently as Pt^{II} analogues.

3.5 Materials and methods

General

All manipulations were performed in air, unless otherwise stated. Pd(OAc)₂, Pd(TFA)₂, 2-phenylpyridine (all purchased from Sigma-Aldrich) and 2-*p*-tolyl-pyridine (purchased from TCI-America) were reagent-grade commercial samples used without further purification. Dichloromethane-*d*₂ and chloroform-*d*₁ were purchased from Cambridge Isotope Laboratories and used as received. [(2-phenylpyridine)Pd(OAc)]₂ (1), [(2-*p*-tolylpyridine)Pd(OAc)]₂ (2) [(2-phenylpyridine)Pd(Cl)]₂ (5), and [(2-phenylpyridine)Pd(en)][Cl] (6) were

prepared using literature procedures.^{16,18,33} ^1H and ^{13}C NMR spectra were recorded at 298 K using a Varian Mercury 300 MHz spectrometer equipped with the VNMRJ software program, version 2.2d. ^1H and ^{13}C NMR spectra were referenced to the residual proton or carbon chemical shifts of the deuterated solvent. The data are reported by chemical shift (ppm) from tetramethylsilane, multiplicity (s, singlet; d, doublet; t, triplet; m, multiplet; dd, double doublet; dt, double triplet), coupling constants (Hz), and integration. Mass spectra were acquired on a Finnigan LCQ ion trap or Agilent 5973 Network mass selective detector and were obtained by peak matching. UV/Vis absorbance spectra were recorded on an Agilent 8453 UV/Vis Spectrometer using a pure sample of the solvent as the background. X-ray crystallographic data were collected on a Bruker KAPPA APEX II instrument, with the crystals mounted on a glass fiber with Paratone-N oil. Structures were determined using direct methods, as implemented in the Bruker AXS software package.

Electrochemistry

Cyclic voltammetry and differential pulse voltammetry were carried out using a 660 Electrochemical Workstation (CH-Instrument, Austin, TX). Measurements were performed at room temperature in CH_2Cl_2 or acetonitrile solutions with 0.1 M TBAPF₆ as the supporting electrolyte. Sample concentration was kept at approximately 1 mM. A scan rate of 0.1 V/s was used for all cyclic voltammetry measurements. Experiments were conducted using a glassy carbon working electrode, a saturated Ag/AgCl reference electrode, and a platinum wire

counter electrode. Ferrocenium/ferrocene (Fc^+/Fc) was used as an internal reference.

Steady-state and time-resolved luminescence

Low-temperature measurements were conducted on samples in 2-methyltetrahydrofuran glasses. Samples were placed in quartz EPR tubes and rigorously degassed with five freeze-pump-thaw cycles. For both time-resolved and steady-state measurements at 77 K, samples were submerged in liquid nitrogen within a homemade quartz optical dewar. Steady-state emission spectra were recorded on a Jobin Yvon Spex Fluorolog-3-11. Sample excitation was achieved via a xenon arc lamp with a single monochromator providing wavelength selection. Right-angle light emission was sorted using a single monochromator and fed into a Hamamatsu R928P photomultiplier tube with photon counting. Short- and long-pass filters were used where appropriate. Spectra were recorded on Datamax software. Time-resolved measurements were carried out using 10 ns pulses at 355 nm from a Spectra-Physics Quanta-Ray Q-switched Nd:YAG laser operating at 10 Hz. Luminescence decays were detected through an Instruments SA (ISA Edison, NJ) model DH10 (1200 grooves/mm) double monochromator and Hamamatsu R928 PMT with a 5-stage socket made by Products for Research (model R928/17149.00301.0040, Bridgewater, NJ). Signals were amplified with a Phillips Scientific 100 MHz bipolar amplifier (100x) and recorded on a Tektronix model TDS-620A digitizing oscilloscope.

Computational details

Quantum chemical calculations were performed using density functional methods of the Amsterdam Density Functional (Version ADF2007.01) package.³⁴ TZP basis sets were used with triple- ξ accuracy sets of Slater-type orbitals, with polarization functions added to all atoms. Relativistic corrections were made using the ZORA (zero-order relativistic approximation) formalism³⁵ and the core electrons were frozen up to 1s for C, N, O, and F; 2p for P and Cl; 3d for Rh and Pd; and 4d for Ir and Pt. The local density approximation of Vosko, Wilk, and Nusair³⁶ was utilized. All quoted electronic structure data from optimized structures use an integration grid of 6.0 and were verified as minima using frequency calculations. Fragment analyses use the MOs of the chosen fragments as the basis set for the molecular calculation. Initial spin-restricted calculations were carried out on the fragments with the geometry that they have in the molecule; thus the fragments were in a prepared singlet state. Neutral fragments were chosen, as this assisted in drawing up the MO diagrams. Topological analyses of the electron density were performed using the XAIM program.³⁷ The *adf2aim* executable, which is provided with the standard source code of the ADF program, was used to convert the tape21 file to a wavefunction (.wfn) file. XAIM was then used to locate and characterize the critical points.

Synthesis and characterization of new compounds

[(2-phenylpyridine)Pd(TFA)]₂ (**3**). Pd(TFA)₂ (0.50 g, 1.50 mmol) was added to a three-neck 250 mL round-bottom flask equipped with a reflux condenser and a stir bar. Chloroform (80 mL, Omnisolv™) and 2-phenylpyridine (0.233 g, 1.50 mmol) were added, and the solution was heated for five hours at reflux. The yellow solution was allowed to cool, then filtered through Celite to remove any palladium black. The solvent was removed *in vacuo* to give a brown oil. The crude product was purified using column chromatography (eluting first with CH₂Cl₂ and then ethyl acetate) to give [(2-phenylpyridine)Pd(TFA)]₂ (**3**) as a yellow powder (0.24 g, 48%). X-ray diffraction quality crystals were grown from saturated solutions of CH₂Cl₂ or acetone. ¹H NMR (300 MHz, chloroform-*d*₁) δ = 7.75 (m, 2H), 7.47 (app td, *J* = 7.5, 0.9, 2H), 7.15 (d, *J* = 8.2, 2H), 6.86 (m, 6H), 6.74 (m, 2H), 6.58 (app t, *J* = 6.4, 2H). ¹³C{¹H} NMR (125 MHz, chloroform-*d*₁) δ = 164.3 (2C), 149.8 (2C), 148.6 (2C), 144.3 (2C), 138.5 (2C), 132.1 (2C), 131.0 (2C), 129.1 (2C), 125.0 (2C), 122.9 (2C), 121.9 (2C), 121.6 (2C), 117.8 (2C). HRMS for [C₂₆H₁₆F₆N₂O₄Pd₂]⁺: calc'd 747.9100 g/mol, found 747.9135 g/mol.

[(2-*p*-tolylpyridine)Pd(TFA)]₂ (**4**). The above procedure was followed, substituting 2-*p*-tolylpyridine (0.255 g, 1.50 mmol), to give [(2-*p*-tolylpyridine)Pd(TFA)]₂ (**4**) as a yellow powder (0.21 g, 36%). X-ray diffraction quality crystals were grown from a saturated solution of CH₂Cl₂. ¹H NMR (300 MHz, dichloromethane-*d*₂) δ = 7.69 (m, 2H), 7.47 (app td, *J* = 7.8, 1.5, 2H), 7.11 (d, *J* = 8.1, 2H), 6.80 (m, 4H), 6.63 (m, 4H), 2.16 (s, 6H). ¹³C{¹H}NMR (125 MHz, dichloromethane-*d*₂) δ = 164.8 (2C),

149.6 (2C), 148.7 (2C) 141.2 (2C), 136.5 (2C), 132.4 (2C), 131.6 (2C), 131.0 (2C), 126.3 (2C), 123.3 (2C), 122.5 (2C), 121.4 (2C), 118.3 (2C), 23.2 (4C). HRMS for $[\text{C}_{28}\text{H}_{20}\text{F}_6\text{N}_2\text{O}_4\text{Pd}_2]^+$: calc'd 775.9414 g/mol, found 775.9418 g/mol.

3.6 References

- (1) (a) Cotton, F. A. *Inorg. Chem.* **1998**, *37*, 5710; (b) Cotton, F. A.; Murillo, C. A.; Bochmann, M. *Advanced Inorganic Chemistry*, 6th ed.; John Wiley & Sons, New York, **1999**, p. 647–652.
- (2) (a) Mann, K. R.; Gordon, J. G.; Gray, H. B. *J. Am. Chem. Soc.* **1975**, *97*, 3553; (b) Mann, K. R.; Gray, H. B. *Adv. Chem. Ser.* **1979**, *173*, 225; (c) Rice, S. F.; Milder, S. J.; Goldbeck, R. A.; Kligler, D. S.; Gray, H. B. *Coord. Chem. Rev.* **1982**, *43*, 349.
- (3) (a) Osborn, R. S.; Rogers, D. *J. Chem. Soc., Dalton Trans.* **1974**, 1002; (b) Connick, W. B.; Marsh, R. E.; Schaefer, W. P.; Gray, H. B. *Inorg. Chem.* **1997**, *36*, 913.
- (4) Carr, N.; Crossley, J. G.; Dent, A. J.; Gouge, J. R.; Greaves, G. N.; Jarrett, P. S.; Orpen, A. G. *J. Chem. Soc., Chem. Commun.* **1990**, 11369.
- (5) (a) Novoa, J. J.; Aullon, G.; Alemany, P.; Alvarez, S. *J. Am. Chem. Soc.* **1995**, *117*, 7169; (b) Aullón, G.; Alvarez, S. *Chem. Eur. J.* **1997**, *3*, 655.
- (6) Roundhill, D. M.; Gray, H. B.; Che, C.-M. *Acc. Chem. Res.* **1989**, *22*, 55.
- (7) (a) Che, C.-M.; Butler, L. G.; Gray, H. B. *J. Am. Chem. Soc.* **1981**, *103*, 7796; (b) Fordyce, W. A.; Brummer, J. G.; Crosby, G. A. *J. Am. Chem. Soc.* **1981**, *103*, 7061.
- (8) Kalsbeck, W. A.; Grover, N.; Thorp, H. H. *Angew. Chem. Int. Ed.* **1991**, *30*, 1517.
- (9) (a) Yip, H.-K.; Lai, T.-F.; Che, C.-M. *J. Chem. Soc. Dalton Trans.* **1991**, 1639; (b) Xia, B.-H.; Che, C.-M.; Zhou, Z.-Y. *Chem. Eur. J.* **2003**, *9*, 3055; (c) Pan, Q.-J.; Zhang, H.-X.; Zhou, X.; Fu, H.-G.; Yu, H.-T. *J. Phys. Chem. A* **2007**, *111*, 287; (d) Clement, S.; Aly, S. M.; Bellows, D.; Fortin, D.; Strohmman, C.; Guyard, L.; Abd-El-Aziz, A. S.; Knorr, M.; Harvey, P. D. *Inorg. Chem.* **2009**, *9*, 4118.
- (10) Bondi, A. *J. Phys. Chem.* **1964**, *68*, 441.
- (11) Cotton, F. A.; Matusz, M.; Poli, R.; Feng, X. *J. Am. Chem. Soc.* **1988**, *110*, 1144.
- (12) Bercaw, J. E.; Day, M. W.; Gollisz, S. R.; Hazari, N.; Henling, L. M.; Labinger, J. A.; Schofer, S. J.; Virgil, S. *Organometallics* **2009**, *28*, 5017.
- (13) (a) Powers, D. C.; Ritter, T. *Nat. Chem.* **2009**, *1*, 302; (b) Deprez, N. R.; Sanford, M. S. *J. Am. Chem. Soc.* **2009**, *131*, 11234.
- (14) (a) Thu, H.-Y.; Yu, W.-Y.; Che, C.-M. *J. Am. Chem. Soc.* **2006**, *128*, 9048; (b) Dinçer, M.; Özdemir, N.; Günay, M. E.; Çetinkaya, B. *Acta Crystallogr. Sect. E: Struct. Rep. Online* **2008**, *E64*, m381.
- (15) The two previously reported structures of **1** are polymorphs.¹⁴ In this paper we report a low temperature structure (100 K) of **1**, which is the same polymorph as

reported by Dinçer and co-workers.^{14b} For the sake of accurate comparison with other compounds reported here, we use the geometrical parameters from our structure in further discussions.

(16) Aiello, I.; Crispini, A.; Ghedini, M.; La Deda, M.; Barigelletti, F. *Inorg. Chim. Acta* **2000**, *308*, 121.

(17) Janiak, C. *J. Chem. Soc., Dalton Trans.* **2000**, 3885.

(18) Craig, C. A.; Watts, R. J. *Inorg. Chem.* **1989**, *28*, 309.

(19) Mann, K. R.; Hill, M. G. *Catal. Lett.* **1991**, *11*, 341.

(20) Ivanov, M. A.; Puzyk, M. V. *Opt. Spectrosc.* **2001**, *91*, 927.

(21) Kim, C. D.; Pillet, S.; Wu, G.; Fullagar, W. K.; Coppens, P. *Acta Crystallogr., Sect. A: Found. Crystallogr.* **2002**, *58*, 133.

(22) Advances in separation techniques have opened the way for more rigorous investigations of the excited state properties of stereoisomers of organic and inorganic compounds; see Keene, F. R. *Coord. Chem. Rev.* **1997**, *166*, 121. Typically, optical isomers have shown minimal differences in excited state behavior; see Rutherford, T. J.; Van Gijte, O.; Kirsch-De Mesmaeker, A.; Keene, F. R. *Inorg. Chem.* **1997**, *36*, 4465, or Browne, W. R.; O'Connor, C. M.; Villani, C.; Vos, J. G. *Inorg. Chem.* **2001**, *40*, 5461. However, differences are more pronounced for geometric isomers, where excited state lifetimes in some cases vary by more than an order of magnitude, see Spalletti, A.; Bartocci, G.; Galiazzo, G.; Macchioni, A.; Mazzucato, U. *J. Phys. Chem. A* **1999**, *103*, 8994, Treadway, J. A.; Chen, P.; Rutherford, T. J.; Keene, F. R.; Meyer, T. J. *J. Phys. Chem. A* **1997**, *101*, 6824, or Booth, E. C.; Bachilo, S. M.; Kanai, M.; Dennis, T. J. S.; Weisman, R. B. *J. Phys. Chem. C* **2007**, *111*, 17720.

(23) See supporting information for more details.

(24) Cloke, F. G. N.; Green, J. C.; Jardine, C. N.; Kuchta, M. C. *Organometallics* **1999**, *18*, 1087.

(25) Bader, R. F. W. *Atoms in Molecules: A Quantum Theory*. Oxford University Press, New York, USA, **1994**.

(26) (a) Bader, R. F. W. *Chem. Rev.* **1991**, *91*, 893; (b) A (3,-1) critical point is a point at which the electron density is a minimum in the direction of the two bonded atoms and a maximum in the two orthogonal directions. It is taken as indicative of a covalent bond.

(27) Che, C.-M.; Butler, L. G.; Gray, H. B.; Crooks, R. M.; Woodruff, W. H. *J. Am. Chem. Soc.* **1983**, *105*, 5492.

(28) (a) Filomena Dos Remedios Pinto, M. A.; Sadler, P. J.; Neidle, S.; Sanderson, M. R.; Subbiah, A.; Kuroda, R. *J. Chem. Soc., Chem. Commun.* **1980**, 13; (b) Marsh, R. E.; Herbstein, F. H. *Acta Crystallogr., Sect. B: Struct. Sci.* **1983**, *39*, 280.

(29) Coleman, A. W.; Eadie, D. T.; Stobart, S. R.; Zaworotko, M. J.; Atwood, J. L. *J. Am. Chem. Soc.* **1982**, *104*, 922.

(30) Mann, K. R.; Lewis, N. S.; Williams, R. M.; Gray, H. B.; Gordon, J. G., II. *Inorg. Chem.* **1978**, *17*, 828.

(31) (a) Novozhilova, I. V.; Volkov, A. V.; Coppens, P. *J. Am. Chem. Soc.* **2003**, *125*, 1079; (b) Pan, Q.-J.; Fu, H.-G.; Yu, H.-T.; Zhang, H.-X. *Inorg. Chem.* **2006**, *45*, 8729.

- (32) Moore C. E, *Atomic Energy Levels, Vol. III (Molybdenum through Lanthanum and Hafnium through Actinium)*, Circular of the National Bureau of Standards 467, U.S. Government Printing Office, Washington DC, (1958).
- (33) Gutierrez, M. A.; Newkome, G. R.; Selbin, J. *J. Organomet. Chem.* **1980**, *202*, 341.
- (34) (a) Fonseca Guerra, C.; Snijder, J. G.; Te Velde, G.; Baerends, E. J. *Theor. Chem. Acc.* **1998**, *99*, 391; (b) Te Velde, G.; Bickelhaupt, F. M.; Baerends, E. J.; Fonseca Guerra, C.; Van Gisbergen, S. J. A.; Snijders, J. G.; Ziegler, T. *J. Comput. Chem.* **2001**, *22*, 931; (c) ADF2007.01, SCM, Theoretical Chemistry, Vrije Universiteit, Amsterdam, The Netherlands, <http://www.scm.com>.
- (35) (a) Vanlenthe, E.; Baerends, E. J.; Snijders, J. G. *J. Chem. Phys.* **1993**, *99*, 4597; (b) Vanlenthe, E.; Baerends, E. J.; Snijders, J. G. *J. Chem. Phys.* **1994**, *101*, 9783; (c) Vanlenthe, E.; Baerends, E. J.; Snijders, J. G. *J. Chem. Phys.* **1996**, *105*, 6505; (d) Vanlenthe, E.; Ehlers, A.; Baerends, E. J. *J. Chem. Phys.* **1999**, *110*, 8943; (e) Vanlenthe, E.; VanLeeuwen, R.; Baerends, E. J.; Snijders, J. G. *J. G. Int. J. Quantum Chem.* **1996**, *57*, 281.
- (36) Vosko, S. H.; Wilk, L.; Nusair, M. *Can. J. Phys.* **1980**, *58*, 1200.
- (37) Alba, J. C. O.; Jané, C. B. *XAIM*, **1998**. (Download free of charge from the web distribution site: <http://www.quimica.urv.es/XAIM/>.)

Chapter 4:

Carbon–chlorine bond formation from a binuclear palladium(II) electrocatalyst

4.1 Abstract

The binuclear Pd^{II} complex, [(benzo[*h*]quinoline)Pd^{II}(μ-OAc)]₂ (Pd^{II}-Pd^{II}), has been shown to catalyze the selective chlorination of benzo[*h*]quinoline. The reaction typically requires the use of the potent oxidant iodosobenzedichloride, PhICl₂, and proceeds through reductive elimination of the Pd^{III}-Pd^{III} intermediate [(benzo[*h*]quinoline)Pd^{III}(μ-OAc)Cl]₂. Electrochemical oxidation of Pd^{II}-Pd^{II} in the presence of chloride at the Pd^{III}-Pd^{II}/Pd^{II}-Pd^{II} potential results in two-electron oxidation with addition of two chloride ions to form the intermediate Cl-Pd^{III}-Pd^{III}-Cl. Selective chlorination of benzo[*h*]quinoline to 10-chlorobenzo[*h*]quinoline proceeds to completion with 10% catalyst loading at potentials below the Cl₂ / 2Cl[•] couple.

4.2 Introduction

Palladium-catalyzed directed C-H functionalization reactions

The development of techniques for carbon-hydrogen bond activation and functionalization is a great challenge in modern chemistry. Important to these reactions is that they are able to be performed with high selectivity under relatively mild conditions that are compatible with other functional groups. Traditional methods for the conversion of C-H bonds to carbon-halogen, carbon-oxygen, carbon-nitrogen, or carbon-carbon bonds rely multiple steps or prefunctionalized starting materials that make their implementation in chemical synthesis more costly and time consuming.

Direct functionalization of C–H bonds, which overcomes these limitations, is a more attractive option. However, the development of these reactions is made more difficult due to the relative inertness of C–H bonds. Further, most substrates possess many C–H bonds, adding difficulty to enforcing selectivity on these reactions. These difficulties can be overcome through metal-catalyzed reactions and the use of substrates with a coordinating ligand to direct a specific C–H bond to the metal center for activation.

This technique, also referred to as cyclometalation, has been employed using Ru, Rh, Pd, and Pt metal centers. However, its use in Pd-catalyzed reactions is particularly interesting. Cyclopalladated Pd^{II} complexes are often tolerant of air and moisture, aiding in the ease of their manipulation. Furthermore, the metal is capable of catalyzing a diverse array of C–H functionalizations, including carbon–carbon, carbon–halogen, carbon–oxygen, and carbon–nitrogen bond-forming reactions. Following cyclometalation, substrate functionalization follows either a reductive route, where Pd^{II} is reduced to Pd⁰, or an oxidative route. The mechanism for oxidative functionalization has been a subject of recent discussion as monometallic Pd^{II/IV} as well as bimetallic Pd^{II}–Pd^{II}/Pd^{III}–Pd^{III} cycles have been proposed.

Oxidative methods for C–H bond functionalization often require strong oxidants to generate the high-valent Pd-intermediates necessary to drive catalysis. In C–O bond formation, common oxidants include iodine(III) reagents (e.g., PhI(OAc)₂) and peroxides. While the use of strong oxidants is the standard, dioxygen has been successfully employed as the terminal oxidant in several

palladium-catalyzed schemes, for example in Wacker-type oxidation,¹⁻⁴ the α -hydroxylation of carbonyl compounds,⁵ as well as in the ligand-directed acetoxylation of 8-methylquinoline-derived substrates.⁶

Similarly, palladium-catalyzed carbon-halogen bond formation often requires strong oxidants. The earliest report of ligand-directed carbon-halogen bond-formation occurred in 1970 and demonstrated the *ortho*-chlorination of azobenzene by Cl_2 .⁷ The utility of this reaction was limited by the necessity for chlorine gas; however, it led to the development of chlorination reactions using alternative “ X^+ ” sources, in particular PhICl_2 and NCS.

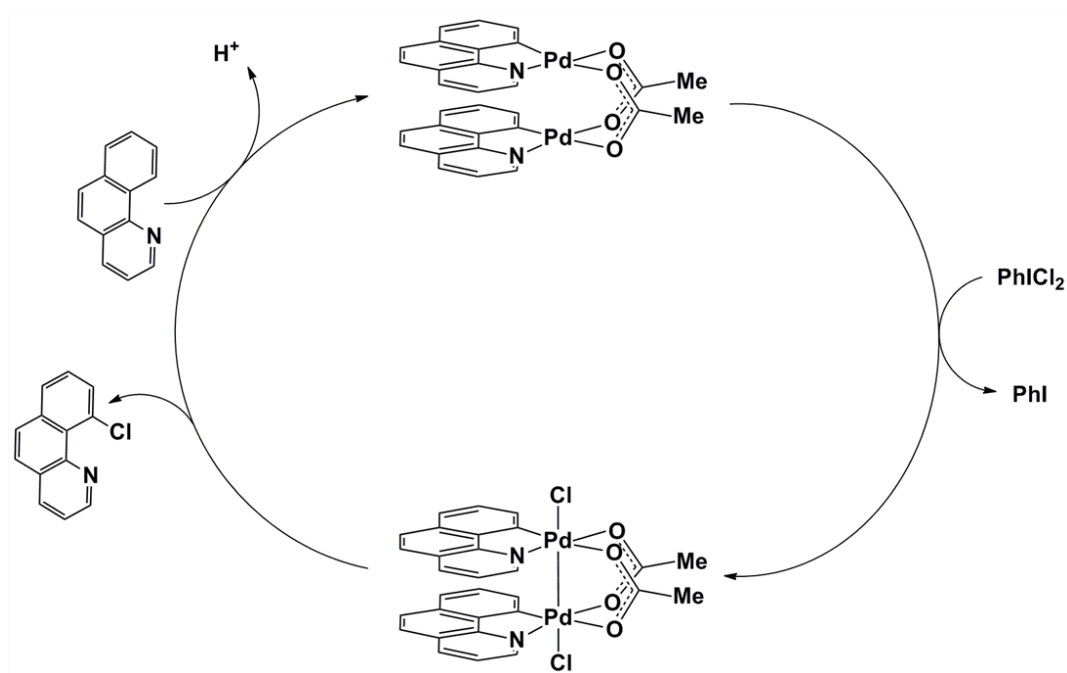
The mechanism for many Pd-catalyzed C-H bond oxidations was believed to proceed through a monometallic Pd^{IV} intermediate. Work by Sanford showed that oxidation of $\text{Pd}^{\text{II}}(\text{ppy})_2$ ($\text{ppy} = 2\text{-phenylpyridine}$) by NCS yielded a six-coordinate $[\text{Pd}^{\text{IV}}(\text{ppy})_2(\text{Cl})(\text{succinamide})]$ species. This species was isolated and shown to undergo competing C-Cl, C-C, and C-N bond-forming reductive elimination reactions.⁸ The results of this and other experiments suggested that monometallic $\text{Pd}^{\text{II/IV}}$ catalytic cycles are viable paths for C-H bond oxidation reactions.

Subsequent investigations into the Pd-catalyzed chlorination of arylpyridine substrates suggest some of these reactions may occur through a binuclear $\text{Pd}^{\text{III}}\text{-Pd}^{\text{III}}$ intermediate, rather than the monometallic Pd^{IV} . Combination of $\text{Pd}(\text{OAc})_2$ with benzo[*h*]quinoline produces the C-H activated dimer $[(\text{benzo}[h]\text{quinoline})\text{Pd}^{\text{II}}(\mu\text{-OAc})_2]$. Upon treatment with PhICl_2 , this species was found to form the $\text{Pd}^{\text{III}}\text{-Pd}^{\text{III}}$ species $[(\text{benzo}[h]\text{quinoline})\text{Pd}^{\text{III}}(\mu\text{-OAc})\text{Cl}]_2$.^{9,10} This complex is stable and low

temperature and has been characterized by x-ray crystallography. Upon warming, the species undergoes reductive elimination, producing 10-chlorobenzo[*h*]quinoline and Pd^{II} products (Scheme 4.1). A binuclear Pd^{II} complex was also implicated in the Pd(OAc)₂-catalyzed chlorination of benzo[*h*]quinoline by NCS.¹¹ Prior to this work, there were few examples of Pd^{III} complexes in organometallic chemistry, the first not occurring until 1987.^{12–15} While the chemistry of Pd⁰, Pd^{II}, and Pd^{IV} complexes are well-established, the reactivity of Pd^{III} complexes are largely unexplored.

Binuclear d⁸–d⁸ complexes

The implication of binuclear Pd^{II} species in catalysis was particularly interesting to us as we had recently completed a detailed study on the electronic structure of complexes that are nearly identical to those used in the study.¹⁶ Pd^{II} dimers are part of a subset of binuclear complexes that feature attractive d⁸–d⁸ interactions between metal centers. The chemistry of d⁸–d⁸ dimers has long been of interest to the group.^{17–20} Binuclear metal complexes are attractive systems for organic transformations due to the opportunity for cooperativity between metal centers. The benefits of cooperativity include lower oxidation potentials, multielectron redox capability, and multiple metal coordination sites for substrate activation.



Scheme 4.1. Selective chlorination of benzo[*h*]quinoline by Pd^{II}-Pd^{II} proceeds through a Pd^{III}-Pd^{III} intermediate that contains two axial chlorides and a Pd-Pd single bond. Following reductive elimination, treatment with Ag⁺ returns the catalyst to its resting state.

The first example of complexes of this type was discovered in 1975, when square-planar Rh^{I} isocyanide complexes were found to form discrete dimers and short oligomers in solution as well as in the solid state.²¹ Dimerization was attributed to a net bonding interaction between the two metal centers. A simple molecular orbital (MO) diagram would suggest no attractive force between the two centers as there is no net metal–metal bond. However, mixing between the nd_{z^2} and $(\text{n}+1)\text{p}_z$ orbitals stabilizes the metal–metal $\text{d}\sigma$ and $\text{d}\sigma^*$ orbitals, resulting in a significant interaction (Figure 4.1).

Subsequent work has identified many more examples of complexes of this type featuring Pt^{II} , Rh^{I} , or Ir^{I} . The chemical properties of this family of complexes are fairly consistent. Most participate in two-center oxidative addition when treated with X_2 ($\text{X} = \text{Cl}, \text{Br}, \text{I}$). As predicted by the MO diagram, these species possess a metal–metal single bond. In addition to chemical properties, photoexcitation of many of these complexes yields species with relatively long triplet lifetimes and interesting photochemical properties. In particular, they are often capable of hydrogen-atom abstraction from organic and organometallic substrates.

Despite over 30 years of work in d^8 – d^8 chemistry, comparatively little attention was paid to binuclear complexes of Pd^{II} . This is largely the result of conclusive evidence for Pd–Pd interactions on the scale of what is observed for complexes of Pt^{II} , Rh^{I} , and Ir^{I} .²² Multiple Pd^{II} – Pd^{II} complexes have been synthesized, including those with metal–metal distances as close as 2.6 Å; however, this was frequently attributed to coordinating ligands forcing a short distance rather

than an attractive Pd–Pd interaction.²³ Despite this work, conclusive evidence for bonding remained elusive.

Interest in Pd^{II}–Pd^{II} complexes was further hampered by a lack of many of the properties that define traditional d⁸–d⁸ chemistry. Prior to our study, few reports existed that had examined explored the properties binuclear Pd^{II} complexes following oxidation.^{12,14,24} The most prominent work was performed by Cotton, who synthesized [Pd₂(hpp)₄] (hpp = 1,3,4,6,7,8-hexahydro-2H-pyrimido[1,2-a]pyrimidine) and treated it with PhICl₂ to yield [Pd₂(hpp)₄Cl₂]. As predicted by the molecular orbital description, this complex possesses a Pd–Pd single bond at a distance of 2.391 Å. While the chemical reactivity was more-or-less maintained,¹² these complexes frequently lack long-lived excited states and therefore also lacked excited-state chemical reactivity. The work by Ritter et al. exploring the role of Pd^{II}–Pd^{II} in oxidative catalysis has led to rejuvenated interest in the field.⁹

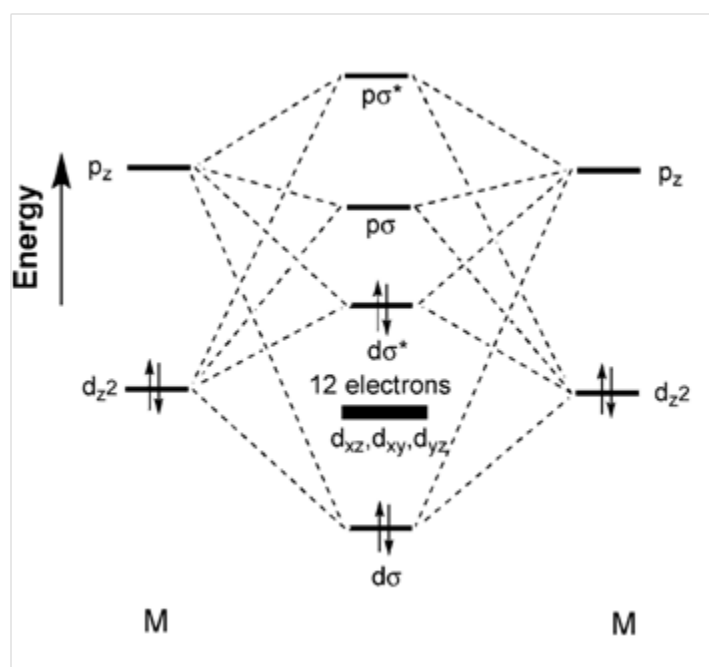


Figure 4.1. Symmetry-allowed mixing between the d_{z^2} and p_z stabilizes the $d\sigma$ and $d\sigma^*$ orbitals, resulting in a net metal–metal bonding interaction, despite no formal metal–metal bond.

Our recent investigation of the electronic structures of binuclear Pd^{II}–Pd^{II} complexes showed a weak metal–metal interaction in the ground state. The complexes possess a metal–metal dσ* HOMO, reminiscent of the electronic structures of the better-known d⁸–d⁸ complexes of Pt^{II}, Rh^I, and Ir^I. However, unlike these compounds, Pd^{II}–Pd^{II} species do not possess a pσ LUMO, which resides at higher energy. This large d–p energy gap leads to decreased mixing between the dσ/dσ* and pσ/pσ* orbitals, and a significantly diminished ground-state metal–metal interaction. Further, the altered electronic structure leads to rapid deactivation of the excited state, precluding excited-state reactivity. While our binuclear species are unable to perform photochemistry typical of related d⁸–d⁸ complexes, we note the ground-state electronic structure is conserved and oxidative chemistry distinctive of d⁸–d⁸ complexes may still be accessed.

The newly discovered catalytic properties of [(benzo[*h*]quinoline)Pd^{II}(μ-OAc)]₂, coupled with our recent investigations into the electronic structure of related species,¹⁶ led us to explore the electronic structure and properties of these Pd^{II}–Pd^{II} complexes following oxidation.

4.3 Results and discussion

Electrochemical properties

Electrochemical oxidation of [(benzo[*h*]quinoline)Pd^{II}(μ-OAc)]₂ (Pd^{II}–Pd^{II}) was conducted in dichloromethane solution. Cyclic voltammograms showed two quasi-reversible waves at 420 mV and 720 mV vs. Fc⁺/Fc. These waves are attributable to successive one-electron oxidations of Pd^{II}–Pd^{II} to form Pd^{II}–Pd^{III}

and Pd^{III}-Pd^{III}, respectively (Figure 4.2). These results are consistent with electrochemical data on the related 2-phenylpyridine and tolyl-pyridine species.¹⁶

In addition to participating in two-center oxidative addition with X₂ (X = Cl, Br, I), many d⁸-d⁸ complexes will also add two equivalents of X when chemically or electrochemically oxidized in the presence of X⁻.^{19,25} This reaction occurs at potentials corresponding to oxidation of M₂ by a single electron. As we expected the oxidative properties of Pd^{II}-Pd^{II} to remain intact, we decided to explore the effects of halide ion on electrochemical oxidation.

It should be noted that addition of large amounts of chloride and bromide ions (> 20-fold molar excess) led to a noticeable loss of color. This is hypothesized to be the result of displacement of the bridging acetate ligands resulting in a halide-bridged dimer. The properties of the chloride-bridged complex [(2-phenylpyridine)Pd^{II}(μ-Cl)]₂ were examined in our electronic structures study. The crystal structures show that this dimer is in a planar conformation, which separates the two palladium centers and eliminates all metal-metal interaction. Lower concentrations of chloride or bromide did not appear to have a significant effect. Additionally, use of the chelating ligand α,α,α',α'-tetramethyl-1,3-benzenedipropionic acid (H₂esp) in place of the two bridging acetates resulted in a complex that was robust to displacement by chloride at very high concentrations.

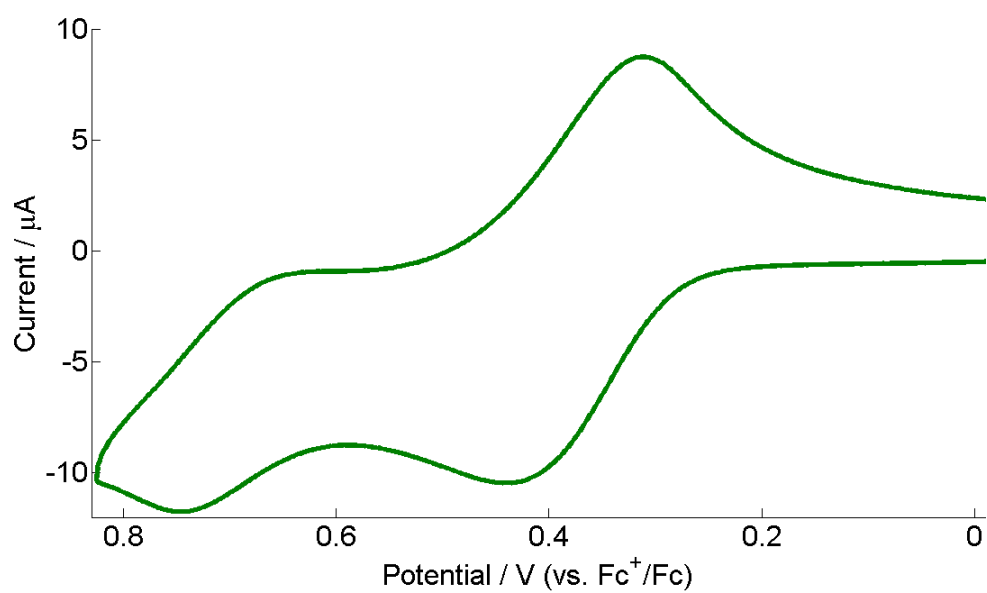


Figure 4.2. Cyclic voltammogram of $\text{Pd}^{\text{II}}-\text{Pd}^{\text{II}}$ in dichloromethane

The addition of tetraethylammonium chloride to [(2-phenylpyridine)Pd^{II}(μ-OAc)]₂ results in noticeable changes to the voltammogram (Figure 4.3). The first wave increases anodically to approximately double its previous current with a concomitant decrease in peak current of the second wave. This behavior is consistent with an ECE mechanism for the formation of the complex [(2-phenylpyridine)Pd^{III}(μ-OAc)Cl]₂. One-electron oxidation of Pd^{II}-Pd^{II} is followed by addition of chloride at one or both axial positions. Addition of chloride lowers the potential required for oxidation of the second electron. A related disproportionation mechanism is also possible. Similar electrochemical behavior is observed following oxidation of [(benzo[*h*]quinoline)Pd^{II}(μ-OAc)]₂ as well as for [(benzo[*h*]quinoline)₂Pd^{II}₂(μ-esp)]. Treatment with bromide has similar effects on the electrochemical behavior; however, the bromine/bromide potential is much closer lower and bromide oxidation obscures the second Pd^{II}-Pd^{II} wave at higher concentrations. The iodine/iodide potential occurs well below the Pd^{II}-Pd^{III}/Pd^{II}-Pd^{II} potential and does not result in any chemical changes to Pd^{II}-Pd^{II}.

Treatment of [(2-phenylpyridine)Pd^{II}(μ-OAc)]₂ with PhI(OAc)₂ was reported to yield a Pd^{III}-Pd^{III} species with axially coordinated acetato groups. When warmed to 40 °C, this complex was found to undergo reductive elimination of acetoxyated 2-phenylpyridine, following a scheme very similar to that presented for the corresponding chlorination reaction. In an effort to test if this reactivity translates to electrochemical reactivity, acetate salts were added to a solution of [(benzo[*h*]quinoline)Pd^{II}(μ-OAc)]₂. Oxidation of the palladium

complex in the presence of acetate showed similar voltammogram to that of oxidation in the presence of chloride. This suggests that axial ligands beyond simple halogens are possible.

Spectroelectrochemical properties

Spectroelectrochemical measurements were employed to further explore the effect of anion addition on electrochemical oxidation. One-electron oxidation of [(benzo[*h*]quinoline)Pd^{II}(μ -OAc)]₂ was first attempted in the absence of any coordinating ions. The relative reversibility of the first wave, and the ~ 300 mV separation between it and the second suggested that the mixed-valence Pd^{II}-Pd^{III} may be stable, at least for brief periods. Previous work by Berry et al. successfully isolated a mixed-valence formamidinate-bridged [Pd₂]⁵⁺ species. The electronic absorption spectrum of the complex showed a large band centered at approximately 900 nm and was attributable to a transition from the lower-lying metal-based d_{π} orbitals (d_{xy} , d_{xz} , d_{yz}) to the singly occupied $d\sigma^*$.

An applied potential of +450 mV vs. Fc⁺/Fc (between the first and second oxidation waves) results in the ingrowth of a broad feature centered at 1010 nm in the UV-vis spectrum (Figure 4.4), which we attribute to a metal-based $d_{\pi} \rightarrow d\sigma^*$ transition. The assignment of this species as [Pd^{II}-Pd^{III}]⁺ is supported by computational results. Theoretical calculations on the [Pd₂]⁵⁺ complex [(2-phenylpyridine)Pd(μ -OAc)]₂⁺ show a $d\sigma^*$ SOMO and predict a metal-based transition at 1022 nm, consistent with experimental results.

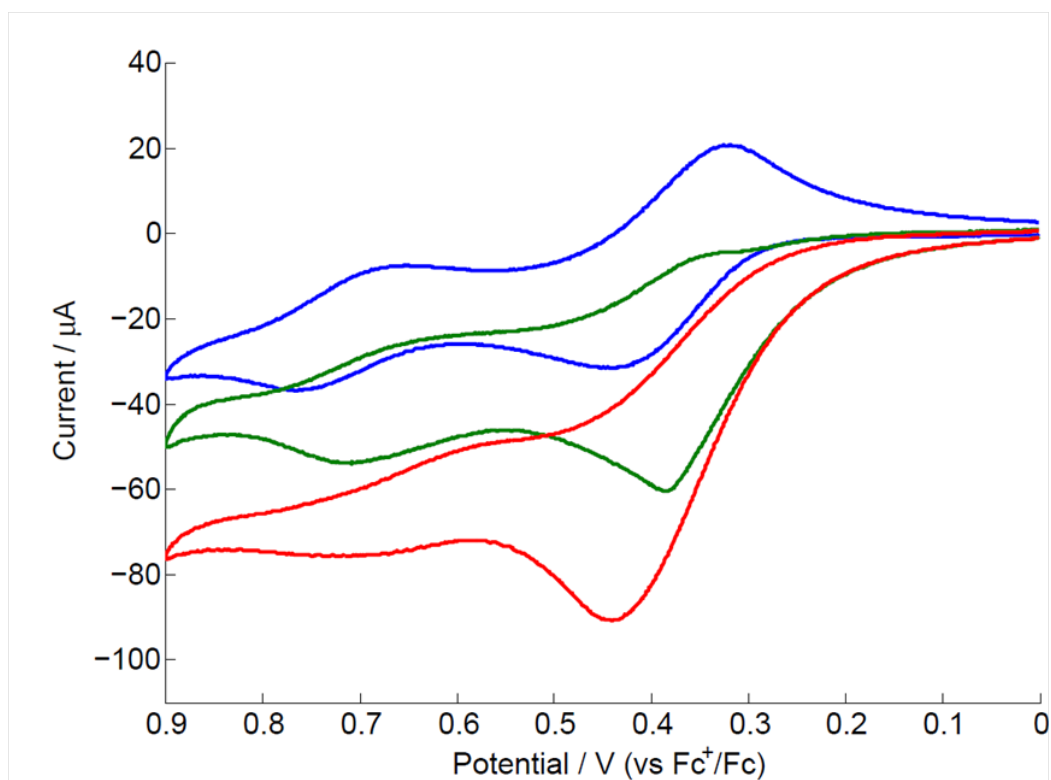


Figure 4.3. Cyclic voltammogram of $[(2\text{-phenylpyridine})\text{Pd}^{\text{II}}(\mu\text{-OAc})_2]$ as chloride concentration is increased from 0 mM (blue), to 1 mM (green), to 2 mM (red)

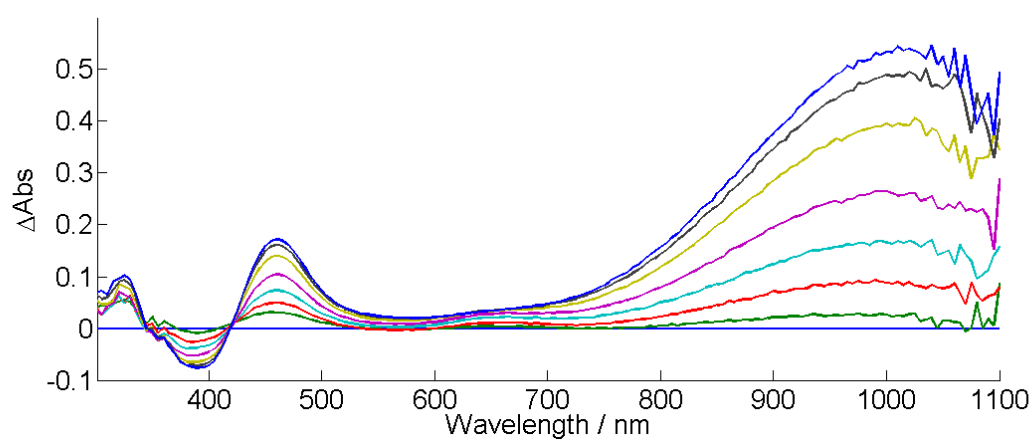


Figure 4.4. Absorbance difference spectrum observed during electrochemical oxidation of Pd^{II} - Pd^{II} at 450 mV vs. Fc^+/Fc

Oxidation at similar potentials in the presence of chloride yields a strikingly different spectrum. Unlike in the halide-free spectrum, no features in the near-IR appear. Instead, a band centered at ~ 425 nm is observed, giving the solution a red-brown color. The UV-vis spectrum closely follows the spectrum observed for the chemically isolable $[(\text{benzo}[h]\text{quinoline})\text{Pd}^{\text{III}}(\mu\text{-OAc})\text{Cl}]_2$ and the new band is attributable to the metal-metal based $d\sigma \rightarrow d\sigma^*$ transition (Figure 4.5). Isosbestic points observed during electrolysis suggest the reaction occurs directly without build-up of an intermediate species. Similar to other d^8 - d^8 complexes, electrochemical reduction of the oxidized product returns the spectrum to its original pre-electrolysis form, suggesting chloride addition is electrochemically reversible, provided it occurs prior to subsequent chemistry. Isolation of this species was unsuccessful, due to its thermal instability and the presence of large amounts of salt needed as electrolyte. Interestingly, one-electron oxidation of $\text{Pd}^{\text{II}}\text{-Pd}^{\text{II}}$, followed by deactivation of the electrode and addition of chloride, results in the formation of $[(\text{benzo}[h]\text{quinoline})\text{Pd}^{\text{III}}(\mu\text{-OAc})\text{Cl}]_2$. While it is impossible to exclude generation of trace amounts of chlorine reacting with $\text{Pd}^{\text{II}}\text{-Pd}^{\text{II}}$ to generate these products, this experiment demonstrates that a scheme proceeding through a $[\text{Pd}_2]^{5+}$ intermediate is viable.

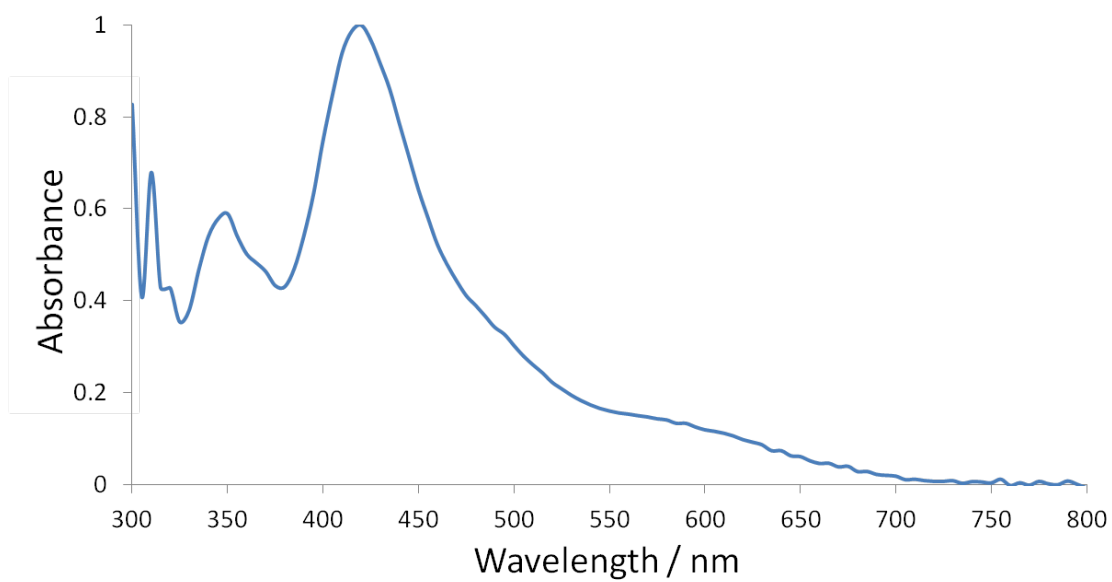
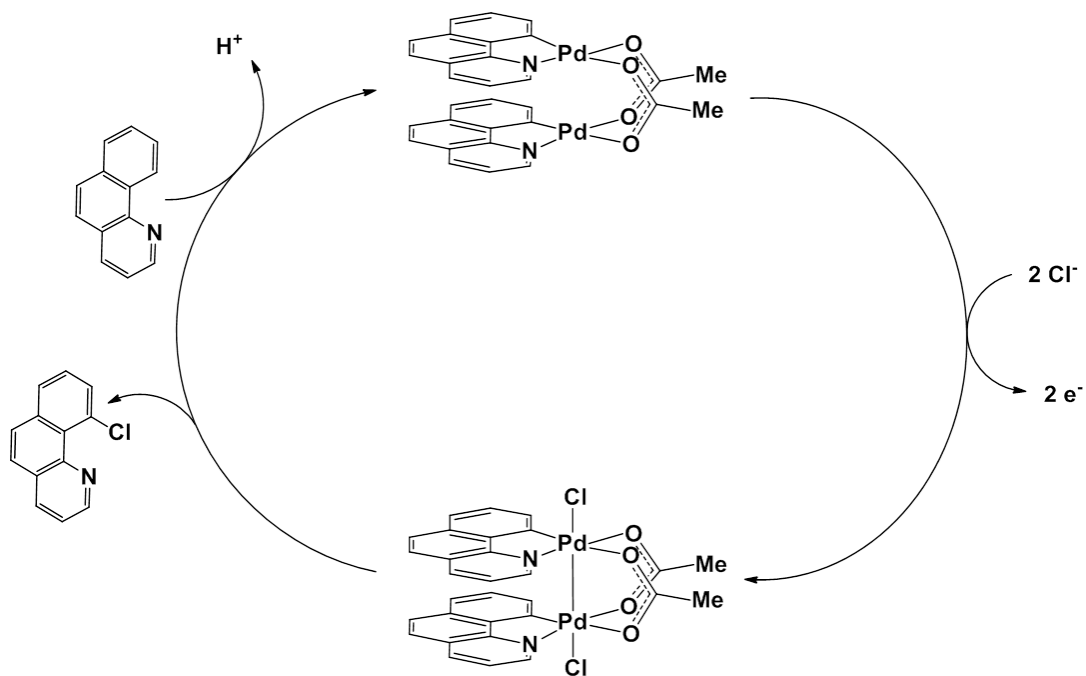


Figure 4.5. UV-vis absorption spectrum of species generated by oxidation of Pd^{II}–Pd^{II} in the presence of chloride

The spectroelectrochemical properties of Pd^{II}–Pd^{II} with other anionic ligands were then examined. In separate experiments, bromide, acetate, and fluoride were added to solutions containing Pd^{II}–Pd^{II} and electrochemically oxidized. Solutions with bromide result in spectra that closely match the spectrum of [(benzo[*h*]quinoline)Pd^{III}(μ-OAc)Br]₂ that is generated chemically from treatment of Pd^{II}–Pd^{II} with Br₂ (Figure 4.6a). Similarly, oxidation in the presence of acetate yields a complex with an absorbance spectrum reminiscent of [(2-phenylpyridine)Pd^{III}(μ-OAc)OAc]₂, which is generated by treatment with PhI(OAc)₂ (Figure 4.6b). Oxidation in the presence of fluoride did not significantly affect the cyclic voltammogram, nor were large changes observed through spectroelectrochemistry. This is not surprising, as attempts to chemically generate [(benzo[*h*]quinoline)Pd^{III}(μ-OAc)F]₂ with XeF₂ were unsuccessful and instead generated linear chains of Pd^{III}.²⁶

Bulk electrolysis

It has been previously established that [(benzo[*h*]quinoline)Pd^{III}(μ-OAc)X]₂ (X= Cl, Br, OAc) will undergo reductive elimination to yield selectively functionalized benzo[*h*]quinoline products. The electrochemical and spectroelectrochemical results strongly suggest that these solutions were being generated in solution. As such, electrochemical generation of these species should result in product formation (Scheme 4.2). An electrocatalytic route to C–Cl, C–Br, and C–O bond-forming reactions is intriguing as the electrochemical potentials required are low relative to traditional oxidants.



Scheme 4.2. Electrocatalytic chlorination of benzo[*h*]quinoline catalyzed by Pd^{II}–Pd^I

A bulk electrolysis cell was purchased featuring a reticulated vitreous carbon working electrode with a large surface area and a fritted auxiliary chamber with platinum wire counter electrode. A mixture of 1 mM equivalent $\text{Pd}^{\text{II}}\text{-Pd}^{\text{II}}$, 10 mM benzo[*h*]quinoline, and 10 mM of tetraethylammonium chloride were combined in 75 mL dichloromethane solution containing 100 mM TBAPF_6 . The auxiliary chamber was filled with an excess of *tris*(acetoacetonato)iron(III) as a sacrificial oxidant. This choice in sacrificial oxidant is advantageous as its potential is insufficient to oxidize $\text{Pd}^{\text{II}}\text{-Pd}^{\text{II}}$ and is electrochemically irreversible, decomposing into *bis*(acetoacetonato)iron(II) and acetylacetonate (Figure 4.7). Further, it is extremely soluble in methylene chloride (> 20 mM). Electrolysis was conducted at approximately +1.0 V (vs. Fc^+ / Fc) and run at room temperature for 48 h. Following electrolysis, > 99% conversion to 10-chlorobenzo[*h*]quinoline was observed with only trace amounts of benzo[*h*]quinoline detected by GC-MS.

Product purification and isolation

Product isolation from electrolyte is easily achieved. Solvent is removed *in vacuo* and the solid is then washed with ether. The TBAPF_6 electrolyte is not soluble and can be recovered by filtration and purified by recrystallization. The supernatant is collected and concentrated. It is then passed through a silica plug eluting with 3:7 ether:hexanes. Removal of solvent 10-chlorobenzo[*h*]quinoline results in 80% yield as a white crystalline solid.

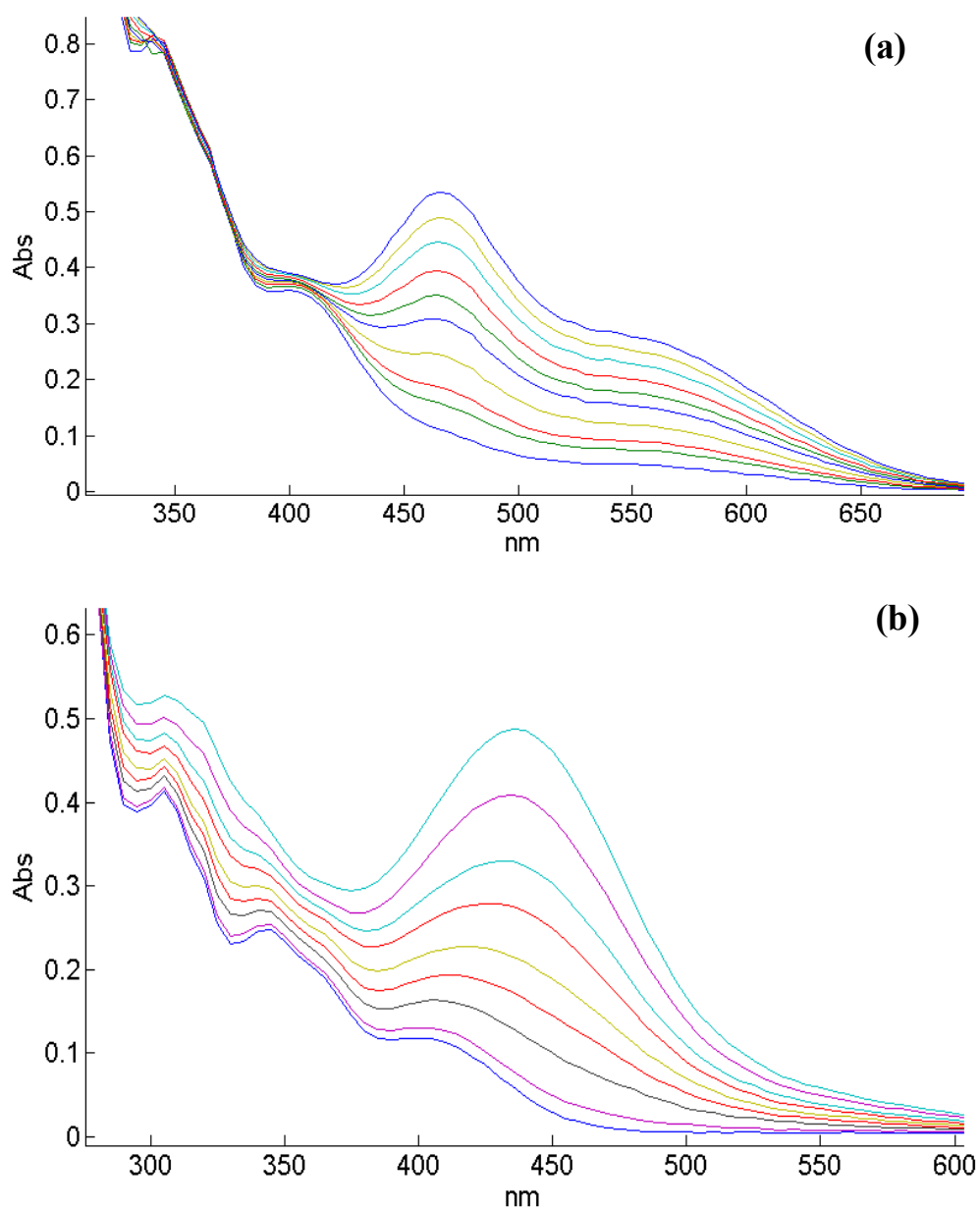


Figure 4.6. UV-vis absorbance spectra Pd^{II}-Pd^{II} following oxidation in the presence of bromide (a) and acetate (b)

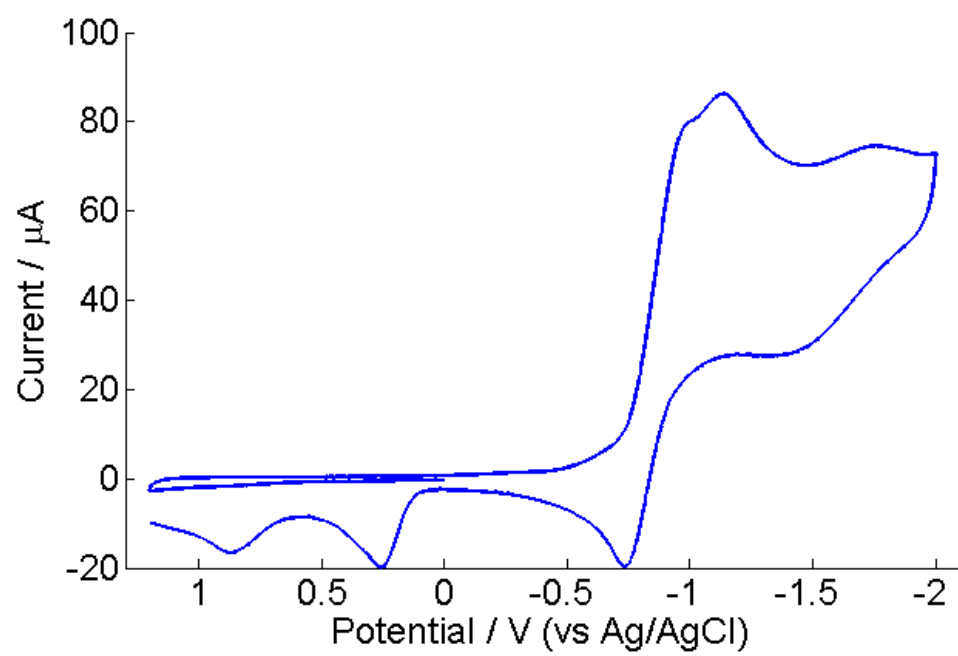


Figure 4.7. Cyclic voltammogram of *tris(acetylacetonato)iron(III)*

Bulk electrolysis at lower potentials was found to generate 10-chlorobenzo[*h*]quinoline, but at sub-catalytic amounts and with minimal current generation. This effect may be a result of resistance in the bulk electrolysis cell. Indeed, cell design was not optimal for effective ion flow and measurements of the potential difference between the reference and working electrodes suggest the applied potential may have been lower than the programmed 1.0 V. However, particularly at these higher potentials, chloride oxidation to chlorine cannot be excluded.

4.4 Concluding remarks

Ongoing studies in our laboratories aim to improve the scope of these electrocatalytic reactions. In summary, we have successfully developed a chemical catalyst for carbon–chlorine bond formation into an efficient electrocatalyst under mild conditions. Capitalizing on the electronic structure and metal–metal interactions between the two palladium(II) centers, we were able to perform two-electron chemistry at the one-electron potential of the complex. Spectroscopic techniques were used to identify reactive intermediates along the proposed catalytic cycle. The properties of these binuclear species may be conducive to more diverse reactivity. Electrocatalytic reactions capable forming C–Br, C–O, C–N, and C–C bonds may be possible from these systems.

4.5 Materials and methods

General

All manipulations were performed in air, unless otherwise stated. Pd(OAc)₂, (purchased from Sigma-Aldrich) and benzo[*h*]quinoline (purchased

from TCI-America) were reagent-grade commercial samples used without further purification. Dichloromethane- d_2 and chloroform- d_1 were purchased from Cambridge Isotope Laboratories and used as received. [(benzo[*h*]quinoline)Pd(μ -OAc)]₂ were prepared using literature procedures.⁹ ¹H and ¹³C NMR spectra were recorded at 298 K using a Varian Mercury 300 MHz spectrometer equipped with the VNMRJ software program, version 2.2d. ¹H and ¹³C NMR spectra were referenced to the residual proton or carbon chemical shifts of the deuterated solvent. The data are reported by chemical shift (ppm) from tetramethylsilane, multiplicity (s, singlet; d, doublet; t, triplet; m, multiplet; dd, double doublet; dt, double triplet), coupling constants (Hz), and integration. Mass spectra were acquired on a Finnigan LCQ ion trap or Agilent 5973 Network mass selective detector and were obtained by peak matching. UV/Vis absorbance spectra were recorded on an Agilent 8453 UV/Vis Spectrometer using a pure sample of the solvent as the background.

Electrochemistry

Cyclic voltammetry and differential pulse voltammetry were carried out using a 660 Electrochemical Workstation (CH-Instruments, Austin, TX). Measurements were performed at room temperature in CH₂Cl₂ solutions with 0.1 M TBAPF₆ as the supporting electrolyte. Concentrations of [(benzo[*h*]quinoline)Pd(μ -OAc)]₂ were kept at approximately 1 mM. Axially coordinating ligands (chloride, bromide, and acetate) were added by titration of a solution containing the corresponding tetraethylammonium salt. A scan rate of 0.1

V/s was used for all cyclic voltammetry measurements. Experiments were conducted using a glassy carbon working electrode, a saturated Ag/AgCl reference electrode, and a platinum wire counter electrode. Ferrocenium/ferrocene (Fc^+/Fc) was used as an internal reference.

Bulk electrolysis experiments were performed on a Pine Instruments WaveNow potentiostat and the data were processed using Igor Pro 5.01 (Wavemetrics). Electrolysis was performed in a bulk electrolysis cell (purchased from BASi MF-1056). The complete bulk cell consists of a 100 mL glass vial, an auxiliary cell with approximately 10 mL volume, a reticulated vitreous carbon working electrode, a 10 cm Pt wire auxiliary electrode, and a Ag/AgCl reference electrode. The auxiliary chamber is separated from the working chamber by a fine-porous frit. Replacement glass parts can be purchased at significantly reduced cost from Ace Glass. Platinum wire can be purchased through Alfa Aesar. The main chamber was filled with 75 mL of 1.0 mM Pd_2 , 10 mM TEACl, and 10 mM benzo[*h*]quinoline. The auxiliary chamber was filled with approximately iron(III) *tris*-(acetylacetonate), which is extremely soluble in dichloromethane and serves as a sacrificial oxidant. Bulk electrolysis was conducted at 100–200 mV beyond the first anodic peak potential (approximately +500–600 mV vs. Fc^+/Fc). Working and auxiliary chambers were stirred during electrolysis. Reaction progress was monitored by a combination of coulometry and GCMS measurements of aliquots taken from the reaction mixture. Bulk electrolysis was allowed to proceed 24–48 h at room temperature.

Product purification and isolation

Following electrolysis, the solution was evaporated to dryness and redissolved in diethylether. This solution was then filtered, removing the majority of ammonium salts. Solvent was removed from the filtrate *in vacuo* and the residue was purified by passing it through a silica plug, eluting with hexanes:diethyl ether (9:1). This afforded the product, 10-chlorobenzo[*h*]quinoline in 82% isolated yield.

¹H-NMR (300 MHz, CDCl₃, 23 °C, δ): 9.12 (dd, *J* = 4.4 Hz, 2.0 Hz, 1H), 8.19 (dd, *J* = 8.3 Hz, *J* = 2.0 Hz, 1H), 7.84 (td, *J* = 7.3 Hz, *J* = 1.0 Hz, 2H), 7.80 (d, *J* = 8.8 Hz, 1H), 7.72 (d, *J* = 8.8 Hz, 1H), 7.59–7.55 (m, 2H).

4.6 References

- (1) Smidt, J.; Hafner, W.; Jira, R.; Sieber, R.; Sedlmeier, J.; Sabel, A. *Angew. Chem.* **1962**, *74*, 93–102.
- (2) Ebner, D. C.; Bagdanoff, J. T.; Ferreira, E. M.; McFadden, R. M.; Caspi, D. D.; Trend, R. M.; Stoltz, B. M. *Chem. Eur. J.* **2009**, *15*, 12978–12992.
- (3) Sigman, M. S.; Jensen, D. R. *Acc. Chem. Res.* **2006**, *39*, 221–229.
- (4) Stahl, S. S. *Angew. Chem. Int. Ed.* **2004**, *43*, 3400–3420.
- (5) Chuang, G. J.; Wang, W.; Lee, E.; Ritter, T. *J. Am. Chem. Soc.* **2011**, *133*, 1760–1762.
- (6) Zhang, J.; Khaskin, E.; Anderson, N. P.; Zavalij, P. Y.; Vedernikov, A. N. *Chem. Commun.* 3625–3627.
- (7) Fahey, D. R. *J. Chem. Soc., Chem. Commun.* **1970**, 417.
- (8) Whitfield, S. R.; Sanford, M. S. *J. Am. Chem. Soc.* **2007**, *129*, 15142–15143.
- (9) Powers, D. C.; Ritter, T. *Nat. Chem.* **2009**, *1*, 302–309.
- (10) Powers, D. C.; Geibel, M. A. L.; Klein, J. E. M. N.; Ritter, T. *J. Am. Chem. Soc.* **2009**, *131*, 17050–17051.
- (11) Powers, D. C.; Xiao, D. Y.; Geibel, M. A. L.; Ritter, T. *J. Am. Chem. Soc.* **2010**, *132*, 14530–14536.
- (12) Cotton, F. A.; Gu, J.; Murillo, C. A.; Timmons, D. J. *J. Am. Chem. Soc.* **1998**, *120*, 13280–13281.
- (13) Khusnutdinova, J. R.; Rath, N. P.; Mirica, L. M. *J. Am. Chem. Soc.* **2010**, *132*, 7303–7305.

- (14) Cotton, F. A.; Koshevoy, I. O.; Lahuerta, P.; Murillo, C. A.; Sanaú, M.; Ubeda, M. A.; Zhao, Q. *J. Am. Chem. Soc.* **2006**, *128*, 13674–13675.
- (15) Blake, A. J.; Holder, A. J.; Hyde, T. I.; Schröder, M. *J. Chem. Soc., Chem. Commun.* **1987**, 987–988.
- (16) Bercaw, J. E.; Durrell, A. C.; Gray, H. B.; Green, J. C.; Hazari, N.; Labinger, J. A.; Winkler, J. R. *Inorg. Chem.* **2010**, *49*, 1801–1810.
- (17) Mann, K. R., Gray, H. B., In *Inorganic Compounds with Unusual Properties—II*, Advances in Chemistry, ACS, **1979**; vol. 173, p. 225–235.
- (18) Smith, D. C.; Gray, H. B. *Coord. Chem. Rev.* **1990**, *100*, 169–181.
- (19) Roundhill, D. M.; Gray, H. B.; Che, C. M. *Acc. Chem. Res.* **1989**, *22*, 55–61.
- (20) Marshall, J. L.; Stobart, S. R.; Gray, H. B. *J. Am. Chem. Soc.* **1984**, *106*, 3027–3029.
- (21) Mann, K. R.; Gordon, J. G.; Gray, H. B. *J. Am. Chem. Soc.* **1975**, *97*, 3553–3555.
- (22) Xia, B.; Che, C.; Zhou, Z. *Chem. Eur. J.* **2003**, *9*, 3055–3064.
- (23) Cotton, F. A.; Matusz, M.; Poli, R.; Feng, X. *J. Am. Chem. Soc.* **1988**, *110*, 1144–1154.
- (24) Berry, J. F.; Bill, E.; Bothe, E.; Cotton, F. A.; Dalal, N. S.; Ibragimov, S. A.; Kaur, N.; Liu, C. Y.; Murillo, C. A.; Nellutla, S.; North, J. M.; Villagrán, D. *J. Am. Chem. Soc.* **2007**, *129*, 1393–1401.
- (25) Bryan, S. A.; Schmehl, R. H.; Roundhill, D. M. *J. Am. Chem. Soc.* **1986**, *108*, 5408–5412.
- (26) Campbell, M. G.; Powers, D. C.; Raynaud, J.; Graham, M. J.; Xie, P.; Lee, E.; Ritter, T. *Nat. Chem.* **2011**, *3*, 949–953.

A p p e n d i x A :

Electron transfer triggered by optical excitation of phenothiazine-*tris(meta-*
phenylene-ethynylene)-(tricarbonyl)(bpy)(py)rhenium(I)

The text in this chapter was taken in part from:
Bingol, B.; Durrell, A. C.; Keller, G. E.; Palmer, J. H.; Grubbs, R. H.; Gray, H. B.
J. Phys. Chem. C **2012**, (in press).

A.1 Abstract

We have investigated excited-state electron transfer in a donor-bridge-acceptor complex containing phenothiazine (PTZ) linked via *tris(meta-phenylene-ethynylene)* to a tricarbonyl(bipyridine)(pyridine)Re(I) unit. Time-resolved luminescence experiments reveal two excited-state (*Re) decay regimes: a multiexponential component with a mean lifetime of 2.7 ns, and a longer monoexponential component of 530 ns in dichloromethane solution. The faster decay is attributed to PTZ → *Re electron transfer in a C-shaped PTZ-bridge-Re conformer (PTZ–Re ~ 7.5 Å). We assign the longer lifetime, which is virtually identical with that of free *Re, to an extended conformer (PTZ–Re > 20 Å). The observed biexponential *Re decay requires that interconversion of PTZ-bridge-Re conformers be slower than 10^6 s^{-1} .

A.2 Introduction

Photoinduced electron transfer (ET) reactions play key roles in artificial photosynthesis^{1–5} and optoelectronic devices.^{6,7} Critical to all of these systems is the precise control of ET rates over long distances. ET has been shown to depend on tunneling distance, donor-acceptor energetics, and chemical structure of the bridge.^{8,9}

Donor-bridge-acceptor complexes allow systematic investigation of the parameters that control ET processes.^{10–14} Paul Barbara was a leading investigator in this area: his work on strongly coupled mixed-valence complexes helped to fix the speed limit for bridge-mediated ET.^{15,16} Complexes with highly conjugated bridges such as oligo(phenylene vinylenes),^{17–19} oligo(flourenes),^{20–22} oligo(*para*-

phenylenes), and oligo(*para*-phenylene ethynylenes)^{23–29} are of particular interest, as they often exhibit wire-like behavior. Electronic coupling mediated by these bridges promotes rapid forward electron transfer, but in many cases equally fast charge recombination limits their deployment in molecular electronic devices.

Donor-acceptor couplings mediated by nonbonded contacts have been investigated in C-shaped complexes containing saturated polycyclic spacers.^{30–37} The rigid spacer fixes donor-acceptor orientation, providing control of the overall topology and allowing investigations of intramolecular ET processes mediated by noncovalent interactions. Importantly, these investigations have shown that electron tunneling can occur over relatively long distances through organic solvents. Flexible bridges allow for minimal through-space donor-acceptor distances that favor through-space (or through-solvent) over through-bond ET pathways.

Here we report the synthesis and photophysical properties of a donor-bridge-acceptor (DBA) (tricarbonyl)(bpy)(py)rhenium(I) (Re) linked to phenothiazine (PTZ) by *tris*(*meta*-phenylene-ethynylene). We chose PTZ-Re to probe the role of the bridge in ET reactions, as prior work has shed light on the coupling between D and A in this pair.^{10–13,38–40}

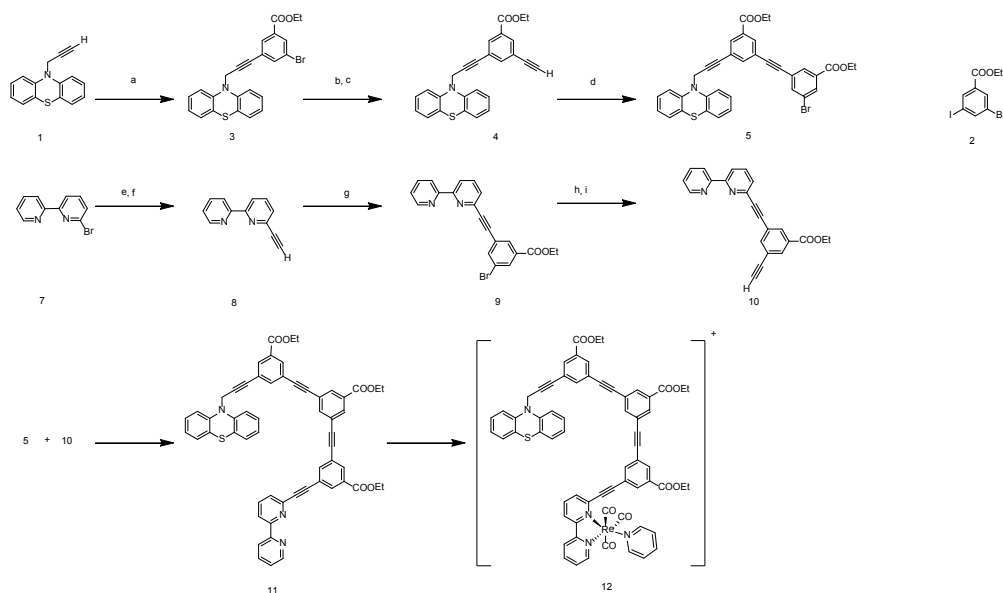
A.3 Results and discussion

Synthesis

In Scheme A.1, a PTZ-bridge ligand (**11**) covalently coupled to a Re acceptor afforded PTZ-bridge-Re (**12**). The electron donor is 10-(prop-2-yn-1-yl)-10H-phenothiazine (**1**), and the bridge contains three phenylene-ethynylene units.

The PTZ-bridge ligand features a terminal bipyridine, which binds strongly to Re(I). Compound **11** was constructed in a stepwise approach using zinc-mediated, palladium-catalyzed cross-coupling reactions in a microwave reactor (with protecting group strategies).⁴¹ More precisely, the synthesis of **11** began with selective coupling of the donor (**1**) to 3-bromo-5-iodobenzoate (**2**). Both **1** and **2** were prepared according to published protocols.^{42,43} Compound **3** was coupled with trimethylsilyl acetylene, followed by removal of the trimethylsilyl group by treatment with tetrabutylammonium fluoride (TBAF) to afford ethynylene-terminated **4**. The alkynyl group of **4** was then coupled to **2** to give phenothiazine-terminated **5** with a bromo functionality. Assembly of **11** required that an ethynylene-terminated bipyridine connected to a phenylene-ethynylene unit (**10**) be linked to **5**. Synthesis of **10** began with commercial 6-bromo-2,2'-bipyridine, which was acetylated and deprotected before reaction with **2** to yield a bromo-bipyridine derivative attached to a phenylene-ethynylene unit (**9**). Acetylation of **9** followed by deprotection with TBAF gave **10**. Subsequent cross-coupling of **10** to **5** yielded the PTZ-bridge ligand (**11**). Metalating **11** with rhenium(I) pentacarbonyl chloride,⁴⁴ followed by reaction with pyridine in the presence of silver perchlorate in the dark, afforded PTZ-bridge-Re (**12**).⁴⁴⁻⁴⁶ A model of the acceptor, $[\text{Re}(\text{CO})_3(\text{bpy})(\text{py})]^+$ (bpy = 2,2'-bipyridine, py = pyridine), also was prepared.^{47,48}

Scheme A.1. Synthesis of PTZ-bridge-Re (12)^a



Reagents and conditions: a) propargyl bromide, K_2CO_3 , toluene, reflux. b) **2**, bis(triphenylphosphine)palladium(II) dichloride, $ZnCl_2$, THF, Et_3N , 100 °C. c) TBAF, THF, room temperature. d) **2**, bis(triphenylphosphine)palladium(II) dichloride, $ZnCl_2$, THF, Et_3N , 100 °C. e) trimethylsilyl acetylene, bis(triphenylphosphine)palladium(II) dichloride, $ZnCl_2$, THF, Et_3N , 100 °C. f) TBAF, THF, room temperature. g) **2**, bis(triphenylphosphine)palladium(II) dichloride, $ZnCl_2$, THF, Et_3N , 100 °C. h) trimethylsilylacetylene, bis(triphenylphosphine)palladium(II) dichloride, $ZnCl_2$, THF, Et_3N , 100 °C. i) TBAF, THF, room temperature. j) bis(triphenylphosphine)palladium(II) dichloride, $ZnCl_2$, THF, Et_3N , 100 °C. k) $Re(CO)_5Cl$, toluene, reflux. l) $AgClO_4$, pyridine, CH_3OH , toluene, 50 °C.

Physical properties

The absorption spectrum of PTZ-bridge-Re in dichloromethane solution displays three main features (Figure A.1a). The intense, high energy bands (260–320 nm) in the spectrum are attributed to ligand-based $\pi\text{-}\pi^*$ transitions. Similar features are also present in the spectrum of 6-ethynyl-2,2'-bipyridine. A band centered at 255 nm characteristic of phenothiazine is absent in the spectrum of the $[\text{Re}(\text{CO})_3(\text{bpy})(\text{py})]^+$ model complex, and a broad feature (340–390 nm), attributable to metal-to-ligand charge transfer (MLCT), is absent in the spectrum of PTZ-bridge.^{49,50} Absorption bands associated with the bridge were not observed; however, broadening of the 255 nm band accompanied cross-coupling of 10-(prop-2-yn-1-yl)-10H-phenothiazine to 3-bromo-5-iodobenzoate.

The steady-state emission spectrum of PTZ-bridge-Re in dichloromethane solution features a broad band centered at 574 nm (Figure A.1b). Quantum yield measurements were performed in CH_2Cl_2 using $[\text{Re}(\text{CO})_3(\text{bpy})(\text{py})]^+$ as a standard. The quantum yield of PTZ-bridge-Re was found to be approximately 10% of the $[\text{Re}(\text{CO})_3(\text{bpy})(\text{py})]^+$ standard (Figure A.2). Higher concentrations of PTZ-bridge-Re did not exhibit linear behavior as a result of intermolecular self-quenching.

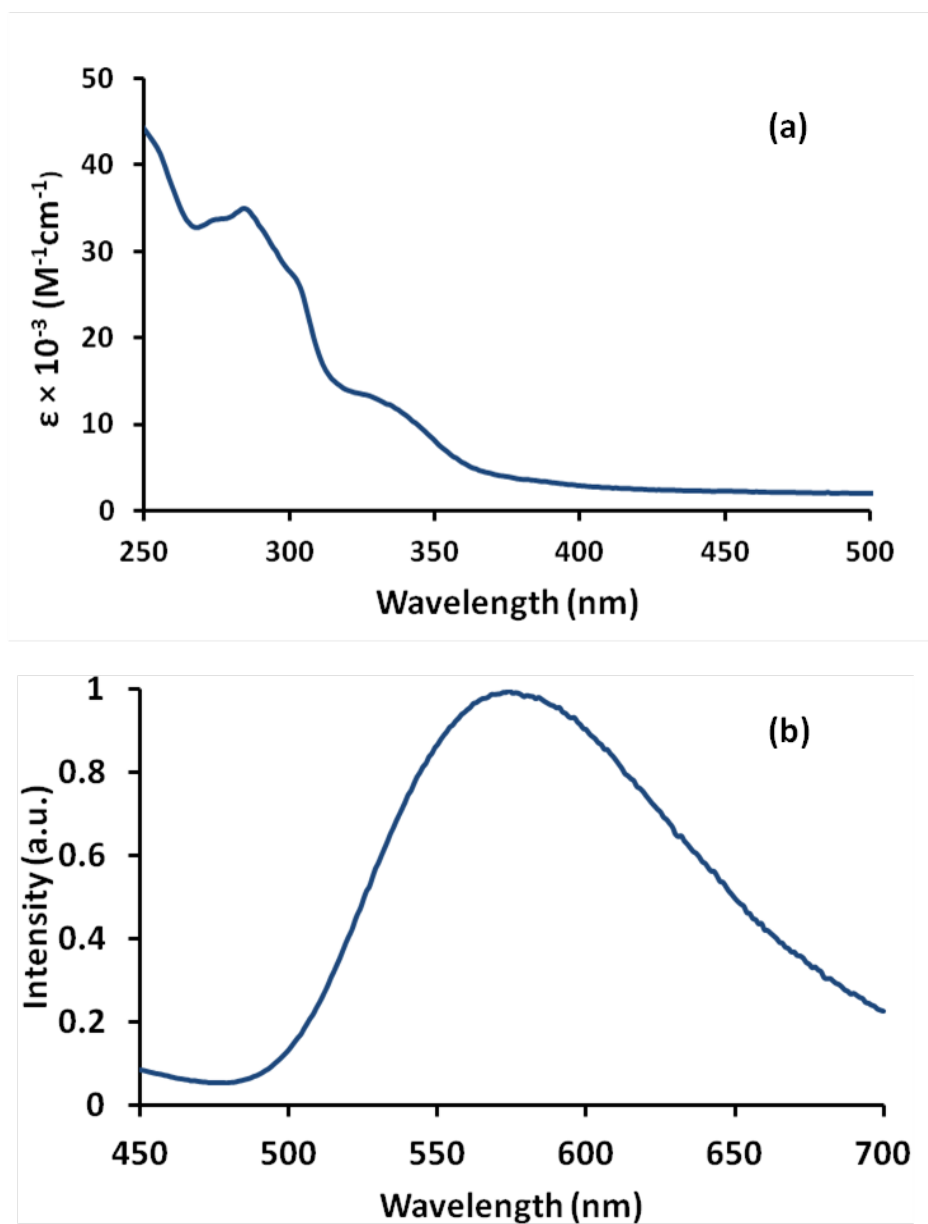


Figure A.1. Absorption (a) and corrected emission (b) spectra of PTZ-bridge-Re in CH_2Cl_2 solution at room temperature

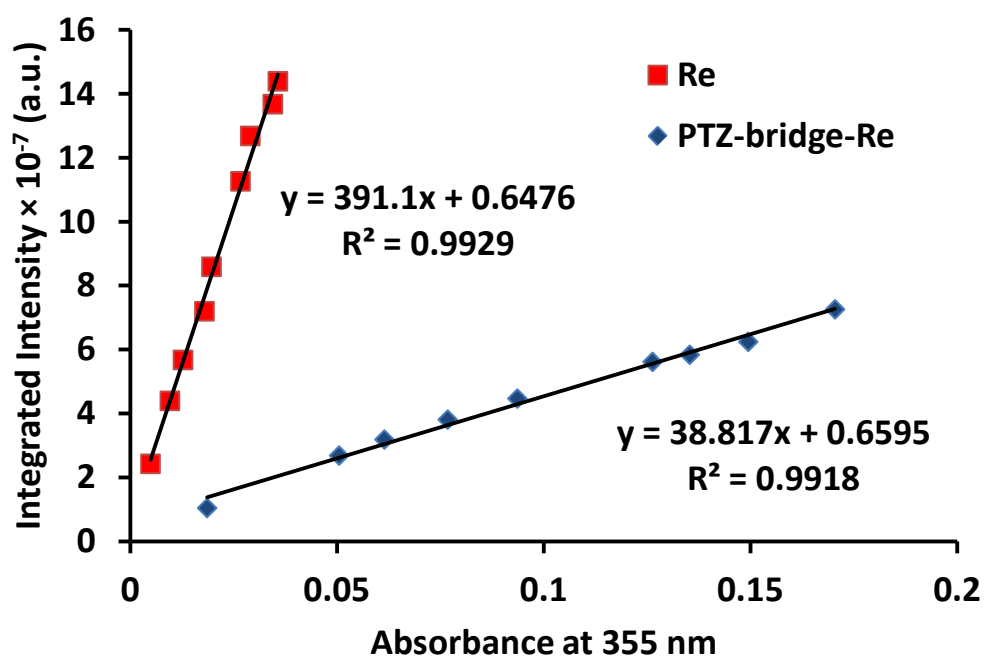


Figure A.2. Quantum yield measurements of PTZ-bridge-Re relative to Re

MLCT emission decay kinetics recorded in degassed dichloromethane solution exhibited two decay regimes. At timescales greater than 50 ns, a 530 ns monoexponential decay lifetime was observed (Figure A.3a). For comparison, the *Re MLCT lifetime of the model complex, $[Re(CO)_3(bpy)(py)]^+$, determined under virtually identical experimental conditions, was 560 ns. The excited-state lifetime and steady-state intensity were found to depend on the concentration of PTZ-bridge- Re in solution. Analysis of the longer component of the excited-state lifetime at a series of concentrations allowed a bimolecular quenching rate constant of $1.1 \times 10^6 M^{-1} s^{-1}$ to be determined. When the lifetime is extrapolated to zero concentration, a natural lifetime of 530 ns is obtained. This value is close to that of the $[Re(CO)_3(bpy)(py)]^+$ model compound (560 ns in degassed CH_2Cl_2 , Figure A.4).

Emission decay in the 0–50 ns range was highly nonexponential (Figure A.3b). Quality fits required at least three exponential terms, resulting in a 3.2–3.4 ns average lifetime, depending on the fit. Alternatively, a stretched-exponential fit gave $\tau = 1.73$ ns and $\beta = 0.57$, indicating a rather broad spread of lifetime values (Figure A.5). A mean value of 2.7–2.8 ns was obtained from a stretched-exponential fit. The presence of several components with different decay kinetics is also confirmed by non-negative least-squares analysis of the numerical inversion of the Laplace transform describing the luminescence intensity decay (Figure A.6). This approach yields a distribution of lifetimes in the 0.2–6 ns range with an average value of $\tau = 1.9$ ns. The decrease in luminescence lifetime and quantum yield is attributed to $PTZ \rightarrow ^*Re$ ET. The complex excited-state behavior suggests

there are multiple geometries accessible to PTZ-bridge-Re that possess distinct ET rates. Charge recombination must be equally rapid; a PTZ radical cation signal was not observed by transient absorption 10 ns after excitation.¹³

Unlike rigid oligo(*para*-phenylene ethynylene) DBA complexes, *meta*-linked species are flexible, allowing short through-space donor-acceptor distances. We applied theoretical calculations using a UFF force field to generate minimized compact (C-shaped) (Figure A.7a) and extended (Figure A.7b) conformations of PTZ-bridge-Re.⁵¹ Intramolecular PTZ \rightarrow *Re ET in the extended conformation was slow (the lifetime was very near that of the model compound). In the C-shaped conformation, the short through-space distance greatly enhances D:A coupling, which in turn promotes PTZ \rightarrow *Re ET. The multiexponential character of the decay is consistent with multiple close-contact geometries that exhibit nanosecond electron transfer rates. Interconversion of the extended and C-shaped conformers must be relatively slow (microsecond range or longer) to be consistent with the observed biphasic *Re decay kinetics.

Analysis of ET rates for DBA systems linked by oligo(*para*-phenylene ethynylene) bridges give exponential distance decay (β) constants of 0.3–0.6 Å⁻¹.^{8,28,52} *Meta*-linked systems are likely to have higher β values compared to their linear *para*-linked counterparts; these values, coupled with an estimated ET rate of $1.6 \times 10^{11} \text{ s}^{-1}$ for [Re(CO)₃(bpy)(py)]⁺ and PTZ at contact,¹³ predict an intramolecular ET rate for extended PTZ-bridge-Re of between $8 \times 10^3 \text{ s}^{-1}$ and $4 \times 10^6 \text{ s}^{-1}$. Molecular modeling of the compact conformation places PTZ and Re within 7.5 Å (C-to-C), consistent with nanosecond ET (Figure A.7).^{53,54}

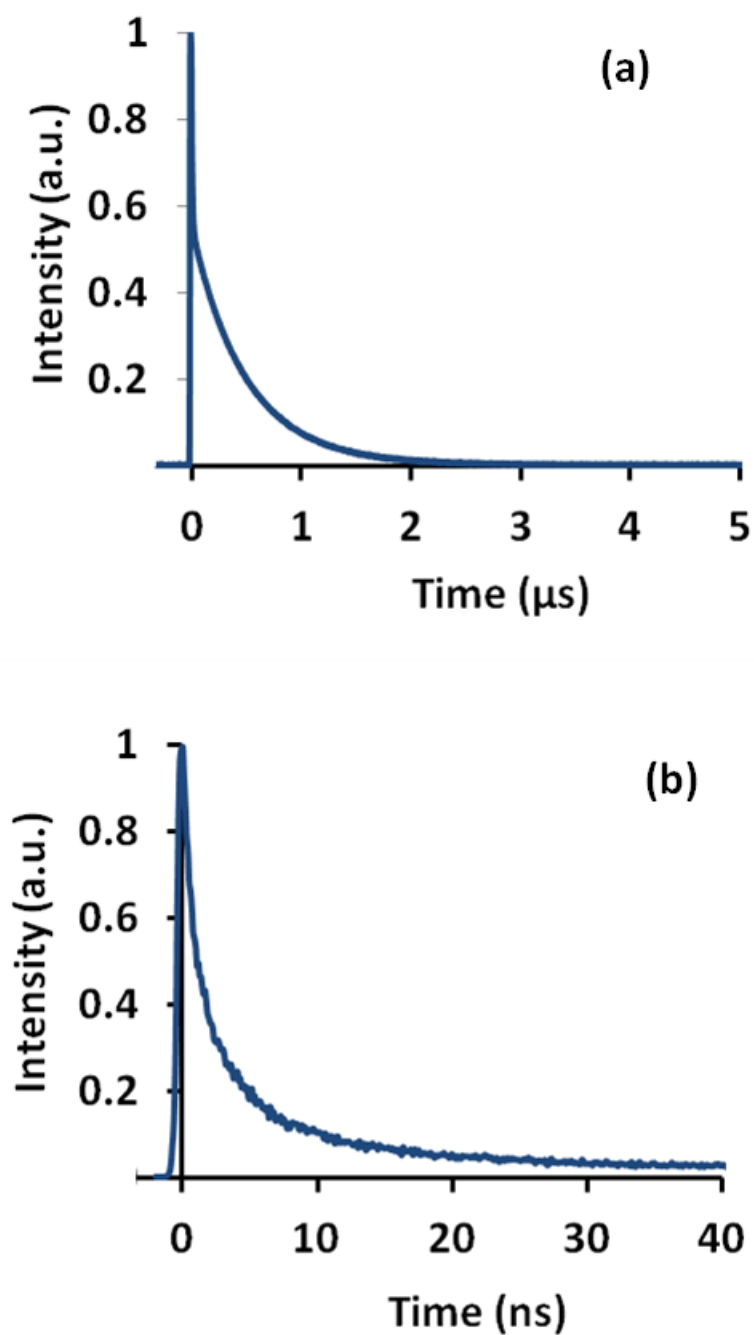


Figure A.3. Time-resolved emission decay profiles of PTZ-bridge-Re: (a) monitored to 5 μs ; (b) monitored to 40 ns

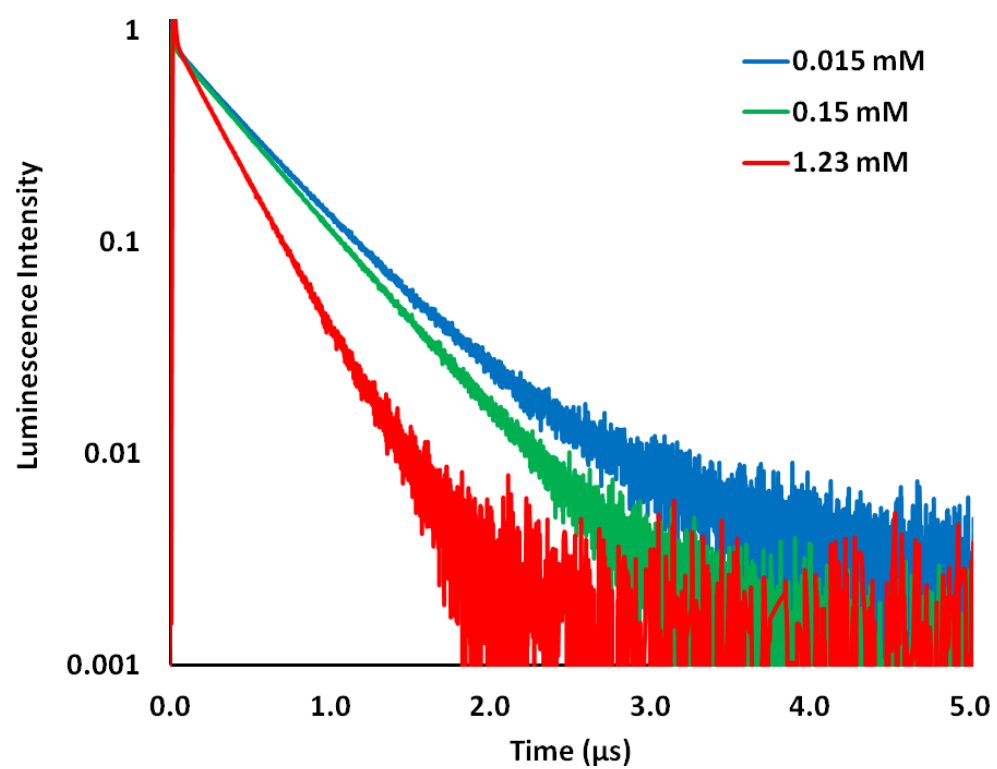


Figure A.4. Concentration-dependent luminescence of PTZ-bridge-Re in CH_2Cl_2

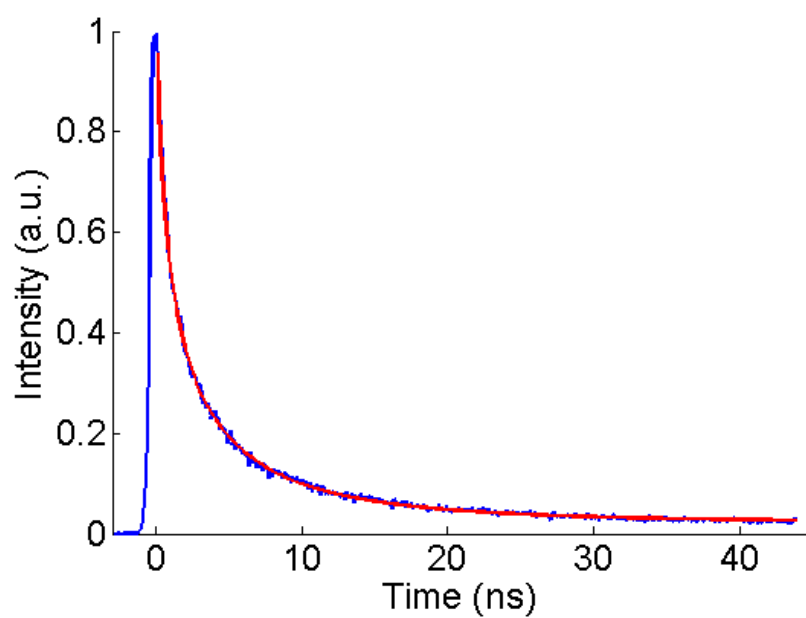


Figure A.5. Stretched-exponential fit of the rapid decay component, $\tau = 1.72$, $\beta = 0.574$, $\langle\tau\rangle = 2.7$ ns

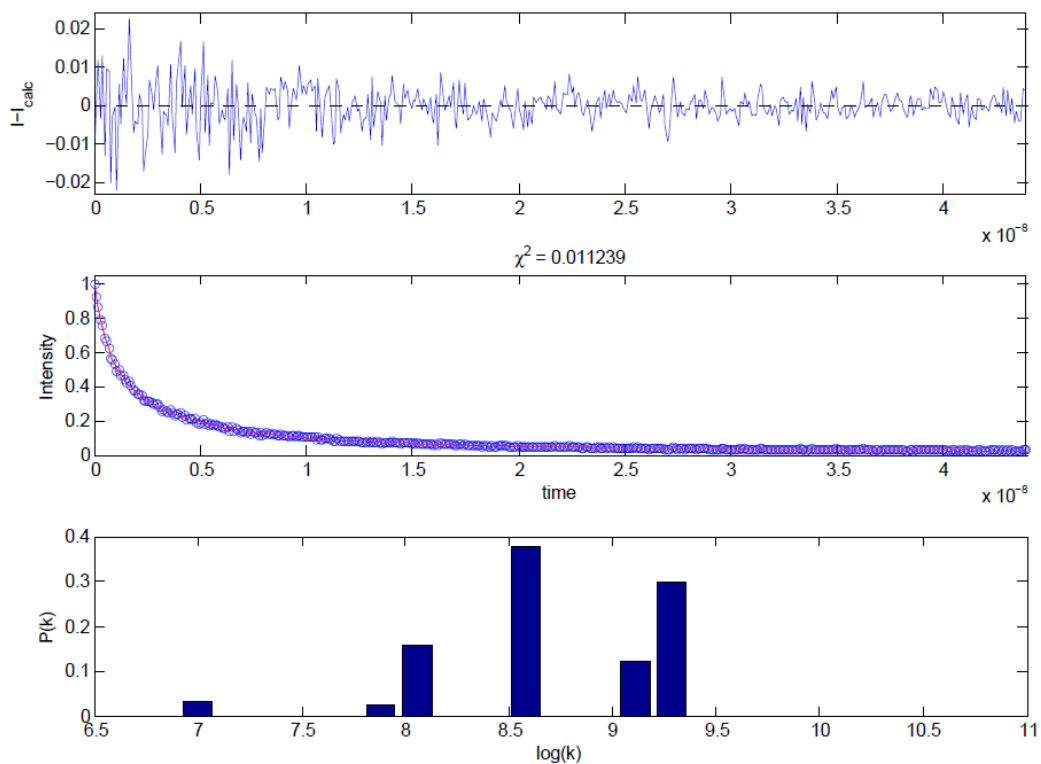


Figure A.6. $P(k)$ distributions extracted from non-negative least squares analysis of the rapid component of the luminescence decay. Top panel: residual difference between observed and calculated intensity with minimized χ^2 . Middle panel: luminescence decay data (circles) fit to a sum of exponentials (line). Bottom panel: probability distribution of rates ($\log(k)$) with an average value of $\tau = 1.9$ ns

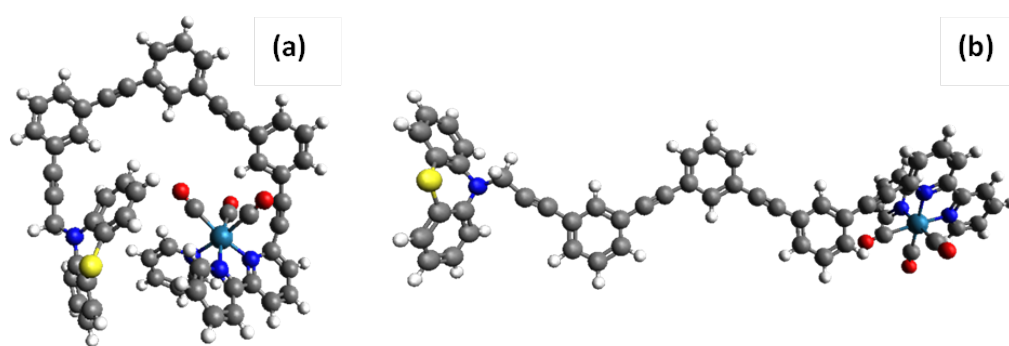


Figure A.7. Structural models: (a) compact conformation of PTZ-bridge-Re; (b) extended conformation of PTZ-bridge-Re. Structures were modeled using Avogadro molecular editing software.⁵⁰

Aggregation studies

Donor-bridge-acceptor complexes containing *meta*-phenylene ethynylene linkages have been shown to aggregate under certain conditions.³ Self-association often leads to enhanced quenching, due to the formation of aggregates with short intermolecular donor-acceptor distances. To verify that no aggregation is occurring in PTZ-bridge-Re, a combination of UV-vis, steady-state fluorescence, and NMR spectroscopies were employed. Absorption and emission spectra of PTZ-bridge-Re at concentrations varying from 32 μM to 1.51 mM did not exhibit significant change in peak position, and increasing concentration did not produce additional spectral features (Figures A.8 and A.9). NMR spectra of PTZ-bridge-Re in dichloromethane solution of concentrations ranging from 0.13 mM to 1.35 mM did not exhibit significant change in the position of resonances, and no additional resonances were observed as concentration was varied (Figure A.10). These results suggest that there is no aggregation under our experimental conditions.

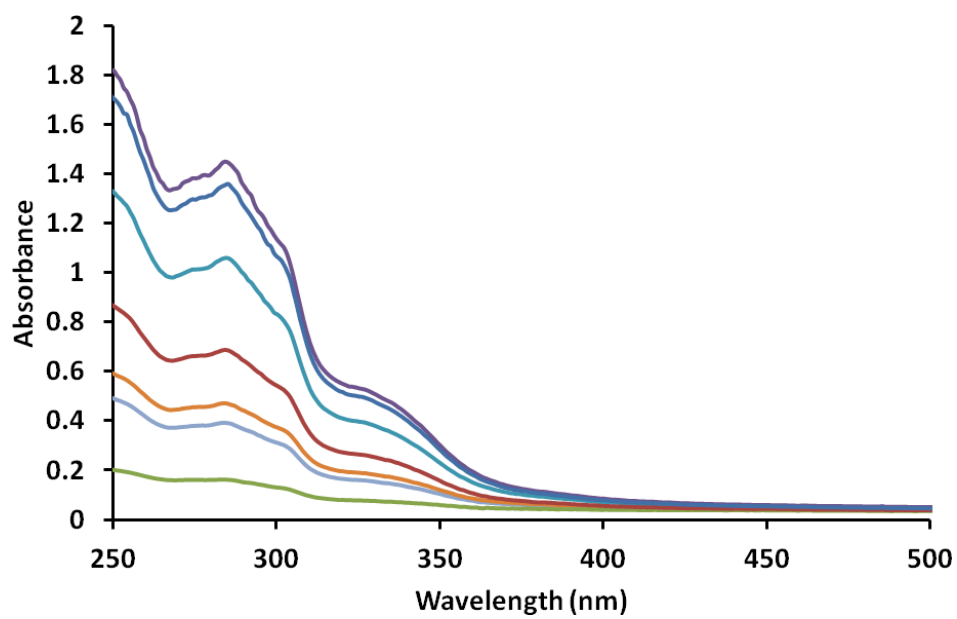


Figure A.8. UV-vis absorption spectra of PTZ-bridge-Re in CH₂Cl₂ at various concentrations

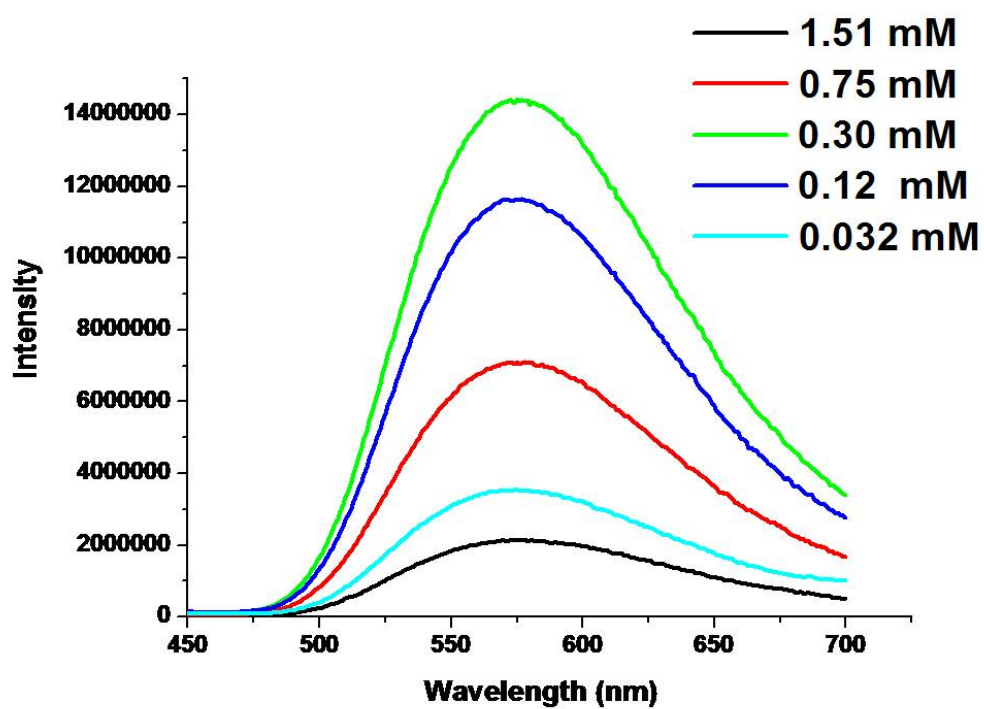


Figure A.9. Steady-state emission spectra of PTZ-bridge-Re in CH₂Cl₂ at various concentrations

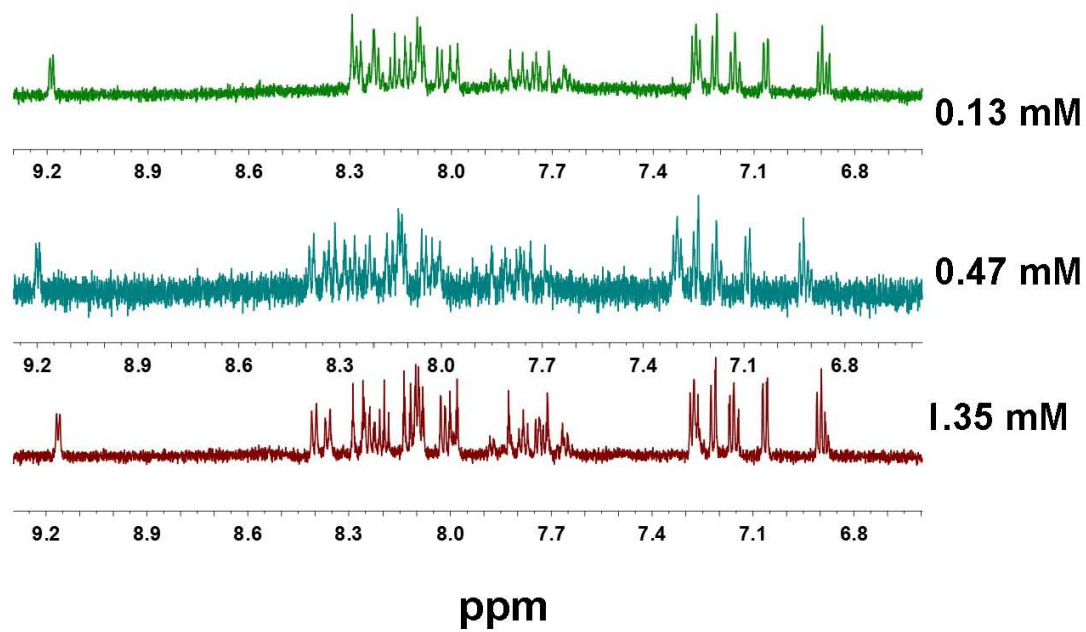


Figure A.10. ^1H -NMR spectra of PTZ-bridge-Re complex in CD_2Cl_2 at various concentrations

Computational modeling

Density-functional theoretical calculations allowed us to determine the relative energies of two rotational conformers of the bridging *tris(meta-phenylene-ethynylene)* ligand. To decrease computational time, we used a model bridge with no ethyl ester groups (Figure A.11). We wanted to examine the possibility that the donor and acceptor can be both close and remote from one another, which would account for the two sets of observed PTZ-bridge-Re emission lifetimes. We found that we could begin with a model where the bridge is in an extended conformation (and fall into one minimum), or from a model of a fully compact state (in which case we calculated a different minimum energy structure). Both of these geometries were validated as true ground states via numerical frequency calculations; there were no imaginary frequencies or unreasonable bond lengths. According to our calculations, the compact and extended conformers are virtually isoenergetic.

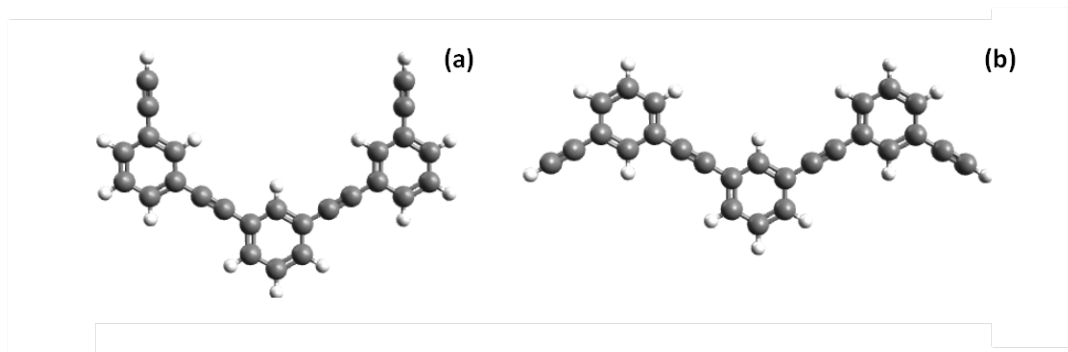


Figure A.11. Calculated *m*-phenylene-ethynylene fragment in the compact (a) and extended (b) conformations obtained from DFT calculations

A.4 Concluding remarks

Electronically excited PTZ-bridge-Re, where a Re electron acceptor is linked by *tris(meta-phenylene-ethynylene)* bridge to a PTZ donor, exhibits very rapid intramolecular electron transfer. Computational modeling suggests that the reaction occurs in a C-shaped conformer with PTZ-Re at 7.5 Å. The observed biphasic decay shows that the conformational dynamics are substantially shorter than the *Re lifetime, which is on the order of a microsecond. In principle, conformational changes in flexible bridges such as *meta-phenylene-ethynylene* could retard charge recombination reactions, extending charge-separated lifetimes. In our case, however, back electron transfer is much faster than conversion to the extended (slow electron transfer) structure, disallowing production of long-lived charge-separated extended structures.

Variations in electrostatic interactions between D:A pairs could be employed in designs that favor compact conformations prior to electron transfer, but strongly destabilize them following ET. A case in point would be to develop a system consisting of a neutral donor (D) and dicationic acceptor (A^{2+}), which would not experience any charge-charge electrostatic interaction until the formation of ET products D^+ and A^+ . The resulting repulsion would destabilize the compact conformer relative to extended structures, allowing charge separation to persist for relatively long times.

We suggest that *tris(meta-phenylene-ethynylene)* could be useful as a linker for such D:A pairs, as spectroscopic measurements conducted on PTZ-bridge-Re show that the compact conformation is favored energetically. Repulsive

electrostatic forces triggered by ET may be sufficient to drive the conformer equilibrium toward extended structures. We postulate that the pair *N,N,N',N'*-tetramethyl-*p*-phenylenediamine (TMPD): ruthenium(II)-*tris*(bipyridine) could be connected by a phenylene-ethynylene bridge by procedures similar to those used to construct PTZ-bridge-Re. ET-triggered conformational change of this DBA complex would be expected to produce long-lived charge separation that could drive useful multielectron redox chemistry.

A.5 Materials and methods

General information. Unless otherwise noted, all starting materials were obtained from commercial suppliers and were used without further purification. All air- or moisture-sensitive reactions were performed under an atmosphere of dry nitrogen. Analytical thin-layer chromatography was performed with Kieselgel F-254 pre-coated TLC plates. Flash column chromatography was carried out with silica gel 60 (230–400 mesh) from EMD Chemicals.

Materials. 6-bromo bipyridine, zinc chloride, bis(triphenylphosphine)palladium(II) dichloride, tetrabutyl ammonium tetrafluoroborate, triethyl amine, silver perchlorate, pyridine, phenothiazine, and propargyl bromide were purchased from Sigma Aldrich. Rhenium pentacarbonyl chloride was obtained from Strem Chemicals.

NMR spectroscopy. NMR spectra were recorded on a INOVA 600 MHz spectrometer equipped with an inverse HCN triple resonance probe with x-, y-, and z-gradients. All spectrometers were running Varian VNMRJ software. Chemical

shifts are expressed in parts per million using residual solvent protons as the internal standard (5.32 ppm for CH₂Cl₂). Coupling constants, J , are reported in Hertz (Hz), and splitting patterns are designated as s (singlet), d (doublet), t (triplet), q (quartet), m (multiplet), and br (broad). MestReNova NMR 5.3.2 software was used to analyze all NMR spectra.

Mass spectrometry. Mass spectra were obtained through the Mass Spectrometry Facility, Department of Chemistry, California Institute of Technology. Fast atom bombardment (FAB) mass spectra were recorded using a Jeol JMS600H high resolution double-focusing mass spectrometer. Electrospray Ionization (ESI) mass spectra were obtained using a Waters Premier Xe time-of-flight mass spectrometer.

Visible spectroscopy. Spectroscopic measurements, including UV-vis, steady-state, and time-resolved luminescence, were carried out at the Beckman Institute Laser Resource Center (BILRC). Prior to any experiments, samples were degassed by three freeze-pump-thaw cycles, unless otherwise noted.

UV-vis spectroscopy. UV-vis absorbance spectra were recorded on an Agilent 8453 UV-vis spectrometer using a pure sample of the solvent as the background.

Steady-state fluorescence spectroscopy. Steady-state emission spectra were recorded on a Jobin Yvon Spex Fluorolog-3-11. A 450W xenon arc lamp was used as the excitation source with a single monochromator providing wavelength selection. Right-angle light emission was sorted using a single monochromator and fed into a Hamamatsu R928P photomultiplier tube with photon counting. Short- and long-pass filters were used where appropriate. Spectra were recorded on Datamax software and plotted with Origin software.

Time-resolved spectroscopy. For experiments focusing on the microsecond timescale, samples were excited at 355 nm with 8 ns pulses from the third harmonic of a Q-switched Nd:YAG laser (Spectra-Physics Quanta-Ray PRO-Series) operating at 10 Hz.

Emission wavelengths were selected using a double monochromator (Instruments SA DH-10) with 1 mm slits. Luminescence was detected with a photomultiplier tube (PMT, Hamamatsu R928). The PMT current was amplified and recorded with a transient digitizer (Tektronix DSA 602). Short- and long-pass filters were employed to remove scattered excitation light. Decay traces were averaged over 500 laser pulses.

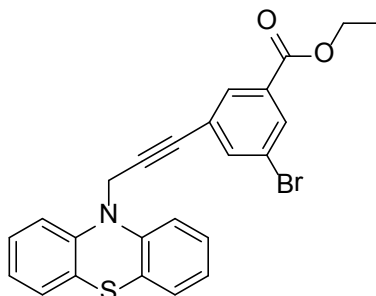
Instruments and electronics in this system were controlled by software written in LabVIEW (National Instruments). Data manipulation was performed and plotted using MATLAB R2008a (Mathworks, Inc.), as well as Microsoft Excel.

For experiments focusing on the nanosecond timescale, samples were excited with 1 ps pulses at 355 nm from the third harmonic of a regeneratively amplified mode-locked Nd:YAG laser operating at 10 Hz. Emission at 560 nm was collected on a picosecond streak camera (Hamamatsu C5680 in photon-counting mode) with a 500 nm long-pass filter to exclude scattered light. The measurements were made under magic-angle conditions and data were collected over a 50 ns sweep range with 8,000 exposures.

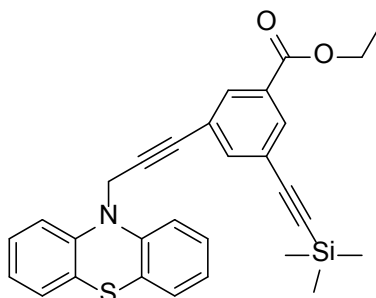
Synthesis and characterization of compounds

Synthesis of 10-(prop-2-yn-1-yl)-10H-phenothiazine (1). 10-(prop-2-yn-1-yl)-10H-phenothiazine was prepared according to literature procedure.⁵⁵

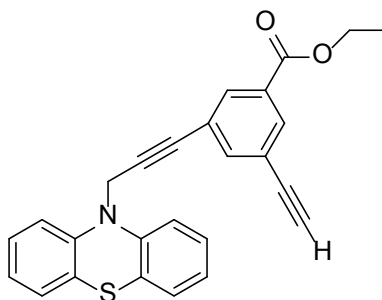
Synthesis of ethyl 3-bromo-5-iodobenzoate (2). Ethyl 3-bromo-5-iodobenzoate was synthesized according to literature procedure.⁵⁶



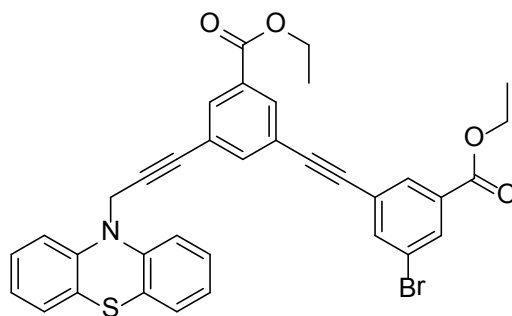
Synthesis of ethyl 3-(3-(10H-phenothiazin-10-yl)prop-1-yn-1-yl)-5-bromobenzoate (3). A microwave flask was charged with **2** (1.55 g, 4.3 mmol), **1** (1.16 g, 4.89 mmol), bis(triphenylphosphine)palladium(II) dichloride (0.102 mg, 0.14 mmol), and zinc chloride (1.108 g, 8.1 mmol), and transferred to the glovebox. Degassed triethylamine (4.86 mL) and tetrahydrofuran (24.36 mL) were added to the mixture in a glovebox and the flask was sealed. The mixture was stirred at 100 °C in the microwave for 2 hours. Purification with flash chromatography using hexane/ethyl acetate (9:0.5) afforded 0.89 g product (Yield: 35%). ¹H NMR (600 MHz, CD₂Cl₂) δ 8.12 (t, *J* = 1.7, 1H), 8.02 (t, *J* = 1.5, 1H), 7.76 (t, *J* = 1.7, 1H), 7.28–7.20 (m, 4H), 7.14 (dd, *J* = 7.6, 1.4, 2H), 6.97 (td, *J* = 7.5, 1.3, 2H), 4.77 (s, 2H), 4.35 (q, *J* = 7.1, 2H), 1.37 (t, *J* = 7.1, 3H). ¹³C NMR (151 MHz, CD₂Cl₂) δ 165.10, 144.89, 138.96, 133.37, 133.19, 132.06, 128.33, 127.76, 125.46, 124.09, 123.75, 122.86, 115.60, 87.81, 84.33, 62.48, 39.85, 14.84. HRMS-ES (*m/z*) [*M*⁺] measured 465.0228, calculated: 465.0221.



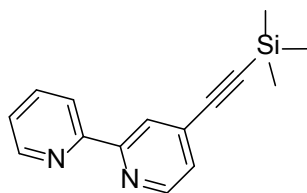
Synthesis of ethyl 3-(3-(10H-phenothiazin-10-yl)prop-1-yn-1-yl)-5-(trimethylsilyl)ethynylbenzoate. A microwave flask was charged with **3** (1.04 g, 2.2 mmol), bis(triphenylphosphine)palladium(II) dichloride (51 mg, 0.072 mmol), and zinc chloride (0.45 g, 3.3 mmol), and transferred to the glovebox. Degassed triethylamine (2.46 mL), degassed trimethylsilylacetylene (0.35 mL, 2.46 mmol), and tetrahydrofuran (11 mL) were added to the mixture in the glovebox and the flask was sealed. The mixture was stirred at 100 °C in the microwave for 2 hours. Purification with flash chromatography using hexane/ethyl acetate (9:0.5) afforded 0.78 g product (Yield: 73%). ¹H NMR (600 MHz, CD₂Cl₂) δ 8.04 (t, *J* = 1.6, 1H), 8.02 (t, *J* = 1.6, 1H), 7.68 (t, *J* = 1.6, 1H), 7.30–7.20 (m, 4H), 7.14 (dd, *J* = 7.6, 1.5, 2H), 6.98 (td, *J* = 7.4, 1.2, 2H), 4.76 (s, 2H), 4.35 (q, *J* = 7.1, 2H), 1.37 (t, *J* = 7.1, 3H), 0.24 (s, 9H). ¹³C NMR (151 MHz, CD₂Cl₂) δ 165.64, 144.94, 139.29, 133.38, 133.10, 132.09, 128.34, 127.75, 124.76, 124.12, 124.04, 123.73, 115.64, 103.61, 87.04, 84.95, 62.27, 47.14, 39.92, 14.90, 0.34. HRMS-ES (*m/z*) [*M*⁺] measured 481.15, calculated: 481.15.



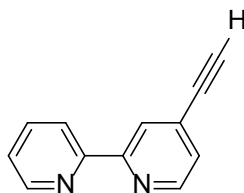
Synthesis of ethyl 3-(3-(10H-phenothiazin-10-yl)prop-1-yn-1-yl)-5-ethynylbenzoate (4). Ethyl 3-(3-(10H-phenothiazin-10-yl)prop-1-yn-1-yl)-5-trimethylsilyl-ethynylbenzoate (0.25 g, 0.53 mmol) was reacted with potassium carbonate (6.25 mg, 0.045 mmol) in a mixture of dichloromethane (1.25 mL) and methanol (3.12 mL). The reaction was allowed to react until the starting material was completely consumed. The reaction was monitored *via* thin layer chromatography. Purification with flash chromatography using hexane/ethyl acetate (9:0.5) afforded 93.3 mg product (Yield: 43%). ^1H NMR (600 MHz, CD_2Cl_2) δ 8.00 (t, $J = 1.6$, 1H), 7.97 (t, $J = 1.6$, 1H), 7.63 (t, $J = 1.7$, 1H), 7.31–7.08 (m, 6H), 6.96 (td, $J = 7.5$, 1.2, 2H), 4.68 (s, 2H), 4.35 (q, $J = 7.1$, 2H), 3.20 (s, 1H), 1.37 (t, $J = 7.1$, 3H). ^{13}C NMR (151 MHz, CD_2Cl_2) δ 165.42, 144.80, 139.41, 133.46, 133.34, 132.03, 128.19, 127.61, 123.99, 123.95, 123.59, 123.51, 115.50, 87.05, 84.65, 82.23, 79.42, 62.19, 39.77, 14.71. HRMS-ES (m/z) [M^+] measured 409.11, calculated: 409.11.



Synthesis of ethyl 3-(3-(10H-phenothiazin-10-yl)prop-1-yn-1-yl)-5-((3-bromo-5-(ethoxycarbonyl)phenyl)ethynyl)benzoate (5). A microwave flask was charged with **2** (0.22 g, 0.62 mmol), **4** (0.26, 0.65 mmol), *bis*(triphenylphosphine)palladium(II) dichloride (1.36 mg, 0.002 mmol), and zinc chloride (0.126 g, 0.93 mmol), and transferred to a glovebox. Degassed triethylamine (0.65 mL) and tetrahydrofuran (3.1 mL) were added to the mixture in the glovebox and the flask was sealed. The mixture was stirred at 100 °C in the microwave for 2 hours. Purification with flash chromatography using hexane/ethyl acetate (18/1) afforded 0.2 g product (Yield: 51%). ¹H NMR (600 MHz, CD₂Cl₂) δ 8.07 (t, *J* = 1.7, 1H), 8.05 (t, *J* = 1.6, 1H), 8.04 (t, *J* = 1.5, 1H), 7.99 (t, *J* = 1.6, 1H), 7.77 (t, *J* = 1.7, 1H), 7.69 (t, *J* = 1.6, 1H), 7.23–7.04 (m, 6H), 6.89 (td, *J* = 7.5, 1.2, 2H), 4.69 (s, 2H), 4.29 (m, 4H), 1.31 (td, *J* = 7.1, 3.2, 6H). ¹³C NMR (151 MHz, CD₂Cl₂) δ 165.38, 164.81, 144.64, 138.73, 138.46, 133.20, 133.08, 133.00, 132.89, 131.98, 131.76, 128.01, 127.42, 125.25, 123.94, 123.77, 123.66, 123.41, 122.67, 115.33, 89.81, 88.71, 86.90, 84.50, 62.19, 62.05, 39.62, 14.51, 14.50. HRMS-ES (*m/z*) [*M*⁺] measured: 637.0718, calculated 637.0745, error: 4.3 ppm.

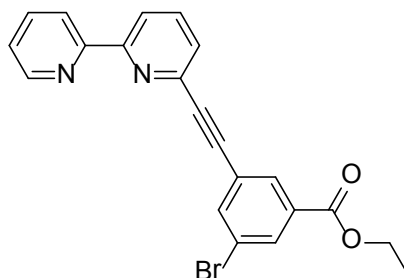


Synthesis of 6-((trimethylsilyl)ethynyl)-2,2'-bipyridine (7). A microwave flask was charged with 6-bromo-2,2'-bipyridine (0.375 g, 1.59 mmol), bis(triphenylphosphine)-palladium(II) dichloride (66 mg, 0.094 mmol), and zinc chloride (0.32 g, 2.34 mmol), and transferred to a glovebox. Degassed triethylamine (3.18 mL), degassed trimethylsilylacetylene (0.45 mL, 3.18 mmol), and tetrahydrofuran (7.95 mL) were added to the mixture in the glovebox and the flask was sealed. The mixture was stirred at 100 °C in the microwave for 3 hours. Purification with flash chromatography using CH₂Cl₂/MeOH (99/1) afforded 0.32 g product (Yield: 79%). ¹H NMR (600 MHz, CD₂Cl₂) δ 8.35 (ddd, *J* = 4.8, 1.8, 0.9, 1H), 8.12 (dt, *J* = 8.0, 1.1, 1H), 8.08 (dd, *J* = 8.0, 1.1, 1H), 7.53 (ddd, *J* = 8.0, 7.5, 1.8, 1H), 7.48 (t, *J* = 7.8, 1H), 7.17 (dd, *J* = 7.7, 1.0, 1H), 7.03 (ddd, *J* = 7.5, 4.8, 1.2, 1H), 0.00 (s, 9H). ¹³C NMR (151 MHz, CD₂Cl₂) δ 156.85, 155.89, 149.76, 142.87, 137.64, 137.48, 128.01, 124.25, 121.60, 121.04, 104.55, 45.62, 0.00. HRMS-ES (*m/z*) [*M*+*H*] observed 252.1160, calculated 253.1161, error 0.4.



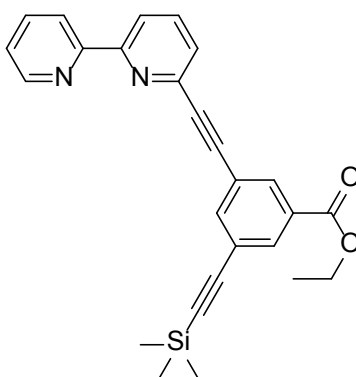
Synthesis of 6-ethynyl-2,2'-bipyridine (8). To a solution of **7** (0.1 g, 0.40 mmol) in tetrahydrofuran (3.5 mL) was added a solution of tetrabutylammonium fluoride

in tetrahydrofuran (0.43 mL, 1.0 M). The solution was allowed to react for 5 min then was concentrated *in vacuo*. The crude product was purified by silica gel column chromatography (CH₂Cl₂/MeOH, 99/1) to give 70 mg product (Yield: 97%). ¹H NMR (600 MHz, CD₂Cl₂) δ 8.67 (ddd, *J* = 4.7, 1.7, 0.9, 1H), 8.46–8.43 (m, 2H), 7.87–7.78 (m, 2H), 7.52 (dd, *J* = 7.6, 1.0, 1H), 7.34 (ddd, *J* = 7.5, 4.8, 1.2, 1H), 3.26 (s, 1H). ¹³C NMR (151 MHz, CD₂Cl₂) δ 157.30, 155.95, 149.94, 142.28, 137.94, 137.68, 128.29, 124.88, 121.78, 121.59, 83.74, 77.25. HRMS-ES (*m/z*) [M⁺] M+H measured 181.0772, calculated 181.0766, error: 3.5.



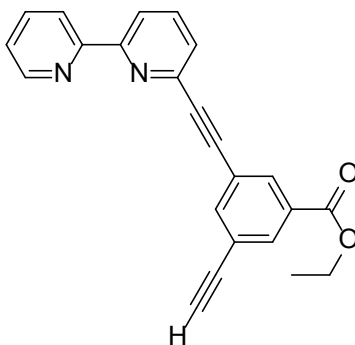
Synthesis of ethyl 3-(2,2'-bipyridin-6-ylethynyl)-5-bromobenzoate (9). A microwave flask was charged with **2** (0.114 g, 0.32 mmol), **8** (0.07 g, 0.39 mmol), *bis*(triphenylphosphine)-palladium(II) dichloride (8.4 mg, 0.012 mmol), and zinc chloride (66 mg, 0.48 mmol), and transferred to a glovebox. Degassed triethylamine (0.38 mL), and degassed tetrahydrofuran (1.61 mL) were added to the mixture in the glovebox and the flask was sealed. The mixture was stirred at 100 °C in the microwave for 3 hours and then it was concentrated *in vacuo*. The crude product was purified by silica gel column chromatography (dichloromethane/methanol, 99/1) to give 70 mg product (Yield: 54%). ¹H NMR (600 MHz, CD₂Cl₂) δ 8.62–8.57 (m, 1H), 8.43–8.29 (m, 2H), 8.16 (t, *J* = 1.5, 1H),

8.13 – 8.07 (m, 1H), 7.89 (t, $J = 1.7$, 1H), 7.80 – 7.76 (m, 2H), 7.51 (dd, $J = 7.6$, 1.0, 1H), 7.27 (ddd, $J = 7.5$, 4.8, 1.1, 1H), 4.31 (q, $J = 7.1$, 2H), 1.33 (t, $J = 7.1$, 3H). ^{13}C NMR (151 MHz, CD_2Cl_2) δ 165.09, 155.96, 149.98, 139.07, 138.00, 137.70, 135.85, 134.08, 133.55, 132.39, 128.26, 125.41, 125.30, 124.90, 123.00, 121.81, 121.51, 91.42, 87.02, 62.52, 14.81. HRMS-ES (m/z) $[\text{M}+\text{H}]$ measured 409.0358, calculated 409.0275, error: 4.1

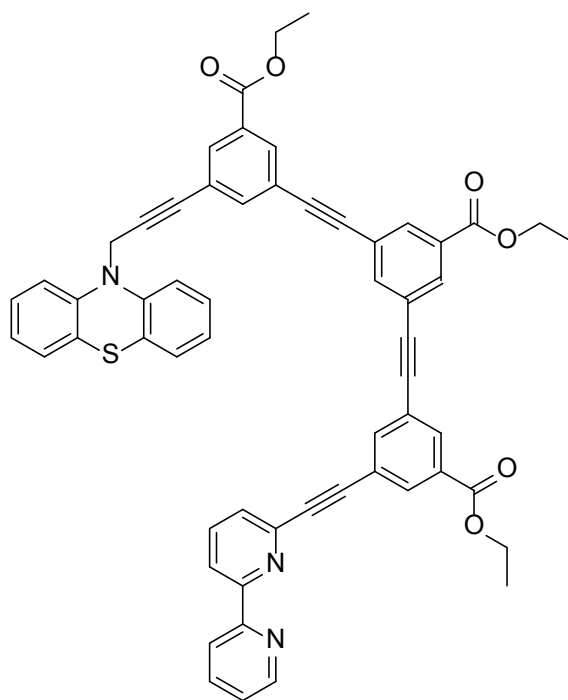


Synthesis of ethyl 3-(2,2'-bipyridin-6-ylethynyl)-5-((trimethylsilyl)ethynyl)benzoate (9a). A microwave flask was charged with **9** (59 mg, 0.144 mmol), *bis*(triphenylphosphine)-palladium(II) dichloride (5.6 mg, 0.0079 mmol), and zinc chloride (30 mg, 0.22 mmol), and transferred to the glovebox. Degassed triethylamine (0.22 mL), degassed trimethylsilylacetylene (30 μL , 0.217 mmol), and degassed tetrahydrofuran (0.72 mL) were added to the mixture in the glovebox and the flask was sealed. The mixture was stirred at 100 $^\circ\text{C}$ in the microwave for 3 hours and then it was concentrated *in vacuo*. The crude product was purified by silica gel column chromatography ($\text{CH}_2\text{Cl}_2/\text{MeOH}$, 99/1) to give 20 mg product (Yield: 33%). ^1H NMR (600 MHz, CD_2Cl_2) δ 8.44–8.38 (m, 1H), 8.27–8.07 (m, 2H), 7.96 (t, $J = 1.6$, 1H), 7.84 (t, $J = 1.6$, 1H), 7.68–7.50 (m,

3H), 7.31 (dd, $J = 7.6, 1.0$, 1H), 7.17–6.98 (m, 1H), 4.11 (q, $J = 7.1$, 2H), 1.13 (t, $J = 7.1$, 3H), 0.00 (s, 9H). HRMS-ES (m/z) [$M+H$] measured 425.1682, calculated 425.1685, error 0.8 ppm.

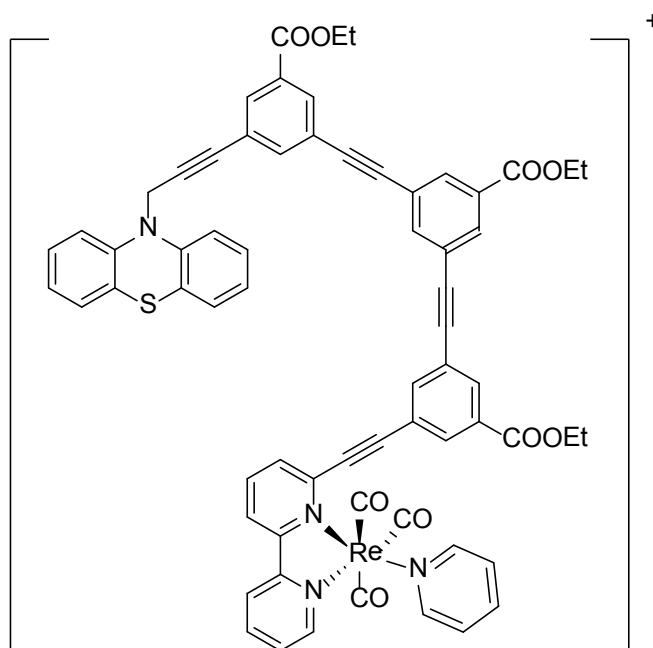


Synthesis of ethyl 3-(2,2'-bipyridin-6-ylethynyl)-5-ethynylbenzoate (10). To a solution of **9a** (0.1 g, 0.23 mmol) in tetrahydrofuran (2.12 mL) was added a solution of tetrabutylammonium fluoride in tetrahydrofuran (0.26 mL, 1.0 M). The solution was allowed to react for 5 min then was concentrated *in vacuo*. The crude product was purified by silica gel column chromatography (CH₂Cl₂/MeOH, 99/1) to give 0.78 g product (Yield: 96%). ¹H NMR (600 MHz, CD₂Cl₂) δ 8.69 (ddd, $J = 4.8, 1.8, 0.9$, 1H), 8.48 (dt, $J = 8.0, 1.1$, 1H), 8.47–8.44 (m, 1H), 8.29 (t, $J = 1.6$, 1H), 8.17 (t, $J = 1.6$, 1H), 7.93 (t, $J = 1.6$, 1H), 7.89–7.87 (m, 2H), 7.60 (dd, $J = 7.6, 1.1$, 1H), 7.37 (ddd, $J = 7.5, 4.8, 1.2$, 1H), 4.40 (q, $J = 7.1$, 2H), 3.26 (s, 1H), 1.42 (t, $J = 7.1$, 3H). ¹³C NMR (151 MHz, CD₂Cl₂) δ 164.83, 156.73, 155.35, 149.26, 142.10, 138.92, 137.26, 136.98, 133.24, 133.10, 131.61, 127.53, 124.17, 123.29, 123.12, 121.11, 120.71, 90.28, 86.39, 81.63, 78.92, 61.66, 14.12. HRMS-ES (m/z) [$M+H$] measured 353.1289, calculated 353.1290, error: 0.3 ppm.



Synthesis of ethyl 3-(3-(10H-phenothiazin-10-yl)prop-1-ynyl)-5-((3-((3-(2,2'-bipyridin-6-ylethynyl)-5-(ethoxycarbonyl)phenyl)ethynyl)-5-ethoxycarbonyl)phenyl)ethynyl)-benzoate (11). A microwave flask was charged with **5** (0.116 g, 0.18 mmol), **10** (0.89 g, 0.25 mmol) bis(triphenylphosphine)-palladium(II) dichloride (5.06 mg, 0.0072 mmol), and zinc chloride (36.57 mg, 0.27 mmol), and transferred to the glovebox. Degassed triethylamine (0.26 mL) and degassed tetrahydrofuran (1.8 mL) were added to the mixture in the glovebox and the flask was sealed. The mixture was stirred at 100 °C in the microwave for 3 hours and then it was concentrated *in vacuo*. The crude product was purified by silica gel column chromatography (CH₂Cl₂/MeOH, 99/1) to give 82 mg product

(Yield: 50%). ^1H NMR (600 MHz, CD_2Cl_2) δ 8.69 (ddd, $J = 4.8, 1.8, 0.9$, 1H), 8.49 (dt, $J = 8.0, 1.1$, 1H), 8.46 (dd, $J = 8.0, 1.1$, 1H), 8.29 (t, $J = 1.6$, 1H), 8.23 (t, $J = 1.6$, 1H), 8.21 (t, $J = 1.6$, 1H), 8.19 (t, $J = 1.6$, 1H), 8.17 (t, $J = 1.6$, 1H), 8.08 (t, $J = 1.6$, 1H), 7.99 (t, $J = 1.6$, 1H), 7.90 (t, $J = 1.6$, 1H), 7.89–7.84 (m, 2H), 7.80 (t, $J = 1.6$, 1H), 7.61 (dd, $J = 7.6, 1.1$, 1H), 7.36 (ddd, $J = 7.5, 4.7, 1.2$, 1H), 7.33–6.94 (m, 8H), 4.79 (s, 2H), 4.47–4.35 (m, 6H), 1.57–1.30 (m, 9H). ^{13}C NMR (151 MHz, CD_2Cl_2) δ 164.80, 156.63, 155.41, 149.16, 144.13, 142.02, 138.30, 138.23, 138.02, 137.16, 136.87, 132.85, 132.77, 132.56, 132.54, 132.47, 132.39, 131.60, 131.57, 131.45, 127.51, 127.44, 126.91, 124.06, 123.55, 123.52, 123.51, 123.40, 123.37, 123.30, 123.26, 122.90, 121.01, 120.60, 114.83, 90.23, 88.90, 88.86, 88.84, 88.81, 86.38, 86.36, 84.01, 61.58, 61.57, 61.53, 39.16, 14.04, 14.036, 14.02. HRMS-ES (m/z) $[\text{M}+\text{H}]$ measured 908.2791, calculated 908.2794, error 0.4.



Synthesis of PTZ-bridge-Re (12). **13** (40 mg, 0.044 mmol) was reacted with rhenium pentacarbonyl chloride in toluene (1.78 mL). After refluxing the reaction mixtures overnight under argon, the reaction mixture was concentrated *in vacuo*. The crude product (32 mg, 0.032 mmol) was reacted with silver perchlorate (8.16 mg, 0.0494 mmol) in methanol/toluene (4:1) mixture for 1 day at room temperature in the dark. Pyridine (76 mg, 0.96 mmol) was added to the reaction mixture and the resulting reaction mixture was stirred at 50 °C for 5 days. Excess pyridine was removed *in vacuo*. The crude product was purified by silica gel column chromatography (CH₂Cl₂/MeOH, 95/5) to give 20 mg product (Yield: 36%). ¹H NMR (600 MHz, CD₂Cl₂) δ 9.16 (dd, *J* = 5.5, 0.8, 1H), 8.46 (d, *J* = 8.3, 1H), 8.42 (dd, *J* = 8.3, 1.1, 1H), 8.30–8.27 (m, 1H), 8.27–8.19 (m, 3H), 8.14 (t, *J* = 1.6, 1H), 8.12–8.09 (m, *J* = 3H), 8.08 (t, *J* = 1.6, 1H), 8.02 (dd, *J* = 7.9, 1.2, 1H), 8.00–7.97 (m, 2H), 7.83 (t, *J* = 1.6, 1H), 7.81–7.69 (m, 3H), 7.31–7.24 (m, 2H), 7.24–6.85 (m, 8H), 4.70 (s, 2H), 4.49–4.19 (m, 6H), 1.33 (m, 9H). ¹³C NMR (151 MHz, CD₂Cl₂) δ 165.42, 165.40, 165.11, 156.96, 156.66, 153.43, 152.38, 147.08, 144.74, 142.09, 141.73, 141.03, 140.48, 139.32, 139.07, 138.83, 138.63, 134.93, 133.79, 133.76, 133.60, 133.33, 133.19, 133.12, 133.00, 132.53, 132.25, 132.09, 131.42, 129.51, 128.11, 127.70, 127.52, 126.47, 125.04, 124.58, 124.20, 123.88, 123.51, 123.08, 122.07, 115.44, 100.35, 90.08, 89.49, 89.30, 89.23, 88.95, 86.99, 84.62, 62.44, 62.23, 62.16, 39.73, 14.64, 14.62. HRMS-FAB (*m/z*) [*M*⁺] measured 1257.2554, calculated 1257.2543.

Fitting of the fast component of PTZ-bridge-Re luminescence decay

The data collected over the first 50 ns were used to determine the kinetics of the more-rapid decay component. Single and double exponential fitting are incapable of adequately representing the data, even when an additional 530 ns decay component is added. A three-exponential equation (plus a fixed 530 ns component) models the data well, with lifetimes, $\tau = 10.0 \pm 0.8, 2.7 \pm 0.2, 0.56 \pm 0.02$ ns, and an average lifetime $\langle\tau\rangle = 3.2$ ns.

A stretched-exponential function plus a fixed 530 ns exponential was applied and produced values of $\tau = 1.72, \beta = 0.574, \langle\tau\rangle = 2.7$ ns (Figure S6). These values were relatively unchanged ($\tau = 1.73, \beta = 0.571, \langle\tau\rangle = 2.8$ ns) when the 530 ns term was removed.

$$y = Ae^{-\left(\frac{t}{\tau}\right)^\beta} + Be^{-\left(\frac{t}{5.3 \times 10^{-7}}\right)}$$

$$\langle\tau\rangle = \frac{t}{\beta} \Gamma(\beta^{-1})$$

In light of the observed non-exponential decay of the faster component (discussed above) we also obtained a rate distribution ($P(k)$) from the numerical inversion of the Laplace transform that describes the time-resolved luminescence intensity $I(t) = \sum P(k)\exp(-kt)$. The data was fit using a MATLAB (The Mathworks) algorithm (LSQNONNEG) that minimizes the sum of the squared deviations (χ^2) between the observed and calculated values of $I(t)$, subject to the non-negativity constraint (non-negative least-squares analysis). This produced a $P(k)$ distribution with lifetimes (τ) in the 0.2–6 ns range and an average value of $\tau = 1.9$ ns, in good agreement with the three exponential and stretched-exponential fits.

Computational modeling

Density functional theoretical calculations were conducted using the ORCA computational chemistry package (F. Neese, version 2.8.0), applying the generalized gradient approximation density functional PW91.⁵⁷ Initial geometry optimizations were performed using a 2 ζ -quality SV-ZORA basis set,⁵⁸ which employs the zeroth-order relativistic approximation (ZORA) to the Dirac equation to account for relativistic effects. Additionally, the conductor-like screening model (COSMO)⁵⁹ of a continuum solvent was used, with parameters appropriate for CH₂Cl₂ solvation, and the empirical van der Waals correction of Grimme was applied.^{60,61} The initial geometry solutions were then used as input to run more intensive calculations with a 3 ζ -quality TZV-ZORA basis set. To test the validity of the calculated geometric parameters, numerical frequency calculations were performed. The lack of any negative (imaginary) frequencies appearing in the list of computed frequencies strongly suggests that we found true minima rather than saddle points on the energy surface.

A.6 References

- (1) Dempsey, J. L.; Winkler, J. R.; Gray, H. B. *Chem. Rev.* **2010**, *110*, 7024.
- (2) Siegbahn, P. E. M.; Blomberg, M. R. A. *Chem. Rev.* **2010**, *110*, 7040.
- (3) Lewis, N. S.; Nocera, D. G. *PNAS* **2006**, *103*, 15729.
- (4) Eisenberg, R.; Gray, H. B. *Inorg. Chem.* **2008**, *47*, 1697.
- (5) Gray, H. B. *Nat. Chem.* **2009**, *1*, 7.
- (6) de Silva, A. P.; Gunaratne, H. Q. N.; Gunnlaugsson, T.; Huxley, A. J. M.; McCoy, C. P.; Rademacher, J. T.; Rice, T. E. *Chem. Rev.* **1997**, *97*, 1515.
- (7) Saragi, T. P. I.; Spehr, T.; Siebert, A.; Fuhrmann-Lieker, T.; Salbeck, J. *Chem. Rev.* **2007**, *107*, 1011.
- (8) Wenger, O. S. *Acc. Chem. Res.* **2011**, *44*, 25.

- (9) Kilså, K.; Kajanus, J.; Macpherson, A. N.; Mårtensson, J.; Albinsson, B. *J. Am. Chem. Soc.* **2001**, *123*, 3069.
- (10) Hanss, D.; Wenger, O. S. *Inorg. Chim. Acta* **2009**, *362*, 3415.
- (11) Walther, M. E.; Wenger, O. S. *ChemPhysChem* **2009**, *10*, 1203.
- (12) Hanss, D.; Walther, M. E.; Wenger, O. S. *Coord. Chem. Rev.* **2010**, *254*, 2584.
- (13) Hanss, D.; Wenger, O. S. *Inorg. Chem.* **2008**, *47*, 9081.
- (14) Hanss, D.; Wenger, O. S. *Inorg. Chem.* **2009**, *48*, 671.
- (15) Tominaga, K.; Kilner, D. A. V.; Johnson, A. E.; Levinger, N. E.; Barbara, P. F. *J. Chem. Phys.* **1993**, *98*, 1228.
- (16) Son, D. H.; Kambhampati, P.; Kee, T. W.; Barbara, P. F. *J. Phys. Chem. A* **2002**, *106*, 4591.
- (17) Wasielewski, M. R. V.; Davis, W. B.; Svec, W. A.; Ratner, M. A. *Nature* **1998**, *396*, 60.
- (18) Sikes, H. D.; Smalley, J. F.; Dudek, S. P.; Cook, A. R.; Newton, M. D.; Chidsey, C. E. D.; Feldberg, S. W. *Science* **2001**, *291*, 1519.
- (19) Giacalone, F.; Segura, J. L.; Martin, N.; Guldi, D. M. *J. Am. Chem. Soc.* **2004**, *126*, 5340.
- (20) Goldsmith, R. H.; Sinks, L. E.; Kelley, R. F.; Betzen, L. J.; Liu, W. H.; Weiss, E. A.; Ratner, M. A.; Wasielewski, M. R. *Proc. Natl. Acad. Sci. USA* **2005**, *102*, 3540.
- (21) Atienza-Castellanos, C.; Wielopolski, M.; Guldi, D. M.; van der Pol, C.; Bryce, M. R.; Filippone, S.; Martin, N. *Chem. Commun.* **2007**, 5164.
- (22) Asaoka, S.; Takeda, N.; Lyoda, T.; Cook, A. R.; Miller, J. R. *J. Am. Chem. Soc.* **2008**, *130*, 11912.
- (23) Eng, M. P.; Martensson, J.; Albinsson, B. *Chem. Eur. J.* **2008**, *14*, 2819.
- (24) Creager, S.; Yu, C. J.; Bamdad, C.; O'Connor, S.; MacLean, T.; Lam, E.; Chong, Y.; Olsen, G. T.; Luo, J. Y.; Gozin, M.; Kayyem, J. F. *J. Am. Chem. Soc.* **1999**, *121*, 1059.
- (25) Albinsson, B.; Eng, M. P.; K., P.; Winters, M. U. *Phys. Chem. Chem. Phys.* **2007**, *9*, 5847.
- (26) Wielopolski, M.; Atienza, C.; Clark, T.; Guldi, D. M.; Martin, N. *Chem. Eur. J.* **2008**, *14*, 6379.
- (27) Kilså, K.; Kajanus, J.; Macpherson, A. N.; Mårtensson, J.; Albinsson, B. *J. Am. Chem. Soc.* **2001**, *123*, 3069.
- (28) Pettersson, K.; Wiberg, J.; Ljungdahl, T.; Mårtensson, J.; Albinsson, B. *J. Phys. Chem. A* **2006**, *110*, 319.
- (29) Creager, S.; Yu, C. J.; Bamdad, C.; O'Connor, S.; MacLean, T.; Lam, E.; Chong, Y.; Olsen, G. T.; Luo, J.; Gozin, M.; Kayyem, J. F. *J. Am. Chem. Soc.* **1999**, *121*, 1059.
- (30) Napper, A. M.; Read, I.; Waldeck, D. H. *J. Phys. Chem. A* **2002**, *106*, 4784.
- (31) Nadenau, J. M.; Liu, M.; Waldeck, D. H.; Zimmt, M. B. *J. Am. Chem. Soc.* **2003**, *125*, 15964.
- (32) Cave, R. J.; Newton, M. D. *J. Phys. Chem.* **1995**, *99*, 17501.

- (33) Kumar, K.; Tepper, R. J.; Zeng, Y.; Zimmt, M. B. *J. Org. Chem.* **1995**, *60*, 4051.
- (34) Han, H.; Zimmt, M. B. *J. Am. Chem. Soc.* **1998**, *120*, 8001.
- (35) Chakrabarti, S.; Liu, M.; Waldeck, D. H.; Oliver, A. M.; Paddon-Row, M. N. *J. Phys. Chem. A* **2009**, *113*, 1040.
- (36) Liu, M.; Maroncelli, M.; Waldeck, D. H.; Oliver, A. M.; Paddon-Row, M. N. *J. Am. Chem. Soc.* **2005**, *127*, 17867.
- (37) Liu, M.; Waldeck, D. H.; Oliver, A. M.; Head, N. J.; Paddon-Row, M. N. *J. Am. Chem. Soc.* **2004**, *126*, 10778.
- (38) Chen, P.; Westmoreland, T. D.; Danielson, E.; Schanze, K. S.; Anthon, D., Neveux, P. E.; Meyer, T. J. *Inorg. Chem.* **1987**, *26*, 1116.
- (39) Chen, P.; Deusing, R.; Graff, D. K.; Meyer, T. J. *J. Phys. Chem.* **1991**, *95*, 5850.
- (40) Chen, P.; Mecklenburg, S. L.; Meyer, T. J. *J. Phys. Chem.* **1993**, *97*, 13126.
- (41) Finke, A. D.; Elleby, E. C.; Boyd, M. J.; Weissman, H.; Moore, J. S. *J. Org. Chem.* **2009**, *74*, 8897.
- (42) Tobe, Y.; Utsumi, N.; Kawabata, K.; Nagami, A.; Adachi, K.; Araki, S.; Sonoda, M.; Hirose, K.; Naemura, K. *J. Am. Chem. Soc.* **2002**, *124*, 5350.
- (43) Sae-Lim, C.; Sandman, D. J.; Foxman, B. M.; Sukwattanasinitt, M. *J. Macromol. Sci. A* **2006**, *43*, 1929.
- (44) Cattaneo, M.; Fagalde, F.; Borsarelli, C. D.; Katz, N. E. *Inorg. Chem.* **2009**, *48*, 3012.
- (45) Cattaneo, M.; Fagalde, F.; Katz, N. E. *Inorg. Chem.* **2006**, *45*, 6884.
- (46) Cattaneo, M.; Fagalde, F.; Katz, N. E.; Borsarelli, C. D.; Parella, T. *Eur. J. Inorg. Chem.* **2007**, *34*, 5323.
- (47) Dattelbaum, J. D.; Abugo, O. O.; Lakowicz, J. R. *Bioconjugate Chem.* **2000**, *11*, 533.
- (48) Guo, X.-Q.; Castellano, F. N.; Li, L.; Szmazinski, H.; Lakowicz, J. R.; Sipior, J. *Anal. Biochem.* **1997**, *254*, 179.
- (49) Vlcek, A., Jr. *Top. Organomet. Chem.* **2010**, *29*, 73.
- (50) Kumar, A. S., S.-S.; Lees, A. J. *Top. Organomet. Chem.* **2010**, *29*, 1.
- (51) Avogadro: an open-source molecular builder and visualization tool. Version 1.0.3. <http://avogadro.openmolecules.net/>.
- (52) Sachs, S. B.; Dudek, S. P.; Hsung, R. P.; Sita, L. R.; Smalley, J. F.; Newton, M. D.; Feldberg, S. W.; Chidsey, C. E. D. *J. Am. Chem. Soc.* **1997**, *119*, 10563.
- (53) Read, I.; Napper, A.; Kaplan, R.; Zimmt, M. B.; Waldeck, D. H. *J. Am. Chem. Soc.* **1999**, *121*, 10976.
- (54) Kumar, K.; Kurnikov, I. V.; Beratan, D. N.; Waldeck, D. H.; Zimmt, M. B. *J. Phys. Chem. A* **1998**, *102*, 5529.
- (55) Sae-Lim, C.; Sandman, D. J.; Foxman, B. M.; Sukwattanasinitt, M. *J. Macromol. Sci. A, Pure Appl. Chem.* **2006**, *43*, 1929.
- (56) Tobe, Y.; Utsumi, N.; Kawabata, K.; Nagami, A.; Adachi, K.; Araki, S.; Sonoda, M.; Hirose, K.; Naemura, K. *J. Am. Chem. Soc.* **2002**, *124*, 5350.
- (57) Perdew, J. P.; Burke, K.; Wang, Y. *Phys. Rev. B* **1996**, *54*, 16533.

- (58) Pantazis, D. A.; Chen, X. Y.; Landis, C. R.; Neese, F. *J. Chem. Theory Comput.* **2008**, *4*, 908.
- (59) Sinnecker, S.; Rajendran, A.; Klamt, A.; Diedenhofen, M.; Neese, F. *J. Phys. Chem. A* **2006**, *110*, 2235.
- (60) Grimme, S. *J. Comput. Chem.* **2004**, *25*, 1463.
- (61) Grimme, S. *J. Comput. Chem.* **2006**, *27*, 1787.

Appendix B:

Photophysics of Ir(III) corroles

The text in this chapter was taken in part from:

Palmer, J. H.; Durrell, A. C.; Gross, Z.; Winkler, J. R.; Gray, H. B. *J. Am. Chem. Soc.* **2010**, *132*, 9230–9231.

B.1 Abstract

My interest in corroles began following Joshua Palmer's synthesis of Ir(III) corroles. He had been interested in exploring their luminescence properties, and I had trained him on the fluorometer. Following his initial round of experiments, he presented data showing luminescence in the near-IR, at the far end of our instrument's detector limit. I immediately dismissed this evidence as nothing more than an instrument artifact. Fortunately, Josh persisted, and as the evidence accumulated, it became evident that something was there. After purchasing a detector with sensitivity deeper in the near-IR, we were able to more fully characterize the photophysical properties of Ir(III) corroles. The results of our initial collaboration resulted in the publication of our work "Near-IR Phosphorescence of Ir(III) Corroles at Ambient Temperature" in the *Journal of the American Chemical Society*. This work is presented here.

The photophysical properties of Ir(III) corroles differ from those of phosphorescent porphyrin complexes, cyclometalated and polyimine Ir(III) compounds, and other luminescent metallocorroles. Ir(III) corrole phosphorescence is observed at ambient temperature at wavelengths much longer (> 800 nm) than those of most Ir(III) phosphors. The solvatochromic behavior of Ir(III)-corrole Soret and Q absorption bands suggests that the lowest singlet excited states (S_2 and S_1) are substantially more polar than the ground state.

B.2 Introduction

Porphyrin complexes displaying phosphorescence at ambient temperatures have been employed for photodynamic therapy,¹ oxygen detection,² and organic light-emitting diodes.³ A great deal of research has been done on d⁸ (mainly Pt^{II}, Pd^{II}, and Au^{III}) complexes,⁴ which emit at relatively long wavelengths (> 600 nm) with lifetimes in the microsecond range. In sharp contrast, d⁶ metalloporphyrins have scarcely been investigated, although room-temperature phosphorescence of ruthenium(II) porphyrins has been reported.⁵

Metalloporphyrins have shown promise as therapeutic agents,⁶ with biodistribution and bioavailability profiles as well as cellular uptake and intracellular locations⁷ determined for fluorescent gallium(III) derivatives.⁸ Although progress has been made, much work remains before we can claim to have developed optimized compounds for optical examination of biological systems.⁹ It would be beneficial to have agents that emit with microsecond lifetimes beyond 700 nm, as the most common obstacles to efficient biological imaging—tissue absorbance and intrinsic fluorescence—could thus be circumvented.

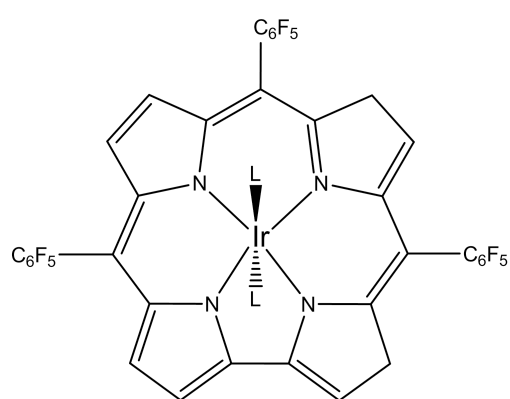
Here we report the photophysical properties of iridium(III) porphyrins,¹⁰ which differ significantly from those of cyclometalated and polyimine Ir(III) compounds,¹¹ other luminescent metalloporphyrins,¹² and free-base porphyrins.¹³ Iridium(III) porphyrin phosphorescence is observed at ambient temperature at wavelengths much longer (> 800 nm) than those of most other luminescent Ir(III)

complexes.¹¹ Our investigations focused on the three corroles shown in Figure B.1. Their absorption spectra are shown in Figure B.2.

B.3. Results and discussion.

Emission spectra were recorded in toluene at 298 and 77 K (Figure B.3). The spectra display two intense features separated by approximately 1400 cm^{-1} . It is likely that a ring-based vibration is excited in the transition to the lower energy component.¹⁴ Excitation spectra conducted at the low- and high-energy bands are identical (Figure B.4). At low temperature, the higher energy emission maximum of each Ir(III) corrole blue shifts by 10 nm (a rigidochromic effect indicating that the transition involves charge transfer)¹⁵ (Figure B.3b). The narrow linewidth and $\sim 1400\text{ cm}^{-1}$ spacing suggest that the emission is from a $\pi \rightarrow \pi^*$ excited state. Electronic structure calculations place an occupied orbital with metal character close to the HOMO in related Ir(III) corroles,¹⁶ indicating that $^3\text{MLCT}$ states will be near those of the lowest corrole-localized excited states. Other investigators have reported that $^3\text{MLCT}$ is the emissive state in cyclometalated Ir(III) complexes.¹⁷

Luminescence quantum yields and lifetimes in degassed and aerated toluene solutions at room temperature (and lifetimes at 77 K) are set out in Table B.1. **1-Ir(tma)₂** and **1b-Ir(tma)₂** have relatively short lifetimes and low quantum yields. **1-Ir(py)₂** exhibits a much higher luminescence quantum yield (1.2%) and a longer lifetime.¹⁸ It is apparent even from these initial results that Ir(III)-corrole photophysical properties depend markedly on the nature of the axial ligand.



1-Ir(tma)₂: X = H, L = tma
1b-Ir(tma)₂: X = Br, L = tma
1-Ir(py)₂: X = H, L = py

Figure B.8. Iridium(III) corroles

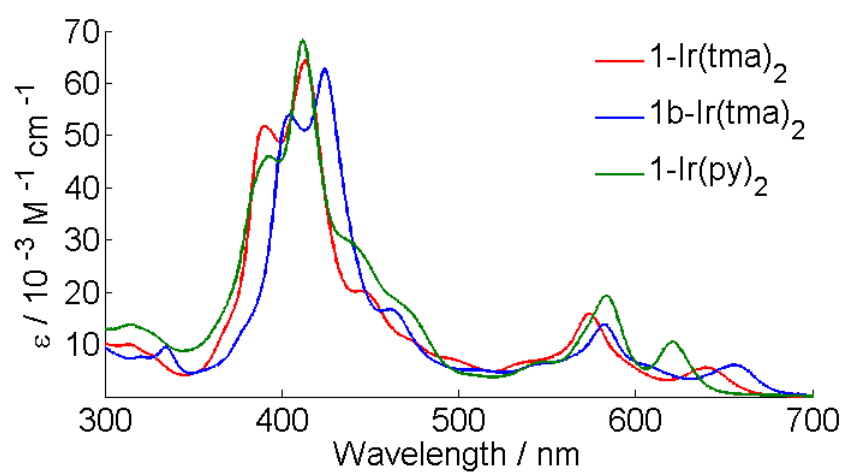


Figure B.2. UV-vis spectra of Ir(III) corroles in toluene solution at 298 K

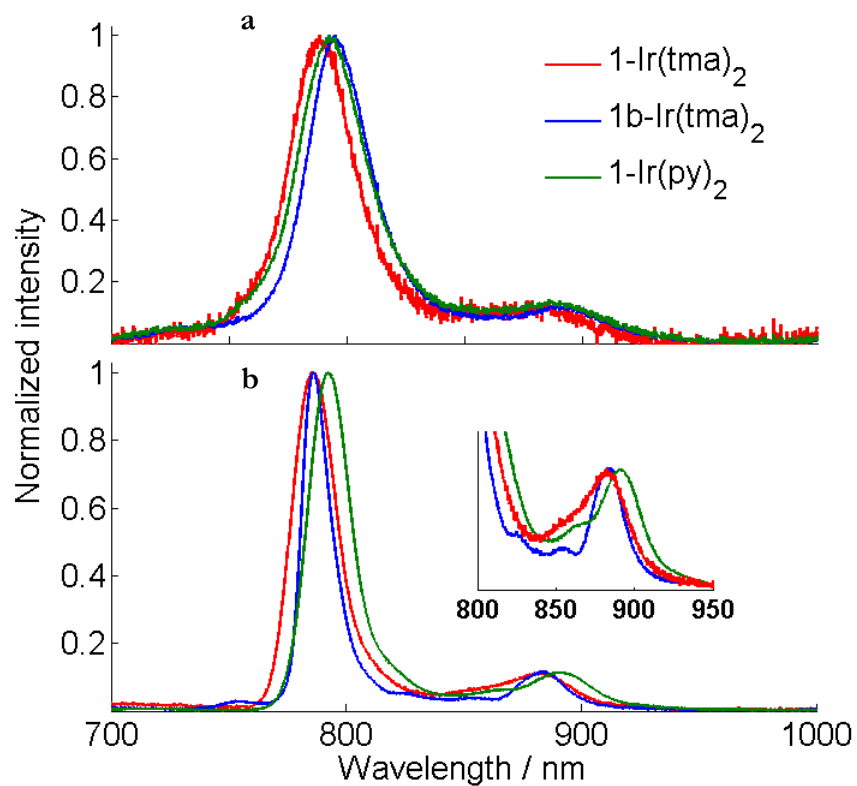


Figure B.3. Emission spectra of Ir(III) corroles in toluene solution ($\lambda_{\text{ex}} = 496.5$ nm) (a) 298 K; (b) 77 K.

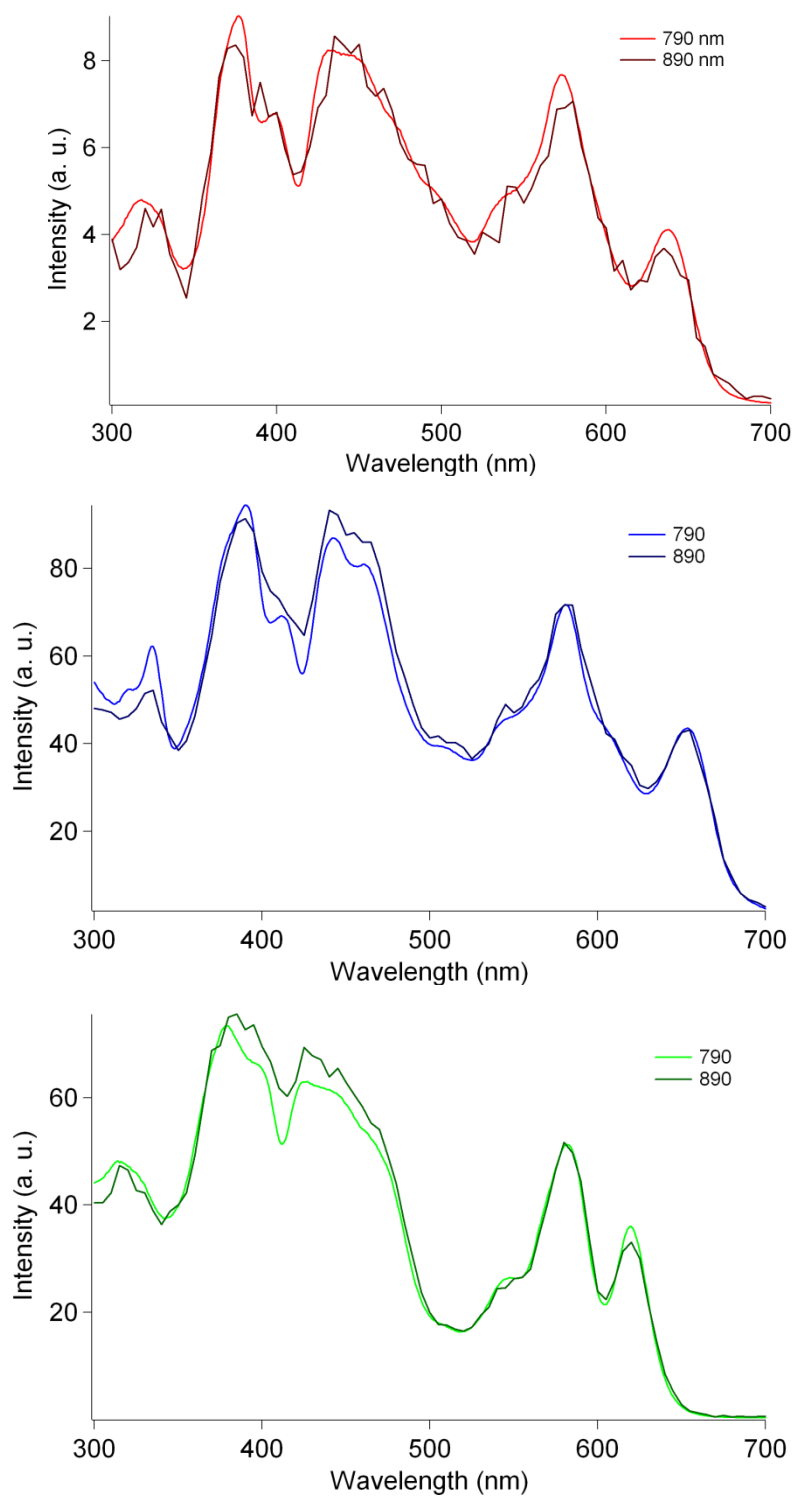


Figure B.4. Normalized excitation profiles of (top to bottom): **1-Ir(tma)₂**, **1b-Ir(tma)₂**, and **1-Ir(py)₂** monitored at emission wavelengths of 790 and 890 nm

Table B.1. Photophysical data for Ir(III) corroles in toluene solution^a

<i>Compound</i>	<i>1-Ir(tma)₂</i>	<i>1b-Ir(tma)₂</i>	<i>1-Ir(py)₂</i>
Φ_{ph}	3.3×10^{-4}	3.9×10^{-3}	1.2×10^{-2}
$\lambda_{\text{Ar}} / \text{nm}$ ($\tau_{\text{Ar}} / \mu\text{s}$)	788 (0.220)	795 (1.19)	792 (4.91)
$\lambda_{77\text{K}} / \text{nm}$ ($\tau_{77\text{K}} / \mu\text{s}$)	786 (2.77)	786 (4.72)	793 (7.69)
$\tau_{\text{air}} / \mu\text{s}$	0.170	0.760	0.380
$k_{\text{r}} / \text{s}^{-1}$	1.5×10^3	3.28×10^3	2.44×10^3
$k_{\text{nr}} / \text{s}^{-1}$	4.54×10^6	8.4×10^5	2.0×10^5

^aAt 298 K unless noted otherwise

The effect of solvent polarizability on Ir(III)–corrole spectra was investigated to probe the extent of charge transfer in initially formed electronic excited states. UV-vis spectra were obtained in a variety of solvents: band maxima were plotted against polarizability f (Figure B.5), defined as $f(n) = (n^2 - 1)/(2n^2 + 1)$,¹⁹ where n is the refractive index of the solvent. (The ground states are relatively nonpolar, so inclusion of a solvent dielectric term is not appropriate.) The strong negative correlation ($R^2 > 0.9$) between the polarizability of the solvent and the energy of the Soret transition indicates that in each case the excited state is substantially more polar than the ground state.²⁰ The Q band maxima display a similar trend (Figure B.6, Table B.2). The striking solvatochromic behavior of Ir(III) corroles potentially could be exploited in optical sensors as well as other applications requiring solvent-based tuning of absorption and emission properties.

Although the Soret solvatochromic shifts of **1-Ir(tma)₂** and **1-Ir(py)₂** are similar, **1b-Ir(tma)₂** exhibits a somewhat weaker trend, which we suggest is attributable to bromine atom “prepolarization” of the electron density on the corrole, thereby decreasing the change in dipole moment upon excitation. But we cannot rule out a simpler explanation, namely, that the initially formed **1b-Ir(tma)₂** excited state is not as polar as those of the other corroles.

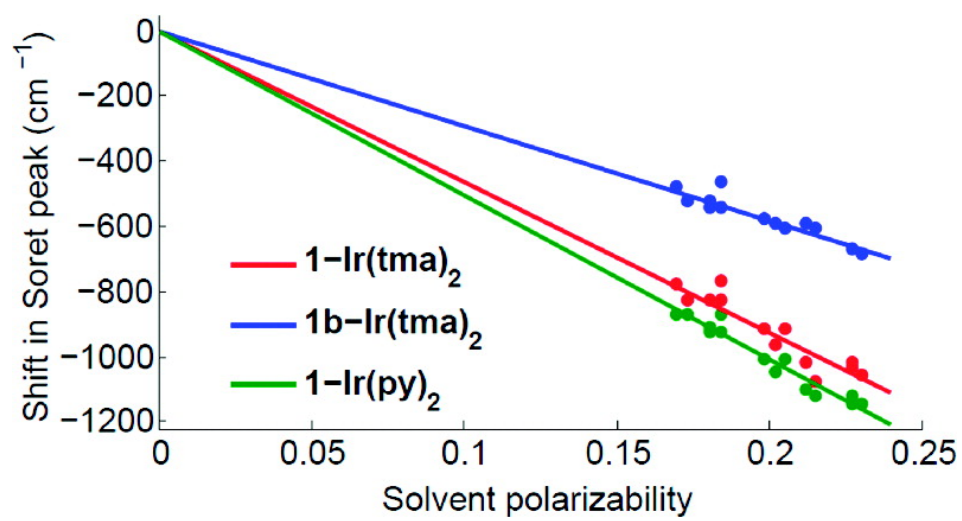


Figure B.5. Spectral shifts of the absorption maxima as a function of solvent polarizability for second Soret band in various solvents

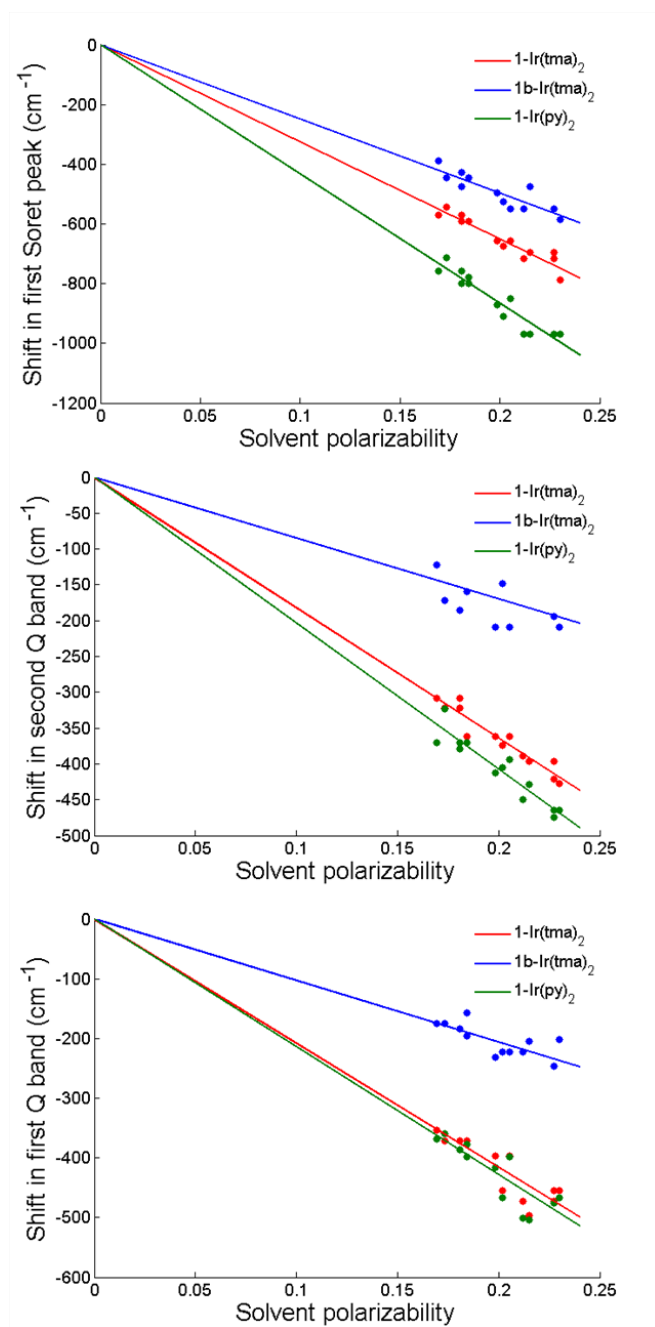


Figure B.6. Spectral shifts of the absorption maxima as a function of solvent polarizability for first Soret band and each Q band in various solvents

Table B.2. Slopes and fitting values for solvatochromic effects on each absorption band in the iridium(III) corroles. The correlation values for the Q bands of **1b-Ir(tma)₂** are probably poor due to the low intensities of those bands at the concentrations examined.

Compound	Band	Slope of shift (f/cm ⁻¹)	Correlation (R ²)
1-Ir(tma)₂	First Soret	-3200	0.90
	Second Soret	-4600	0.90
	First Q band	-2100	0.77
	Second Q band	-1800	0.91
1b-Ir(tma)₂	First Soret	-2500	0.78
	Second Soret	-2900	0.95
	First Q band	-1000	0.60
	Second Q band	-850	0.25
1-Ir(py)₂	First Soret	-4300	0.90
	Second Soret	-5000	0.94
	First Q band	-2100	0.75
	Second Q band	-2000	0.89

B.4 Concluding remarks

Our work has established that Ir(III) corroles phosphoresce in the near-infrared region at ambient temperatures with lifetimes and quantum yields that depend strongly on the nature of the axial ligands. We conclude from emission band shapes and vibronic splittings taken together with results from electronic structure calculations that the phosphorescence in each case is attributable to a transition from a corrole $\pi \rightarrow \pi^*$ triplet state that likely has some $^3\text{MLCT}$ character.

B.5 Materials and methods

All reagents were purchased from Sigma-Aldrich and were used as received without further purification. All solvents were purchased through the VWR stockroom at Caltech. Solution-state UV-vis absorption spectra were measured using a Cary 50 scanning spectrophotometer with a pulsed xenon lamp as the excitation source. The error in reported wavelength values is at most 0.5 nm. Extinction coefficients were measured for gravimetrically prepared solutions of iridium corroles in toluene, and should be accurate to $\pm 10\%$.

Steady-state and time-resolved emission measurements were conducted at the Beckman Institute Laser Resource Center. Emission spectra were recorded on samples dissolved in solution (room temperature) or frozen glass (77 K). Samples were degassed by three freeze-pump-thaw cycles. For steady-state emission spectra, the 496.5 nm line of an argon ion laser (Coherent Inova 70) was used to excite samples. Right-angle emission was collected via with a Melles Griot Fiber Optic Spectrometer (MGSPEC-2048-SPU). Quantum yields were obtained by

comparing signal intensity to a tetraphenylporphyrin standard. Absorption values for the samples at 496.5 nm were recorded on a Hewlett-Packard 8451A diode array spectrophotometer.

For time-resolved measurements, samples were excited at 440 nm. Pulses of 8 ns duration from the third harmonic of a Q-switched Nd:YAG laser (Spectra-Physics Quanta-Ray PRO-Series) operating at 10 Hz were used to pump an optical parametric oscillator (OPO, Spectra-Physics Quanta-Ray MOPO-700) to provide laser pulses at 440 nm. Emitted light was detected with a photomultiplier tube (PMT, Hamamatsu R928). PMT current was amplified and recorded using a transient digitizer (Tektronix DSA 602).

Excitation spectra were recorded on a Jobin Yvon Spex Fluorolog-3-11. Sample excitation was achieved via a xenon arc lamp with a monochromator providing wavelength selection. The excitation wavelength was scanned between 300 nm and 700 nm and recorded at 790 nm and 890 nm. Slits of 2 and 10 nm bandpass were used for excitation and emission, respectively. Right-angle light emission was sorted using a monochromator and fed into a Hamamatsu R928P photomultiplier tube with photon counting. Short- and long-pass filters were used where appropriate.

Resonance Raman spectra were recorded using the 488 nm line of an argon ion laser (Coherent Inova 70). Scattered light was sorted by a 0.75 m spectrograph (Spex 750M) and detected with a liquid-nitrogen-cooled CCD (Princeton Instruments).

Synthesis

5,10,15-tris(pentafluorophenyl)corrolatoiridium(III) bis(trimethylamine), 1-Ir(tma)₂.

H₃tpfc (80 mg), [Ir(cod)Cl]₂ (335 mg), and K₂CO₃ (140 mg) were dissolved/suspended in 150 mL of degassed THF, and the mixture was refluxed under argon for 90 min (until the corrole fluorescence was negligible to the eye upon long-wave irradiation with a hand-held lamp). Tma N-oxide (110 mg) was added, and the solution was allowed to slowly cool to room temperature while open to the laboratory atmosphere. Column chromatography of the black solution (silica, 4:1 hexanes:CH₂Cl₂) provided purple crystals of **1-Ir(tma)₂** (30 mg, 27% yield). ¹H NMR (CD₂Cl₂): δ 8.93 (d, 2H), 8.54 (d, 2H), 8.42 (d, 2H), 8.12 (d, 2H), -2.96 (s, 18H). ¹⁹F NMR (CD₂Cl₂): δ -139.1 (m, 6H), -156.2 (m, 3H), -164.3 (m, 6H). MS (ESI): 1105.1 ([M⁺]), 1046.0 ([M⁺-tma]), 986.5 ([M⁺-2tma]). UV-vis (toluene, nm, ε in M⁻¹cm⁻¹ x 10⁻³): 390 (51.9), 413 (64.3), 574 (15.9), 640 (5.64).

2,3,7,8,12,13,17,18-octabromo-5,10,15-

tris(pentafluorophenyl)corrolatoiridium(III) bis(trimethylamine), 1b-Ir(tma)₂.

Complex **1-Ir(tma)₂** (15 mg) and Br₂ (70 μL) were dissolved in 20 mL MeOH and stirred overnight. Column chromatography (silica, 4:1 hexanes:CH₂Cl₂) of the red solution provided green crystals of **1b-Ir(tma)₂** (15 mg, 63% yield). ¹H NMR (CD₂Cl₂): δ -2.59 (s, 18H). ¹⁹F NMR (CD₂Cl₂): δ -138.4 (q, 2H), -139.0 (q, 4H), -153.9 (t, 3H), -164.4 (m, 4H), -164.7 (m, 2H). UV-vis (toluene, nm, ε in M⁻¹cm⁻¹ x 10⁻³): 404 (54.0), 424 (62.8), 582 (13.9), 656 (6.15).

5,10,15-tris(pentafluorophenylcorrolato)iridium(III) bis-pyridine, 1-Ir(py)₂.

H₃tpfc (40 mg), [Ir(cod)Cl]₂ (170 mg), and K₂CO₃ (70 mg) were dissolved/suspended in 75 mL of degassed THF, and the mixture was heated at reflux under argon for 90 min. Pyridine (1 mL) was added, and the solution was allowed to slowly cool to room temperature while open to the laboratory atmosphere. Column chromatography of the forest green mixture (silica, 4:1 hexanes:CH₂Cl₂ followed by 3:2 hexanes:CH₂Cl₂) provided a bright green solution, from which thin, green crystals of **1-Ir(py)₂** (26 mg, 50% yield) could be grown by addition of methanol followed by slow evaporation. ¹H NMR (CDCl₃): δ 8.84 (d, 2H, J = 4.5), 8.53 (d, 2H, J = 4.8), 8.32 (d, 2H, J = 4.8), 8.17 (d, 2H, J = 4.5), 6.21 (t, 2H, J = 7.8), 5.19 (t, 4H, J = 7.0), 1.72 (d, 4H, J = 5.1). ¹⁹F NMR (CDCl₃): δ -138.68 (m, 6F), -154.84 (t, 2F, J = 22.2), -155.20 (t, 1F, J = 22.2), -163.28 (m, 4F), -163.65 (m, 2F). MS (ESI): 1144.1 ([M⁺]). UV-vis (toluene, nm, ε x 10⁻³ M⁻¹cm⁻¹): 392 (46.1), 412 (68.3), 584 (19.4), 621 (10.6).

Plotting of solvatochromic effects

The refraction of the sodium D line at 20 °C in a given solvent was taken to represent its refractive index, n_D^{20} , or simply n . The polarizability of a solvent $[f(n)]$ is related to its refractive index *via* the following relationship: $f(n) = (n^2 - 1)/(2n^2 + 1)$. The extent of the solvatochromic effect exhibited by an absorbing species in a given solvent is then determined by the slope of the line $E_f = E_v - (\text{solv})[f(n)]$, where E_f is the absorption energy in the solvent, E_v is the absorption energy in vacuum, and (solv) is a factor related to the magnitude of the change in the dipole moment of the chromophore upon excitation. In this formalism, the y-intercept of the line is equal to the theoretical gas-phase absorption energy of the transition under examination. We have made our solvatochromism plots by setting this value equal to zero and plotting the extent of red-shifting in a variety of solvents. This allows for facile comparison of the three corroles, such that the steepness of the slope scales with the magnitude of the separation between the ground- and excited-state dipole moments. In all cases, the excited state is more polar than the ground state.

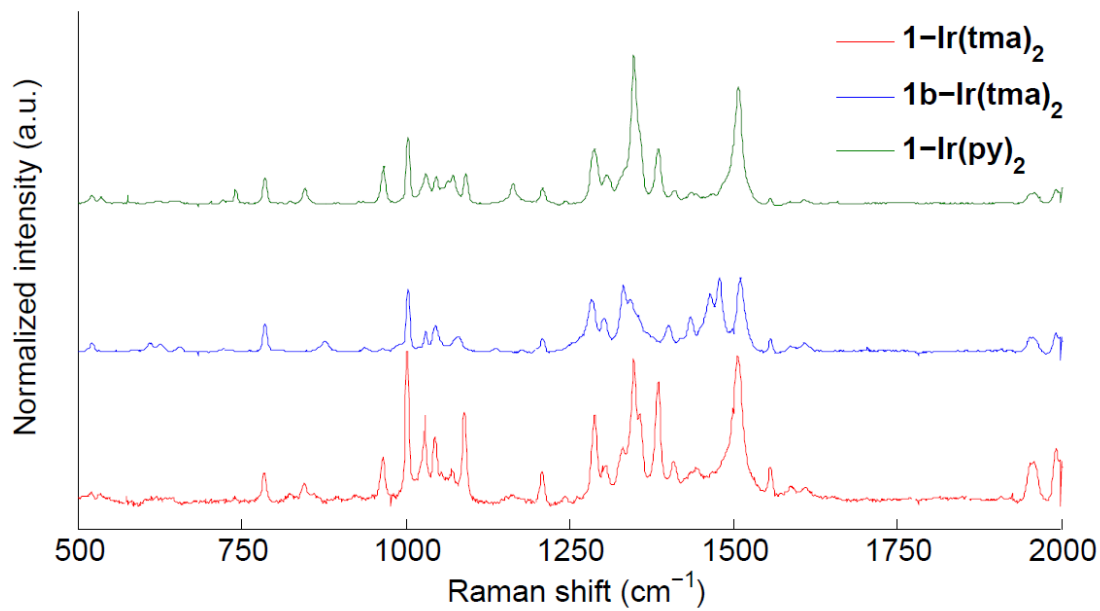


Figure B.7. Raman spectra of **1-Ir(tma)₂**, **1b-Ir(tma)₂**, and **1-Ir(py)₂**. Sample excitation into the Soret was achieved with the 488 nm line of an argon ion laser.

Acknowledgment: This work was supported by the NSF Center for Chemical Innovation (CCI Powering the Planet, Grants CHE-0802907 and CHE-0947829), the US-Israel BSF, CCSER (Gordon and Betty Moore Foundation), and the Arnold and Mabel Beckman Foundation.

B.6 References

- (1) Zenkevich, E.; Sagun, E.; Knyukshto, V.; Shulga, A.; Mironov, A.; Efremova, O.; Bonnett, R.; Phinda Songca, S.; Kassem, M. *J. Photochem. Photobiol. B: Bio.* **1996**, *33*, 171–180.
- (2) Papkovsky, D. B.; Ponomarev, G. V.; Trettnak, W.; O'Leary, P. *Anal. Chem.* **1995**, *67*, 4112–4117.
- (3) (a) Kwong, R. C.; Sibley, S.; Baldo, M. A.; Forrest, S. R.; Thompson, M. E. *Chem. Mater.* **1999**, *11*, 3709–3713. (b) Antipas, A.; Dolphin, D.; Gouterman, M.; Johnson, E. C. *J. Am. Chem. Soc.* **1978**, *100*, 7705–7709.
- (4) (a) Sun, Y.; Borek, C.; Hanson, K.; Djurovich, P. I.; Thompson, M. E.; Brooks, J.; Brown, J. J.; Forrest, S. R. *App. Phys. Lett.* **2007**, *90*, 213503/1–213503/3. (b) Wiehe, A.; Stollberg, H.; Runge, S.; Paul, A.; Senge, M. O.; Roder, B. *J. Porph. Phthal.* **2001**, *5*, 853–860.
- (5) Tait, C. D.; Holten, D.; Barley, M. H.; Dolphin, D.; James, B. R. *J. Am. Chem. Soc.* **1985**, *107*, 1930–1934, and references therein.
- (6) (a) Okun, Z.; Kupershmidt, L.; Amit, T.; Mandel, S.; Bar-Am, O.; Youdim, M. B. H.; Gross, Z. *ACS Chem. Biol.* **2009**, *4*, 910–914. (b) Agadjanian, H.; Ma, J.; Rentsendorj, A.; Valluripalli, V.; Hwang, J. Y.; Mahammed, A.; Farkas, D. L.; Gray, H. B.; Gross, Z.; Medina-Kauwe, L. K. *Proc. Nat. Acad. Sci.* **2009**, *106*, 6100–6105.
- (7) Agadjanian, H.; Weaver, J. J.; Mahammed, A.; Rentsendorj, A.; Bass, S.; Kim, J.; Domchowski, I. J.; Margalit, R.; Gray, H. B.; Gross, Z.; Medina-Kauwe, L. K. *Pharmaceutical Res.* **2006**, *23*, 367–377.
- (8) Weaver, J. J.; Sorasaene, K.; Sheikh, M.; Goldschmidt, R.; Tkachenko, E.; Gross, Z.; Gray, H. B. *J. Porph. Phthal.* **2004**, *8*, 76–81.
- (9) Hwang, J. Y.; Agadjanian, H.; Medina-Kauwe, L. K.; Gross, Z.; Gray, H. B.; Sorasaene, K.; Farkas, D. L. *SPIE* **2008**, *6859*, 68590G.
- (10) (a) Palmer, J. H.; Day, M. W.; Wilson, A. D.; Henling, L. M.; Gross, Z.; Gray, H. B. *J. Am. Chem. Soc.* **2008**, *130*, 7786–7787. (b) Palmer, J. H.; Mahammed, A.; Lancaster, K. M.; Gross, Z.; Gray, H. B. *Inorg. Chem.* **2009**, *48*, 9308–9315.

- (11) (a) Dixon, I. M.; Collin, J.-P.; Sauvage, J.-P.; Flamigni, L.; Encinas, S.; Barigelletti, F. *Chem. Soc. Rev.* **2000**, *29*, 385–391. (b) Tsuboyama, A.; Iwawaki, H.; Furugori, M.; Mukaide, T.; Kamatani, J.; Igawa, S.; Moriyama, T.; Miura, S.; Takiguchi, T.; Okada, S.; Hoshino, M.; Ueno, K. *J. Am. Chem. Soc.* **2003**, *125*, 12971–12979. (c) Hung, J.-Y.; Chi, Y.; Pai, I.-H.; Yu, Y.-C.; Lee, G.-H.; Chou, P.-T.; Wong, K.-T.; Chen, C.-C.; Wu, C.-C. *Dalton Trans.* **2009**, *33*, 6472–6475. (d) Shin, C. H.; Huh, J. O.; Lee, M. H.; Do, Y. *Dalton Trans.* **2009**, *33*, 6476–6479.
- (12) (a) Flamigni, L.; Gryko, D. T. *Chem. Soc. Rev.* **2009**, *38*, 1635–1646. (b) Nardis, S.; Mandoj, F.; Paolesse, R.; Fronczek, F. R.; Smith, K. M.; Prodi, L.; Montalti, M.; Battistini, G. *Eur. J. Inorg. Chem.* **2007**, *16*, 2345–2352. (c) Poulin, J.; Stern, C.; Guilard, R.; Harvey, P. D. *Photochem. Photobiol.* **2006**, *82*, 171–176. (d) Liu, X.; Mahammed, A.; Tripathy, U.; Gross, Z.; Steer, R. P. *Chem. Phys. Lett.* **2008**, *459*, 113–118.
- (13) Ding, T.; Alemán, E. A.; Modarelli, D. A.; Ziegler, C. J. *J. Phys. Chem. A.* **2005**, *109*, 7411–7417.
- (14) Steene, E.; Wondimagegn, T.; Ghosh, A. *Inorg. Biochem.* **2002**, *88*, 113–118.
- (15) Chen, P.; Meyer, T. J. *Chem. Rev.* **1998**, *98*, 1439–1478.
- (16) Dong, S. S.; Nielsen, R. J.; Palmer, J. H.; Gray, H. B.; Gross, Z.; Dasgupta, S.; Goddard, W. A. *Inorg. Chem.* **2011**, *50*, 764–770.
- (17) Rausch, A. F.; Thompson, M. E.; Yersin, H. *J. Phys. Chem. A.* **2009**, *113*, 5927–5932.
- (18) Ir(III) complexes with 3% quantum yields have been used successfully to stain living cells. See: Yu, M.; Zhao, Q.; Shi, L.; Li, F.; Zhou, Z.; Yang, H.; Yi, T.; Huang, C. *Chem. Commun.* **2008**, 2115–2117.
- (19) Lakowicz, J. R. *Principles of Fluorescence Spectroscopy*, 2nd. Ed. Kluwer Academic/Plenum Publishers, New York, **1999**.
- (20) (a) Marcus, R.A. *J. Chem Phys.* **1965**, *43*, 1261–1274. (b) Mody, V. V.; Fitzpatrick, M. B.; Zabaneh, S. S.; Czernuszewicz, R. S.; Galezowski, M.; Gryko, D. T. *J. Porph. Pthal.* **2009**, *13*, 1040–1052.

Appendix C:

Supporting information: Electronic structures of Pd^{II} dimers

The data presented here represents much of the raw data used to fully characterize the electronic properties of the dipalladium(II) species. It is presented largely without comment.

Electrochemistry

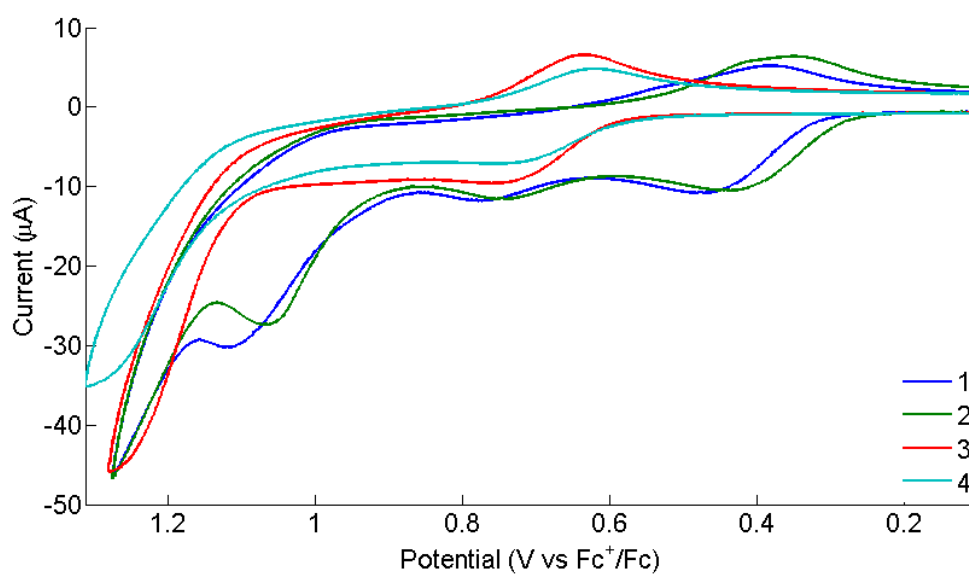


Figure C.1. Cyclic voltammograms of **1–4** in CH₂Cl₂

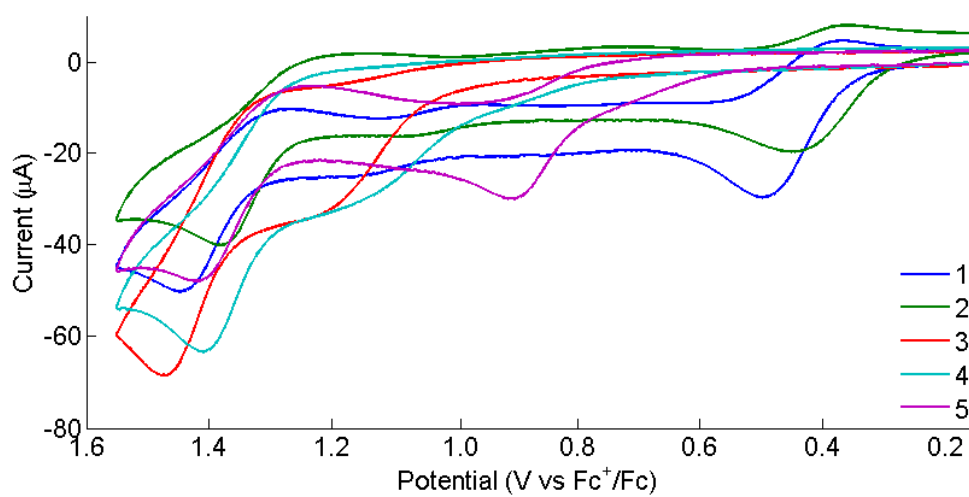


Figure C.2. Cyclic voltammograms of **1–5** in MeCN

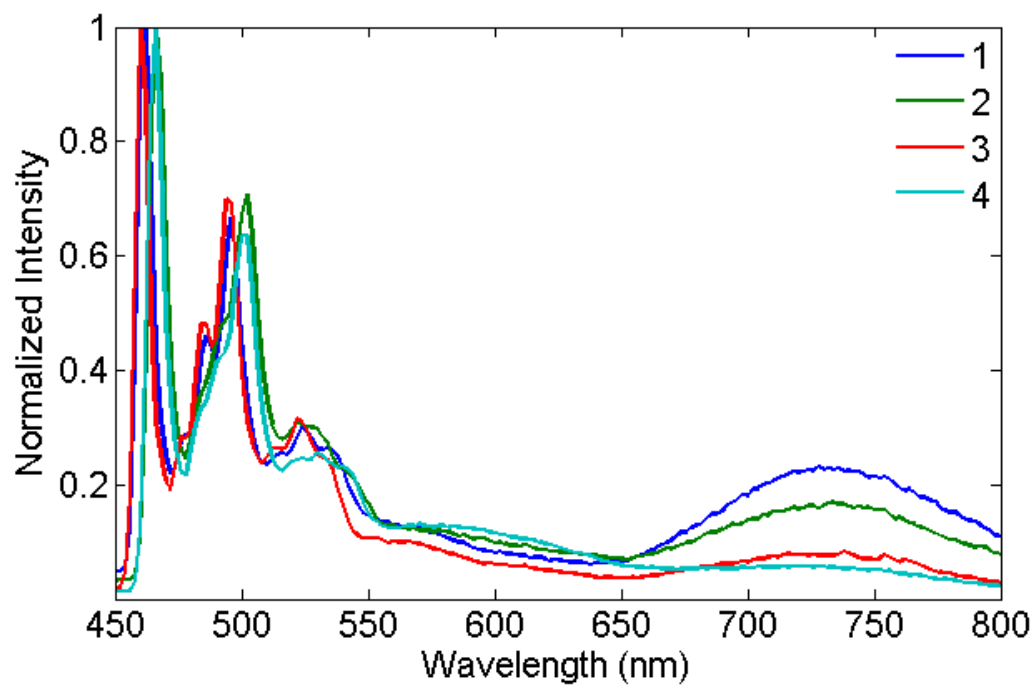


Figure C.3. Steady-state emission spectra of **1–4**, 77 K, $\lambda_{\text{ex}} = 355$ nm

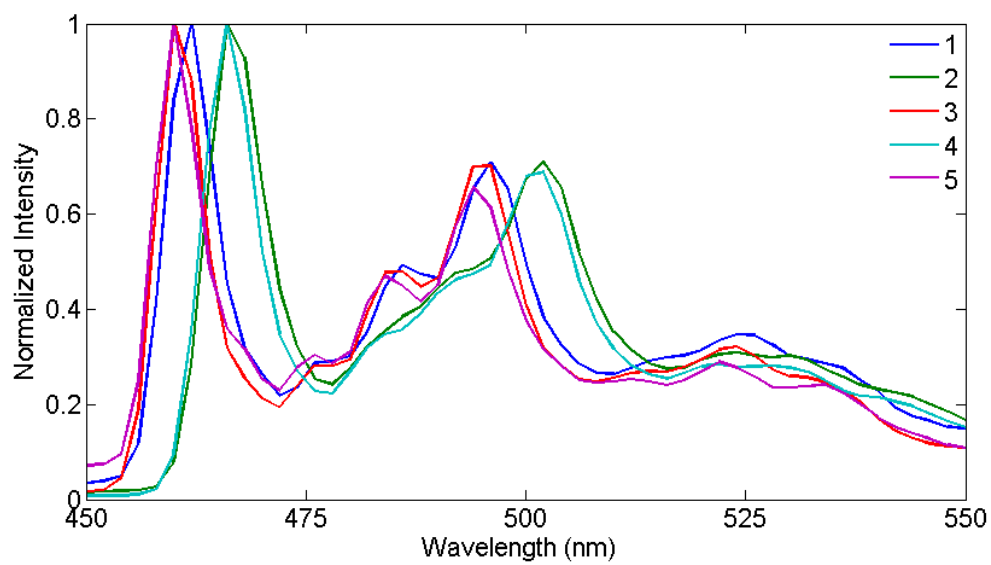


Figure C.4. Steady-state emission spectra of **1–5**, 77 K, $\lambda_{\text{ex}} = 355$ nm

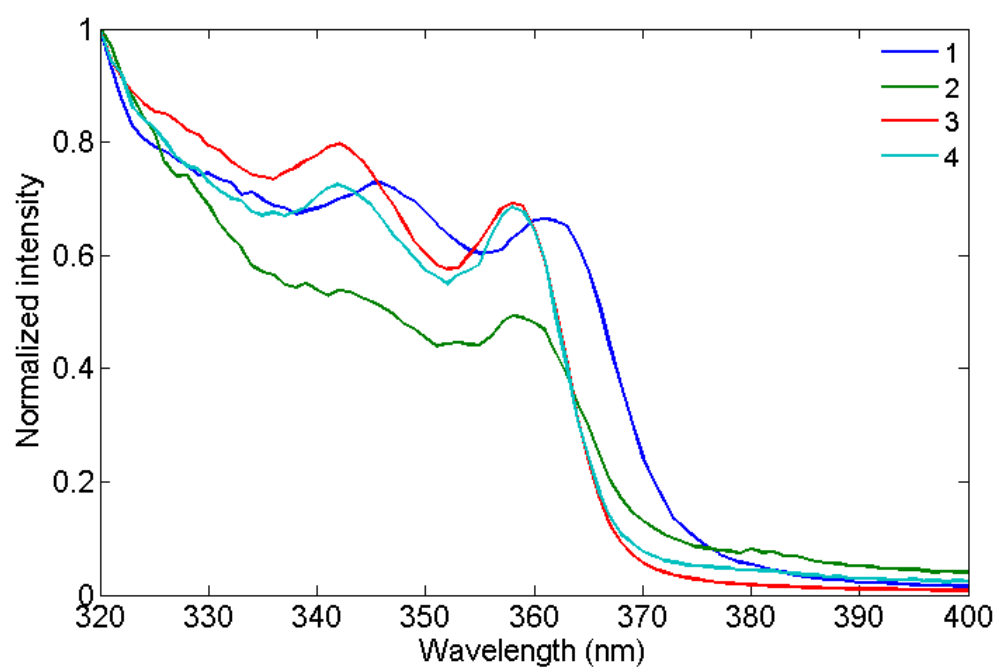


Figure C.5. Excitation spectrum of 1–4, 77 K, $\lambda_{em} = 460$ nm

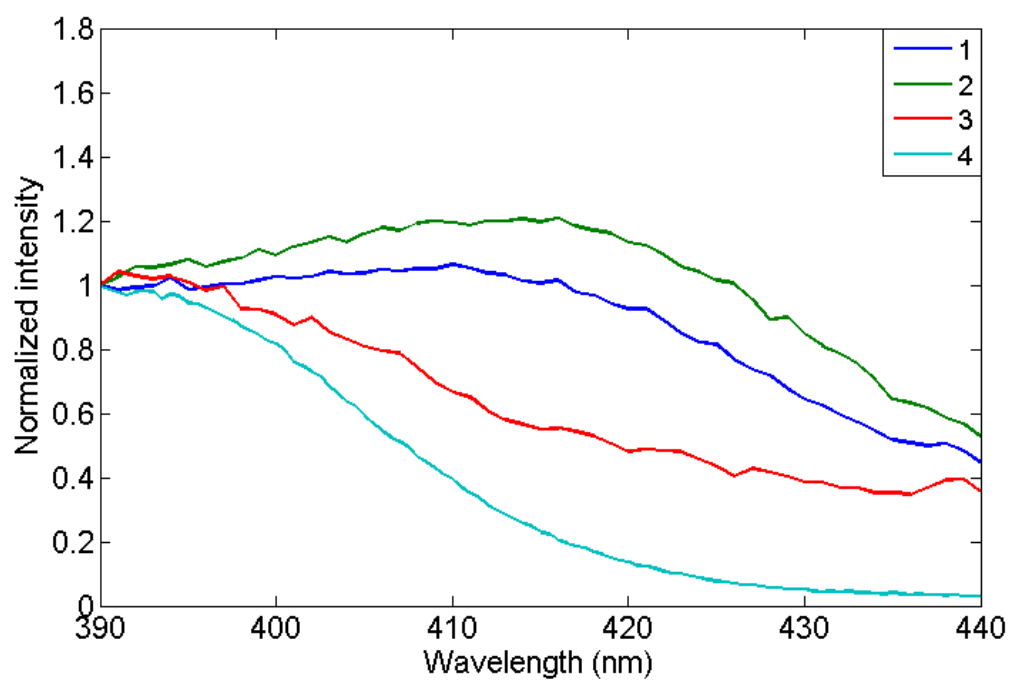


Figure C.6. Excitation spectrum of **1–4**, 77 K, $\lambda_{em} = 790$ nm

Time-resolved luminescence decay

Time-resolved data were collected in MTHF glasses at 77 K. All lifetimes are reported in microseconds and the prefactors reflect the intensity of the signal in mV. The short-lived fluorescence components observed at 460 nm were not fit, as their lifetimes exceeded the limits of the instrument ($\tau < 20$ ns).

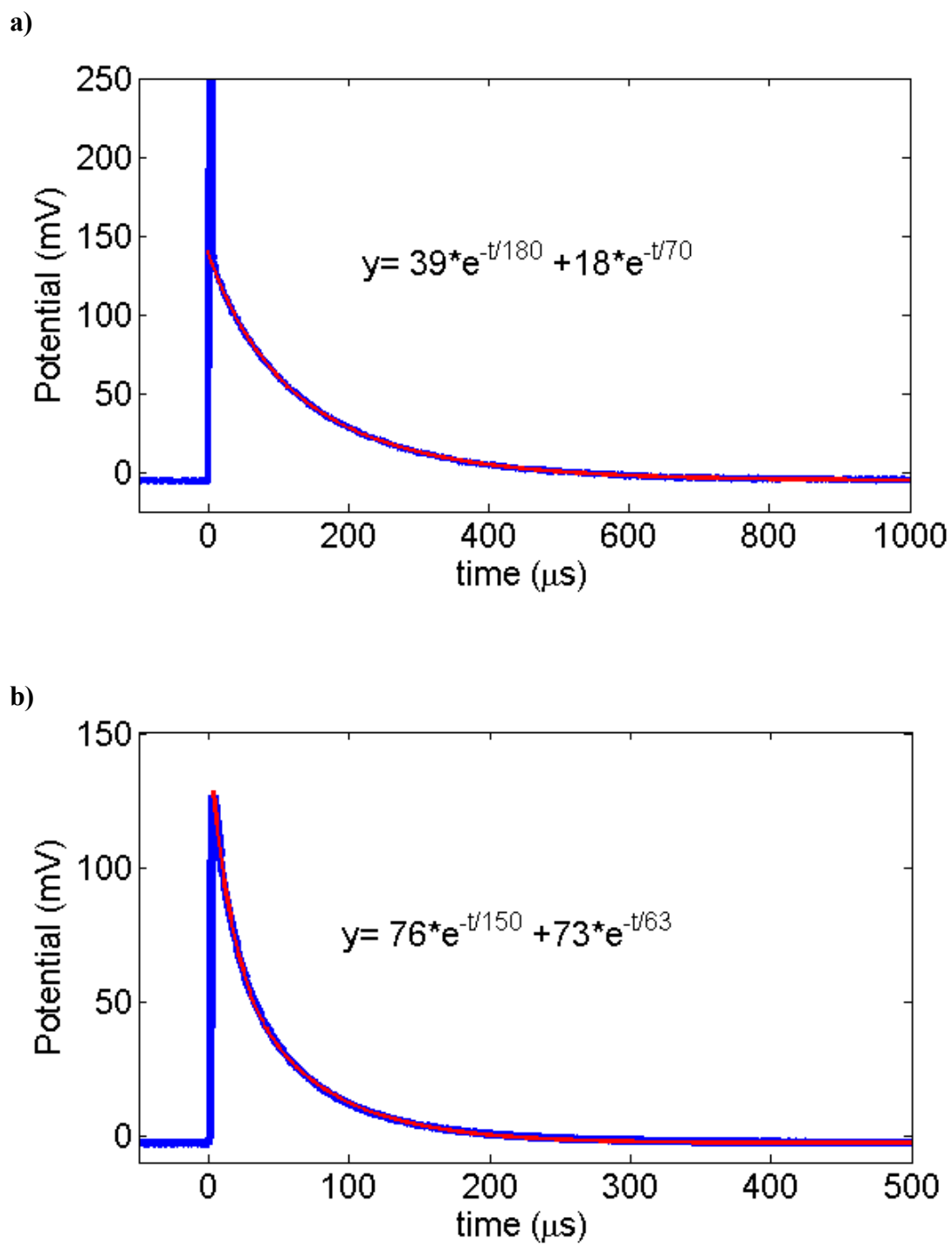


Figure C.7. Luminescence decay of **1** at 77 K at 460 nm (a) and 720 nm (b)

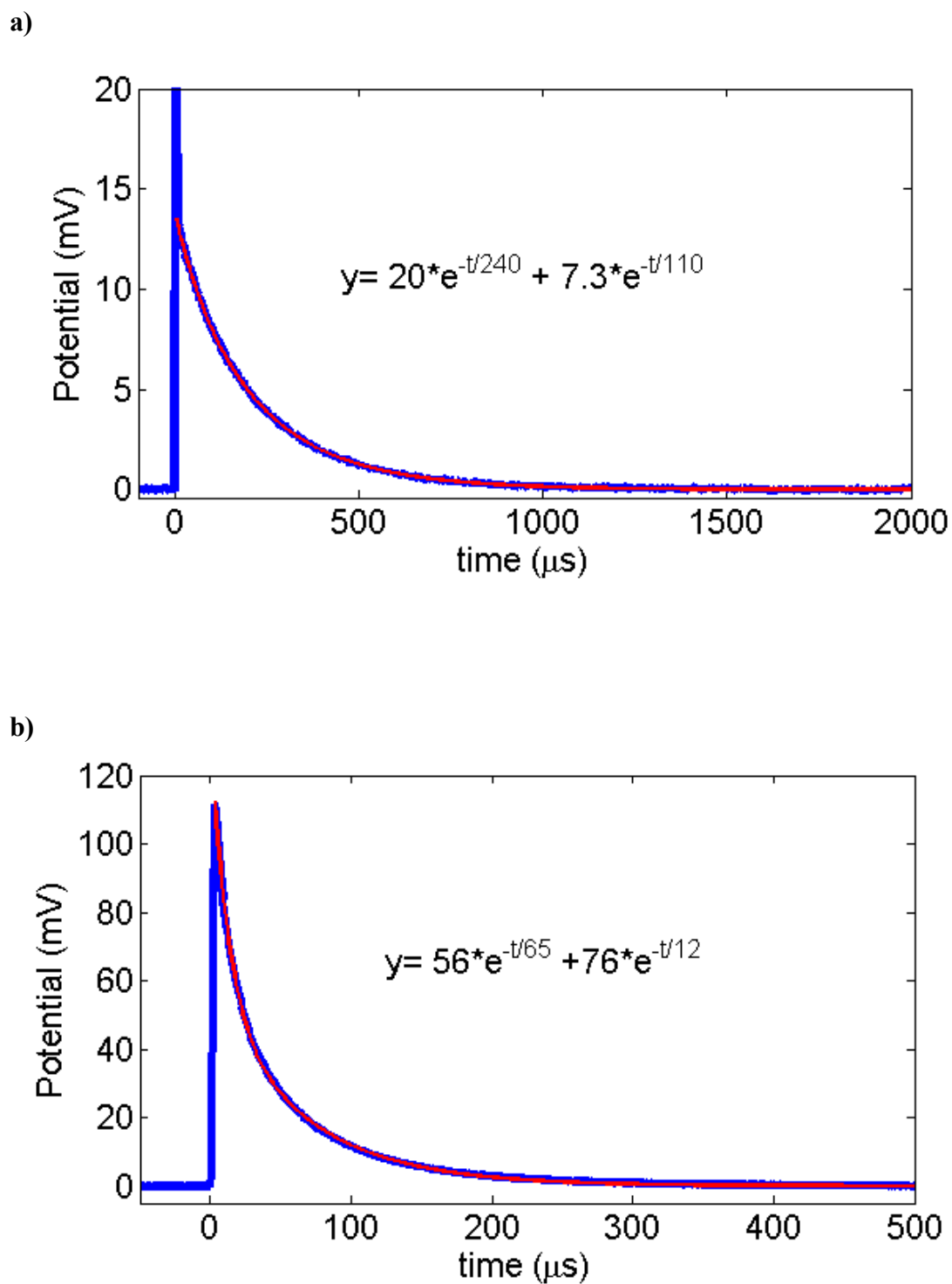


Figure C.8. Luminescence decay of **2** at 77 K at 460 nm (a) and 720 nm (b)

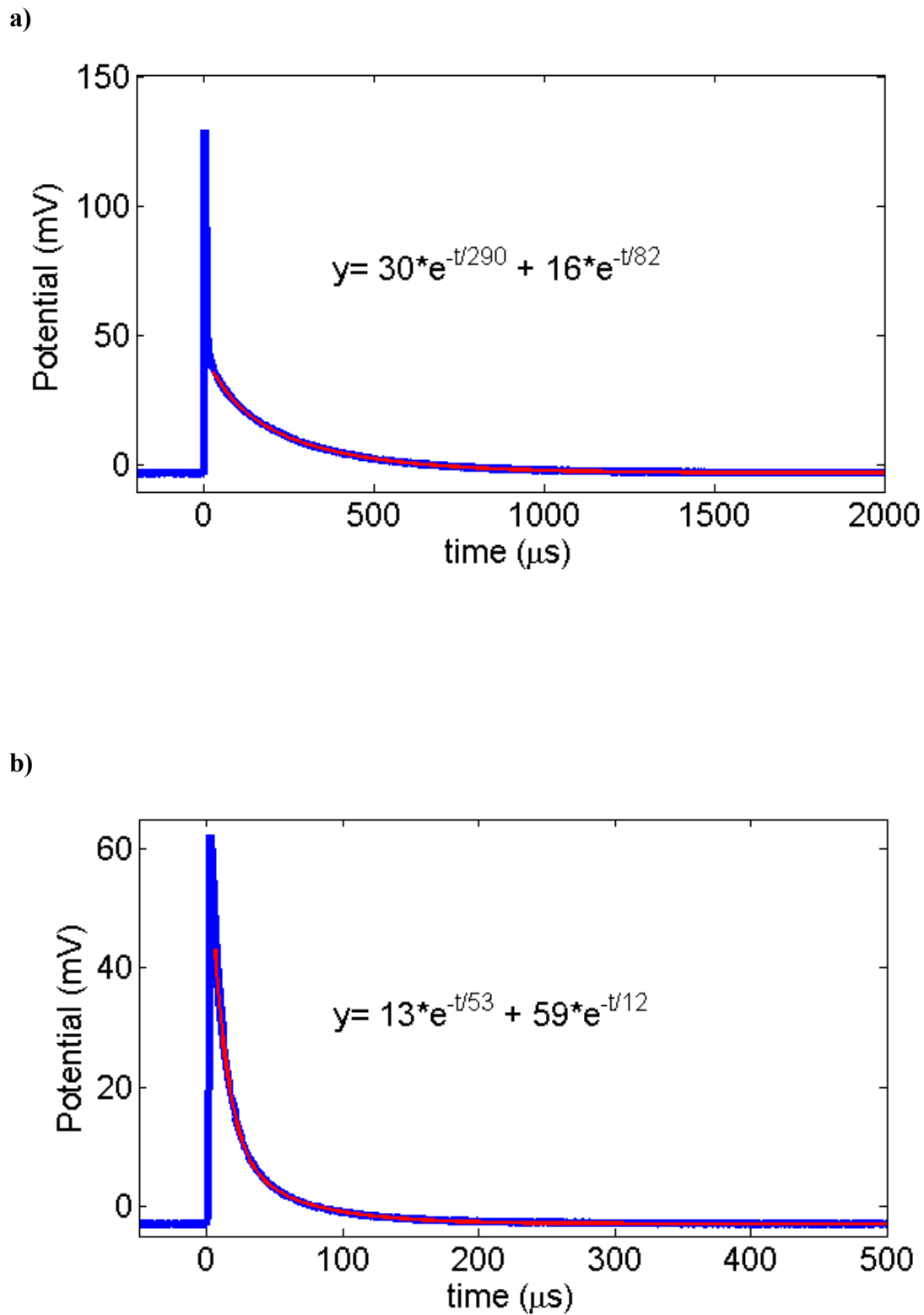
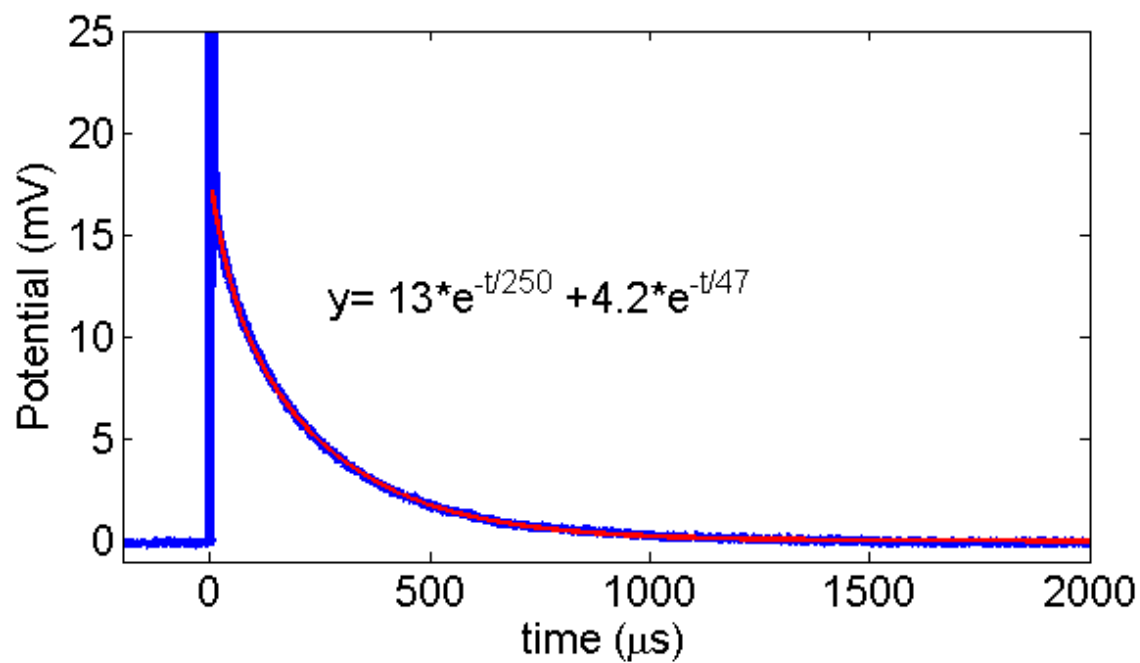


Figure C.9. Luminescence decay of **3** at 77 K at 460 nm (a) and 720 nm (b)

a)



b)

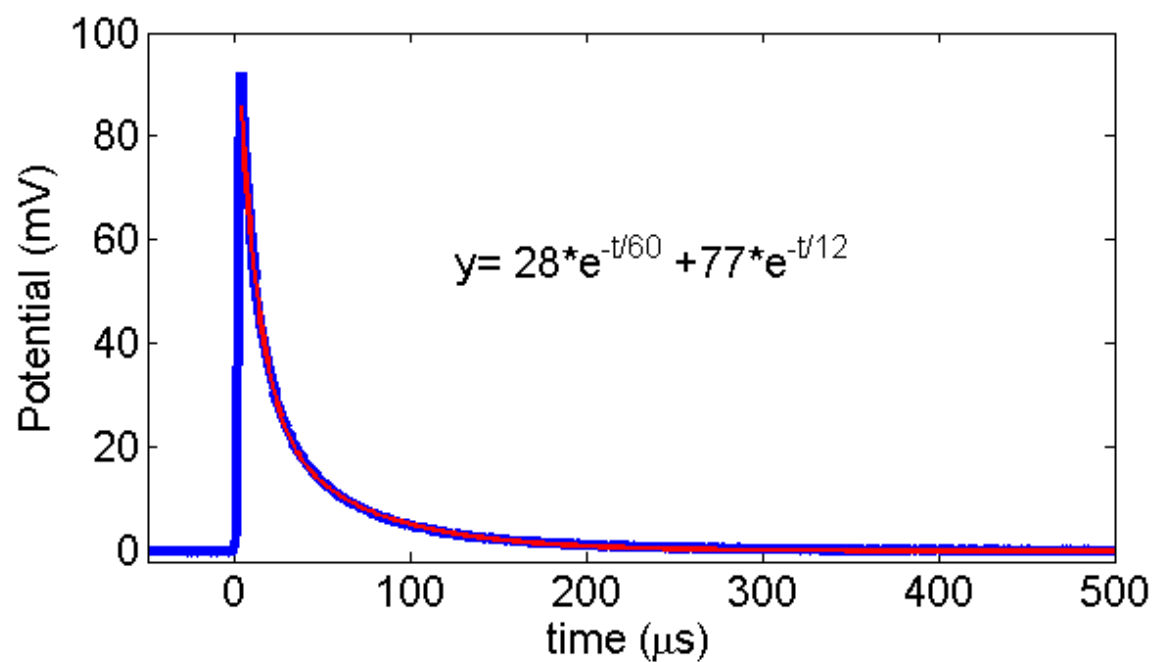


Figure C.10. Luminescence decay of **4** at 77 K at 460 nm (a) and 720 nm (b)

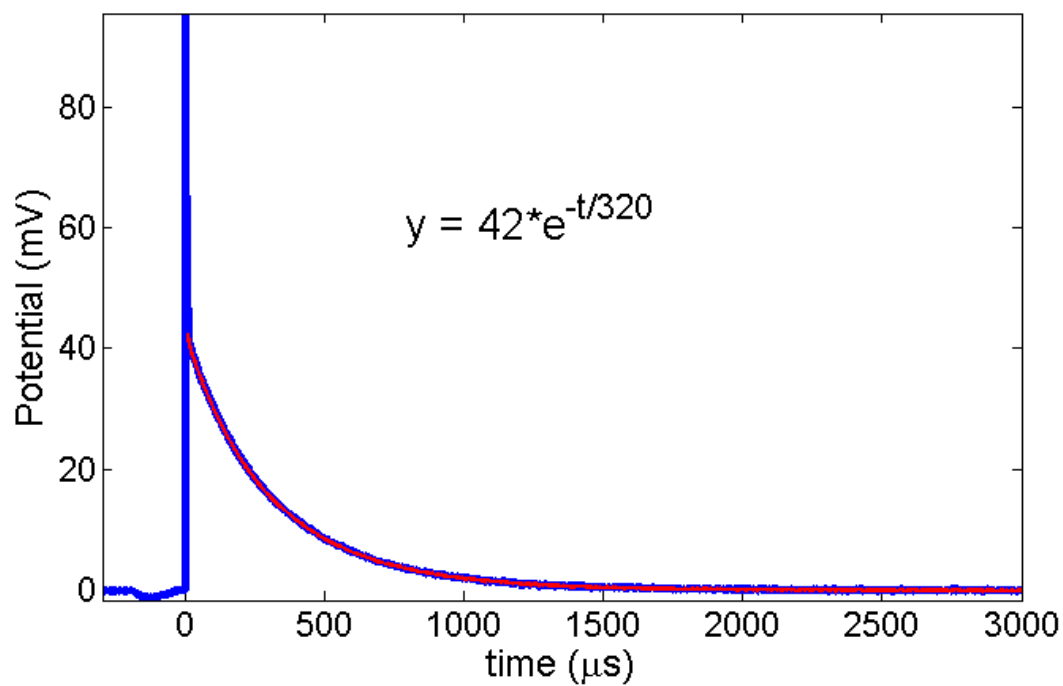


Figure C.11. Luminescence decay of **5** at 77 K at 460 nm. No luminescence observed at higher wavelengths

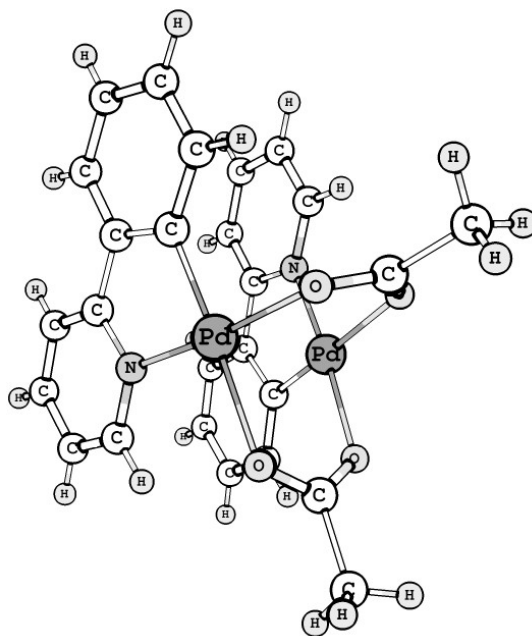
Density Functional Theory

XYZ coordinates of optimized structures

Compound 1

Atom	X	Y	Z (Angstrom)
1.Pd	-0.015348	-1.411688	0.087827
2.Pd	0.015348	1.411688	0.087827
3.O	-1.500074	1.073325	1.480057
4.O	-1.434283	-1.178652	1.484098
5.C	-1.864868	-0.059158	1.884683
6.C	-2.948716	-0.104711	2.911512
7.H	-3.922853	-0.087146	2.394642
8.H	-2.891036	-1.032063	3.495669
9.H	-2.895562	0.778455	3.561457
10.O	1.500074	-1.073325	1.480057
11.O	1.434283	1.178652	1.484098
12.C	2.948716	0.104711	2.911512
13.C	1.864868	0.059158	1.884683
14.H	2.891036	1.032063	3.495669
15.H	2.895562	-0.778455	3.561457
16.H	3.922853	0.087146	2.394642
17.N	-1.250971	1.847612	-1.353349
18.C	-2.571072	1.888701	-1.187181
19.C	-3.427210	2.155687	-2.233800
20.C	-2.891637	2.373012	-3.494219
21.C	-1.523280	2.335998	-3.659037
22.C	-0.702720	2.082700	-2.569541
23.H	-2.912908	1.703127	-0.164559
24.H	-4.503654	2.190641	-2.056975
25.H	-3.544563	2.577341	-4.346602
26.H	-1.067027	2.513086	-4.636009
27.C	0.735972	2.075293	-2.555547
28.C	0.702720	-2.082700	-2.569541
29.C	-0.735972	-2.075293	-2.555547
30.C	1.538420	2.341708	-3.659102
31.C	1.523280	-2.335998	-3.659037
32.C	-1.538420	-2.341708	-3.659102
33.C	2.911745	2.377383	-3.517244
34.C	2.891637	-2.373012	-3.494219
35.C	-2.911745	-2.377383	-3.517244
36.C	3.478860	2.154550	-2.268587
37.C	3.427210	-2.155687	-2.233800
38.C	-3.478860	-2.154550	-2.268587
39.C	2.683763	1.877334	-1.166354

40.C	2.571072	-1.888701	-1.187181
41.C	-2.683763	-1.877334	-1.166354
42.C	1.305437	1.824233	-1.294263
43.N	1.250971	-1.847612	-1.353349
44.C	-1.305437	-1.824233	-1.294263
45.H	1.082697	2.533435	-4.636259
46.H	1.067027	-2.513086	-4.636009
47.H	-1.082697	-2.533435	-4.636259
48.H	3.547700	2.592693	-4.379214
49.H	3.544563	-2.577341	-4.346602
50.H	-3.547700	-2.592693	-4.379214
51.H	4.565591	2.207922	-2.151998
52.H	4.503654	-2.190641	-2.056975
53.H	-4.565591	-2.207922	-2.151998
54.H	3.136506	1.720651	-0.181717
55.H	2.912908	-1.703127	-0.164559
56.H	-3.136506	-1.720651	-0.181717

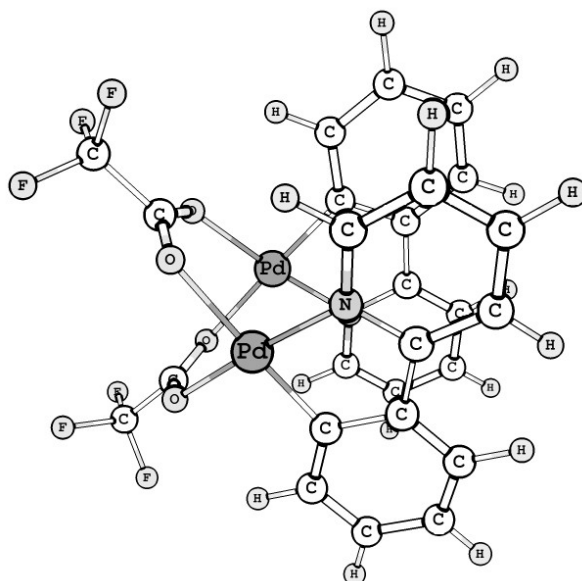


Compound 3

Atom	X	Y	Z (Angstrom)
1.Pd	8.405940	11.170688	6.682973

2.Pd	9.001517	13.190823	4.756391
3.F	7.079164	15.977153	8.120844
4.F	5.603517	14.470104	8.594779
5.F	5.470082	15.558200	6.735815
6.F	4.597094	10.168097	4.230325
7.F	5.853791	10.236662	2.468456
8.F	4.717854	11.983236	3.061309
9.O	7.405606	12.881381	7.530108
10.O	7.696986	14.350726	5.819304
11.O	6.788729	10.851505	5.461157
12.O	7.340858	12.278520	3.779528
13.N	10.061647	11.326680	7.788633
14.N	10.394366	12.100990	3.824211
15.C	10.269199	12.267519	8.712638
16.C	11.471881	12.390683	9.380600
17.C	12.501210	11.512787	9.079994
18.C	12.284293	10.537067	8.127796
19.C	11.054715	10.449032	7.486170
20.C	10.685090	9.477863	6.482796
21.C	11.517303	8.467413	5.997072
22.C	11.048383	7.584143	5.042243
23.C	9.745747	7.703454	4.575671
24.C	8.911619	8.709194	5.046605
25.C	9.371637	9.614885	5.992632
26.C	10.162554	11.184600	2.881609
27.C	11.158434	10.345477	2.421651
28.C	12.435232	10.456151	2.948014
29.C	12.696740	11.467241	3.847759
30.C	11.659127	12.276938	4.293235
31.C	11.778833	13.334581	5.271905
32.C	12.979175	13.743021	5.852454
33.C	12.992056	14.798155	6.747314
34.C	11.804097	15.452756	7.051938
35.C	10.598204	15.036233	6.492729
36.C	10.571473	13.970067	5.606973
37.C	6.640393	11.420865	4.352452
38.C	5.418459	10.948421	3.529983
39.C	7.223331	13.948384	6.913065
40.C	6.314490	14.995154	7.600201
41.H	9.435697	12.945347	8.923437
42.H	11.584648	13.173704	10.134477
43.H	13.462235	11.596472	9.598608
44.H	13.058431	9.810716	7.863235
45.H	12.550079	8.359411	6.349619
46.H	11.694875	6.792211	4.651382

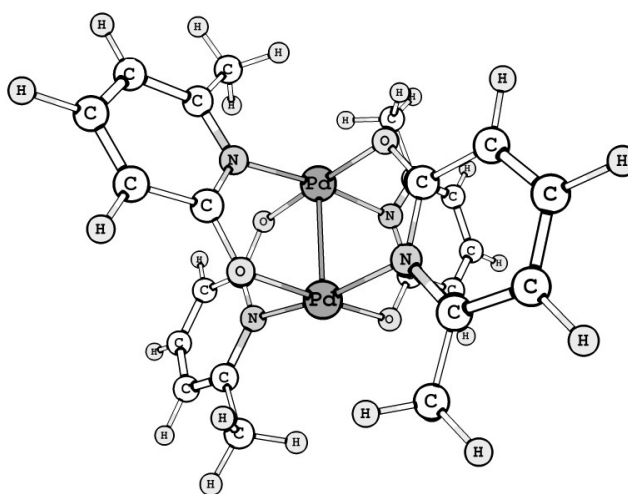
47.H	9.381634	6.999025	3.819931
48.H	7.888276	8.778246	4.662483
49.H	9.142531	11.112712	2.485189
50.H	10.938711	9.593410	1.659871
51.H	13.192187	9.725314	2.643267
52.H	13.704748	11.647066	4.232876
53.H	13.910029	13.234055	5.581135
54.H	13.929122	15.129747	7.205167
55.H	11.820920	16.310846	7.732551
56.H	9.665135	15.558403	6.733072



Compound a

Atom	X	Y	Z (Angstrom)
1.Pd	1.264011	0.000000	0.000000
2.Pd	-1.264011	0.000000	0.000000
3.O	-1.225263	1.487607	-1.323780
4.O	1.225263	-1.487607	-1.323780
5.O	-1.225263	-1.487607	1.323780
6.O	1.225263	1.487607	1.323780
7.N	1.106177	1.332913	-1.518155
8.N	-1.106177	-1.332913	-1.518155
9.N	1.106177	-1.332913	1.518155
10.N	-1.106177	1.332913	1.518155
11.C	-0.108147	1.839090	-1.874483
12.C	-0.162808	2.805087	-2.903456
13.C	0.979195	3.194345	-3.545370
14.C	2.201988	2.632104	-3.182307
15.C	2.230322	1.704645	-2.166369
16.C	0.108147	-1.839090	-1.874483
17.C	0.162808	-2.805087	-2.903456
18.C	-0.979195	-3.194345	-3.545370
19.C	-2.201988	-2.632104	-3.182307
20.C	-2.230322	-1.704645	-2.166369
21.C	-0.108147	-1.839090	1.874483
22.C	-0.162808	-2.805087	2.903456
23.C	0.979195	-3.194345	3.545370
24.C	2.201988	-2.632104	3.182307
25.C	2.230322	-1.704645	2.166369
26.C	0.108147	1.839090	1.874483
27.C	0.162808	2.805087	2.903456
28.C	-0.979195	3.194345	3.545370
29.C	-2.201988	2.632104	3.182307
30.C	-2.230322	1.704645	2.166369
31.H	3.133162	-2.908137	3.682893
32.H	0.929753	-3.938703	4.346450
33.H	-1.149053	-3.202883	3.155006
34.H	-1.149053	3.202883	-3.155006
35.H	0.929753	3.938703	-4.346450
36.H	3.133162	2.908137	-3.682893
37.H	1.149053	-3.202883	-3.155006
38.H	-0.929753	-3.938703	-4.346450
39.H	-3.133162	-2.908137	-3.682893
40.H	1.149053	3.202883	3.155006
41.H	-0.929753	3.938703	4.346450
42.H	-3.133162	2.908137	3.682893
43.C	-3.485168	1.051892	1.729359

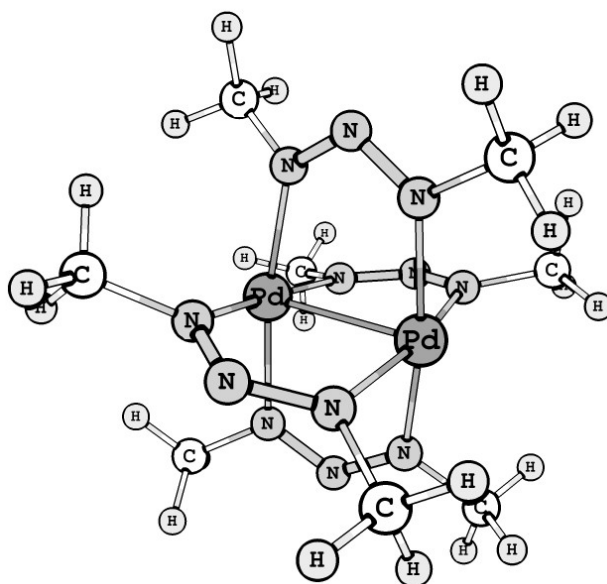
44.H	-4.341820	1.412962	2.315728
45.H	-3.666891	1.248293	0.658826
46.H	-3.395675	-0.042091	1.844057
47.C	-3.485168	-1.051892	-1.729359
48.H	-3.666891	-1.248293	-0.658826
49.H	-3.395675	0.042091	-1.844057
50.H	-4.341820	-1.412962	-2.315728
51.C	3.485168	1.051892	-1.729359
52.H	3.666891	1.248293	-0.658826
53.H	3.395675	-0.042091	-1.844057
54.H	4.341820	1.412962	-2.315728
55.C	3.485168	-1.051892	1.729359
56.H	4.341820	-1.412962	2.315728
57.H	3.666891	-1.248293	0.658826
58.H	3.395675	0.042091	1.844057



Compound b

Atom	X	Y	Z (Angstrom)
1.N	-0.901383	-0.843200	-1.928842
2.N	-1.455852	1.646117	-0.660848
3.N	-0.510441	2.512108	-0.669410
4.N	0.679138	2.158806	-0.348112
5.N	0.195731	-0.641199	-2.561591
6.N	1.200875	-0.134247	-1.947277
7.N	1.474688	-1.708610	0.417026
8.N	0.509360	-2.507722	0.687152

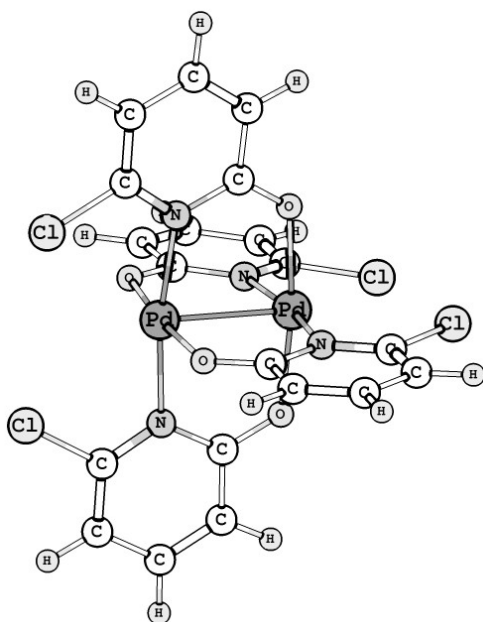
9.N	-0.699977	-2.087168	0.632586
10.N	0.954379	0.574095	2.003745
11.N	-0.197052	0.645049	2.564231
12.N	-1.253273	0.406904	1.877040
13.Pd	1.241168	0.256988	0.031680
14.Pd	-1.241557	-0.256750	-0.027799
15.C	-1.889962	-1.556902	-2.678778
16.H	-2.011866	-2.581180	-2.282413
17.H	-2.866018	-1.051186	-2.599374
18.H	-1.585329	-1.620613	-3.737029
19.C	2.305836	0.194556	-2.795405
20.H	3.244122	-0.195407	-2.366277
21.H	2.148584	-0.231371	-3.800533
22.H	2.411009	1.292743	-2.885792
23.C	2.767593	-2.321853	0.407883
24.H	3.454829	-1.788540	1.087488
25.H	2.684791	-3.377011	0.715919
26.H	3.202011	-2.277836	-0.607207
27.C	-1.680177	-3.064692	1.003160
28.H	-1.219475	-3.855073	1.619643
29.H	-2.480614	-2.572719	1.581295
30.H	-2.145574	-3.528620	0.111765
31.C	-2.478700	0.692710	2.557952
32.H	-2.273903	0.940316	3.612598
33.H	-2.988452	1.551230	2.082988
34.H	-3.161142	-0.172430	2.503048
35.C	1.628492	3.229736	-0.324931
36.H	2.157985	3.239338	0.644683
37.H	2.388421	3.099952	-1.119259
38.H	1.112219	4.194357	-0.466376
39.C	2.059040	0.674846	2.907387
40.H	2.778564	1.432080	2.552648
41.H	1.698342	0.943521	3.914174
42.H	2.593259	-0.291741	2.967177
43.C	-2.709074	2.131916	-1.151566
44.H	-2.644863	3.217154	-1.336995
45.H	-2.974248	1.622070	-2.096114
46.H	-3.513208	1.925636	-0.423961



Compound c

Atom	X	Y	Z (Angstrom)
1.Pd	0.000000	0.000000	1.278900
2.Pd	0.000000	0.000000	-1.279033
3.Cl	1.745299	-0.789015	-3.719094
4.Cl	-1.745299	0.789015	-3.719094
5.Cl	-1.212059	-1.481652	3.719031
6.Cl	1.212059	1.481652	3.719031
7.O	0.995361	1.725601	-1.217104
8.O	1.656566	-1.106672	1.217015
9.O	-0.995361	-1.725601	-1.217104
10.O	-1.656566	1.106672	1.217015
11.N	1.124957	1.674332	1.120125
12.N	1.750835	-1.002252	-1.120230
13.N	-1.124957	-1.674332	1.120125
14.N	-1.750835	1.002252	-1.120230
15.C	1.403170	2.224100	-0.103992
16.C	2.179126	3.404169	-0.151221
17.C	2.649068	3.973573	0.998825
18.C	2.366170	3.393866	2.236028
19.C	1.604779	2.255095	2.225920
20.C	2.243420	-1.372135	0.103947

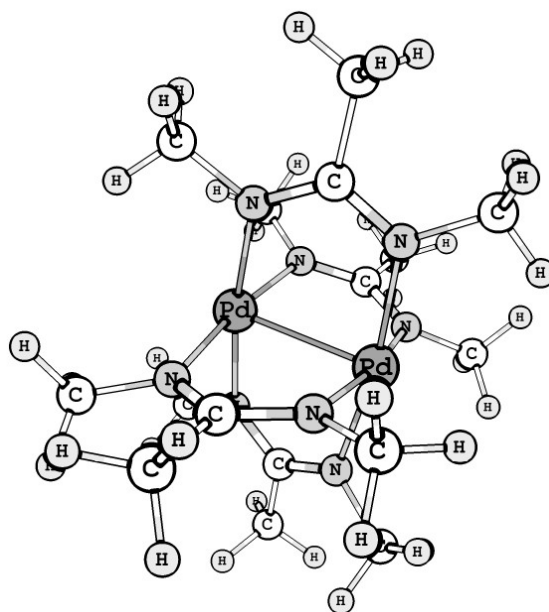
21.C	3.461917	-2.086177	0.151417
22.C	4.136120	-2.387733	-0.998449
23.C	3.626341	-1.992603	-2.235692
24.C	2.439062	-1.309376	-2.225889
25.C	-1.403170	-2.224100	-0.103992
26.C	-2.179126	-3.404169	-0.151221
27.C	-2.649068	-3.973573	0.998825
28.C	-2.366170	-3.393866	2.236028
29.C	-1.604779	-2.255095	2.225920
30.C	-2.243420	1.372135	0.103947
31.C	-3.461917	2.086177	0.151417
32.C	-4.136120	2.387733	-0.998449
33.C	-3.626341	1.992603	-2.235692
34.C	-2.439062	1.309376	-2.225889
35.H	-2.720832	-3.805724	3.181278
36.H	-3.252363	-4.885209	0.951427
37.H	-2.379322	-3.818696	-1.141799
38.H	2.379322	3.818696	-1.141799
39.H	3.252363	4.885209	0.951427
40.H	2.720832	3.805724	3.181278
41.H	3.824347	-2.369582	1.142113
42.H	5.081035	-2.937446	-0.950891
43.H	4.127527	-2.203768	-3.180743
44.H	-3.824347	2.369582	1.142113
45.H	-5.081035	2.937446	-0.950891
46.H	-4.127527	2.203768	-3.180743



Compound d

Atom	X	Y	Z (Angstrom)
1.Pd	-0.001348	-0.003657	-1.270687
2.Pd	0.000573	-0.003941	1.267476
3.N	-1.036355	1.715600	-1.134027
4.N	-0.626264	1.907213	1.145346
5.N	1.729089	1.019246	-1.141064
6.N	1.904947	0.633055	1.145825
7.N	1.018038	-1.735443	-1.148418
8.N	0.636992	-1.909764	1.140109
9.N	-1.728470	-1.027821	-1.147703
10.N	-1.903757	-0.648618	1.140689
11.C	-1.099463	2.391461	0.005070
12.C	2.384293	1.116877	0.008590
13.C	1.118346	-2.389397	0.002026
14.C	-2.401491	-1.089311	-0.007645
15.C	1.704187	-2.223450	-2.306451
16.H	1.410764	-3.256783	-2.582933
17.H	1.464704	-1.572046	-3.159078
18.H	2.809447	-2.216129	-2.191355
19.C	1.818500	-3.711965	-0.010995
20.H	1.235762	-4.467916	-0.566924
21.H	2.787672	-3.617539	-0.528904
22.H	2.005401	-4.090145	1.002388
23.C	0.546227	-2.723920	2.314232
24.H	0.269494	-3.773456	2.098339
25.H	1.484341	-2.737378	2.909236
26.H	-0.241227	-2.311187	2.964758
27.C	-2.724236	-0.618904	2.314371
28.H	-3.117937	-1.616621	2.597417
29.H	-2.119453	-0.251741	3.156002
30.H	-3.595795	0.063494	2.219062
31.C	-3.779544	-1.673733	0.000794
32.H	-3.776527	-2.695258	0.422266
33.H	-4.447102	-1.069237	0.635314
34.H	-4.209184	-1.719422	-1.008998
35.C	-2.191347	-1.709850	-2.318172
36.H	-2.656796	-2.689370	-2.097606
37.H	-2.921035	-1.115038	-2.908431
38.H	-1.327863	-1.902844	-2.974243
39.C	-0.544972	2.713629	2.326786
40.H	-1.527532	2.873557	2.817199
41.H	0.098536	2.196591	3.054660
42.H	-0.092417	3.709238	2.147246

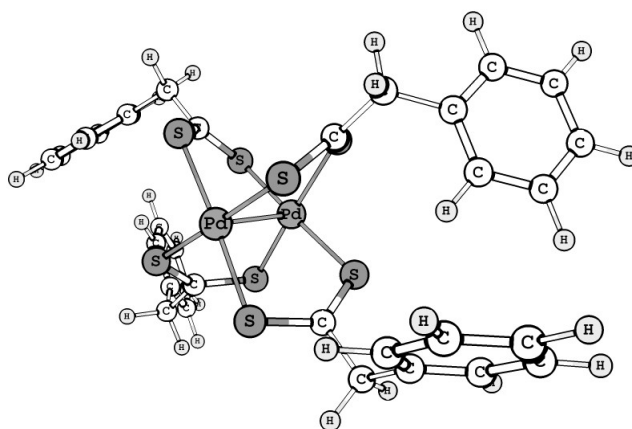
43.C	-1.751860	3.738121	-0.016676
44.H	-2.847862	3.628600	-0.101418
45.H	-1.545186	4.309000	0.898093
46.H	-1.419337	4.326366	-0.887118
47.C	-1.710420	2.196124	-2.300527
48.H	-1.903418	1.345600	-2.973272
49.H	-2.685810	2.669795	-2.076799
50.H	-1.107806	2.933302	-2.873039
51.C	2.714127	0.553681	2.324620
52.H	2.283575	-0.210112	2.991321
53.H	3.758945	0.251975	2.118672
54.H	2.743525	1.504458	2.898379
55.C	3.706379	1.816912	-0.005057
56.H	4.452137	1.251626	-0.591686
57.H	3.603517	2.800989	-0.492869
58.H	4.101877	1.973982	1.006675
59.C	2.219944	1.704758	-2.298195
60.H	1.556753	1.484470	-3.146638
61.H	2.237104	2.808789	-2.173346
62.H	3.244734	1.392603	-2.586579



Compound e

Atom	X	Y	Z (Angstrom)
1.Pd	0.000000	0.000000	1.573542
2.Pd	0.000000	0.000000	-1.105541
3.S	-2.162553	-0.809085	1.644804
4.S	-0.841421	2.148563	1.659921
5.S	-1.579099	-1.677986	-1.201531
6.S	-1.693879	1.568707	-1.195281
7.C	-2.493975	-1.615868	0.207416
8.C	-1.707856	2.429906	0.241937
9.C	-3.786900	-2.376081	0.182077
10.C	-2.662375	3.586102	0.300922
11.C	-4.764056	-1.869729	-0.836420
12.C	-5.192383	-0.546668	-0.808590
13.C	-6.109088	-0.091250	-1.740781
14.C	-6.609120	-0.948584	-2.710077
15.C	-6.185605	-2.267471	-2.742936
16.C	-5.265331	-2.722210	-1.810980
17.C	-4.058525	3.137460	0.627641
18.C	-5.088255	3.344885	-0.280773
19.C	-6.381825	2.945644	0.016216
20.C	-6.656415	2.321156	1.222014
21.C	-5.631133	2.105989	2.131902
22.C	-4.341119	2.512797	1.837120
23.H	-3.557635	-3.434896	-0.030362
24.H	-4.230135	-2.340810	1.192296
25.H	-2.664438	4.110441	-0.667476
26.H	-2.304141	4.292873	1.069425
27.H	-4.798229	0.143775	-0.048081
28.H	-6.432661	0.954413	-1.699338
29.H	-7.332460	-0.585134	-3.447041
30.H	-6.572619	-2.951182	-3.504819
31.H	-4.923378	-3.763304	-1.838848
32.H	-4.868152	3.834574	-1.236231
33.H	-7.186132	3.130412	-0.702139
34.H	-7.675583	2.000133	1.455671
35.H	-5.839986	1.615827	3.087262
36.H	-3.525758	2.336220	2.549996
37.S	2.162553	0.809085	1.644804
38.S	0.841421	-2.148563	1.659921
39.S	1.579099	1.677986	-1.201531
40.S	1.693879	-1.568707	-1.195281
41.C	2.493975	1.615868	0.207416
42.C	1.707856	-2.429906	0.241937

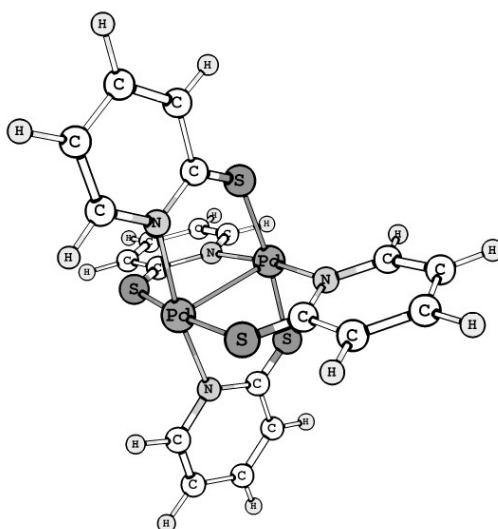
43.C	3.786900	2.376081	0.182077
44.C	2.662375	-3.586102	0.300922
45.C	4.764056	1.869729	-0.836420
46.H	3.557635	3.434896	-0.030362
47.H	4.230135	2.340810	1.192296
48.C	4.058525	-3.137460	0.627641
49.H	2.664438	-4.110441	-0.667476
50.H	2.304141	-4.292873	1.069425
51.C	5.192383	0.546668	-0.808590
52.C	5.265331	2.722210	-1.810980
53.C	5.088255	-3.344885	-0.280773
54.C	4.341119	-2.512797	1.837120
55.C	6.109088	0.091250	-1.740781
56.H	4.798229	-0.143775	-0.048081
57.C	6.185605	2.267471	-2.742936
58.H	4.923378	3.763304	-1.838848
59.C	6.381825	-2.945644	0.016216
60.H	4.868152	-3.834574	-1.236231
61.C	5.631133	-2.105989	2.131902
62.H	3.525758	-2.336220	2.549996
63.C	6.609120	0.948584	-2.710077
64.H	6.432661	-0.954413	-1.699338
65.H	6.572619	2.951182	-3.504819
66.C	6.656415	-2.321156	1.222014
67.H	7.186132	-3.130412	-0.702139
68.H	5.839986	-1.615827	3.087262
69.H	7.332460	0.585134	-3.447041
70.H	7.675583	-2.000133	1.455671



Compound f

Atom	X	Y	Z (Angstrom)
1.Pd	1.318882	0.018442	-0.004188

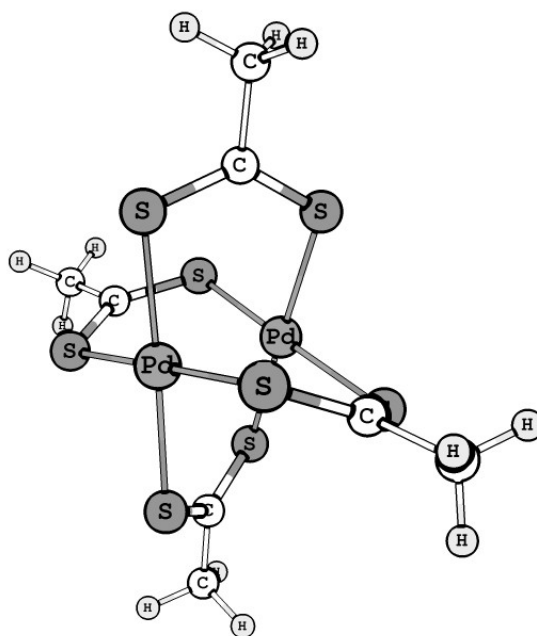
2.Pd	-1.318882	-0.018442	-0.004188
3.S	-1.359885	1.734423	-1.513117
4.S	1.359885	-1.734423	-1.513117
5.S	-1.312218	-1.775636	1.500981
6.S	1.312218	1.775636	1.500981
7.N	1.349786	1.356298	-1.514685
8.N	-1.349786	-1.356298	-1.514685
9.N	1.383676	-1.312507	1.510915
10.N	-1.383676	1.312507	1.510915
11.C	0.266431	1.990334	-2.020918
12.C	0.457512	2.954747	-3.028915
13.C	1.710500	3.256418	-3.488127
14.C	2.809111	2.582263	-2.955973
15.C	2.575375	1.646549	-1.982469
16.C	-0.266431	-1.990334	-2.020918
17.C	-0.457512	-2.954747	-3.028915
18.C	-1.710500	-3.256418	-3.488127
19.C	-2.809111	-2.582263	-2.955973
20.C	-2.575375	-1.646549	-1.982469
21.C	0.319000	-1.976144	2.018508
22.C	0.536194	-2.924453	3.036253
23.C	1.795971	-3.179781	3.505095
24.C	2.874574	-2.474562	2.972396
25.C	2.615533	-1.556958	1.988063
26.C	-0.319000	1.976144	2.018508
27.C	-0.536194	2.924453	3.036253
28.C	-1.795971	3.179781	3.505095
29.C	-2.874574	2.474562	2.972396
30.C	-2.615533	1.556958	1.988063
31.H	3.899374	-2.633963	3.313289
32.H	1.947456	-3.924603	4.292372
33.H	-0.338399	-3.446839	3.434077
34.H	-0.431679	3.452821	-3.425540
35.H	1.841334	4.014289	-4.266581
36.H	3.829992	2.779742	-3.288599
37.H	0.431679	-3.452821	-3.425540
38.H	-1.841334	-4.014289	-4.266581
39.H	-3.829992	-2.779742	-3.288599
40.H	0.338399	3.446839	3.434077
41.H	-1.947456	3.924603	4.292372
42.H	-3.899374	2.633963	3.313289
43.H	-3.413624	0.966630	1.530045
44.H	-3.390549	-1.079226	-1.525323
45.H	3.390549	1.079226	-1.525323
46.H	3.413624	-0.966630	1.530045



Compound g

Atom	X	Y	Z (Angstrom)
1.Pd	-0.501075	-1.249450	0.002655
2.Pd	0.501075	1.249450	0.002655
3.S	-2.336510	-0.617680	1.250175
4.S	-0.617859	1.788151	1.941511
5.C	-1.953354	0.779441	2.105559
6.S	-1.690386	-0.874610	-1.939425
7.S	1.270245	-2.048232	-1.233328
8.S	0.617859	-1.788151	1.941511
9.S	-1.270245	2.048232	-1.233328
10.S	1.690386	0.874610	-1.939425
11.S	2.336510	0.617680	1.250175
12.C	-1.952973	0.779450	-2.100579
13.C	1.952973	-0.779450	-2.100579
14.C	1.953354	-0.779441	2.105559
15.C	2.903145	-1.182914	-3.175525
16.H	2.418575	-1.056669	-4.158388
17.H	3.805047	-0.552925	-3.163580
18.H	3.186309	-2.240852	-3.071942
19.C	2.943805	-1.199873	3.136463
20.H	3.829434	-1.629164	2.638391
21.H	3.279694	-0.341014	3.736306

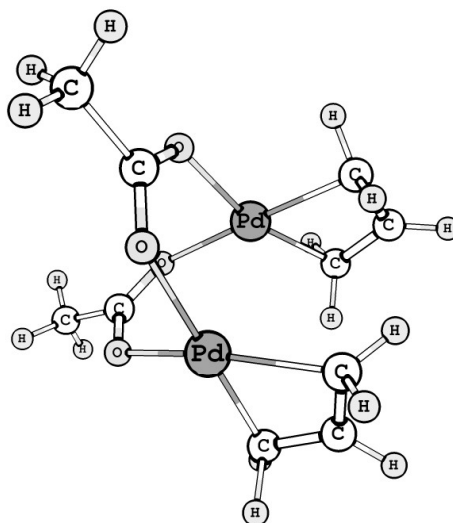
22.H	2.519580	-1.971618	3.795634
23.C	-2.943805	1.199873	3.136463
24.H	-3.829434	1.629164	2.638391
25.H	-3.279694	0.341014	3.736306
26.H	-2.519580	1.971618	3.795634
27.C	-2.903145	1.182914	-3.175525
28.H	-2.418575	1.056669	-4.158388
29.H	-3.805047	0.552925	-3.163580
30.H	-3.186309	2.240852	-3.071942



Compound h

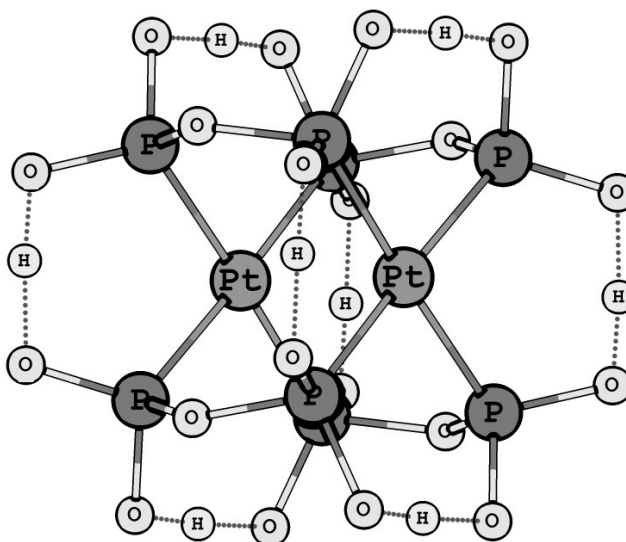
Atom	X	Y	Z (Angstrom)
1.Pd	-0.241391	1.209384	0.782951
2.Pd	-0.180446	-1.198104	-0.766736
3.O	0.987196	0.105674	1.995307
4.O	1.411503	-1.527232	0.490925
5.O	1.389817	1.659366	-0.379055
6.O	1.000408	0.039115	-1.909852
7.C	-1.590072	2.611297	0.006913

8.C	-1.374273	-2.790937	-0.133494
9.C	1.614170	-0.906405	1.572347
10.C	2.706166	-1.438956	2.442581
11.H	2.903691	-0.760680	3.282034
12.H	3.615498	-1.583954	1.840214
13.H	2.411055	-2.428889	2.825827
14.C	1.610773	1.054260	-1.466915
15.C	2.686262	1.613075	-2.340582
16.H	3.271743	0.797196	-2.788016
17.H	3.330038	2.298147	-1.773780
18.H	2.212823	2.170837	-3.165559
19.C	-2.159795	-1.822451	-0.787097
20.C	-1.779031	-1.444710	-2.090426
21.H	-2.226945	-0.557683	-2.548589
22.H	-1.387468	-2.195895	-2.787402
23.H	-0.949793	-3.629190	-0.699328
24.H	-1.506939	-2.955357	0.939936
25.H	-2.870605	-1.215713	-0.212913
26.C	-2.279467	1.511804	0.544911
27.C	-2.016340	1.169982	1.887765
28.H	-2.784389	0.804647	-0.125698
29.H	-2.360777	0.207760	2.277836
30.H	-1.865467	1.960678	2.633139
31.H	-1.385313	3.490840	0.630958
32.H	-1.602146	2.780485	-1.074079



Compound Pt-pop

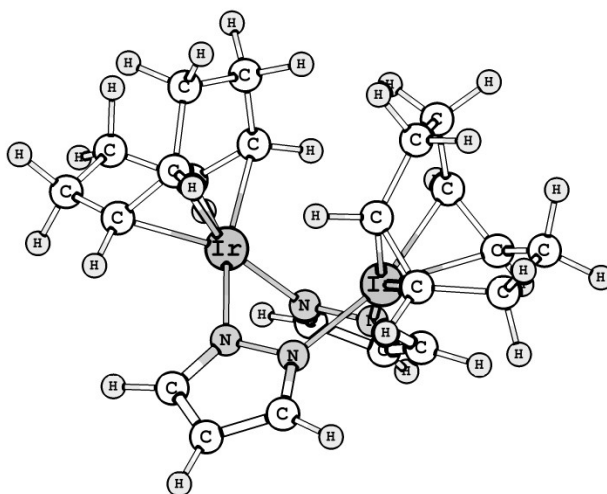
Atom	X	Y	Z (Angstrom)
1.Pt	1.344705	-0.432943	0.152621
2.P	2.076525	1.006043	-1.522572
3.P	1.040940	-2.165667	-1.386568
4.P	0.730669	-1.932427	1.827031
5.P	1.798215	1.244792	1.695919
6.O	2.471138	0.367008	-2.873936
7.O	3.264581	1.944377	-1.073902
8.H	3.180497	2.084155	0.048679
9.O	-0.553120	-2.321185	-1.805023
10.O	1.768566	-1.962412	-2.768313
11.H	2.098618	-0.879022	-2.859224
12.O	1.391535	-3.584411	-0.873656
13.O	1.191276	-3.420350	1.561339
14.H	1.289588	-3.552040	0.445090
15.O	1.163006	-1.559840	3.263294
16.O	0.914242	2.132703	-1.868633
17.O	3.001194	2.158205	1.351288
18.O	1.989615	0.739122	3.178420
19.H	1.601369	-0.315675	3.256278
20.Pt	-1.344385	0.433054	-0.152563
21.P	-2.076768	-1.006024	1.522922
22.O	-2.478207	-0.364435	2.871381
23.O	-3.261869	-1.947922	1.074362
24.H	-3.180811	-2.084046	-0.048905
25.O	-0.911656	-2.130550	1.870640
26.P	-0.728137	1.931821	-1.827290
27.P	-1.042821	2.165489	1.386401
28.O	0.550050	2.318460	1.809400
29.P	-1.798675	-1.244105	-1.695830
30.O	-3.004497	-2.153694	-1.351301
31.O	-1.987144	-0.740706	-3.179419
32.H	-1.598504	0.314117	-3.257327
33.O	-1.773823	1.964150	2.766826
34.H	-2.104387	0.881534	2.857351
35.O	-1.391255	3.584552	0.872584
36.O	-1.190202	3.419401	-1.562055
37.H	-1.289245	3.550941	-0.445396
38.O	-1.157122	1.556327	-3.263876



Compound j

Atom	X	Y	Z (Angstrom)
1.Ir	-0.185905	0.010207	1.546019
2.N	-1.205522	1.541593	0.673423
3.C	-1.737286	2.695238	1.099630
4.C	-2.104251	3.458103	0.000436
5.C	1.278157	-1.443125	2.007400
6.C	0.244605	-1.466921	2.972004
7.C	2.646655	-0.877714	2.299802
8.C	0.357627	-0.865337	4.341560
9.H	-1.848501	2.895689	2.163139
10.N	-1.474864	-1.303588	0.671060
11.C	1.436414	1.300995	1.930383
12.C	0.566978	1.284614	3.044616
13.N	-1.206374	1.541125	-0.673551
14.C	-1.738332	2.695088	-1.099114
15.C	2.758634	0.594608	1.908373
16.C	0.925115	0.552358	4.315661
17.N	-1.475077	-1.304415	-0.671751
18.C	-2.300660	-2.268939	1.099246
19.Ir	-0.187042	0.008264	-1.546657
20.H	-1.850312	2.896097	-2.162382

21.C	-2.300692	-2.269965	-1.099252
22.C	-2.858690	-2.905620	0.000274
23.C	1.278607	-1.443257	-2.008040
24.C	1.435184	1.300729	-1.927739
25.C	0.245548	-1.466929	-2.973289
26.C	0.566496	1.285406	-3.042429
27.H	-3.596367	-3.704974	0.000453
28.C	2.646987	-0.876538	-2.298706
29.C	2.757797	0.595312	-1.905280
30.C	0.358614	-0.862885	-4.341891
31.C	0.925645	0.555076	-4.313984
32.H	-2.602812	4.425050	0.000869
33.H	1.237425	-2.215027	1.224827
34.H	-0.484668	-2.286127	2.891674
35.H	3.410328	-1.463202	1.760565
36.H	2.867607	-1.012323	3.374724
37.H	0.964325	-1.515967	5.004562
38.H	-0.655044	-0.842558	4.779609
39.H	1.357314	2.161486	1.248879
40.H	-0.110924	2.142058	3.162340
41.H	3.156433	0.666532	0.882168
42.H	3.491502	1.119163	2.555259
43.H	2.025933	0.530493	4.414910
44.H	0.553294	1.115332	5.187879
45.H	-2.468595	-2.425093	2.162313
46.H	-2.468009	-2.426791	-2.162321
47.H	1.238183	-2.215783	-1.226083
48.H	1.355232	2.160090	-1.244839
49.H	-0.483063	-2.286836	-2.894327
50.H	-0.111583	2.142906	-3.158741
51.H	2.868775	-1.009406	-3.373603
52.H	3.410720	-1.462165	-1.759778
53.H	3.154743	0.666488	-0.878653
54.H	3.490791	1.121138	-2.550960
55.H	-0.654272	-0.839365	-4.779751
56.H	0.965464	-1.512396	-5.006139
57.H	2.026458	0.534254	-4.412853
58.H	0.553602	1.119029	-5.185366



Compound k

Atom	X	Y	Z (Angstrom)
1.Rh	-0.125563	1.476608	1.322813
2.C	-0.829828	1.898338	3.079839
3.N	-1.286016	2.243905	4.095857
4.C	1.696703	1.520388	1.978132
5.N	2.808727	1.471494	2.326121
6.C	0.521718	1.475244	-0.497882
7.N	0.872227	1.482688	-1.611447
8.C	-1.937067	1.346562	0.651927
9.N	-3.018646	1.182672	0.246129
10.Rh	0.126003	-1.479468	1.324489
11.C	0.829623	-1.902567	3.080140
12.C	-1.694131	-1.525083	1.982130
13.C	-0.523199	-1.476125	-0.494704
14.C	1.935389	-1.347648	0.651304
15.N	1.284096	-2.248915	4.096695
16.N	-2.805772	-1.477078	2.331614
17.N	-0.873925	-1.482747	-1.608259
18.N	3.016105	-1.181750	0.243517
19.C	4.140058	1.376043	2.735411
20.H	4.576982	2.379106	2.860074
21.H	4.207026	0.838348	3.693805
22.H	4.729351	0.826485	1.982729
23.C	-1.831550	2.730365	5.287219
24.H	-1.828904	3.832268	5.282576
25.H	-2.869314	2.380404	5.399111
26.H	-1.243063	2.376452	6.147389
27.C	1.831455	-2.726294	5.291002
28.H	2.129055	-1.885596	5.937021

29.H	1.092879	-3.341755	5.827711
30.H	2.717456	-3.345103	5.078534
31.C	-4.138857	-1.364518	2.730298
32.H	-4.416343	-0.300734	2.821681
33.H	-4.798528	-1.850654	1.993716
34.H	-4.292555	-1.850911	3.705794
35.C	-4.303069	0.940182	-0.245330
36.H	-4.825323	1.888848	-0.444825
37.H	-4.247963	0.362404	-1.181166
38.H	-4.889104	0.361863	0.487703
39.C	4.299405	-0.926562	-0.244358
40.H	4.465624	0.161456	-0.320303
41.H	5.058093	-1.363165	0.424168
42.H	4.425830	-1.371398	-1.243653
43.C	-1.266030	-1.490808	-2.948515
44.H	-1.388894	-0.458072	-3.315852
45.H	-0.509704	-2.003281	-3.563878
46.H	-2.224078	-2.020624	-3.066214
47.C	1.269501	1.498406	-2.950301
48.H	1.376145	2.534297	-3.308923
49.H	2.234051	0.980824	-3.069805
50.H	0.519400	0.987108	-3.575398

